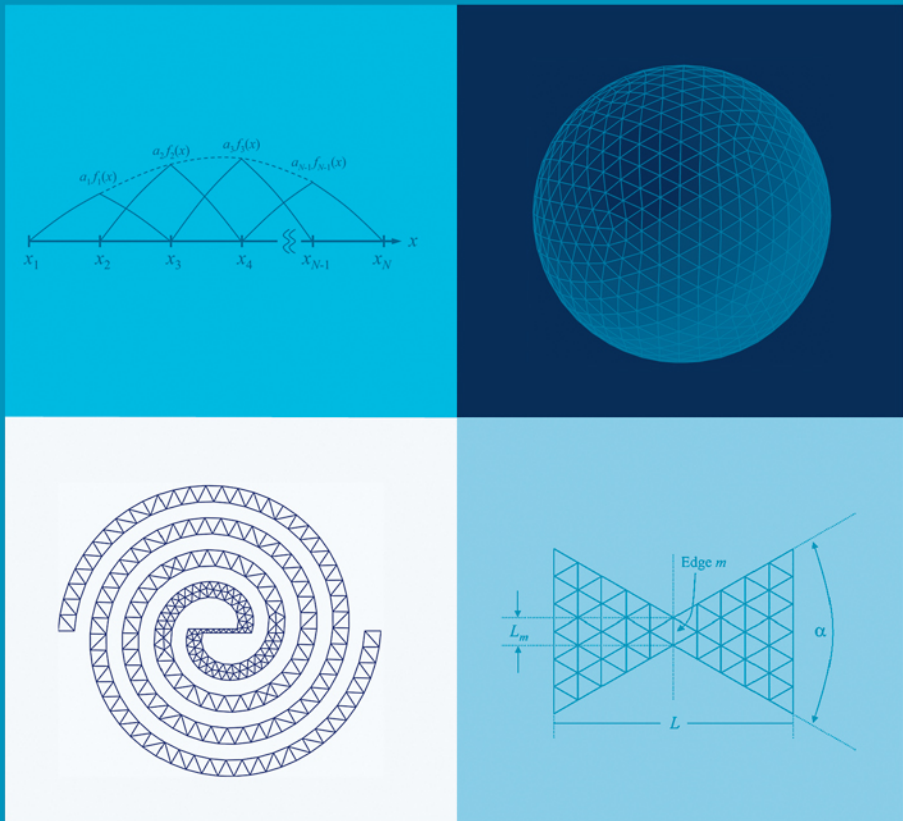


The Method of Moments in Electromagnetics



Walton C. Gibson

The Method of Moments in Electromagnetics

Walton C. Gibson

<http://www.tripointindustries.com>
kalla@tripoint.org



Chapman & Hall/CRC

Taylor & Francis Group

Boca Raton London New York

Chapman & Hall/CRC is an imprint of the
Taylor & Francis Group, an **informa** business

Chapman & Hall/CRC
Taylor & Francis Group
6000 Broken Sound Parkway NW, Suite 300
Boca Raton, FL 33487-2742

© 2008 by Taylor & Francis Group, LLC

Chapman & Hall/CRC is an imprint of Taylor & Francis Group, an Informa business

No claim to original U.S. Government works

Printed in the United States of America on acid-free paper

10 9 8 7 6 5 4 3 2 1

International Standard Book Number-13: 978-1-4200-6145-1 (Hardcover)

This book contains information obtained from authentic and highly regarded sources. Reprinted material is quoted with permission, and sources are indicated. A wide variety of references are listed. Reasonable efforts have been made to publish reliable data and information, but the author and the publisher cannot assume responsibility for the validity of all materials or for the consequences of their use.

Except as permitted under U.S. Copyright Law, no part of this book may be reprinted, reproduced, transmitted, or utilized in any form by any electronic, mechanical, or other means, now known or hereafter invented, including photocopying, microfilming, and recording, or in any information storage or retrieval system, without written permission from the publishers.

For permission to photocopy or use material electronically from this work, please access www.copyright.com (<http://www.copyright.com/>) or contact the Copyright Clearance Center, Inc. (CCC) 222 Rosewood Drive, Danvers, MA 01923, 978-750-8400. CCC is a not-for-profit organization that provides licenses and registration for a variety of users. For organizations that have been granted a photocopy license by the CCC, a separate system of payment has been arranged.

Trademark Notice: Product or corporate names may be trademarks or registered trademarks, and are used only for identification and explanation without intent to infringe.

Library of Congress Cataloging-in-Publication Data

Gibson, Walton C.

The method of moments in electromagnetics / Walton C. Gibson.

p. cm.

Includes bibliographical references and index.

ISBN 978-1-4200-6145-1 (alk. paper)

1. Electromagnetism--Data processing. 2. Electromagnetic fields--Mathematical models. 3. Moments method (Statistics) 4. Electromagnetic theory--Data processing. 5. Integral equations--Numerical solutions. I. Title.

QC665.E4.G43 2008

530.14'1015118--dc22

2007037311

Visit the Taylor & Francis Web site at
<http://www.taylorandfrancis.com>

and the CRC Press Web site at
<http://www.crcpress.com>

Contents

Preface	ix
Acknowledgments	xiii
About the Author	xv
Chapter 1 Computational Electromagnetics	1
1.1 Computational Electromagnetics Algorithms	1
1.1.1 Low-Frequency Methods	2
1.1.2 High-Frequency Methods	2
References	4
Chapter 2 A Brief Review of Electromagnetics	5
2.1 Maxwell's Equations	5
2.2 Electromagnetic Boundary Conditions	6
2.3 Formulations for Radiation	6
2.3.1 Three-Dimensional Green's Function	8
2.3.2 Two-Dimensional Green's Function	9
2.4 Vector Potentials	10
2.4.1 Magnetic Vector Potential	11
2.4.2 Electric Vector Potential	12
2.4.3 Comparison of Radiation Formulas	13
2.5 Near and Far Fields	14
2.5.1 Near Field	15
2.5.2 Far Field	16
2.6 Equivalent Problems	18
2.6.1 Surface Equivalent	18
2.6.2 Physical Equivalent	20
2.7 Surface Integral Equations	25
2.7.1 Electric Field Integral Equation	25
2.7.2 Magnetic Field Integral Equation	26
2.7.3 Combined Field Integral Equation	28

References	30
Chapter 3 The Method of Moments	33
3.1 Electrostatic Problems	33
3.1.1 Charged Wire	34
3.1.2 Charged Plate	39
3.2 The Method of Moments	43
3.2.1 Point Matching	44
3.2.2 Galerkin's Method	44
3.3 Common Two-Dimensional Basis Functions	45
3.3.1 Pulse Functions	45
3.3.2 Piecewise Triangular Functions	45
3.3.3 Piecewise Sinusoidal Functions	46
3.3.4 Entire-Domain Functions	47
3.3.5 Number of Basis Functions	47
3.4 Solution of Matrix Equations	48
3.4.1 Gaussian Elimination	48
3.4.2 LU Decomposition	50
3.4.3 Condition Number	52
3.4.4 Iterative Methods	53
3.4.5 Examples	57
3.4.6 Commonly Used Matrix Algebra Software	58
References	61
Chapter 4 Thin Wires	63
4.1 Thin Wire Approximation	63
4.2 Thin Wire Excitations	65
4.2.1 Delta-Gap Source	65
4.2.2 Magnetic Frill	66
4.2.3 Plane Wave	67
4.3 Solving Hallén's Equation	68
4.3.1 Symmetric Problems	69
4.3.2 Asymmetric Problems	71
4.4 Solving Pocklington's Equation	72
4.4.1 Solution by Pulse Functions and Point Matching	73
4.5 Thin Wires of Arbitrary Shape	73
4.5.1 Redistribution of EFIE Differential Operators	74
4.5.2 Solution Using Triangle Basis and Testing Functions	75
4.5.3 Solution Using Sinusoidal Basis and Testing Functions	77
4.5.4 Lumped and Distributed Impedances	78
4.6 Examples	79
4.6.1 Comparison of Thin Wire Models	79
4.6.2 Circular Loop Antenna	83
4.6.3 Folded Dipole Antenna	86
4.6.4 Two-Wire Transmission Line	87

4.6.5	Matching a Yagi Antenna	89
References		94
Chapter 5	Two-Dimensional Problems	95
5.1	Two-Dimensional EFIE	95
5.1.1	EFIE for a Strip: TM Polarization	95
5.1.2	Generalized EFIE: TM Polarization	100
5.1.3	EFIE for a Strip: TE Polarization	102
5.1.4	Generalized EFIE: TE Polarization	107
5.2	Two-Dimensional MFIE	109
5.2.1	MFIE: TM Polarization	109
5.2.2	MFIE: TE Polarization	111
5.3	Examples	113
5.3.1	Scattering by an Infinite Cylinder: TM Polarization	113
5.3.2	Scattering by an Infinite Cylinder: TE Polarization	115
References		124
Chapter 6	Bodies of Revolution	125
6.1	BOR Surface Description	125
6.2	Surface Current Expansion on a BOR	126
6.3	EFIE for a Conducting BOR	127
6.3.1	EFIE Matrix Elements	127
6.3.2	Excitation	130
6.3.3	Scattered Field	134
6.4	MFIE for a Conducting BOR	136
6.4.1	MFIE Matrix Elements	137
6.4.2	Excitation	140
6.4.3	Scattered Field	141
6.5	Notes on Software Implementation	141
6.5.1	Parallelization	141
6.5.2	Convergence	142
6.6	Examples	142
6.6.1	Galaxy	142
6.6.2	Conducting Sphere	142
6.6.3	EMCC Benchmark Targets	145
6.6.4	Biconic Reentry Vehicle	152
6.6.5	Summary of Examples	159
References		159
Chapter 7	Three-Dimensional Problems	161
7.1	Representation of Three-Dimensional Surfaces	161
7.2	Surface Currents on a Triangle	164
7.2.1	Edge Finding Algorithm	165
7.3	EFIE for Three-Dimensional Conducting Surfaces	167
7.3.1	EFIE Matrix Elements	167

7.3.2	Singular Matrix Element Evaluation	168
7.3.3	EFIE Excitation Vector Elements	176
7.3.4	Radiated Field	178
7.4	MFIE for Three-Dimensional Conducting Surfaces	179
7.4.1	MFIE Matrix Elements	179
7.4.2	MFIE Excitation Vector Elements	184
7.4.3	Radiated Field	184
7.4.4	Accuracy of RWG Functions in MFIE	184
7.5	Notes on Software Implementation	185
7.5.1	Memory Management	185
7.5.2	Parallelization	185
7.6	Considerations for Modeling with Triangles	187
7.6.1	Triangle Aspect Ratios	187
7.6.2	Watertight Meshes and T-Junctions	188
7.7	Examples	188
7.7.1	Serenity	189
7.7.2	RCS of a Sphere	189
7.7.3	EMCC Plate Benchmark Targets	189
7.7.4	Strip Dipole Antenna	198
7.7.5	Bowtie Antenna	199
7.7.6	Archimedean Spiral Antenna	201
7.7.7	Summary of Examples	204
	References	205
Chapter 8	The Fast Multipole Method	209
8.1	The Matrix-Vector Product	210
8.2	Addition Theorem	210
8.2.1	Wave Translation	212
8.3	FMM Matrix Elements	213
8.3.1	EFIE Matrix Elements	213
8.3.2	MFIE Matrix Elements	214
8.3.3	CFIE Matrix Elements	215
8.3.4	Matrix Transpose	215
8.4	One-Level Fast Multipole Algorithm	215
8.4.1	Grouping of Basis Functions	215
8.4.2	Near and Far Groups	216
8.4.3	Number of Multipoles	216
8.4.4	Sampling Rates and Integration	218
8.4.5	Transfer Functions	219
8.4.6	Radiation and Receive Functions	220
8.4.7	Near-Matrix Elements	220
8.4.8	Matrix-Vector Product	221
8.4.9	Computational Complexity	222
8.5	Multi-Level Fast Multipole Algorithm (MLFMA)	222
8.5.1	Grouping via Octree	222

8.5.2	Matrix-Vector Product	223
8.5.3	Interpolation Algorithms	227
8.5.4	Transfer Functions	229
8.5.5	Radiation and Receive Functions	230
8.5.6	Interpolation Steps in MLFMA	230
8.5.7	Computational Complexity	231
8.6	Notes on Software Implementation	231
8.6.1	Initial Guess in Iterative Solution	231
8.6.2	Memory Management	232
8.6.3	Parallelization	234
8.6.4	Vectorization	234
8.7	Preconditioning	235
8.7.1	Diagonal Preconditioner	235
8.7.2	Block Diagonal Preconditioner	236
8.7.3	Inverse LU Preconditioner	236
8.7.4	Sparse Approximate Inverse	237
8.8	Examples	240
8.8.1	Bistatic RCS of a Sphere	240
8.8.2	EMCC Benchmark Targets	240
8.8.3	Summary of Examples	245
	References	252
Chapter 9	Integration	255
9.1	One-Dimensional Integration	255
9.1.1	Centroidal Approximation	255
9.1.2	Trapezoidal Rule	256
9.1.3	Simpson's Rule	258
9.1.4	One-Dimensional Gaussian Quadrature	259
9.2	Integration over Triangles	260
9.2.1	Simplex Coordinates	260
9.2.2	Radiation Integrals with a Constant Source	262
9.2.3	Radiation Integrals with a Linear Source	265
9.2.4	Gaussian Quadrature on Triangles	267
	References	269
Index		271

Preface

The method of moments for electromagnetic field problems was first described at length in Harrington's classic book,¹ and undoubtedly was in use long before that. Since that time computer technology has grown at a staggering pace, and computational electromagnetics and the moment method have followed closely behind. Though numerous journal papers and graduate theses have been dedicated to the MOM, few textbooks have been written for those who are unfamiliar with it. For a graduate student who is starting into computational electromagnetics, or the professional who needs to apply the MOM to field problems, this sets the barrier to entry fairly high.

This author feels that a new book describing the moment method in electromagnetics is necessary. The first reason is because of the lack of a good introductory graduate-level text on the moment method. Though many universities offer courses in computational electromagnetics, the course material often comprises a disjoint collection of journal papers or copies of the instructor's own notes. Many of these materials often omit key information or reference other papers, which forces the student to spend their time searching for information instead of focusing on the course material. The second reason is the hope that a concise, up-to-date reference book will significantly benefit researchers and practicing professionals in the field of CEM. This book has several key features that set it apart from others of its kind:

1. *A straightforward, systematic introduction to the moment method.* This book begins with a review of frequency-domain electromagnetic theory and develops the Green's functions and integral equations of radiation and scattering. Subsequent chapters are dedicated to solving these integral equations for thin wires, bodies of revolution, and two and three-dimensional problems. With this material behind them, the student or researcher will be well equipped for more advanced MOM topics encountered in the literature.
2. *A clear, concise summary of equations.* One of the fundamental problems encountered by this author is that expressions for MOM matrix elements are almost never found in the literature. Most often, a paper refers to another paper or to private communications, which is of no benefit to the learning student. This book derives or summarizes the matrix elements used in every MOM problem, and examples are computed using the expressions summarized in the text.

¹ R. F. Harrington, *Field Computation by Moment Methods*, Krieger Publishing Co., Inc., 1968.

3. *A focus on radiation and scattering problems.* This book is primarily focused on scattering and radiation problems. Therefore, we will consider many practical examples such as antenna impedance calculation and radar cross section prediction. Each example is presented in a straightforward manner with a careful explanation of the approach as well as explanation of the results.
4. *An up-to-date reference.* The material contained within is presented in the context of current-day computing technology and includes up-to-date material such as the fast multipole method that is now finding common use in CEM.

This book is for a one- or two-semester course in computational electromagnetics and a reference for the practicing engineer. It is expected that the reader will be familiar with time-harmonic electromagnetic fields and vector calculus, as well as differential equations and linear algebra. The reader should also have some basic experience with computer programming in a language such as C or FORTRAN or a mathematical environment such as MATLAB. Because some of the expressions in this book require the calculation of special functions, the reader at least should be aware of what they are and be able to calculate them.

This book comprises nine chapters:

Chapter 1 presents a very brief overview of computational electromagnetics and some commonly used numerical techniques in this field.

Chapter 2 begins by reviewing some necessary background material on time-harmonic electromagnetic fields. We next develop expressions for radiation and scattering, vector potentials, and the two- and three-dimensional Green's functions. We then discuss surface equivalents and derive the electric and magnetic field integral equations for conducting surfaces.

Chapter 3 introduces the solution of integral equations by converting the problem into a linear system. The method of moments is formalized, and commonly used two-dimensional basis functions are covered. We then discuss the solution of matrix equations, Gaussian elimination, LU decomposition, condition numbers, iterative solvers, and preconditioning.

Chapter 4 is dedicated to scattering and radiation by thin wires. We derive the thin wire kernel and the Hallén and Pocklington thin wire integral equations, and show how to solve them. We then apply the MOM to thin wires of arbitrary shape, and consider several practical thin wire problems.

Chapter 5 applies the moment method to two-dimensional problems. The electric and magnetic field integral equations are applied to problems of TM and TE polarization, and expressions are summarized that can be applied to general two-dimensional boundaries.

Chapter 6 considers three-dimensional objects that can be described as bodies of revolution. The application of the MOM to this problem follows the treatment of Harrington and Mautz, with additional derivations and discussion. We then look at the radar cross section predictions of rotationally symmetric objects and compare them to measurements.

Chapter 7 covers three-dimensional surfaces of arbitrary shape. We discuss modeling of surfaces by triangular facets, and devote significant effort to summarizing the expressions used to evaluate singular potential integrals over triangular elements. We then consider several radar cross section problems and the input impedance calculations of some three-dimensional antennas.

Chapter 8 introduces the fast multipole method and its use with iterative solvers and the moment method. We cover the addition theorem, wave translation, and single- and multi-level fast multipole algorithms. The treatment is concise and contains all the information required to successfully implement the FMM in a new or existing moment method code.

Chapter 9 discusses some commonly used methods of numerical integration including the trapezoidal and Simpson's rule, area coordinates, and Gaussian quadrature in one dimension and over planar triangular elements.

Throughout this text, an $e^{j\omega t}$ time convention is assumed and suppressed throughout. We use SI units except for some examples where the test articles have dimensions in inches or feet. Numbers in parentheses () refer to equations, and numbers in brackets [] are citations. Scalar quantities are written in an italic font (*a*), vectors and matrices in bold (**a**), and unit vectors written using caret notation ($\hat{\mathbf{a}}$).

Acknowledgments

This book is a result of my experience as a student of electromagnetics and as a developer of computational electromagnetics codes. My walk down this path began early with my interest in the power of the computer, as well as the mysteries behind radio waves and antennas. I received my first real introduction to electromagnetics as an undergraduate student at Auburn University, and my professor Thomas Shumpert encouraged me to pursue the subject at the graduate level. At the University of Illinois, I learned a great deal about electromagnetics from Weng Chew and my graduate advisor Jianming Jin. During my subsequent work on the Tripoint Industries code suite *lucernhammer*, I encountered many different challenges in mathematics as well as software algorithms, programming and optimization. Without the help of my many friends and colleagues, it is possible I would not have completed this path at all. Therefore, I would like to thank the following people who provided me with useful assistance, advice and information when it was needed:

Jason Amos
Michael J. Perry
John L. Griffin
Scott Kelley
Paul Burns
Jay Higley
Andy Harrison
Sally Colocco
Enrico Poggio
Bassem R. Mahafza

I would like to give extra special thanks to Sally Colocco and Andy Harrison for proofreading this manuscript prior to publication.

About the Author



Walton C. Gibson was born in Birmingham, Alabama in 1975. He received the bachelor of science degree in electrical engineering from Auburn University in 1996, and the Master of Science degree from the University of Illinois at Urbana-Champaign in 1998. His professional interests include electromagnetic theory, computational electromagnetics, radar cross section prediction, numerical algorithms and software engineering. He is the owner of Tripoint Industries, Inc., and the author of the industry-standard *lucernhammer* electromagnetic signature prediction software. He is a licensed amateur radio operator (callsign K4LLA), with interests in antenna building and low-frequency RF propagation. He currently resides in Huntsville, Alabama.

Chapter 1

Computational Electromagnetics

Before the digital computer was developed, the analysis and design of electromagnetic devices and structures were largely experimental. Once the computer and numerical languages such as FORTRAN came along, people immediately began using them to tackle electromagnetic problems that could not be solved analytically. This led to a flurry of development in a field now referred to as computational electromagnetics (CEM). Many powerful numerical analysis techniques have been developed in this area in the last 50 years. As the power of the computer continues to grow, so do the nature of the algorithms applied as well as the complexity and size of the problems that can be solved.

While the data gleaned from experimental measurements are invaluable, the entire process can be costly in terms of money and the manpower required to do the required machine work, assembly, and measurements at the range. One of the fundamental drives behind reliable computational electromagnetics algorithms is the ability to simulate the behavior of devices and systems before they are actually built. This allows the engineer to engage in levels of customization and optimization that would be painstaking or even impossible if done experimentally. CEM also helps to provide fundamental insights into electromagnetic problems through the power of computation and computer visualization, making it one of the most important areas of engineering today.

1.1 COMPUTATIONAL ELECTROMAGNETICS ALGORITHMS

The extremely wide range of electromagnetic problems has led to the development of many different CEM algorithms, each with its own benefits and limitations. These algorithms are typically classified as so-called “exact” or “low-frequency” and “approximate” or “high-frequency” methods and further sub-classified into time- or frequency-domain methods. We will quickly summarize some of the most commonly used methods to provide some context in how the moment method fits in the CEM environment.

1.1.1 Low-Frequency Methods

Low-frequency (LF) methods are so-named because they solve Maxwell's Equations with no implicit approximations and are typically limited to problems of small electrical size due to limitations of computation time and system memory. Though computers continue to grow more powerful and solve problems of ever increasing size, this nomenclature will likely remain common in the literature.

1.1.1.1 Finite Difference Time Domain Method

The finite difference time-domain (FDTD) method [1, 2] uses the method of finite differences to solve Maxwell's Equations in the time domain. Application of the FDTD method is usually very straightforward: the solution domain is typically discretized into small rectangular or curvilinear elements, with a “leap frog” in time used to compute the electric and magnetic fields from one another. FDTD excels at analysis of inhomogeneous and nonlinear media, though its demands for system memory are high due to the discretization of the entire solution domain, and it suffers from dispersion issues as well and the need to artificially truncate the solution boundary. FDTD finds applications in packaging and waveguide problems, as well as in the study of wave propagation in complex dielectrics.

1.1.1.2 Finite Element Method

The finite element method (FEM) [3, 4] is a method used to solve frequency-domain boundary valued electromagnetic problems by using a variational form. It can be used with two- and three-dimensional canonical elements of differing shape, allowing for a highly accurate discretization of the solution domain. The FEM is often used in the frequency domain for computing the frequency field distribution in complex, closed regions such as cavities and waveguides. As in the FDTD method, the solution domain must be truncated, making the FEM unsuitable for radiation or scattering problems unless combined with a boundary integral equation approach [3].

1.1.1.3 Method of Moments

The method of moments (MOM) is a technique used to solve electromagnetic boundary or volume integral equations in the frequency domain. Because the electromagnetic sources are the quantities of interest, the MOM is very useful in solving radiation and scattering problems. In this book, we focus on the practical solution of boundary integral equations of radiation and scattering using this method.

1.1.2 High-Frequency Methods

Electromagnetic problems of large size have existed long before the computers that could solve them. Common examples of larger problems are those of radar cross

section prediction and calculation of an antenna's radiation pattern when mounted on a large structure. Many approximations have been made to the equations of radiation and scattering to make these problems tractable. Most of these treat the fields in the asymptotic or high-frequency (HF) limit and employ ray-optics and edge diffraction. When the problem is electrically large, many asymptotic methods produce results that are accurate enough on their own or can be used as a "first pass" before a more accurate though computationally demanding method is applied.

1.1.2.1 Geometrical Theory of Diffraction

The geometrical theory of diffraction (GTD) [5, 6] uses ray-optics to determine electromagnetic wave propagation. The spreading, amplitude intensity and decay in a ray bundle are computed using from Fermat's principle and the radius of curvature at reflection points. The GTD attempts to account for the fields diffracted by edges, allowing for a calculation of the fields in shadow regions. The GTD is fast but often yields poor accuracy for more complex geometries.

1.1.2.2 Physical Optics

Physical optics (PO) [7] is a method for approximating the high-frequency surface currents, allowing a boundary integration to be performed to obtain the fields. As we will see, the PO and the MOM are used to solve the same integral equation, though the MOM calculates the surface currents directly instead of approximating them. While robust, PO does not account for the fields diffracted by edges or those from multiple reflections, so supplemental corrections are usually added to it. The PO method is used extensively in high-frequency reflector antenna analyses, as well as many radar cross section prediction codes.

1.1.2.3 Physical Theory of Diffraction

The physical theory of diffraction (PTD) [8, 9] is a means for supplementing the PO solution by adding the effects of nonuniform currents at the diffracting edges of an object. PTD is commonly used in high-frequency radar cross section and scattering analyses.

1.1.2.4 Shooting and Bouncing Rays

The shooting and bouncing ray (SBR) method [10, 11] was developed to predict the multiple-bounce backscatter from complex objects. It uses the ray-optics model to determine the path and amplitude of a ray bundle, but uses a PO-based scheme that integrates surface currents deposited by the ray at each bounce point. The SBR method is often used in scattering codes to account for multiple reflections on a surface or that encountered inside a cavity, and as such it supplements PO and the PTD. The SBR method is also used to predict wave propagation and scattering

in complex urban environments to determine the coverage for cellular telephone service.

REFERENCES

- [1] A. Taflove and S. C. Hagness, *Computational Electrodynamics: The Finite-Difference Time-Domain Method*. Artech House, 3rd ed., 2005.
- [2] K. Kunz and R. Luebbers, *The Finite Difference Time Domain Method for Electromagnetics*. CRC Press, 1993.
- [3] J. Jin, *The Finite Element Method in Electromagnetics*. John Wiley and Sons, 1993.
- [4] J. L. Volakis, A. Chatterjee, and L. C. Kempel, *Finite Element Method for Electromagnetics*. IEEE Press, 1998.
- [5] J. B. Keller, “Geometrical theory of diffraction,” *J. Opt. Soc. Amer.*, vol. 52, 116–130, February 1962.
- [6] R. G. Kouyoumjian and P. H. Pathak, “A uniform geometrical theory of diffraction for an edge in a perfectly conducting surface,” *Proc. IEEE*, vol. 62, 1448–1461, November 1974.
- [7] C. A. Balanis, *Advanced Engineering Electromagnetics*. John Wiley and Sons, 1989.
- [8] P. Ufimtsev, “Approximate computation of the diffraction of plane electromagnetic waves at certain metal bodies (i and ii),” *Sov. Phys. Tech.*, vol. 27, 1708–1718, August 1957.
- [9] A. Michaeli, “Equivalent edge currents for arbitrary aspects of observation,” *IEEE Trans. Antennas Propagat.*, vol. 23, 252–258, March 1984.
- [10] S. L. H. Ling and R. Chou, “Shooting and bouncing rays: Calculating the RCS of an arbitrarily shaped cavity,” *IEEE Trans. Antennas Propagat.*, vol. 37, 194–205, February 1989.
- [11] S. L. H. Ling and R. Chou, “High-frequency RCS of open cavities with rectangular and circular cross sections,” *IEEE Trans. Antennas Propagat.*, vol. 37, 648–652, May 1989.

Chapter 2

A Brief Review of Electromagnetics

Solving electromagnetic problems requires the application of Maxwell's Equations with the appropriate formulation and boundary conditions. In this chapter we present a review of the electromagnetic theory pertinent to moment method problems. We will summarize Maxwell's Equations and formulations for radiation, and derive Green's functions introduced in those relationships. We will then discuss vector potentials, near and far radiated fields, and equivalent problems. We then derive the surface integral equations of radiation and scattering, which we solve using the moment method in subsequent chapters.

2.1 MAXWELL'S EQUATIONS

Given a homogeneous medium with constituent parameters ϵ and μ , the electric and magnetic fields must satisfy the frequency-domain Maxwell equations

$$\nabla \times \mathbf{E} = -\mathbf{M} - j\omega\mu\mathbf{H} \quad (2.1)$$

$$\nabla \times \mathbf{H} = \mathbf{J} + j\omega\epsilon\mathbf{E} \quad (2.2)$$

$$\nabla \cdot \mathbf{D} = q_e \quad (2.3)$$

$$\nabla \cdot \mathbf{B} = q_m \quad (2.4)$$

where $\mathbf{D} = \epsilon\mathbf{E}$, $\mathbf{B} = \mu\mathbf{H}$, and the time dependence $e^{j\omega t}$ has been assumed and will be suppressed throughout this text. Though the magnetic current \mathbf{M} and charge q_m are not physically realizable quantities, they are often employed as mathematical tools to solve radiation and scattering problems, as discussed in Section 2.6.

2.2 ELECTROMAGNETIC BOUNDARY CONDITIONS

At the interface between regions of different dielectric parameters, the generalized electromagnetic boundary conditions are written as

$$-\hat{\mathbf{n}} \times (\mathbf{E}_2 - \mathbf{E}_1) = \mathbf{M}_s \quad (2.5)$$

$$\hat{\mathbf{n}} \times (\mathbf{H}_2 - \mathbf{H}_1) = \mathbf{J}_s \quad (2.6)$$

$$\hat{\mathbf{n}} \cdot (\mathbf{D}_2 - \mathbf{D}_1) = q_e \quad (2.7)$$

$$\hat{\mathbf{n}} \cdot (\mathbf{B}_2 - \mathbf{B}_1) = q_m \quad (2.8)$$

where any of \mathbf{M} , \mathbf{J} , q_e or q_m may be present, and $\hat{\mathbf{n}}$ is the normal vector on the interface pointing from region 2 to 1. For the interface between a dielectric (region 2) and a perfect electric conductor (PEC, region 1), the boundary conditions become

$$-\hat{\mathbf{n}} \times \mathbf{E}_2 = 0 \quad (2.9)$$

$$\hat{\mathbf{n}} \times \mathbf{H}_2 = \mathbf{J}_s \quad (2.10)$$

$$\hat{\mathbf{n}} \cdot \mathbf{D}_2 = q_e \quad (2.11)$$

$$\hat{\mathbf{n}} \cdot \mathbf{B}_2 = 0 \quad (2.12)$$

and between a dielectric and perfect magnetic conductor (PMC) they are

$$-\hat{\mathbf{n}} \times \mathbf{E}_2 = \mathbf{M}_s \quad (2.13)$$

$$\hat{\mathbf{n}} \times \mathbf{H}_2 = 0 \quad (2.14)$$

$$\hat{\mathbf{n}} \cdot \mathbf{D}_2 = 0 \quad (2.15)$$

$$\hat{\mathbf{n}} \cdot \mathbf{B}_2 = q_m \quad (2.16)$$

2.3 FORMULATIONS FOR RADIATION

The electromagnetic radiation problem involves obtaining the fields everywhere in space due to a set of electric and magnetic currents. Scattering problems can be considered as radiation problems where local currents are generated by a different set of currents or an impressed field. Let us start from first principles and derive an integral equation of radiation when only electric current \mathbf{J} and charge q_e exist ($\mathbf{M} = q_m = 0$). To begin, we take the curl of (2.1) and combine it with (2.2) to get

$$\nabla \times \nabla \times \mathbf{E} = -j\omega\mu\nabla \times \mathbf{H} = \omega^2\mu\epsilon\mathbf{E} - j\omega\mu\mathbf{J} \quad (2.17)$$

or

$$\nabla \times \nabla \times \mathbf{E} - \omega^2\mu\epsilon\mathbf{E} = -j\omega\mu\mathbf{J} \quad (2.18)$$

Using the vector identity

$$\nabla \times \nabla \times \mathbf{E} = \nabla(\nabla \cdot \mathbf{E}) - \nabla^2\mathbf{E} \quad (2.19)$$

we write this as

$$\nabla(\nabla \cdot \mathbf{E}) - \nabla^2 \mathbf{E} - k^2 \mathbf{E} = -j\omega\mu\mathbf{J} \quad (2.20)$$

where k is the wavenumber, $k = w\sqrt{\mu\epsilon} = 2\pi/\lambda$. Substituting (2.3) into the above we get

$$\nabla^2 \mathbf{E} + k^2 \mathbf{E} = j\omega\mu\mathbf{J} + \frac{\nabla q_e}{\epsilon} \quad (2.21)$$

Employing the equation of continuity

$$\nabla \cdot \mathbf{J} = -j\omega q_e \quad (2.22)$$

allows us to obtain

$$\nabla^2 \mathbf{E} + k^2 \mathbf{E} = j\omega\mu\mathbf{J} - \frac{1}{j\omega\epsilon} \nabla(\nabla \cdot \mathbf{J}) \quad (2.23)$$

Since Maxwell's Equations are linear, we can consider \mathbf{J} to be a superposition of point sources distributed over some volume. Therefore, if we know the response of a point source, we can solve the original problem by integrating this response over the volume. We now make use of this idea to convert (2.23) into an integral equation. Since (2.23) comprises three separate scalar equations, let us consider just the \hat{x} component, which is

$$\nabla^2 E_x + k^2 E_x = j\omega\mu(J_x + \frac{1}{k^2} \frac{\partial}{\partial x} \nabla \cdot \mathbf{J}) \quad (2.24)$$

We now introduce the Green's function $G(\mathbf{r}, \mathbf{r}')$, which satisfies the scalar Helmholtz equation [1]

$$\nabla^2 G(\mathbf{r}, \mathbf{r}') + k^2 G(\mathbf{r}, \mathbf{r}') = -\delta(\mathbf{r}, \mathbf{r}') \quad (2.25)$$

and assuming that $G(\mathbf{r}, \mathbf{r}')$ is known, we can obtain E_x via

$$E_x(\mathbf{r}) = -j\omega\mu \iiint_V G(\mathbf{r}, \mathbf{r}') \left[J_x(\mathbf{r}') + \frac{1}{k^2} \frac{\partial}{\partial x} \nabla' \cdot \mathbf{J}(\mathbf{r}') \right] d\mathbf{r}' \quad (2.26)$$

Generalizing to the full vector form, we write

$$\mathbf{E}(\mathbf{r}) = -j\omega\mu \iiint_V G(\mathbf{r}, \mathbf{r}') \left[\mathbf{J}(\mathbf{r}') + \frac{1}{k^2} \nabla' \nabla' \cdot \mathbf{J}(\mathbf{r}') \right] d\mathbf{r}' \quad (2.27)$$

where the integral is performed over the support of \mathbf{J} . By a similar derivation, the radiated magnetic field due to magnetic current \mathbf{M} and charge q_m is

$$\mathbf{H}(\mathbf{r}) = -j\omega\epsilon \iiint_V G(\mathbf{r}, \mathbf{r}') \left[\mathbf{M}(\mathbf{r}') + \frac{1}{k^2} \nabla' \nabla' \cdot \mathbf{M}(\mathbf{r}') \right] d\mathbf{r}' \quad (2.28)$$

To use these equations, we must now find the solution to (2.25) and obtain $G(\mathbf{r}, \mathbf{r}')$.

2.3.1 Three-Dimensional Green's Function

To solve the three-dimensional scalar Helmholtz equation

$$\nabla^2 G(\mathbf{r}, \mathbf{r}') + k^2 G(\mathbf{r}, \mathbf{r}') = -\delta(\mathbf{r}, \mathbf{r}') \quad (2.29)$$

we will first consider the homogeneous version, and then match the boundary conditions of the inhomogeneous case to obtain a unique solution. Since $G(\mathbf{r}, \mathbf{r}')$ is the solution for a point electromagnetic source, it must exhibit spherical symmetry in three dimensions. Therefore, we will retain only the radial term of the Laplacian and write

$$\nabla^2 G = \frac{1}{r^2} \frac{d}{dr} \left(r^2 \frac{dG}{dr} \right) = \frac{d^2 G}{dr^2} + \frac{2}{r} \frac{dG}{dr} \quad (2.30)$$

Next, we observe that

$$\frac{1}{r} \frac{d^2(rG)}{dr^2} = \frac{1}{r} \frac{d}{dr} \left[r \frac{dG}{dr} + G \right] = \frac{d^2 G}{dr^2} + \frac{2}{r} \frac{dG}{dr} \quad (2.31)$$

and if we substitute in the function rG for $r > 0$, we can write

$$\frac{d^2(rG)}{dr^2} + k^2(rG) = 0 \quad (2.32)$$

Via inspection, we can now write

$$G = A \frac{e^{-jkr}}{r} + B \frac{e^{jkr}}{r} \quad (2.33)$$

which comprises incoming and outgoing waves. Because the solution must contain only outgoing waves and we have used the time factor $e^{j\omega t}$, we will retain only the first term, hence

$$G = A \frac{e^{-jkr}}{r} \quad (2.34)$$

Since the value of the Green's function depends only on the relative distance r between the source and observation points \mathbf{r} and \mathbf{r}' , we will use the notation $G(\mathbf{r}, \mathbf{r}')$, where $r = |\mathbf{r} - \mathbf{r}'|$. We should point out that the phase convention of the exponential in the Green's function is not standard throughout the literature. The phase as defined in (2.34) is standard in most electrical engineering references, however other references [2, 3] define the Green's function with a positive exponent, assuming the time harmonic term $e^{-j\omega t}$.

We must now match the boundary conditions to determine a unique solution solution. Since the wave must decay to zero with increasing r , this requires that $G(\mathbf{r}, \mathbf{r}') \rightarrow 0$ as $r \rightarrow \infty$. The expression for $G(\mathbf{r}, \mathbf{r}')$ already satisfies this condition as written. We must now match it at the location of the point source ($r = 0$), allowing us to determine A . To do so, let us integrate (2.25) over a spherical volume of radius

a around the source. Substituting (2.34) for $G(\mathbf{r}, \mathbf{r}')$, we get

$$A \iiint_V \left[\nabla \cdot \nabla \left(\frac{e^{-jkr}}{r} \right) + k^2 \frac{e^{-jkr}}{r} \right] dV = -1 \quad (2.35)$$

To evaluate the the first term, we use the divergence theorem to write

$$\iiint_V \nabla \cdot \nabla \left(\frac{e^{-jkr}}{r} \right) dV = \iint_S \hat{\mathbf{n}} \cdot \nabla \left(\frac{e^{-jkr}}{r} \right) dS \quad (2.36)$$

On the sphere, $\hat{\mathbf{n}} = \hat{\mathbf{r}}$, therefore

$$\iint_S \hat{\mathbf{r}} \cdot \nabla \left(\frac{e^{-jkr}}{r} \right) dS = \iint_S \frac{\partial}{\partial r} \left(\frac{e^{-jkr}}{r} \right) dS \quad (2.37)$$

which is

$$4\pi a^2 \left[\frac{\partial}{\partial r} \left(\frac{e^{-jkr}}{r} \right) \right]_{r=a} \quad (2.38)$$

Taking the limit as $a \rightarrow 0$, we get

$$\lim_{a \rightarrow 0} 4\pi a^2 \left[\frac{\partial}{\partial r} \left(\frac{e^{-jkr}}{r} \right) \right]_{r=a} = -4\pi \quad (2.39)$$

The second term is

$$k^2 \int_0^a \frac{e^{-jkr}}{r} 4\pi r^2 dr = 4\pi k^2 \int_0^a r e^{-jkr} dr \quad (2.40)$$

By inspection, this integral tends to zero as $a \rightarrow 0$. Therefore,

$$A = \frac{1}{4\pi} \quad (2.41)$$

and

$$G(\mathbf{r}, \mathbf{r}') = \frac{e^{-jk|\mathbf{r}-\mathbf{r}'|}}{4\pi|\mathbf{r}-\mathbf{r}'|} \quad (2.42)$$

which is the electrodynamic Green's function in three dimensions.

2.3.2 Two-Dimensional Green's Function

The scalar Helmholtz equation in two dimensions can be written as

$$\nabla^2 G(\rho, \rho') + k^2 G(\rho, \rho') = -\delta(\rho, \rho') \quad (2.43)$$

The solutions to the above for the homogeneous case are the Hankel functions of the first and second kinds of order zero. Because we know the solution comprises

outgoing waves only, we write

$$G(\rho, \rho') = A H_0^{(2)}(k|\rho - \rho'|) \quad (2.44)$$

To obtain A , we use the small-argument approximation to the Hankel function [4]

$$H_0^{(2)}(k\rho) \approx 1 - j\frac{2}{\pi} \log\left(\frac{\gamma k \rho}{2}\right) \quad \rho \rightarrow 0 \quad (2.45)$$

and integrate (2.43) over a very small circle of radius a centered at the origin, yielding

$$A \iint_S \left[\nabla \cdot \nabla + k^2 \right] \left[1 - j\frac{2}{\pi} \log\left(\frac{\gamma k \rho}{2}\right) \right] dS = -1 \quad (2.46)$$

Using the divergence theorem, the first term is converted to a line integral yielding

$$-j\frac{2}{\pi} \int_0^{2\pi} \nabla \left[\log\left(\frac{\gamma k \rho}{2}\right) \right] \rho d\phi = -4j \quad (2.47)$$

The second term is

$$k^2 \int_0^a \left[1 - j\frac{2}{\pi} \log\left(\frac{\gamma k \rho}{2}\right) \right] 2\pi\rho d\rho \quad (2.48)$$

The first part of the integral goes to zero as $a \rightarrow 0$. Integrating the second part yields

$$4jk^2 \int_0^a \log\left(\frac{\gamma k \rho}{2}\right) \rho d\rho = \left[\frac{\rho^2}{2} \log\left(\frac{\gamma k \rho}{2}\right) - \frac{\rho^2}{4} \right] \Big|_0^a \quad (2.49)$$

The above goes to zero since

$$\lim_{\rho \rightarrow 0} \rho^2 \log \rho = 0 \quad (2.50)$$

Therefore,

$$A = -\frac{j}{4} \quad (2.51)$$

and the two-dimensional electrodynamic Green's function is then

$$G(\rho, \rho') = -\frac{j}{4} H_0^{(2)}(k|\rho - \rho'|) \quad (2.52)$$

2.4 VECTOR POTENTIALS

In Section 2.3 we derived expressions that allow us to determine the radiated field everywhere in space from a electric or magnetic current distribution. In many cases

of practical interest, however, it may be difficult or impossible to directly solve these equations for the fields. To remedy this, we derive a set of auxiliary vector potentials that can also be used to solve for the radiated fields. These potentials are obtained via integrals of the currents, and the radiated fields are obtained directly from the potentials. Vector potential formulations are used extensively in the analysis of antenna radiation and scattering problems, and we will use them frequently throughout this book. These formulations are very similar to the integral equations derived in Section 2.3, with slight differences that will be addressed.

2.4.1 Magnetic Vector Potential

We will first derive a magnetic vector potential for a homogeneous, source-free region. We begin by observing that since the magnetic field \mathbf{H} is always solenoidal, it can be written as the curl of another vector \mathbf{A} , which is arbitrary. Therefore, we write

$$\mathbf{H} = \frac{1}{\mu} \nabla \times \mathbf{A} \quad (2.53)$$

Substituting the above into (2.1), we get

$$\nabla \times \mathbf{E} = -j\omega \nabla \times \mathbf{A} \quad (2.54)$$

which can be written as

$$\nabla \times (\mathbf{E} + j\omega \mathbf{A}) = 0 \quad (2.55)$$

We next use the identity

$$\nabla \times (-\nabla \Phi_e) = 0 \quad (2.56)$$

to write

$$\mathbf{E} = -j\omega \mathbf{A} - \nabla \Phi_e \quad (2.57)$$

where Φ_e is an arbitrary *electric scalar potential*. We next use the identity

$$\nabla \times \nabla \times \mathbf{A} = \nabla(\nabla \cdot \mathbf{A}) - \nabla^2 \mathbf{A} \quad (2.58)$$

and take the curl of both sides of (2.53), which allows us to write

$$\mu \nabla \times \mathbf{H} = \nabla(\nabla \cdot \mathbf{A}) - \nabla^2 \mathbf{A} \quad (2.59)$$

and combining this with equation (2.2) leads to

$$\mu \mathbf{J} + j\omega \mu \epsilon \mathbf{E} = \nabla(\nabla \cdot \mathbf{A}) - \nabla^2 \mathbf{A} \quad (2.60)$$

Substituting (2.57) into the above leads to

$$\mu \mathbf{J} + j\omega \mu \epsilon (-j\omega \mathbf{A} - \nabla \Phi_e) = \nabla(\nabla \cdot \mathbf{A}) - \nabla^2 \mathbf{A} \quad (2.61)$$

which is

$$\nabla^2 \mathbf{A} + k^2 \mathbf{A} = -\mu \mathbf{J} + \nabla(\nabla \cdot \mathbf{A} + j\omega \mu \epsilon \Phi_e) \quad (2.62)$$

We have already defined the curl of \mathbf{A} in (2.53), however we have not yet defined its divergence. We are therefore free to set it to whatever we wish as long as we remain consistent with that definition in the future. Therefore, we will choose the divergence of \mathbf{A} to be

$$\nabla \cdot \mathbf{A} = -j\omega\mu\epsilon\Phi_e \quad (2.63)$$

which conveniently simplifies (2.62) to

$$\nabla^2 \mathbf{A} + k^2 \mathbf{A} = -\mu \mathbf{J} \quad (2.64)$$

which is an inhomogeneous vector Helmholtz equation for \mathbf{A} . We can now obtain the electric field everywhere in the source-free region via the expression

$$\mathbf{E} = -j\omega\mathbf{A} - \nabla\Phi_e = -j\omega\mathbf{A} - \frac{j}{\omega\mu\epsilon}\nabla(\nabla \cdot \mathbf{A}) \quad (2.65)$$

where \mathbf{A} is written in terms of a convolution of the current \mathbf{J} and the Green's function $G(\mathbf{r}, \mathbf{r}')$:

$$\mathbf{A}(\mathbf{r}) = \mu \iiint_V G(\mathbf{r}, \mathbf{r}') \mathbf{J}(\mathbf{r}') d\mathbf{r}' = \mu \iiint_V \mathbf{J}(\mathbf{r}') \frac{e^{-jk|\mathbf{r}-\mathbf{r}'|}}{4\pi|\mathbf{r}-\mathbf{r}'|} d\mathbf{r}' \quad (2.66)$$

2.4.1.1 Two-Dimensional Magnetic Vector Potential

The corresponding magnetic vector potential in two dimensions is obtained by way of (2.52) and is

$$\mathbf{A}(\boldsymbol{\rho}) = -\frac{j\mu}{4} \iint_S \mathbf{J}(\boldsymbol{\rho}') H_0^{(2)}(k|\boldsymbol{\rho} - \boldsymbol{\rho}'|) d\boldsymbol{\rho}' \quad (2.67)$$

2.4.2 Electric Vector Potential

By the symmetry of Maxwell's Equations, we can derive similar expressions for the electric vector potential \mathbf{F} . We will not repeat the derivation, and simply summarize the expressions below:

$$\mathbf{E} = \frac{1}{\epsilon} \nabla \times \mathbf{F} \quad (2.68)$$

$$\Phi_m = -\frac{1}{j\omega\mu\epsilon} \nabla \cdot \mathbf{F} \quad (2.69)$$

$$\nabla^2 \mathbf{F} + k^2 \mathbf{F} = -\epsilon \mathbf{M} \quad (2.70)$$

$$\mathbf{H} = -j\omega\mathbf{F} - \nabla\Phi_m = -j\omega\mathbf{F} - \frac{j}{\omega\mu\epsilon}\nabla(\nabla \cdot \mathbf{F}) \quad (2.71)$$

$$\mathbf{F}(\mathbf{r}) = \epsilon \iiint_V \mathbf{M}(\mathbf{r}') G(\mathbf{r}, \mathbf{r}') d\mathbf{r}' = \epsilon \iiint_V \mathbf{M}(\mathbf{r}') \frac{e^{-jk|\mathbf{r}-\mathbf{r}'|}}{4\pi|\mathbf{r}-\mathbf{r}'|} d\mathbf{r}' \quad (2.72)$$

2.4.2.1 Two-Dimensional Electric Vector Potential

Similarly, the two-dimensional electric vector potential is

$$\mathbf{F}(\rho) = -\frac{j\epsilon}{4} \iint_S \mathbf{M}(\rho') H_0^{(2)}(k|\rho - \rho'|) d\rho' \quad (2.73)$$

2.4.3 Comparison of Radiation Formulas

The expression for the electric field in (2.65) appears very similar to what was derived in (2.27). These equations are generally equivalent, however the vector differential operators on the second term of (2.65) are outside the integral sign and operate on the observation coordinates, whereas in (2.27) they are inside the integral sign and operate on the source coordinates. To show their equivalence, we must demonstrate that

$$\mathbf{I}(\mathbf{r}) = \nabla \nabla \cdot \iiint_V G(\mathbf{r}, \mathbf{r}') \mathbf{J}(\mathbf{r}') d\mathbf{r}' = \iiint_V G(\mathbf{r}, \mathbf{r}') \nabla' \nabla' \cdot \mathbf{J}(\mathbf{r}') d\mathbf{r}' \quad (2.74)$$

To begin, we make use of the vector identity

$$\nabla \cdot [G(\mathbf{r}, \mathbf{r}') \mathbf{J}(\mathbf{r}')] = [\nabla G(\mathbf{r}, \mathbf{r}')] \cdot \mathbf{J}(\mathbf{r}') + G(\mathbf{r}, \mathbf{r}') \nabla \cdot \mathbf{J}(\mathbf{r}') \quad (2.75)$$

and since $\mathbf{J}(\mathbf{r}')$ is not a function of the unprimed coordinates, we can write

$$\mathbf{I}(\mathbf{r}) = \nabla \nabla \cdot \iiint_V G(\mathbf{r}, \mathbf{r}') \mathbf{J}(\mathbf{r}') d\mathbf{r}' = \nabla \iiint_V [\nabla G(\mathbf{r}, \mathbf{r}')] \mathbf{J}(\mathbf{r}') d\mathbf{r}' \quad (2.76)$$

Because of the symmetry of the Green's function,

$$\nabla G(\mathbf{r}, \mathbf{r}') = -\nabla' G(\mathbf{r}, \mathbf{r}') \quad (2.77)$$

and the above becomes

$$\mathbf{I}(\mathbf{r}) = -\nabla \iiint_V [\nabla' G(\mathbf{r}, \mathbf{r}')] \mathbf{J}(\mathbf{r}') d\mathbf{r}' \quad (2.78)$$

By using the previous vector identity we can write the above as a sum of two integrals:

$$\mathbf{I}(\mathbf{r}) = \nabla \iiint_V G(\mathbf{r}, \mathbf{r}') \nabla' \cdot \mathbf{J}(\mathbf{r}') d\mathbf{r}' - \nabla \iiint_V \nabla' \cdot [G(\mathbf{r}, \mathbf{r}') \mathbf{J}(\mathbf{r}')] d\mathbf{r}' \quad (2.79)$$

We now make use of the divergence theorem to convert the second integral into an integral over the surface S bounding the volume V :

$$\mathbf{I}(\mathbf{r}) = \nabla \iiint_V G(\mathbf{r}, \mathbf{r}') \nabla' \cdot \mathbf{J}(\mathbf{r}') d\mathbf{r}' - \nabla \iint_S \hat{\mathbf{n}} \cdot [G(\mathbf{r}, \mathbf{r}') \mathbf{J}(\mathbf{r}')] d\mathbf{r}' \quad (2.80)$$

and since $\mathbf{J}(\mathbf{r}')$ is completely enclosed inside V , it is zero on S . Hence the second integral is zero and we are left with

$$\mathbf{I}(\mathbf{r}) = \nabla \iiint_V G(\mathbf{r}, \mathbf{r}') \nabla' \cdot \mathbf{J}(\mathbf{r}') d\mathbf{r}' \quad (2.81)$$

We must now move the remaining gradient operator under the integral sign, which results in

$$\mathbf{I}(\mathbf{r}) = - \iiint_V \nabla' G(\mathbf{r}, \mathbf{r}') \nabla' \cdot \mathbf{J}(\mathbf{r}') d\mathbf{r}' \quad (2.82)$$

where we have again employed the symmetry of the Green's function. We must now move the gradient so that it operates on the $\nabla' \cdot \mathbf{J}(\mathbf{r}')$ term. To do so we use the vector identity

$$\nabla' G(\mathbf{r}, \mathbf{r}') \nabla' \cdot \mathbf{J}(\mathbf{r}') = \nabla' [G(\mathbf{r}, \mathbf{r}') \nabla' \cdot \mathbf{J}(\mathbf{r}')] - G(\mathbf{r}, \mathbf{r}') \nabla' \nabla' \cdot \mathbf{J}(\mathbf{r}') \quad (2.83)$$

to write

$$\mathbf{I}(\mathbf{r}) = \iiint_V G(\mathbf{r}, \mathbf{r}') \nabla' \nabla' \cdot \mathbf{J}(\mathbf{r}') d\mathbf{r}' - \iiint_V \nabla' [G(\mathbf{r}, \mathbf{r}') \nabla' \cdot \mathbf{J}(\mathbf{r}')] d\mathbf{r}' \quad (2.84)$$

Now we look at the second term, which we expect should equal zero. To show this, we apply the following result of the divergence theorem:

$$\iiint_V \nabla' f(\mathbf{r}) dV = \iint_S f(\mathbf{r}) dS \quad (2.85)$$

to write the above as

$$\mathbf{I}(\mathbf{r}) = \iiint_V G(\mathbf{r}, \mathbf{r}') \nabla' \nabla' \cdot \mathbf{J}(\mathbf{r}') d\mathbf{r}' - \iint_S G(\mathbf{r}, \mathbf{r}') \nabla' \cdot \mathbf{J}(\mathbf{r}') d\mathbf{r}' \quad (2.86)$$

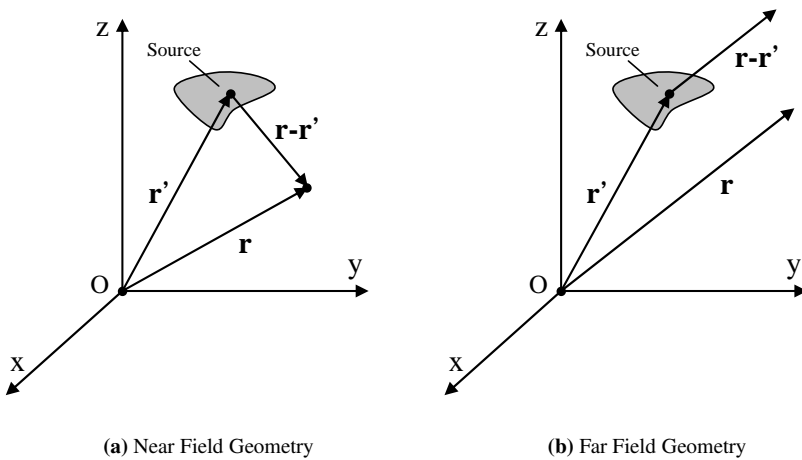
The bounding surface S can be made large enough so that $\mathbf{J}(\mathbf{r}')$ has zero value, leaving only

$$\mathbf{I}(\mathbf{r}) = \iiint_V G(\mathbf{r}, \mathbf{r}') \nabla' \nabla' \cdot \mathbf{J}(\mathbf{r}') d\mathbf{r}' \quad (2.87)$$

that is the desired result. This equivalence is valid everywhere except at points where $G(\mathbf{r}, \mathbf{r}')$ exhibits a singularity, i.e., $\mathbf{r} = \mathbf{r}'$.

2.5 NEAR AND FAR FIELDS

In practical situations one typically needs the value of the electromagnetic field at locations close to or far away from the source of radiation. The value of the *near field*, or the field close to the radiating source, is desirable in applications such as antenna fuzing and electronics packaging. The *far field*, or the field very far away from the radiating source, is most often desired in scattering and radar cross section problems. In this section, we quickly summarize the relationships for near and far field radiation, which we will refer to in later chapters.

**Figure 2.1:** Near and far field geometry.

2.5.1 Near Field

Let us obtain expressions for the fields at a point close to a radiating source, as illustrated in Figure 2.1a. Recall that the magnetic field radiated by an electric current can be obtained from (2.53) and (2.66) and is

$$\mathbf{H}(\mathbf{r}) = \frac{1}{\mu} \nabla \times \mathbf{A}(\mathbf{r}) = \nabla \times \iiint_V \mathbf{J}(\mathbf{r}') \frac{e^{-jkr}}{4\pi r} d\mathbf{r}' \quad (2.88)$$

where $r = |\mathbf{r} - \mathbf{r}'|$. Moving the curl operator under the integral sign and using the vector identity

$$\nabla \times [f \mathbf{J}(\mathbf{r}')] = (\nabla f) \times \mathbf{J}(\mathbf{r}') + f [\nabla \times \mathbf{J}(\mathbf{r}')] \quad (2.89)$$

we write the above as

$$\mathbf{H}(\mathbf{r}) = - \iiint_V \mathbf{J}(\mathbf{r}') \times \nabla \left(\frac{e^{-jkr}}{4\pi r} \right) d\mathbf{r}' \quad (2.90)$$

where $\nabla \times \mathbf{J}(\mathbf{r}') = 0$. Taking the gradient of the Green's function yields

$$\nabla \left(\frac{e^{-jkr}}{4\pi r} \right) = -(\mathbf{r} - \mathbf{r}') \left(\frac{1 + jkr}{4\pi r^3} \right) \quad (2.91)$$

and using this result we can write the expression for the magnetic field as

$$\mathbf{H}(\mathbf{r}) = - \iiint_V [(\mathbf{r} - \mathbf{r}') \times \mathbf{J}(\mathbf{r}')] \frac{1 + jkr}{4\pi r^3} d\mathbf{r}' \quad (2.92)$$

Expanding into its rectangular components, the above can be written as [1]

$$\begin{aligned} H_x(\mathbf{r}) &= \iiint_V [(z - z')J_y - (y - y')J_z] \frac{1 + jkr}{4\pi r^3} dx' dy' dz' \\ H_y(\mathbf{r}) &= \iiint_V [(x - x')J_z - (z - z')J_x] \frac{1 + jkr}{4\pi r^3} dx' dy' dz' \\ H_z(\mathbf{r}) &= \iiint_V [(y - y')J_x - (x - x')J_y] \frac{1 + jkr}{4\pi r^3} dx' dy' dz' \end{aligned} \quad (2.93)$$

and using (2.2) we obtain the corresponding electric field:

$$\begin{aligned} E_x(\mathbf{r}) &= \iiint_V [G_1 J_x + B(x - x')G_2] e^{-jkr} dx' dy' dz' \\ E_y(\mathbf{r}) &= \iiint_V [G_1 J_y + B(y - y')G_2] e^{-jkr} dx' dy' dz' \\ E_z(\mathbf{r}) &= \iiint_V [G_1 J_z + B(z - z')G_2] e^{-jkr} dx' dy' dz' \end{aligned} \quad (2.94)$$

where

$$B = (x - x')J_x + (y - y')J_y + (z - z')J_z \quad (2.95)$$

and

$$G_1 = \frac{-1 - jkr + k^2 r^2}{4\pi r^3} \quad (2.96)$$

and

$$G_2 = \frac{3 + 3jkr - k^2 r^2}{4\pi r^5} \quad (2.97)$$

We can use (2.93) and (2.94) to numerically calculate the radiated fields at any point close to a known electric current distribution. The fields due to a known magnetic current distribution can also be obtained via a derivation mirroring the above.

2.5.2 Far Field

When the observation point is located very far away from the source ($kr \gg 1$), approximations can be made that greatly simplify the computation of the radiated field. In this case the vectors \mathbf{r} and $\mathbf{r} - \mathbf{r}'$ are virtually parallel, as shown in Figure 2.1b. Under this assumption, we can reasonably approximate r as [1]

$$r = \begin{cases} r - \mathbf{r}' \cdot \hat{\mathbf{r}} & \text{for phase variations} \\ r & \text{for amplitude variations} \end{cases} \quad (2.98)$$

Looking at (2.65), we see that the first term on the right-hand side contributes to fields varying according to $1/r$ and the second term to fields that vary according to

$1/r^2, 1/r^3$, etc., because of the differential operators. In the far field we expect that only those fields varying according to $1/r$ will have significant amplitude. These components behave like a plane wave with no components along the direction of propagation. The far electric field will therefore be computed as

$$\mathbf{E}(\mathbf{r}) = -j\omega \mathbf{A}(\mathbf{r}) \quad (2.99)$$

and the magnetic field obtained from the electric field as

$$\mathbf{H}(\mathbf{r}) = \frac{1}{\eta} \hat{\mathbf{r}} \times \mathbf{E}(\mathbf{r}) \quad (2.100)$$

where we have assumed the field to be a plane wave propagating along the vector $\hat{\mathbf{r}}$.

2.5.2.1 Three-Dimensional Far Field

We can write the expression for the far-zone electric field by using (2.98) with (2.99), resulting in the well-known expression

$$\mathbf{E}(\mathbf{r}) = -\frac{j\omega\mu}{4\pi} \frac{e^{-jk r}}{r} \iiint_V \mathbf{J}(\mathbf{r}') e^{jk \mathbf{r}' \cdot \hat{\mathbf{r}}} d\mathbf{r}' \quad (2.101)$$

For scattering problems with an incident field \mathbf{E}^i and scattered far field \mathbf{E}^s , the three-dimensional radar cross section σ_{3D} is defined as [1]

$$\sigma_{3D} = 4\pi r^2 \frac{|\mathbf{E}^s|^2}{|\mathbf{E}^i|^2} = 4\pi r^2 |\mathbf{E}^s|^2 \quad (2.102)$$

where it is usually assumed that $|\mathbf{E}^i| = 1$ for computational convenience.

2.5.2.2 Two-Dimensional Far Field

In two dimensions the radiated far electric field is given by

$$\mathbf{E}(\rho) = -j\omega \mathbf{A}(\rho) = -\frac{\omega\mu}{4} \int \mathbf{J}(\rho') H_0^{(2)}(k|\rho - \rho'|) d\rho' \quad (2.103)$$

Using the large-argument approximation of the Hankel function [4]

$$H_n^{(2)}(k\rho) \approx \sqrt{\frac{2j}{\pi k\rho}} j^n e^{-jk\rho} \quad \rho \rightarrow \infty \quad (2.104)$$

and (2.98) we write

$$H_0^{(2)}(k\rho) = \sqrt{\frac{2j}{\pi k\rho}} e^{-jk\rho} e^{jk\rho' \cdot \hat{\rho}} \quad (2.105)$$

and the far electric field becomes

$$\mathbf{E}(\rho) = -\omega \mu \sqrt{\frac{j}{8\pi k}} \frac{e^{-jk\rho}}{\sqrt{\rho}} \int \mathbf{J}(\rho') e^{jk\rho' \cdot \hat{\rho}} d\rho' \quad (2.106)$$

For scattering problems with an incident field \mathbf{E}^i and scattered far field \mathbf{E}^s , the two-dimensional radar cross section σ_{2D} is defined as [1]

$$\sigma_{2D} = 2\pi r \frac{|\mathbf{E}^s|^2}{|\mathbf{E}^i|^2} = 2\pi r |\mathbf{E}^s|^2 \quad (2.107)$$

where it is usually assumed that $|\mathbf{E}^i| = 1$.

2.6 EQUIVALENT PROBLEMS

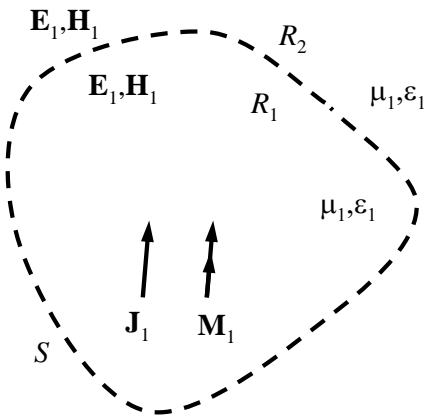
To solve radiation and scattering problems, it is often useful to formulate the problem in terms of an equivalent one that may be easier or more convenient to solve in the region of interest. These equivalents are often written in terms of surface currents that mathematically modify or eliminate the presence of obstacles present in the original problem. In this section we discuss various methods used to formulate these equivalents. Our focus on surface equivalents is an important one as many integral equations are derived from equivalent problems, and we will spend the rest of this book discussing practical approaches to solving these equations via the moment method.

2.6.1 Surface Equivalent

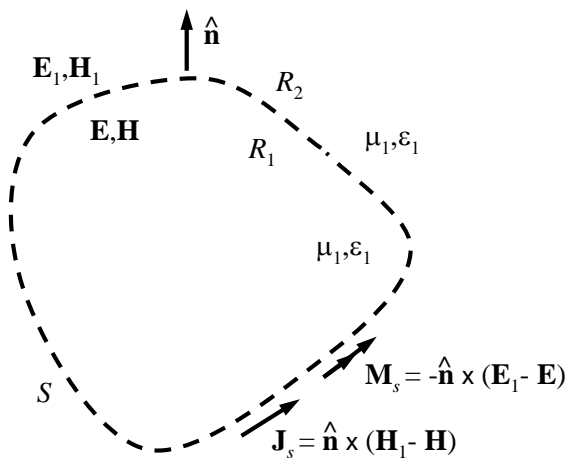
The *surface equivalence theorem* (or *Huygen's Principle*) states that every point on an advancing wavefront is itself a source of radiated waves. By this theorem, an actual radiating source can be replaced by a fictitious set of different but *equivalent* sources. These currents are placed on an arbitrary closed surface enclosing the original sources. By matching the appropriate boundary conditions, these currents will generate the same radiated field outside the closed surface as the original sources. The theorem allows us to determine the far field of a radiating structure if the near field is known, or to create a surface integral equation that can be solved for the currents induced on an object by an incident field (Section 2.7).

To begin, consider electric and magnetic currents \mathbf{J}_1 and \mathbf{M}_1 that radiate the fields \mathbf{E}_1 and \mathbf{H}_1 in a homogeneous space with properties ϵ_1 and μ_1 as shown in Figure 2.2a. To create a set of equivalent sources, we enclose \mathbf{J}_1 and \mathbf{M}_1 by a fictitious surface S dividing the space into two regions, R_1 and R_2 . We also assume the values of \mathbf{E}_1 and \mathbf{H}_1 are known everywhere on S . We now place on S the surface currents \mathbf{J}_s and \mathbf{M}_s subject to the boundary conditions

$$\mathbf{J}_s = \hat{\mathbf{n}} \times (\mathbf{H}_1 - \mathbf{H}) \quad (2.108)$$



(a) Original Problem



(b) Equivalent Problem

Figure 2.2: Surface equivalence theorem.

$$\mathbf{M}_s = -\hat{\mathbf{n}} \times (\mathbf{E}_1 - \mathbf{E}) \quad (2.109)$$

where the fields \mathbf{E} and \mathbf{H} inside S remain undefined for now. Since R_1 and R_2 have the same dielectric properties, \mathbf{J}_s and \mathbf{M}_s radiate in a homogeneous environment and (2.65) and (2.71) may be used to obtain the radiated fields everywhere in R_2 . This is called the *surface equivalent* and is depicted in Figure 2.2b. It should be noted that in this case only \mathbf{E}_1 or \mathbf{H}_1 needs to be known on S , since the other can be obtained by the Maxwell Equations (2.1) or (2.2).

Because the fields \mathbf{E} and \mathbf{H} inside S are totally arbitrary, let us further generalize the surface equivalence theorem. Consider first the problem of Figure 2.3a, where external currents \mathbf{J}_1 and \mathbf{M}_1 and internal currents \mathbf{J}_2 and \mathbf{M}_2 create the fields \mathbf{E}_a and \mathbf{H}_a everywhere. Next, consider the similar problem of Figure 2.3b, where external currents \mathbf{J}_4 and \mathbf{M}_4 and internal currents \mathbf{J}_3 and \mathbf{M}_3 create the fields \mathbf{E}_b and \mathbf{H}_b everywhere. Let us now create a problem that is *externally* equivalent to Figure 2.3a and *internally* equivalent to Figure 2.3b. To do so, the fields and sources outside S should remain the same as in Figure 2.3a and those inside S the same as in Figure 2.3b. The surface currents on S must satisfy the boundary conditions, hence

$$\mathbf{J}_s = \hat{\mathbf{n}} \times (\mathbf{H}_a - \mathbf{H}_b) \quad (2.110)$$

$$\mathbf{M}_s = -\hat{\mathbf{n}} \times (\mathbf{E}_a - \mathbf{E}_b) \quad (2.111)$$

This is illustrated in Figure 2.4a. By similar arguments, we can create an equivalent that is *internally* equivalent to Figure 2.3a and *externally* equivalent to Figure 2.3b. In this case, the currents satisfy the boundary conditions

$$\mathbf{J}_s = \hat{\mathbf{n}} \times (\mathbf{H}_b - \mathbf{H}_a) \quad (2.112)$$

$$\mathbf{M}_s = -\hat{\mathbf{n}} \times (\mathbf{E}_b - \mathbf{E}_a) \quad (2.113)$$

This is illustrated in Figure 2.4b.

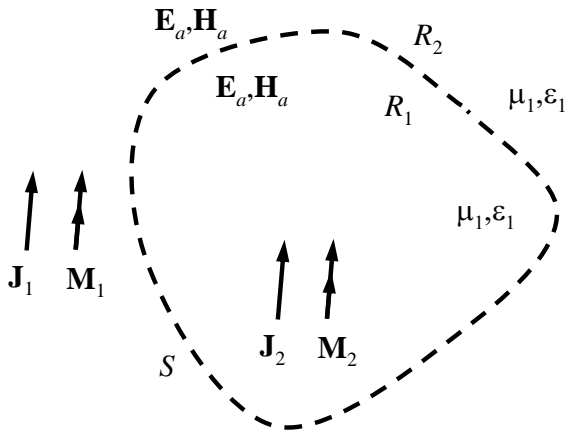
2.6.2 Physical Equivalent

Let us consider a concept very important in the area of scattering and radiation problems called the *physical equivalent*. Suppose that we have currents \mathbf{J}_1 and \mathbf{M}_1 that generate the fields \mathbf{E}_1 and \mathbf{H}_1 in a homogeneous region with parameters ϵ_1 and μ_1 . If we now introduce a conducting object into the region, the reflected (or *scattered*) fields \mathbf{E}^s and \mathbf{H}^s are created, as illustrated in Figure 2.5a. Our goal is to obtain these scattered fields, so we will create an equivalent problem that allows us to remove the conducting object and replace it with equivalent surface currents. Let us apply the boundary conditions on the electric and magnetic fields at the surface of the scatterer. Over the boundary, the total tangential electric field must be zero, hence

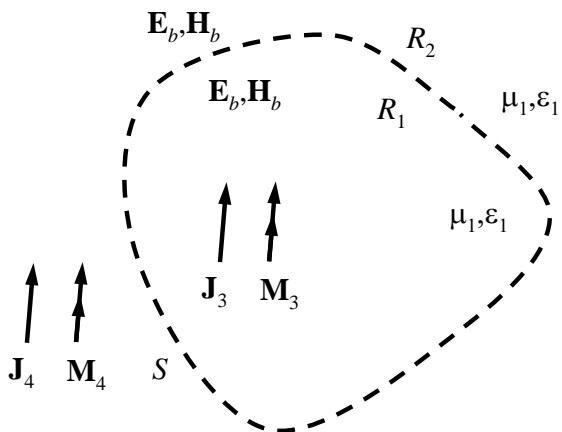
$$-\hat{\mathbf{n}} \times (\mathbf{E} - \mathbf{E}^t) = -\hat{\mathbf{n}} \times (\mathbf{E}_1 + \mathbf{E}^s) = \mathbf{M}_s = 0 \quad (2.114)$$

and the total tangential magnetic field must equal the induced electric current density:

$$\hat{\mathbf{n}} \times (\mathbf{H} - \mathbf{H}^t) = \hat{\mathbf{n}} \times (\mathbf{H}_1 + \mathbf{H}^s) = \mathbf{J}_s \quad (2.115)$$

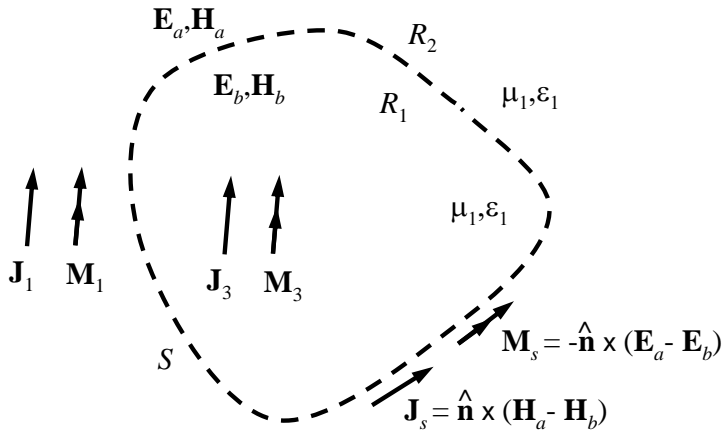


(a) Original External Problem

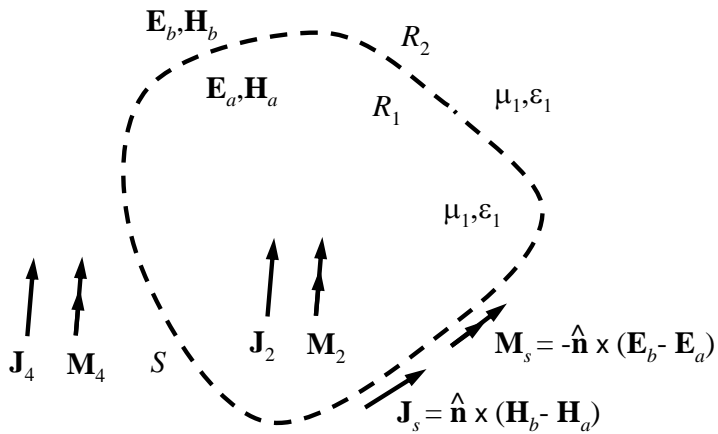


(b) Original Internal Problem

Figure 2.3: Original problems.

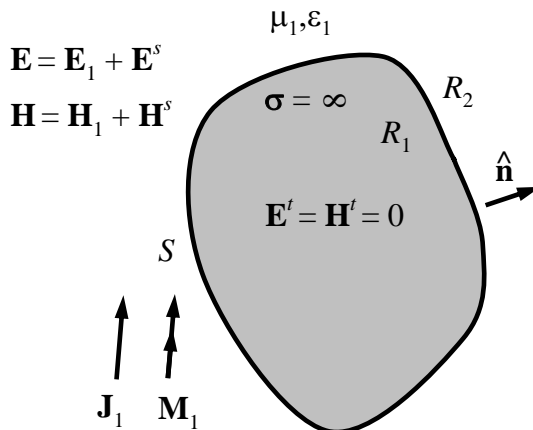


(a) External Equivalent Currents

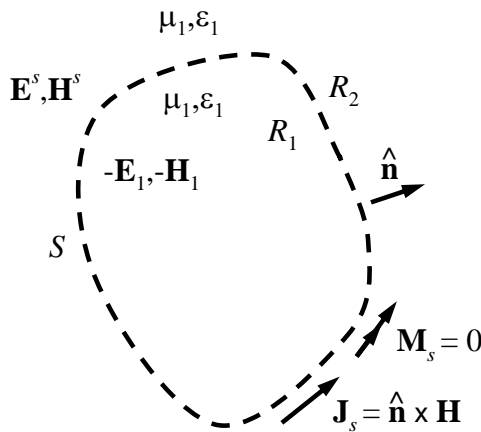


(b) Internal Equivalent Currents

Figure 2.4: Surface equivalent problems.



(a) Original Problem



(b) Equivalent Problem

Figure 2.5: Physical equivalent.

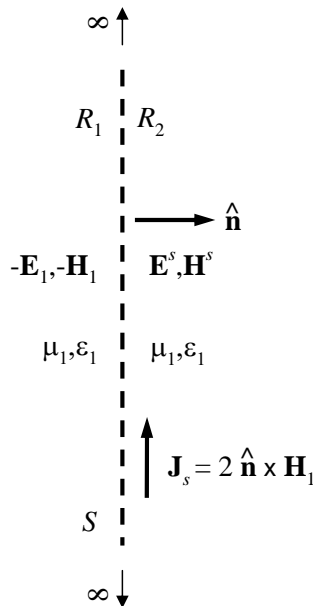


Figure 2.6: Physical optics approximation.

The above two equations form the equivalent problem shown in Figure 2.5b, which we refer to as the *physical equivalent*. Unfortunately, the induced current \mathbf{J}_s depends on the known incident field \mathbf{H}_1 as well as the the *unknown* scattered field \mathbf{H}^s . In Section 2.7 we will use (2.114) and (2.115) to create a set of integral equations that depend only on the incident field and the induced currents, which we can then solve by the method of moments.

If we assume the object to be an infinitely large and flat conductor as in Figure 2.6, the scattered magnetic field will be equal in amplitude and phase to the incident field. The induced current can then be written as

$$\mathbf{J}_s = 2\hat{\mathbf{n}} \times \mathbf{H}_1 \quad (2.116)$$

This expression is known as the physical optics (PO) approximation, and because of its simplicity it has been widely used in the areas of radar cross section prediction and reflector antenna analysis. Because its accuracy is limited to near-specular angles, its results are usually improved by the addition of edge effects through other asymptotic methods such as the physical theory of diffraction (PTD) [5, 6]. In Section 9.2.2.2, the PO approximation in (2.116) is used in the far-zone electric field integral (2.101) and evaluated analytically for planar triangles.

2.7 SURFACE INTEGRAL EQUATIONS

Scattering problems can be considered as radiation problems where the locally radiating currents are generated by other currents or fields. Antenna analysis is consequently a scattering problem, where antenna currents are excited via an externally applied voltage source. Radar cross section (RCS) problems involve incident electromagnetic radiation generated by external sources, creating currents on the scatterer that re-radiate a *scattered field*.

Radiation problems require an integration of known currents \mathbf{J} and \mathbf{M} to obtain the fields by way of (2.27) or (2.28). In scattering problems, the currents of (2.27) and (2.28) are unknown quantities. Therefore, solving a scattering problem involves two steps:

1. Solving an integral equation for unknown local currents \mathbf{J} or \mathbf{M} created by an external but known incident field \mathbf{E}^i or \mathbf{H}^i
2. Integrating the induced currents \mathbf{J} or \mathbf{M} to obtain the scattered fields \mathbf{E}^s and \mathbf{H}^s

In this section, we will derive the well-known electric and magnetic field integral equations of scattering for perfectly conducting objects, based on the physical equivalent described in Section 2.6.2.

2.7.1 Electric Field Integral Equation

The radiated electric field is obtained from the induced surface current via

$$\mathbf{E}^s(\mathbf{r}) = -j\omega\mu \iint_S G(\mathbf{r}, \mathbf{r}') \left[\mathbf{J}(\mathbf{r}') + \frac{1}{k^2} \nabla' \nabla' \cdot \mathbf{J}(\mathbf{r}') \right] d\mathbf{r}' \quad (2.117)$$

We can eliminate the dependence on $\mathbf{E}^s(\mathbf{r})$ in (2.117) by enforcing the boundary conditions on the tangential electric field:

$$\hat{\mathbf{n}}(\mathbf{r}) \times \mathbf{E}^s(\mathbf{r}) = -\hat{\mathbf{n}}(\mathbf{r}) \times \mathbf{E}^i(\mathbf{r}) \quad (2.118)$$

where $\hat{\mathbf{n}}(\mathbf{r})$ is the surface normal. This allows us to write the above in terms of the known incident electric field $\mathbf{E}_i(\mathbf{r})$ as

$$-\frac{j}{\omega\mu} \hat{\mathbf{n}}(\mathbf{r}) \times \mathbf{E}^i(\mathbf{r}) = \hat{\mathbf{n}}(\mathbf{r}) \times \iint_S G(\mathbf{r}, \mathbf{r}') \left[\mathbf{J}(\mathbf{r}') + \frac{1}{k^2} \nabla' \nabla' \cdot \mathbf{J}(\mathbf{r}') \right] d\mathbf{r}' \quad (2.119)$$

Equation (2.119) is known as the electric field integral equation (EFIE) for a perfectly conducting surface. Once solved for the unknown current $\mathbf{J}(\mathbf{r})$, the radiated field everywhere can be obtained via (2.65). The EFIE is also commonly written using the magnetic vector potential $\mathbf{A}(\mathbf{r})$ as

$$-\frac{j}{\omega\mu} \hat{\mathbf{n}}(\mathbf{r}) \times \mathbf{E}^i(\mathbf{r}) = \hat{\mathbf{n}}(\mathbf{r}) \times \left[\mathbf{A}(\mathbf{r}) + \frac{1}{k^2} \nabla \nabla \cdot \mathbf{A}(\mathbf{r}) \right] \quad (2.120)$$

$$-\frac{j}{\omega\mu} \left[\mathbf{t}(\mathbf{r}) \cdot \mathbf{E}^i(\mathbf{r}) \right] = \mathbf{t}(\mathbf{r}) \cdot \iint_S \left[1 + \frac{1}{k^2} \nabla \nabla \cdot \right] \mathbf{J}(\mathbf{r}') G(\mathbf{r}, \mathbf{r}') d\mathbf{r}' \quad (2.121)$$

where the gradient and divergence operate on the observation coordinates. Depending on the type of problem, it may be advantageous to use one form over the other, which we will do in later chapters.

The EFIE is a Fredholm integral equation of the first kind, where the current appears inside the integral sign only. Because the derivation did not impose any constraint on the shape of the scatterer, the EFIE may be applied to closed surfaces as well as open, thin objects. For thin surfaces, the current $\mathbf{J}(\mathbf{r})$ represents the vector sum of the current density on both sides of the scatterer [1].

2.7.2 Magnetic Field Integral Equation

A similar equation can also be derived by enforcing the boundary conditions on the magnetic field on the surface of a conducting object. From the physical equivalent of (2.115), the induced current $\mathbf{J}(\mathbf{r})$ on the surface is given by

$$\hat{\mathbf{n}}(\mathbf{r}) \times [\mathbf{H}^i(\mathbf{r}) + \mathbf{H}^s(\mathbf{r})] = \mathbf{J}(\mathbf{r}) \quad (2.122)$$

The scattered magnetic field is obtained via (2.53), yielding

$$\mathbf{H}_s(\mathbf{r}) = \frac{1}{\mu} \nabla \times \mathbf{A}(\mathbf{r}) = \nabla \times \iint_S G(\mathbf{r}, \mathbf{r}') \mathbf{J}(\mathbf{r}') d\mathbf{r}' \quad (2.123)$$

If we now take the limit as \mathbf{r} approaches S from the outside of the object ($\mathbf{r} \rightarrow S^+$), we can substitute the expression for \mathbf{H}_s from (2.123) into (2.122), which yields

$$\mathbf{J}(\mathbf{r}) = \hat{\mathbf{n}}(\mathbf{r}) \times \mathbf{H}^i(\mathbf{r}) + \lim_{\mathbf{r} \rightarrow S^+} \left[\hat{\mathbf{n}}(\mathbf{r}) \times \nabla \times \iint_S G(\mathbf{r}, \mathbf{r}') \mathbf{J}(\mathbf{r}') d\mathbf{r}' \right] \quad (2.124)$$

Let us now move the curl operator inside the integral sign by using the vector identity

$$\nabla \times [\mathbf{J}(\mathbf{r}') G(\mathbf{r}, \mathbf{r}')] = G(\mathbf{r}, \mathbf{r}') \nabla \times \mathbf{J}(\mathbf{r}') - \mathbf{J}(\mathbf{r}') \times \nabla G(\mathbf{r}, \mathbf{r}') \quad (2.125)$$

Since the curl operates on the observation coordinates, $\nabla \times \mathbf{J}(\mathbf{r}') = 0$, and we use the fact that $\nabla G(\mathbf{r}, \mathbf{r}') = -\nabla' G(\mathbf{r}, \mathbf{r}')$ to write (2.124) as

$$\hat{\mathbf{n}}(\mathbf{r}) \times \mathbf{H}^i(\mathbf{r}) = \mathbf{J}(\mathbf{r}) - \lim_{\mathbf{r} \rightarrow S^+} \left[\hat{\mathbf{n}}(\mathbf{r}) \times \iint_S \mathbf{J}(\mathbf{r}') \times \nabla' G(\mathbf{r}, \mathbf{r}') d\mathbf{r}' \right] \quad (2.126)$$

To evaluating the radiation integral in (2.126), we must determine its value when \mathbf{r} approaches \mathbf{r}' from outside S . To do so, we break the integral into two parts and

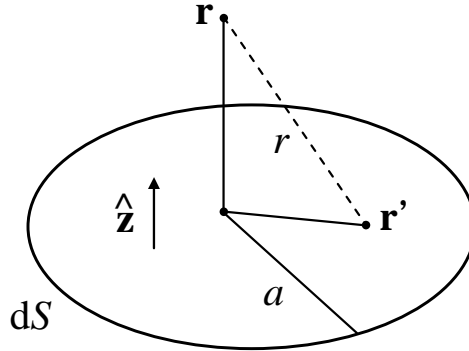


Figure 2.7: Small area in S .

compute the limit as $\mathbf{r} \rightarrow \mathbf{r}'$ following [7]:

$$\hat{\mathbf{n}}(\mathbf{r}) \times \left[\iint_{S-\delta S} \mathbf{J}(\mathbf{r}') \times \nabla' G(\mathbf{r}, \mathbf{r}') d\mathbf{r}' + \iint_{\delta S} \mathbf{J}(\mathbf{r}') \times \nabla' G(\mathbf{r}, \mathbf{r}') d\mathbf{r}' \right] \quad (2.127)$$

where δS is a very small, circular region of radius a in S located close to \mathbf{r} , as shown in Figure 2.7. Choosing the center of δS as the origin of a local cylindrical coordinate system, we can write

$$|\mathbf{r} - \mathbf{r}'| = \sqrt{(\rho')^2 + (z - z')^2} \quad (2.128)$$

and the Green's function inside δS can be written approximately as

$$G(\mathbf{r}, \mathbf{r}') = \frac{e^{-jk|\mathbf{r}-\mathbf{r}'|}}{4\pi|\mathbf{r}-\mathbf{r}'|} \approx \frac{1}{4\pi\sqrt{(\rho')^2 + (z - z')^2}} \quad |\mathbf{r} - \mathbf{r}'| \ll 1 \quad (2.129)$$

The gradient in cylindrical coordinates is

$$\nabla' = \frac{\partial}{\partial \rho'} \hat{\rho} + \frac{1}{\rho'} \frac{\partial}{\partial \phi'} \hat{\phi} + \frac{\partial}{\partial z'} \hat{z} \quad (2.130)$$

and because $\hat{\mathbf{n}}(\mathbf{r}) = \hat{\mathbf{z}}$ inside δS and $\mathbf{J}(\mathbf{r}')$ is everywhere tangential to δS , we write

$$\hat{\mathbf{z}} \times \mathbf{J}(\mathbf{r}') \times \nabla' G(\mathbf{r}, \mathbf{r}') = \mathbf{J}(\mathbf{r}') \left[\frac{\partial}{\partial z'} G(\mathbf{r}, \mathbf{r}') \right] \quad (2.131)$$

which is

$$\mathbf{J}(\mathbf{r}') \left[\frac{\partial}{\partial z'} G(\mathbf{r}, \mathbf{r}') \right] = \mathbf{J}(\mathbf{r}') \frac{z}{4\pi[(\rho')^2 + (z - z')^2]^{3/2}} \quad (2.132)$$

Because δS is very small, we will assume that $\mathbf{J}(\mathbf{r}')$ is constant and approximately equal to $\mathbf{J}(\mathbf{r})$. We now write the integral over δS as

$$\hat{\mathbf{n}}(\mathbf{r}) \times \iint_{\delta S} \mathbf{J}(\mathbf{r}') \times \nabla' G(\mathbf{r}, \mathbf{r}') d\mathbf{r}' = \frac{\mathbf{J}(\mathbf{r})}{2} \int_0^a \frac{z\rho'}{[(\rho')^2 + z^2]^{3/2}} d\rho' \quad (2.133)$$

where we have set $z' = 0$ for convenience. Integrating this expression we get

$$\frac{\mathbf{J}(\mathbf{r})}{2} \left[\frac{z}{|z|} - \frac{z}{\sqrt{a^2 + z^2}} \right] \quad (2.134)$$

and taking the limit as z approaches 0 from above yields

$$\lim_{z \rightarrow 0^+} \frac{\mathbf{J}(\mathbf{r})}{2} \left[\frac{z}{|z|} - \frac{z}{\sqrt{a^2 + z^2}} \right] = \frac{\mathbf{J}(\mathbf{r})}{2} \quad (2.135)$$

Using this result, (2.126) can now be written as

$$\hat{\mathbf{n}}(\mathbf{r}) \times \mathbf{H}^i(\mathbf{r}) = \frac{\mathbf{J}(\mathbf{r})}{2} - \hat{\mathbf{n}}(\mathbf{r}) \times \iint_{S-\delta S} \mathbf{J}(\mathbf{r}') \times \nabla' G(\mathbf{r}, \mathbf{r}') d\mathbf{r}' \quad (2.136)$$

where the contribution from the infinitesimally small area δS is now a part of the $\mathbf{J}(\mathbf{r})/2$ term. Equation (2.136) is known as the magnetic field integral equation (MFIE) for a perfectly conducting surface. In cases where the small area δS is not locally planar, such as the apex of a cone or an edge between two planar facets, a modification to (2.136) is required. It was shown in [7] that the result of (2.135) should be modified to take into account the exterior solid angle Ω_0 , resulting in

$$\frac{\Omega_0}{4\pi} \mathbf{J}(\mathbf{r}) \quad (2.137)$$

Applying the above to (2.136) results in the modified MFIE

$$\hat{\mathbf{n}}(\mathbf{r}) \times \mathbf{H}^i(\mathbf{r}) = \left[1 - \frac{\Omega_0(\mathbf{r})}{4\pi} \right] \mathbf{J}(\mathbf{r}) - \hat{\mathbf{n}}(\mathbf{r}) \times \iint_{S-\delta S} \mathbf{J}(\mathbf{r}') \times \nabla' G(\mathbf{r}, \mathbf{r}') d\mathbf{r}' \quad (2.138)$$

For smooth geometries, the exterior solid angle is $\Omega_0 = 2\pi$ at every field point and (2.138) reduces to (2.136). When an object has sharp corners or edges, the solid angle can be adjusted, as was done in [8] for three-dimensional objects with RWG basis functions (Chapter 7). We will use the MFIE of (2.136) throughout this book.

Once (2.136) is solved for the unknown current $\mathbf{J}(\mathbf{r})$, the radiated field everywhere can be obtained via (2.65). The MFIE is a Fredholm integral equation of the second kind, where $\mathbf{J}(\mathbf{r})$ appears inside and outside an integral sign. Because it is derived from the physical equivalent, in theory it will produce results equivalent to those obtained from the EFIE. However, because it is derived using a limiting argument for closed scatterers, it cannot be applied to open or thin objects like the EFIE. Due to the presence of the gradient operator, its kernel is more singular than the EFIE, and the numerical results can also differ from those of the EFIE.

2.7.3 Combined Field Integral Equation

When applied to a closed surface, the EFIE and MFIE cannot produce a unique solution for all frequencies. This is because homogeneous solutions exist that satisfy

the boundary conditions with zero incident field. These spurious solutions correspond to interior resonant modes of the object itself and radiate no field outside the object. This problem typically appears within a small bandwidth about the resonant frequency, where the results contain the desired solution plus some amount of the unwanted resonant solution. The fundamental reason for this is the tangential components of a single incident field are not sufficient to uniquely determine the surface currents at these resonant frequencies [9]. One method for eliminating this problem is the application of an extended boundary condition, where the original integral equations are modified or augmented such that the value of the field inside the object is explicitly forced to be zero [7, 9]. The dual-surface electric and magnetic integral equations (DSEFIE, DSMFIE) [10] are examples of such extended boundary conditions. In these formulations, a second surface is placed just inside the original surface. The appropriate boundary condition for the internal fields on this surface is used to generate an additional integral equation. The combination of this new equation with the original one results in a combined equation that produces a unique solution for the current at all frequencies. This method, however, requires additional effort in generating the secondary surface, and the number of unknowns in the MOM matrix system increases by a factor of two, increasing processor time and demands for system memory.

The de facto method of eliminating the resonance problem is a linear combination of the EFIE and MFIE, referred to as the combined field integral equation (CFIE). This new equation enforces the boundary conditions on the electric *and* magnetic fields and is free of spurious solutions, as the null spaces of the EFIE and MFIE differ. The CFIE is [11]

$$\text{CFIE} = \alpha \cdot \text{EFIE} + \frac{j}{k}(1 - \alpha) \cdot \text{MFIE} \quad (2.139)$$

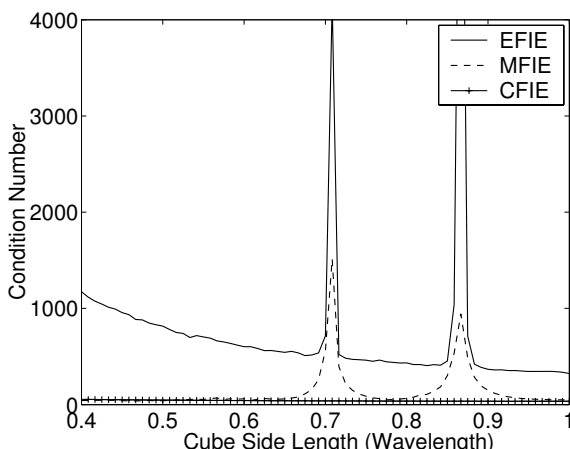


Figure 2.8: EFIE, MFIE and CFIE condition numbers for cube.

where the constant α is chosen so that the spurious solution is eliminated, with $0.2 \leq \alpha \leq 0.5$ typically representing a good choice. The condition numbers of the EFIE, MFIE and CFIE are shown in Figure 2.8 for a perfectly conducting cube of varying side length. The MOM with RWG basis functions is used, as described in Chapter 7. The resonances occur at approximately 0.7λ and 0.87λ for both the EFIE and MFIE, however the CFIE is observed to be resonance-free. Note also that the condition numbers are not of the same magnitude; this will be discussed in Section 3.4.3.

The CFIE is attractive as it does not require the generation of an auxiliary surface or the sampling of points internal to the surface. It also results in the same number of unknowns as the EFIE and MFIE by themselves. The downside of this method is that in cases where the surface has extremely narrow edges and tips, the MFIE cannot be relied on to produce accurate results [10].

REFERENCES

- [1] C. A. Balanis, *Advanced Engineering Electromagnetics*. John Wiley and Sons, 1989.
- [2] W. C. Chew, *Waves and Fields In Inhomogeneous Media*. IEEE Press, 1995.
- [3] P. M. Morse and H. Feshbach, *Methods of Theoretical Physics*. McGraw-Hill, 1953.
- [4] M. Abramowitz and I. Stegun, *Handbook of Mathematical Functions*. National Bureau of Standards, 1966.
- [5] K. M. Mitzner, “Incremental length diffraction coefficients,” Tech. Rep. AFAL-TR-73-296, Northrop Corporation, Aircraft Division, April 1974.
- [6] A. Michaeli, “Equivalent edge currents for arbitrary aspects of observation,” *IEEE Trans. Antennas Propagat.*, vol. 32, 252–257, March 1984.
- [7] N. Morita, N. Kumagai, and J. R. Mautz, *Integral Equation Methods for Electromagnetics*. Artech House, 1990.
- [8] J. M. Rius, E. Úbeda, and J. Parrón, “On the testing of the magnetic field integral equation with RWG basis functions in the method of moments,” *IEEE Trans. Antennas Propagat.*, vol. 49, 1550–1553, November 2001.
- [9] A. F. Peterson, S. L. Ray, and R. Mittra, *Computational Methods for Electromagnetics*. IEEE Press, 1998.
- [10] R. A. Shore and A. D. Yaghjian, “Dual-surface integral equations in electromagnetic scattering,” *IEEE Trans. Antennas Propagat.*, vol. 53, 1706–1709, May 2005.

- [11] W. C. Chew, J. M. Jin, E. Michielssen, and J. Song, *Fast and Efficient Algorithms in Computational Electromagnetics*. Artech House, 2001.

Chapter 3

The Method of Moments

In Chapter 2 we reviewed pertinent electromagnetic concepts and derived a set of integral equations used to solve radiation and scattering problems. For most problems of practical interest, these equations cannot be solved analytically. Therefore, we must employ computational methods to obtain a solution. In this chapter we introduce the method of moments (MOM), a numerical technique used to convert these integral equations into a linear system that can be solved numerically using a computer.

We will first analyze some simple electrostatic problems by converting their respective integral equations into a linear system. We will then formally define the MOM, discuss the expansion of an unknown function by a sum of weighted basis functions, and compare and contrast point matching and the method of Galerkin. We will then discuss common methods for solving linear equations such as Gaussian elimination and LU decomposition, as well as iterative solvers. With this done, we will be ready to consider various applications of the moment method in subsequent chapters.

3.1 ELECTROSTATIC PROBLEMS

Because electrostatic problems are relatively simple compared to electrodynamic ones, they provide a good context for introducing algorithms used to solve integral equations. Recall that the electric potential at a point \mathbf{r} due to an electric charge density q_e is given by the integral

$$\phi_e(\mathbf{r}) = \iiint_V \frac{q_e(\mathbf{r}')}{4\pi\epsilon|\mathbf{r} - \mathbf{r}'|} d\mathbf{r}' \quad (3.1)$$

If we know $q_e(\mathbf{r}')$, we can obtain the electric potential everywhere. If we instead know the electric potential but not the charge density, (3.1) becomes an integral equation for an unknown charge density. We will now solve this problem numerically for a pair of practical examples, the charged wire and plate.

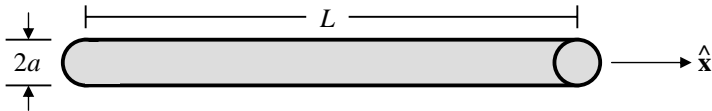


Figure 3.1: Thin wire dimensions.

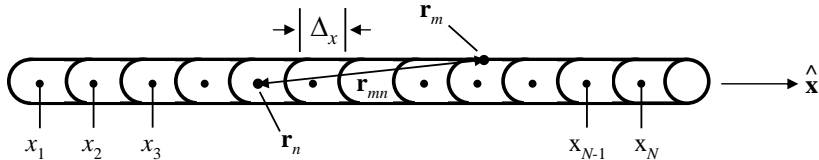


Figure 3.2: Thin wire segmentation.

3.1.1 Charged Wire

Consider a thin, conducting wire of length L and radius a oriented along the x axis, as shown in Figure 3.1. If the radius of the wire is very small compared to the length ($a \ll L$), the electric potential on the wire can be expressed via the integral

$$\phi_e(\mathbf{r}) = \int_0^L \frac{q_e(x')}{4\pi\epsilon|\mathbf{r} - \mathbf{r}'|} dx' \quad (3.2)$$

where

$$|\mathbf{r} - \mathbf{r}'| = \sqrt{(x - x')^2 + (y - y')^2} \quad (3.3)$$

With the intent of converting (3.2) into a linear system of equations, let us subdivide the wire into N subsegments, each of length Δ_x , as shown in Figure 3.2. Within each subsegment, we assume that the charge density has a constant value so that $q_e(x')$ is piecewise constant over the length of the wire. Mathematically, we write this as

$$q_e(x') = \sum_{n=1}^N a_n f_n(x') \quad (3.4)$$

where a_n are unknown weighting coefficients, and $f_n(x')$ is a set of pulse functions that are constant on one segment but zero on all other segments, i.e.

$$f_n(x') = \begin{cases} 0 & x' < (n-1)\Delta_x \\ 1 & (n-1)\Delta_x \leq x' \leq n\Delta_x \\ 0 & x' > n\Delta_x \end{cases} \quad (3.5)$$

Let us now assign the potential on the wire a value of $\phi_e = 1V$. Substituting (3.4) into (3.2) then yields

$$1 = \int_0^L \sum_{n=1}^N a_n f_n(x') \frac{1}{4\pi\epsilon|\mathbf{r} - \mathbf{r}'|} dx' \quad (3.6)$$

Using the above definition of the pulse function, we can rewrite this as

$$1 = \frac{1}{4\pi\epsilon} \sum_{n=1}^N a_n \int_{(n-1)\Delta_x}^{n\Delta_x} \frac{1}{|\mathbf{r} - \mathbf{r}'|} dx' \quad (3.7)$$

where we now have a sum of integrals, each over the domain of a single pulse function. Let us now fix the source points so that they are on the wire axis, and the observation point to be on the wire's surface. This choice ensures that there is no singularity in the integrand. The denominator of the integrand now becomes

$$|\mathbf{r} - \mathbf{r}'| = \sqrt{(x - x') + a^2} \quad (3.8)$$

and (3.7) can be written as

$$\begin{aligned} 4\pi\epsilon &= a_1 \int_0^{\Delta_x} \frac{1}{\sqrt{(x - x') + a^2}} dx' + a_2 \int_{\Delta_x}^{2\Delta_x} \frac{1}{\sqrt{(x - x') + a^2}} dx' + \dots \\ &+ a_{N-1} \int_{(N-2)\Delta_x}^{(N-1)\Delta_x} \frac{1}{\sqrt{(x - x') + a^2}} dx' + a_N \int_{(N-1)\Delta_x}^{N\Delta_x} \frac{1}{\sqrt{(x - x') + a^2}} dx' \end{aligned} \quad (3.9)$$

which comprises one equation in N unknowns. We can solve this equation by common matrix algebra routines if we can obtain N equations in N unknowns. To do so, let us choose N independent observation points x_m on the surface of the wire, each at the center of a wire segment. Doing so yields

$$\begin{aligned} 4\pi\epsilon &= a_1 \int_0^{\Delta_x} \frac{1}{\sqrt{(x_1 - x') + a^2}} dx' + \dots + a_N \int_{(N-1)\Delta_x}^{N\Delta_x} \frac{1}{\sqrt{(x_1 - x') + a^2}} dx' \\ &\quad \vdots \\ 4\pi\epsilon &= a_1 \int_0^{\Delta_x} \frac{1}{\sqrt{(x_N - x') + a^2}} dx' + \dots + a_N \int_{(N-1)\Delta_x}^{N\Delta_x} \frac{1}{\sqrt{(x_N - x') + a^2}} dx' \end{aligned} \quad (3.10)$$

that comprises the matrix system $\mathbf{Z}\mathbf{a} = \mathbf{b}$,

$$\left[\begin{array}{cccccc} z_{11} & z_{12} & z_{13} & \dots & z_{1N} \\ z_{21} & z_{22} & z_{23} & \dots & z_{2N} \\ z_{31} & z_{32} & z_{33} & \dots & z_{3N} \\ \vdots & \vdots & \vdots & \ddots & \vdots \\ z_{N1} & z_{N2} & z_{N3} & \dots & z_{NN} \end{array} \right] \left[\begin{array}{c} a_1 \\ a_2 \\ a_3 \\ \vdots \\ a_N \end{array} \right] = \left[\begin{array}{c} b_1 \\ b_2 \\ b_3 \\ \vdots \\ b_N \end{array} \right] \quad (3.11)$$

The individual matrix elements z_{mn} are

$$z_{mn} = \int_{(n-1)\Delta_x}^{n\Delta_x} \frac{1}{\sqrt{(x_m - x') + a^2}} dx' \quad (3.12)$$

and the right-hand side (RHS) vector elements b_m are

$$b_m = 4\pi\epsilon \quad (3.13)$$

3.1.1.1 Matrix Element Evaluation

The integral for the matrix elements for this problem can be evaluated in closed form. Performing this integration yields [1] (Equation 200.01)

$$z_{mn} = \log \left[\frac{(x_b - x_m) + \sqrt{(x_b - x_m)^2 - a^2}}{(x_a - x_m) + \sqrt{(x_a - x_m)^2 - a^2}} \right] \quad (3.14)$$

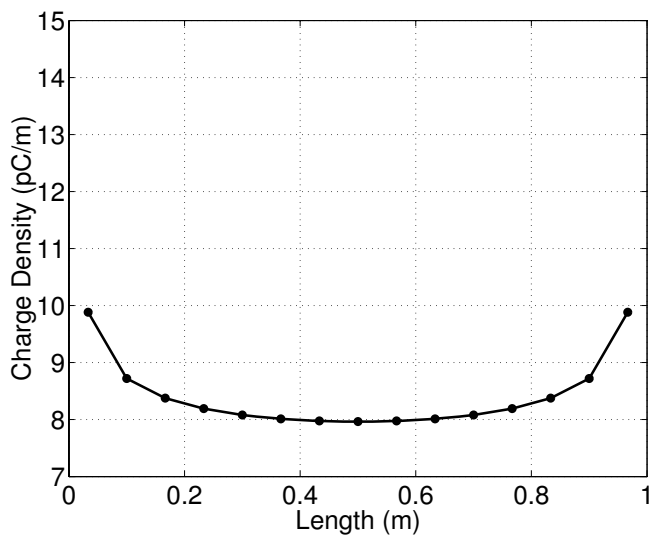
where $x_b = n\Delta_x$ and $x_a = (n-1)\Delta_x$. Note that the linear geometry of this problem yields a matrix that is symmetric toeplitz, i.e.,

$$\mathbf{Z} = \begin{bmatrix} z_1 & z_2 & z_3 & \dots & z_N \\ z_2 & z_1 & z_2 & \dots & z_{N-1} \\ z_3 & z_2 & z_1 & \dots & z_{N-2} \\ \vdots & \vdots & \vdots & \ddots & \vdots \\ z_N & z_{N-1} & z_{N-2} & \dots & z_1 \end{bmatrix} \quad (3.15)$$

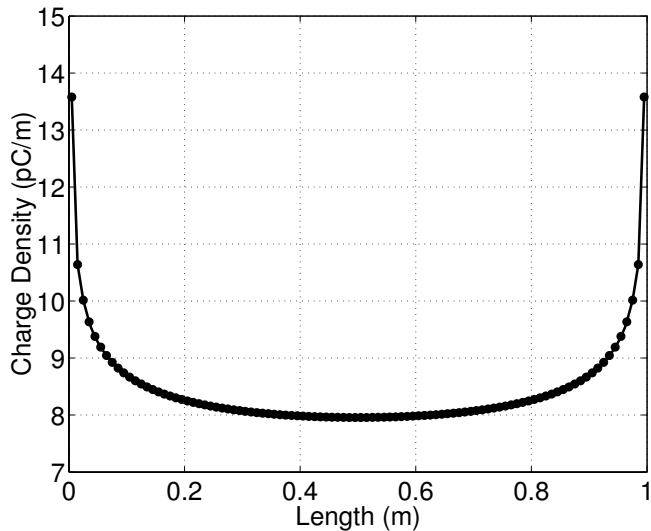
where only the first row of the matrix needs to be computed.

3.1.1.2 Solution

In Figures 3.3a and 3.3b we show the computed charge density on the wire using 15 and 100 segments, respectively. The representation of the charge at the lower level of discretization is somewhat crude, as expected. The increase to 100 unknowns greatly increases the fidelity of the result. Using the computed charge density, we then compute the potential at 100 points along the wire via (3.2). The potential using 15 charge segments is shown in Figure 3.4a. While the voltage is near the expected value of 1V, it is not of constant value, especially near the ends of the wire. Figure 3.4b shows the potential obtained using 100 charge segments. The voltage is now nearly constant across the entire wire, except at the endpoints. Because we used a uniform segment size for the wire, the charge density tends to be somewhat oversampled in the middle of the wire and undersampled near the ends. As a result, the variation of the charge near the ends of the wire is not represented as accurately as in the center, and the computed voltage tends to diverge from the true value. Many

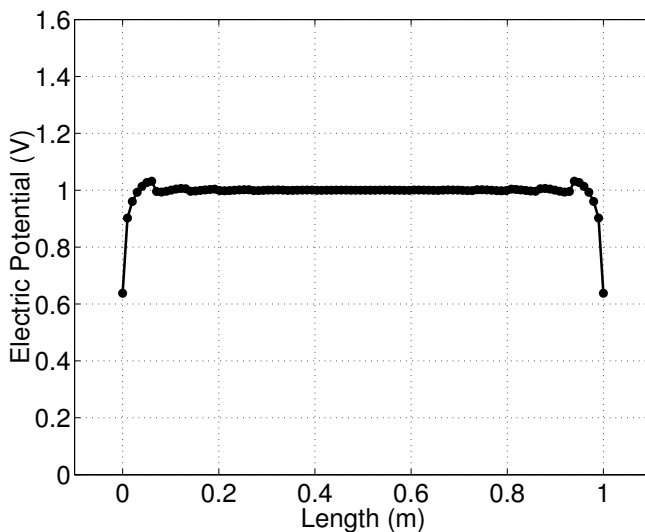


(a) 15 Segments

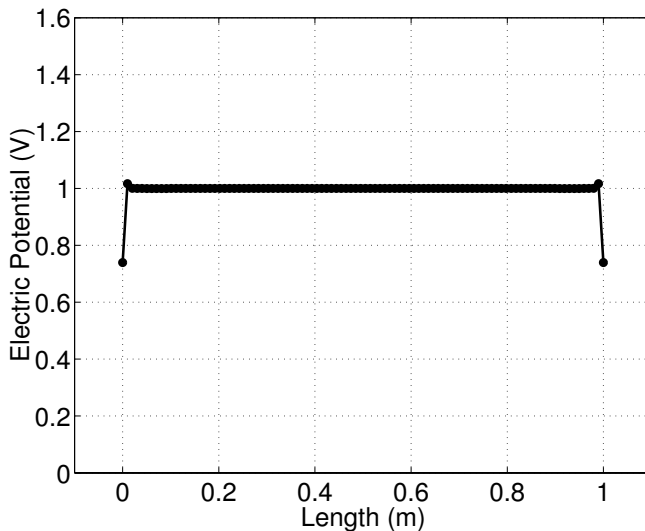


(b) 100 Segments

Figure 3.3: Straight wire charge distribution.



(a) 15 Segments



(b) 100 Segments

Figure 3.4: Straight wire potential.

realistic shapes have irregular surface features such as cracks, gaps and corners that give rise to a more rapid variation in the solution at those points. In an attempt to increase accuracy, it is often advantageous to employ a denser level of discretization in the areas we expect the most variation.

3.1.2 Charged Plate

We next consider the similar problem of a thin, charged conducting square plate of side length L , as shown in Figure 3.5. The potential on the plate is given by the integral

$$\phi_e(\mathbf{r}) = \int_{-\frac{L}{2}}^{\frac{L}{2}} \int_{-\frac{L}{2}}^{\frac{L}{2}} \frac{q_e(x', y')}{4\pi\epsilon|\mathbf{r} - \mathbf{r}'|} dx' dy' \quad (3.16)$$

Fixing the plate to a potential of 1V as before, (3.16) becomes

$$4\pi\epsilon = \int_{-\frac{L}{2}}^{\frac{L}{2}} \int_{-\frac{L}{2}}^{\frac{L}{2}} \frac{q_e(x', y')}{\sqrt{(x - x')^2 + (y - y')^2}} dx' dy' \quad (3.17)$$

We now subdivide the plate into N square patches of side length $2a$ and area $\Delta_s = 4a^2$, and assume the charge to be of constant value within each patch. We then choose N independent observation points, each at the center of a patch. Doing so yields a matrix equation with elements z_{mn} given by

$$z_{mn} = \iint_{S_n} \frac{1}{\sqrt{(x_m - x')^2 + (y_m - y')^2}} dx' dy' \quad (3.18)$$

where S_n represents the area of patch n . Right-hand side vector elements remain the same as in (3.13).

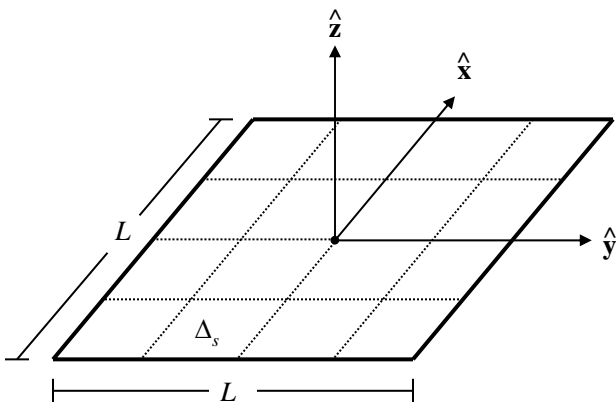


Figure 3.5: Thin charged plate dimensions.

3.1.2.1 Matrix Element Evaluation

When the observation and source patches are the same ($m = n$), the integrand has a singularity and the integral must be evaluated analytically. These matrix elements are called *self terms* and represent the most dominant interactions between elements. We will devote significant attention to the evaluation of self-term matrix elements in this book. The self-term integral for the charged plate is

$$z_{mm} = \int_{-a}^a \int_{-a}^a \frac{1}{\sqrt{(x')^2 + (y')^2}} dx' dy' \quad (3.19)$$

Performing the innermost integration yields [1] (Equation 200.01)

$$z_{mm} = \int_{-a}^a \log \left[\frac{\sqrt{a^2 + (y')^2} + a}{\sqrt{a^2 + (y')^2} - a} \right] dy' \quad (3.20)$$

and performing the second integration yields [2]

$$z_{mm} = 2a \log \left[y + \sqrt{a^2 + y^2} \right] + y \log \left[\frac{y^2 + 2a(a + \sqrt{a^2 + y^2})}{y^2} \right] \Big|_{-a}^a \quad (3.21)$$

which reduces to

$$z_{mm} = \frac{2a}{\pi\epsilon} \log(1 + \sqrt{2}) \quad (3.22)$$

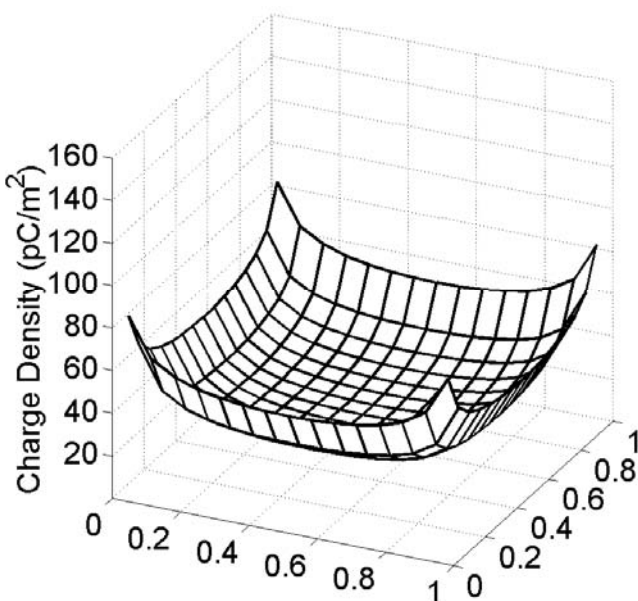
For patches that do not overlap ($m \neq n$) we will use a simple centroidal approximation to the integral, resulting in

$$z_{mn} = \frac{\Delta_s}{\sqrt{(x_m - x_n)^2 + (y_m - y_n)^2}} \quad (3.23)$$

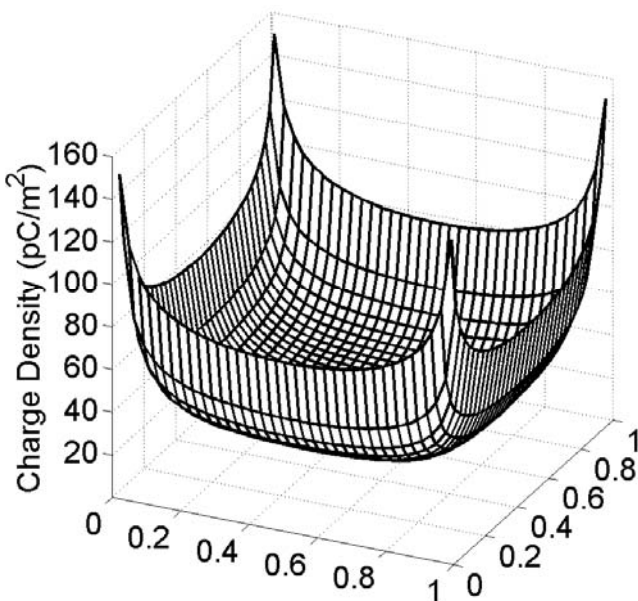
where x_n and y_n are chosen to be at the center of the source patch. This approximation is not very accurate for elements that are close together physically but not overlapping, however it serves to illustrate the problem. In these cases, an analytic or adaptive numerical integration should be used instead. These elements are called the *near terms*, and we will also consider them in greater detail later.

3.1.2.2 Solution

Figures 3.6a and 3.6b show the computed surface charge densities obtained using 15 and 35 patches in the x and y directions, which result in 225 and 1225 unknowns, respectively. Figures 3.7a and 3.7b show the surface charge densities on the patches along the diagonal of the plate. As in the case of the thin wire, the electric charge accumulates near the corners and the edges of the plate, and our solution could benefit from additional discretization density in those areas.

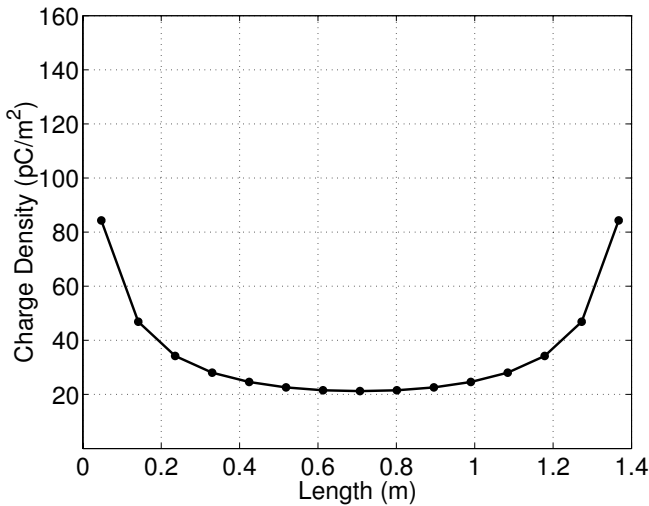


(a) 225 Patches

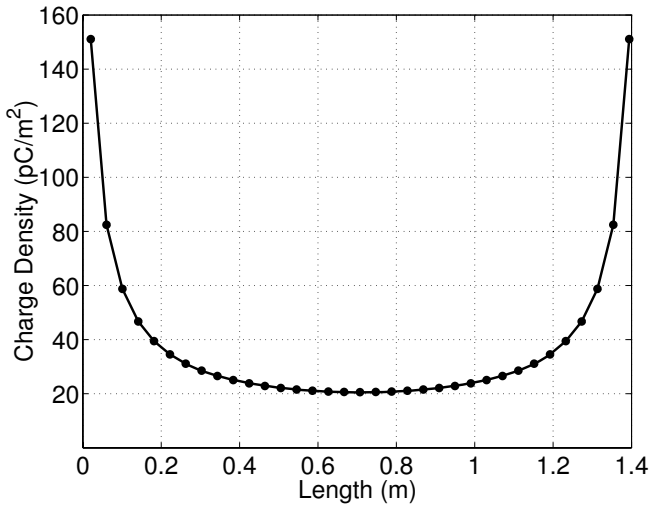


(b) 1225 Patches

Figure 3.6: Charge distribution on square plate.



(a) 225 Patches



(b) 1225 Patches

Figure 3.7: Potential on square plate diagonal.

3.2 THE METHOD OF MOMENTS

In the previous section, we considered the problem of computing an unknown charge distribution on a thin wire or plate at a known potential. Our basic approach was to expand the unknown quantity using a set of known functions with unknown coefficients. We then converted the resulting equation into a linear system of equations by enforcing the boundary conditions, in this case the electric potential, at a number of points on the object. The resulting linear system was then solved numerically for the unknown coefficients. Let us formalize this process by introducing a method of weighted residuals known as the method of moments (MOM). Consider the generalized problem [3]

$$L(f) = g \quad (3.24)$$

where L is a linear operator, g is a known forcing function, and f is unknown. In electromagnetic problems, L is typically an integro-differential operator, f is the unknown function (charge, current) and g is a known excitation source (incident field). Let us now expand f into a sum of N weighted *basis functions*,

$$f = \sum_{n=1}^N a_n f_n \quad (3.25)$$

where a_n are unknown weighting coefficients. Because L is linear, substitution of the above into (3.24) yields

$$\sum_{n=1}^N a_n L(f_n) \approx g \quad (3.26)$$

where the residual is

$$R = g - \sum_{n=1}^N a_n L(f_n) \quad (3.27)$$

The basis functions are chosen to model the expected behavior of the unknown function throughout its domain, and can be scalars or vectors depending on the problem. If the basis functions have local support in the domain, they are called *local* or *subsectional* basis functions. If their support spans the entire problem domain, they are called *global* or *entire-domain* basis functions. In this book we focus primarily on local basis functions.

Let us now generalize the method by which the boundary conditions were previously enforced. We define an inner product or *moment* between a basis function $f_n(\mathbf{r}')$ and a *testing* or *weighting* function $f_m(\mathbf{r})$ as

$$\langle f_m, f_n \rangle = \int_{f_m} f_m(\mathbf{r}) \cdot \int_{f_n} f_n(\mathbf{r}') d\mathbf{r}' d\mathbf{r} \quad (3.28)$$

where the integrals are line, surface, or volume integrals depending on the basis and testing functions. Requiring the inner product of each testing function with the

residual function to be zero yields

$$\sum_{n=1}^N a_n \langle f_m, L(f_n) \rangle = \langle f_m, g \rangle \quad (3.29)$$

which results in the $N \times N$ matrix equation $\mathbf{Z}\mathbf{a} = \mathbf{b}$ with matrix elements

$$z_{mn} = \langle f_m, L(f_n) \rangle \quad (3.30)$$

and right-hand side vector elements

$$b_m = \langle f_m, g \rangle \quad (3.31)$$

In the MOM, each basis function interacts with all others by means of the Green's function and the resulting system matrix is full. All the elements of the matrix must therefore be explicitly stored in memory. This can be compared to other algorithms such as the finite element method, where the matrix is typically sparse, symmetric and banded, with many elements of each matrix row being zero [4].

3.2.1 Point Matching

In Sections 3.1.1 and 3.1.2, we enforced the boundary conditions by testing the integral equation at a set of discrete points on the object. This is equivalent to using a delta function as the weighting function in (3.28):

$$w_m(\mathbf{r}) = \delta(\mathbf{r}) \quad (3.32)$$

This method is referred to as *point matching* or *point collocation*. There are significant advantages as well as disadvantages to this method. One benefit is that in evaluating the matrix elements, no integral is required over the range of the testing function, only that of the source function. The primary disadvantage is that the boundary conditions are matched only at discrete locations throughout the solution domain, allowing them to assume a different value at points other than those used for testing. In many cases the results may still be quite good, and we will use point matching to solve several of the two-dimensional problems in Chapter 5.

3.2.2 Galerkin's Method

For testing we are free to use whatever functions we wish, however for many problems the choice of testing function is crucial to obtaining a good solution. One of the most commonly used is the *method of Galerkin*, where the basis functions themselves are used as the testing functions. This has the advantage of enforcing the boundary conditions throughout the solution domain, instead of at discrete points as with point matching. We will solve many problems in this book using Galerkin-type testing.

3.3 COMMON TWO-DIMENSIONAL BASIS FUNCTIONS

The most important characteristic of a basis function is that it reasonably represents the behavior of the unknown function throughout its domain. If the solution has a high level of variation throughout a particular region, using pulse basis functions may not be as good a choice as a linear or higher-order function. The choice of basis function also determines the complexity encountered in evaluating the MOM matrix elements, which can be very difficult in some cases. We will now briefly consider some two-dimensional local basis functions commonly used in moment method problems, as well as entire-domain functions.

3.3.1 Pulse Functions

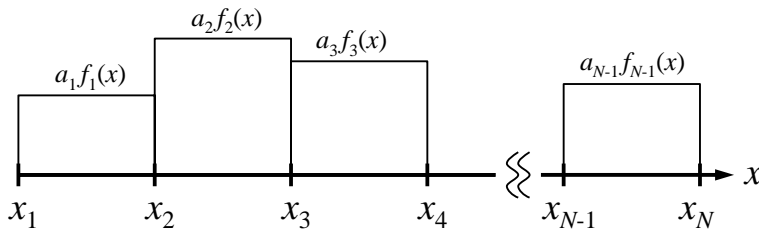


Figure 3.8: Pulse functions.

A set of pulse basis functions is depicted in Figure 3.8, where the domain has been divided into N points with $N - 1$ subsegments/pulses. In our figure the segments all have equal lengths, however this is not required. The pulse function is defined as

$$f_n(x) = 1 \quad x_n \leq x \leq x_{n+1} \quad (3.33)$$

$$f_n(x) = 0 \quad \text{elsewhere} \quad (3.34)$$

Pulse functions comprise a simple and crude approximation to the solution over each segment, but they can greatly simplify the evaluation of MOM matrix elements. Note that since the derivative of pulse functions is impulsive, they cannot be used when L contains a derivative with respect to x [5].

3.3.2 Piecewise Triangular Functions

Where pulse functions are constant on a single segment, a triangle function spans two segments and varies from zero at the outer points to unity at the center. A set of triangle functions is shown in Figure 3.9. The domain has been divided into N points and $N - 1$ subsegments, resulting in $N - 2$ basis functions. We have again depicted the segments as being of equal length, however this is not required. Since adjacent

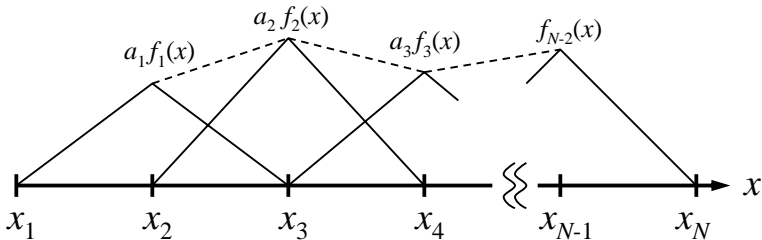


Figure 3.9: Triangle functions (end condition 1).

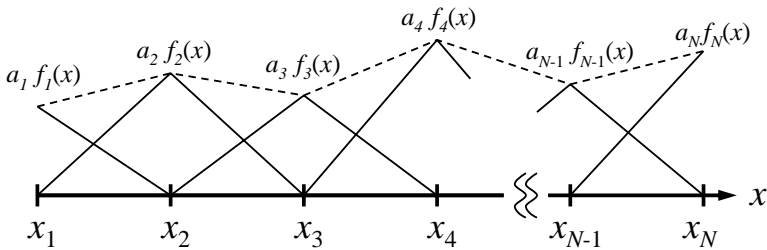


Figure 3.10: Triangle functions (end condition 2).

functions overlap by one segment, triangles provide a piecewise linear variation of the solution between segments. A triangle function is defined as

$$f_n(x) = \frac{x - x_{n-1}}{x_n - x_{n-1}} \quad x_{n-1} \leq x \leq x_n \quad (3.35)$$

$$f_n(x) = \frac{x_{n+1} - x}{x_{n+1} - x_n} \quad x_n \leq x \leq x_{n+1} \quad (3.36)$$

These functions may be used when L contains a derivative with respect to x [5]. This property is important when considering the redistribution of differential operators, such as the manipulation of the EFIE in Section 4.5.1.

Note that the configuration of Figure 3.9 forces the solution to zero at x_1 and x_N . This configuration may be desirable when the value of the solution at the ends of the domain is known to be zero a priori, however it should not be used if the solution may be nonzero. If we instead add a *half triangle* to the first and last segments, the solution will no longer be forced to zero. This is illustrated in Figure 3.10, where there are now a total of N basis functions.

3.3.3 Piecewise Sinusoidal Functions

Piecewise sinusoid functions are similar to triangle functions, as illustrated in Figure 3.11. They are often used in the analysis of wire antennas because of their ability to

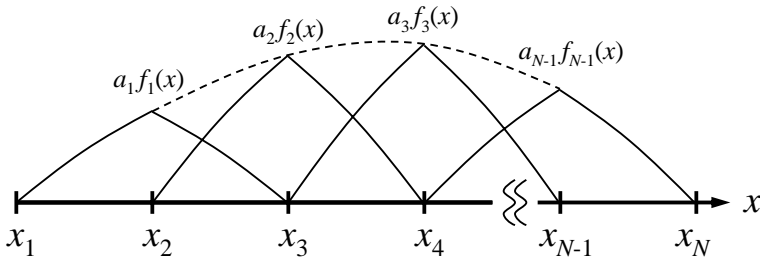


Figure 3.11: Piecewise sinusoidal functions.

represent sinusoidal current distributions. These functions are defined as

$$f_n(x) = \frac{\sin k(x - x_{n-1})}{\sin k(x_n - x_{n-1})} \quad x_{n-1} \leq x \leq x_n \quad (3.37)$$

$$f_n(x) = \frac{\sin k(x_{n+1} - x)}{\sin k(x_{n+1} - x_n)} \quad x_n \leq x \leq x_{n+1} \quad (3.38)$$

where k is the wavenumber, and the length of the segments is generally much less than the period of the sinusoid.

3.3.4 Entire-Domain Functions

Unlike their local counterparts, entire-domain functions are defined everywhere throughout the problem domain. One might have reason to use entire-domain functions if certain information about the solution is known a priori. The solution may be faithfully modeled by a sum of weighted polynomials or sines and cosines, for example. For example, the current $I(x)$ on a thin dipole antenna of length L might be represented by the sum [6]

$$I(x) = \sum_{n=1}^N a_n (1 - |x/L|)^m \quad (3.39)$$

where the testing procedure is still performed as before. After solving the matrix equation, only the first few coefficients a_n may be required to accurately represent the current in the above sum.

A disadvantage of entire-domain functions is that it may not be feasible to apply them to a geometry of arbitrary shape. As a result, local basis functions are most often applied to MOM problems in the literature.

3.3.5 Number of Basis Functions

In a given problem, the number of basis functions (unknowns) must be chosen so they adequately represent the solution. Because we are concerned with time-harmonic

problems, we must model the amplitude as well as the phase behavior of the solution. For linear basis functions such as the triangle of Section 3.3.2, it is a common “rule of thumb” that at least ten unknowns per wavelength should be used to represent a sinusoid. This number should increase for areas where the amplitude may vary significantly such as as gaps, cracks and edges on a surface. Using higher-order basis functions can reduce the unknown count at the expense of increased complexity in the MOM formulation. Such higher-order functions are covered in detail in more advanced references.

The number of unknowns always increases with the size of the problem. The rate of this increase depends on whether the problem domain is a line, surface, or volume. In the MOM, N increases linearly for one-dimensional problems and exponentially for the surface problems considered in Chapter 7. The resulting number may be as small as a few hundred, or it may grow into the thousands or even millions for very large problems. This has significant consequences in terms of the system memory requires to store an $N \times N$ matrix system, as well as the compute time required to solve it. We discuss several methods for solving matrix problems in Section 3.4.

3.4 SOLUTION OF MATRIX EQUATIONS

In this section we will first discuss Gaussian elimination (GE) and LU decomposition, methods that perform a straightforward factorization of a matrix. These algorithms require a compute time of the order $O(N^3)$, where N is the number of unknowns. These methods work very well when N is small, however for larger problems the factorization time may grow prohibitively large. Even though the power of the computer continues to grow year to year, this will always be a challenge because even larger problems are always on the mind of the engineer. We then discuss several iterative solver algorithms, which have become increasingly popular in recent years. Instead of modifying the system matrix, the bulk of the effort is spent computing products between the system matrix and a vector updated at each iteration. While the full matrix must still be stored, the overall compute time is of the order $O(MN^2)$, where N^2 is the operations for the matrix-vector product and M is the number of iterations. More recently, techniques such as the fast multipole method (FMM) [7] and the adaptive integral method (AIM) [8] have been developed to allow fast calculation of interactions between basis function groups. Combined with an iterative solver, they eliminate the need to store many of the small-valued matrix elements and greatly accelerate the matrix-vector product. We will consider the FMM in detail in Chapter 8.

3.4.1 Gaussian Elimination

Gaussian elimination is a simple method of reducing a matrix to row echelon form through the use of elementary row operations. Once this has been done, the unknown vector is obtained through simple backsubstitution. To illustrate this operation, let us

form the augmented matrix from the $N \times N$ matrix equation $\mathbf{Ax} = \mathbf{b}$:

$$\left[\begin{array}{cccc|c} a_{11} & a_{12} & a_{13} & \dots & a_{1N} & b_1 \\ a_{21} & a_{22} & a_{23} & \dots & a_{2N} & b_2 \\ a_{31} & a_{32} & a_{33} & \dots & a_{3N} & b_3 \\ \vdots & \vdots & \vdots & \ddots & \vdots & \vdots \\ a_{N1} & a_{N2} & a_{N3} & \dots & a_{NN} & b_N \end{array} \right] \quad (3.40)$$

We start with the first row and divide every entry by a_{11} , leaving a 1 on the diagonal. For every row below this, we then subtract a multiple of this row so that a zero remains in the first column. The result is

$$\left[\begin{array}{ccccc|c} 1 & a'_{12} & a'_{13} & \dots & a'_{1N} & b'_1 \\ 0 & a'_{22} & a'_{23} & \dots & a'_{2N} & b'_2 \\ 0 & a'_{32} & a'_{33} & \dots & a'_{3N} & b'_3 \\ \vdots & \vdots & \vdots & \ddots & \vdots & \vdots \\ 0 & a'_{N2} & a'_{N3} & \dots & a'_{NN} & b'_N \end{array} \right] \quad (3.41)$$

We repeat this same operation for the second row and all rows below that until only ones remain on the diagonal and the lower triangle is zero. The original matrix equation now reads

$$\left[\begin{array}{ccccc|c} 1 & a'_{12} & a'_{13} & \dots & a'_{1N} & b'_1 \\ 0 & 1 & a'_{23} & \dots & a'_{2N} & b'_2 \\ 0 & 0 & 1 & \dots & a'_{3N} & b'_3 \\ \vdots & \vdots & \vdots & \ddots & \vdots & \vdots \\ 0 & 0 & 0 & \dots & 1 & b'_N \end{array} \right] \quad (3.42)$$

The solution to this system is obtained through the following backsubstitution operations:

$$x_N = b'_N \quad (3.43)$$

$$x_i = b'_i - \sum_{k=i+1}^N a'_{ik} x_k \quad i < N \quad (3.44)$$

The elimination requires a total of $N^3/3$ operations, and $N^2/2$ for the backsubstitution. Note that the row operations leading to (3.42) modify the right-hand side vector as well. This will be undesirable with multiple right-hand sides, as they must all be precomputed and available when performing the elimination. We will circumvent this limitation in the next section with LU decomposition.

3.4.1.1 Pivoting

When performing the row operations for Gaussian elimination, the values of the diagonal entries (the *pivots*) were not addressed. A problem arises when one of these entries is zero, and if the relative magnitude of the pivot is small, roundoff errors may become a problem in the subsequent multiplies and subtractions. Because the augmented matrix system is not altered by exchanging any two rows, the current row can be exchanged with any of the ones below it that contain the “strongest” diagonal entry (one of greatest magnitude). This is referred to as *partial pivoting*. An exchange of rows *and* columns in the matrix is called *full pivoting* and requires recording the permutations of the solution vector as well [9].

3.4.2 LU Decomposition

As previously discussed, a factorization that does not modify the right-hand side vector will be more advantageous than Gaussian elimination. Therefore let us consider the factorization of the matrix \mathbf{A} into lower and upper triangular parts. We can write this as

$$\mathbf{LU} = \mathbf{A} \quad (3.45)$$

where

$$\mathbf{LU} = \begin{bmatrix} l_{11} & 0 & 0 & \dots & 0 \\ l_{21} & l_{22} & 0 & \dots & 0 \\ l_{31} & l_{32} & l_{33} & \dots & 0 \\ \vdots & \vdots & \vdots & \ddots & \vdots \\ l_{N1} & l_{N2} & l_{N3} & \dots & l_{NN} \end{bmatrix} \begin{bmatrix} u_{11} & u_{12} & u_{13} & \dots & u_{1N} \\ 0 & u_{22} & u_{23} & \dots & u_{2N} \\ 0 & 0 & u_{33} & \dots & u_{3N} \\ \vdots & \vdots & \vdots & \ddots & \vdots \\ 0 & 0 & 0 & \dots & u_{NN} \end{bmatrix} \quad (3.46)$$

Using this decomposition, we can solve the following equation:

$$\mathbf{A} \cdot \mathbf{x} = (\mathbf{L} \cdot \mathbf{U}) \cdot \mathbf{x} = \mathbf{L} \cdot (\mathbf{U} \cdot \mathbf{x}) = \mathbf{b} \quad (3.47)$$

by first solving the equation

$$\mathbf{L} \cdot \mathbf{y} = \mathbf{b} \quad (3.48)$$

where \mathbf{y} is obtained through the forward substitution

$$y_1 = \frac{b_1}{l_{11}} \quad (3.49)$$

$$y_i = \frac{1}{l_{ii}} \left[b_i - \sum_{k=1}^{i-1} l_{ik} y_k \right] \quad i > 1 \quad (3.50)$$

and then by solving

$$\mathbf{U} \cdot \mathbf{x} = \mathbf{y} \quad (3.51)$$

where \mathbf{x} is obtained through the back substitution

$$x_N = \frac{y_N}{u_{NN}} \quad (3.52)$$

$$x_i = \frac{1}{u_{ii}} \left[y_i - \sum_{k=i+1}^N u_{ik} x_k \right] \quad i < N \quad (3.53)$$

The remaining task is to determine the elements of \mathbf{L} and \mathbf{U} . If we carry out the matrix multiplication \mathbf{LU} , we will have N^2 equations for the $N^2 + N$ unknowns l_{ij} and u_{ij} . Because the diagonal is represented twice, we are free to specify N of the unknowns ourselves, so we choose

$$l_{ii} = 1 \quad i = 1, 2, \dots, N \quad (3.54)$$

hence

$$\mathbf{LU} = \begin{bmatrix} 1 & 0 & 0 & \dots & 0 \\ l_{21} & 1 & 0 & \dots & 0 \\ l_{31} & l_{32} & 1 & \dots & 0 \\ \vdots & \vdots & \vdots & \ddots & \vdots \\ l_{N1} & l_{N2} & l_{N3} & \dots & 1 \end{bmatrix} \begin{bmatrix} u_{11} & u_{12} & u_{13} & \dots & u_{1N} \\ 0 & u_{22} & u_{23} & \dots & u_{2N} \\ 0 & 0 & u_{33} & \dots & u_{3N} \\ \vdots & \vdots & \vdots & \ddots & \vdots \\ 0 & 0 & 0 & \dots & u_{NN} \end{bmatrix} \quad (3.55)$$

and we can immediately set $u_{11} = a_{11}$. Multiplying \mathbf{L} by the first column of \mathbf{U} , we obtain

$$\begin{aligned} l_{21} &= \frac{a_{21}}{u_{11}} \\ l_{31} &= \frac{a_{31}}{u_{11}} \\ &\dots \end{aligned} \quad (3.56)$$

and doing the same with the second column of \mathbf{U} yields $u_{12} = a_{12}$ and

$$\begin{aligned} u_{22} &= a_{22} - l_{21}u_{12} \\ l_{32} &= \frac{1}{u_{22}} [a_{32} - l_{31}u_{12}] \\ l_{42} &= \frac{1}{u_{22}} [a_{42} - l_{41}u_{12}] \\ &\dots \end{aligned} \quad (3.57)$$

which leads to a generalized method known as *Crout's Algorithm*. For each column $j = 1, 2, \dots, N$, we first solve for the elements of \mathbf{U} on and above the diagonal, i.e.,

$$u_{ij} = a_{ij} - \sum_{k=1}^{i-1} l_{ik} u_{kj} \quad i = 1, 2, \dots, j \quad (3.58)$$

and then for elements of \mathbf{L} below the diagonal,

$$l_{ij} = \frac{1}{u_{jj}} \left[a_{ij} - \sum_{k=1}^{j-1} l_{ik} u_{kj} \right] \quad i = j + 1, j + 2, \dots, N \quad (3.59)$$

Following this algorithm, the elements needed at each step will have already been computed when they are needed. The matrix \mathbf{A} can therefore be factored *in place*, requiring no additional storage for \mathbf{L} and \mathbf{U} . A practical LU decomposition algorithm will also incorporate partial pivoting to ensure numerical stability at each step of the process. The operation count for the LU decomposition and back substitution is of the same complexity as Gaussian elimination.

Once the factorization is completed, it can then be reused for an arbitrary number of right-hand sides. The factored matrix can then be written to disk and read back in later if needed, negating the need to compute and factor the matrix a second time.

3.4.3 Condition Number

Given the matrix system $\mathbf{Ax} = \mathbf{b}$, it is desirable to know the impact on the solution \mathbf{x} given any inaccuracies in the estimate of \mathbf{b} . If after computing the singular value decomposition (SVD) of \mathbf{A} we observe a large difference between the largest and smallest singular values, we know that small changes in \mathbf{b} may result in large changes in \mathbf{x} . Let us now define the *condition number* of a matrix, which is

$$\kappa(\mathbf{A}) = \|\mathbf{A}^{-1}\| \|\mathbf{A}\| \quad (3.60)$$

where $\|\cdot\|$ is a matrix norm. If we choose the 2-norm, then the condition number is given by

$$\kappa(\mathbf{A}) = \frac{\lambda_{max}(\mathbf{A})}{\lambda_{min}(\mathbf{A})} \quad (3.61)$$

where $\lambda_{min}(\mathbf{A})$ and $\lambda_{max}(\mathbf{A})$ are the minimum and maximum eigenvalues of \mathbf{A} , respectively [10]. The condition number is important because many elements of the MOM matrix and right-hand side vectors are obtained by numerical integration. Small errors in these can be magnified by a matrix that is poorly conditioned. The condition number is also important to iterative methods such as those in the next section, as it has a direct impact on their relative rates of convergence.

3.4.3.1 EFIE and MFIE

Because the EFIE and MFIE are the key integral equations used in this book, it is important we know how they impact the condition number of the resulting system matrix. The EFIE contains an *unbounded* operator [10] that causes its eigenvalues to be large or infinite in many cases. As a result, the EFIE is well known for producing a poorly conditioned matrix. The MFIE comprises an *identity-plus-compact* operator

whose eigenvalues are always finite, and is known for producing a well-conditioned matrix, although it cannot be applied to open or thin surfaces like the EFIE. These behaviors are illustrated in Figure 2.8. The condition number of the EFIE grows larger with a decrease in electrical size, which is due to the unbounded operator. The EFIE condition number also increases with the discretization density, which may present challenges for larger problems. The condition number of the MFIE remains well behaved except at resonant frequencies, and that of the CFIE is also small. Though the presence of the EFIE is observed to increase the condition number of the CFIE, the problem is not as severe as using the EFIE alone, and the CFIE becomes the preferred approach for many MOM problems.

3.4.4 Iterative Methods

Iterative methods do not modify the original matrix, and instead start with an approximation or “guess” for the solution vector and attempt to minimize a residual vector at each iteration. At the core of each lies the update operation

$$\mathbf{x}_{k+1} = \mathbf{x}_k + \alpha_k \mathbf{p}_k \quad (3.62)$$

where the new estimate of the solution \mathbf{x}_{k+1} is obtained from the previous solution \mathbf{x}_k and a search direction \mathbf{p}_k , with α_k a constant. The residual at each step is

$$\mathbf{r}_{k+1} = \mathbf{A}\mathbf{x}_{k+1} - \mathbf{b} \quad (3.63)$$

The computational burden of these methods lies in one or more matrix-vector products at each iteration. In this section we will briefly discuss several commonly used iterative methods and present a template that the user can use to write routines of their own. Because the iterative solver algorithms comprise simple operations such as simple vector and matrix-vector products, they are easy and quick to implement in software, even if the user does not fully understand their underlying principles.

3.4.4.1 Conjugate Gradient

The conjugate gradient (CG) algorithm is a method for solving a matrix system where \mathbf{A} is symmetric and positive definite. It is related to the method of steepest Descent and minimizes a quadratic function by generating a sequence of conjugate-direction search vectors that are \mathbf{A} -orthogonal at each step [11, 12]. Because a general moment method matrix is neither symmetric or positive definite, the CG algorithm cannot be directly applied. Instead, we can apply CG to the following system called the “normal equations”:

$$\mathbf{A}^\dagger \mathbf{A} \mathbf{x} = \mathbf{A}^\dagger \mathbf{b} \quad (3.64)$$

where \mathbf{A}^\dagger denotes the conjugate transpose, and $\mathbf{A}^\dagger \mathbf{A}$ is symmetric and positive definite. An algorithm [12] for the preconditioned CG method for the normal

Initial steps:

 Guess \mathbf{x}_0
 $\mathbf{r}_0 = \mathbf{b} - \mathbf{A}\mathbf{x}_0$
 $\tilde{\mathbf{r}}_0 = \mathbf{A}^\dagger \mathbf{r}_0$
 $\mathbf{z}_0 = \mathbf{M}^{-1} \tilde{\mathbf{r}}_0$
 $\mathbf{p}_0 = \mathbf{z}_0$

For $i = 1, 2, \dots$, until convergence, do

$\mathbf{w}_{i-1} = \mathbf{A}\mathbf{p}_{i-1}$
 $\alpha_{i-1} = (\mathbf{z}_{i-1}^* \cdot \tilde{\mathbf{r}}_{i-1}) / \|\mathbf{w}_{i-1}\|_2^2$
 $\mathbf{x}_i = \mathbf{x}_{i-1} + \alpha_{i-1} \mathbf{p}_{i-1}$
 $\mathbf{r}_i = \mathbf{r}_{i-1} - \alpha_{i-1} \mathbf{w}_{i-1}$
 If $\|\mathbf{r}_i\|_2 < \epsilon \|\mathbf{b}\|_2$, stop iteration
 $\tilde{\mathbf{r}}_i = \mathbf{A}^\dagger \mathbf{r}_i$
 $\mathbf{z}_i = \mathbf{M}^{-1} \tilde{\mathbf{r}}_i$
 $\beta_{i-1} = (\mathbf{z}_i^* \cdot \tilde{\mathbf{r}}_i) / (\mathbf{z}_{i-1}^* \cdot \tilde{\mathbf{r}}_{i-1})$
 $\mathbf{p}_i = \mathbf{z}_i + \beta_{i-1} \mathbf{p}_{i-1}$

end

Figure 3.12: Preconditioned conjugate gradient (CGNR) algorithm.

equations is summarized in Figure 3.12, where \mathbf{M} is a preconditioner matrix. This algorithm requires two matrix-vector products per iteration, one with \mathbf{A} and one with \mathbf{A}^\dagger .

The CG method has been used extensively for electromagnetic field problems, and the relationship between the matrix eigenvalues and convergence of the CG studied [13, 14, 15, 16]. For a matrix system with N unknowns, the CG theoretically converges to the exact solution in at most N iterations, assuming there are no roundoff errors, and the residual error decreases at each step. For many practical radiation and scattering problems, the CG performs extremely well. Due to the ill conditioning of some matrix systems however, the convergence rate of the CG may be very slow and may effectively stagnate without any additional decrease in the residual norm, suggesting that a preconditioner may be needed.

3.4.4.2 Biconjugate Gradient

The biconjugate gradient (BiCG) method was developed by Lanczos [17] and is applicable to general, nonsymmetric systems. BiCG approaches the problem by generating a pair of bi-orthogonal residual sequences using \mathbf{A} and \mathbf{A}^T . An algorithm [18] for the preconditioned BiCG method is summarized in Figure 3.13. This algorithm requires two matrix-vector products per iteration, one with \mathbf{A} and one with \mathbf{A}^T . The residual error of the BiCG does not necessarily decrease at each step and convergence may be observed to be erratic, but it does exhibit good performance for many problems.

Initial steps:

Guess \mathbf{x}_0
 $\mathbf{r}_0 = \mathbf{b} - \mathbf{Ax}_0$
 $\tilde{\mathbf{r}}_0 = \mathbf{r}_0$

For $i = 1, 2, \dots$, until convergence:

$\mathbf{z}_{i-1} = \mathbf{M}^{-1} \mathbf{r}_{i-1}$
 $\tilde{\mathbf{z}}_{i-1} = (\mathbf{M}^T)^{-1} \tilde{\mathbf{r}}_{i-1}$
 $\rho_{i-1} = \mathbf{z}_{i-1} \cdot \tilde{\mathbf{r}}_{i-1}$
If $\rho_{i-1} = 0$ method fails
If $i = 1$
 $\mathbf{p}_i = \mathbf{z}_{i-1}$
 $\tilde{\mathbf{p}}_i = \tilde{\mathbf{z}}_{i-1}$
else
 $\beta_{i-i} = \rho_{i-1} / \rho_{i-2}$
 $\mathbf{p}_i = \mathbf{z}_{i-1} + \beta_{i-1} \mathbf{p}_{i-1}$
 $\tilde{\mathbf{p}}_i = \tilde{\mathbf{z}}_{i-1} + \beta_{i-1} \tilde{\mathbf{p}}_{i-1}$
endif
 $\mathbf{q}_i = \mathbf{Ap}_i$
 $\tilde{\mathbf{q}}_i = \mathbf{A}^T \tilde{\mathbf{p}}_i$
 $\alpha_i = \rho_{i-1} / (\tilde{\mathbf{p}}_i \cdot \mathbf{q}_i)$
 $\mathbf{x}_i = \mathbf{x}_{i-1} + \alpha_i \mathbf{p}_i$
 $\mathbf{r}_i = \mathbf{r}_{i-1} - \alpha_i \mathbf{q}_i$
If $\|\mathbf{r}_i\|_2 < \epsilon \|\mathbf{b}\|_2$, stop iteration
 $\tilde{\mathbf{r}}_i = \tilde{\mathbf{r}}_{i-1} - \alpha_i \tilde{\mathbf{q}}_i$
end

Figure 3.13: Preconditioned biconjugate gradient (BiCG) algorithm.

3.4.4.3 Conjugate Gradient Squared

The conjugate gradient squared (CGS) algorithm [19] is a method that avoids using the transpose of \mathbf{A} and attempts to obtain a faster rate of convergence than CG and BiCG. The method does converge faster in many cases, though because of its more aggressive formulation it is also more sensitive to residual errors and may diverge quickly if the system is ill-conditioned. An algorithm [18] for the preconditioned CGS method is summarized in Figure 3.14. This algorithm requires two matrix-vector products with \mathbf{A} per iteration.

3.4.4.4 Biconjugate Gradient Stabilized

The biconjugate gradient stabilized (BiCG-Stab) algorithm is similar to the CGS but attempts to avoid its irregular convergence patterns [18]. An algorithm for the preconditioned BiCG-Stab method is summarized in Figure 3.15. This algorithm

Initial steps:

Guess \mathbf{x}_0
 $\mathbf{r}_0 = \mathbf{b} - \mathbf{Ax}_0$
 $\tilde{\mathbf{r}} = \mathbf{r}_0$

For $i = 1, 2, \dots$, until convergence:

$\rho_{i-1} = \mathbf{r}_{i-1} \cdot \tilde{\mathbf{r}}$
If $\rho_{i-1} = 0$ method fails
If $i = 1$
 $\mathbf{u}_1 = \mathbf{r}_0$
 $\mathbf{p}_1 = \mathbf{u}_1$
else
 $\beta_{i-i} = \rho_{i-1}/\rho_{i-2}$
 $\mathbf{u}_i = \mathbf{r}_{i-1} + \beta_{i-1}\mathbf{q}_{i-1}$
 $\mathbf{p}_i = \mathbf{u}_i + \beta_{i-1}(\mathbf{q}_{i-1} + \beta_{i-1}\mathbf{p}_{i-1})$
endif
 $\hat{\mathbf{p}} = \mathbf{M}^{-1}\mathbf{p}_i$
 $\hat{\mathbf{v}} = \mathbf{A}\hat{\mathbf{p}}$
 $\alpha_i = \rho_{i-1}/(\tilde{\mathbf{r}} \cdot \hat{\mathbf{v}})$
 $\mathbf{q}_i = \mathbf{u}_i - \alpha_i\hat{\mathbf{v}}$
 $\hat{\mathbf{u}} = \mathbf{M}^{-1}(\mathbf{u}_i + \mathbf{q}_i)$
 $\mathbf{x}_i = \mathbf{x}_{i-1} + \alpha_i\hat{\mathbf{u}}$
 $\hat{\mathbf{q}} = \mathbf{A}\hat{\mathbf{u}}$
 $\mathbf{r}_i = \mathbf{r}_{i-1} - \alpha_i\hat{\mathbf{q}}_i$
If $\|\mathbf{r}_i\|_2 < \epsilon\|\mathbf{b}\|_2$, stop iteration
end

Figure 3.14: Preconditioned conjugate gradient squared (CGS) algorithm.

requires two matrix-vector products with \mathbf{A} per iteration. Note that there are two end-condition tests in this algorithm.

3.4.4.5 Stopping Criteria

In each iterative method we need to know when to terminate the iteration. Since we do not know the solution vector \mathbf{x} , we cannot compute the error vector

$$\mathbf{e}_i = \mathbf{x} - \mathbf{x}_i \quad (3.65)$$

We instead compute the residual norm N_i , defined as

$$N_i = \frac{\|\mathbf{r}_n\|}{\|\mathbf{b}\|} = \frac{\|\mathbf{Ax}_i - \mathbf{b}\|}{\|\mathbf{b}\|} \quad (3.66)$$

We terminate the iteration after the residual norm goes below a predefined value, such as 10^{-3} . Note that the residual norm is only an indirect measure of the amount

Initial steps:

Guess \mathbf{x}_0

$$\mathbf{r}_0 = \mathbf{b} - \mathbf{A}\mathbf{x}_0$$

$$\tilde{\mathbf{r}} = \mathbf{r}_0$$

For $i = 1, 2, \dots$, until convergence:

$$\rho_{i-1} = \mathbf{r}_{i-1} \cdot \tilde{\mathbf{r}}$$

If $\rho_{i-1} = 0$ method fails

If $i = 1$

$$\mathbf{p}_1 = \mathbf{r}_0$$

else

$$\beta_{i-i} = (\rho_{i-1}/\rho_{i-2})(\alpha_{i-1}/\omega_{i-1})$$

$$\mathbf{p}_i = \mathbf{r}_{i-1} + \beta_{i-1}(\mathbf{p}_{i-1} - \omega_{i-1}\mathbf{v}_{i-1})$$

endif

$$\hat{\mathbf{p}} = \mathbf{M}^{-1}\mathbf{p}_i$$

$$\mathbf{v}_i = \mathbf{A}\hat{\mathbf{p}}$$

$$\alpha_i = \rho_{i-1}/(\tilde{\mathbf{r}} \cdot \mathbf{v}_i)$$

$$\mathbf{s} = \mathbf{r}_{i-1} - \alpha_i\mathbf{v}_i$$

Check norm of s , if small enough set $\mathbf{x}_i = \mathbf{x}_{i-1} + \alpha_i\hat{\mathbf{p}}$, stop

$$\hat{\mathbf{s}} = \mathbf{M}^{-1}\mathbf{s}$$

$$\mathbf{t} = \mathbf{A}\hat{\mathbf{s}}$$

$$\omega_i = (\mathbf{t} \cdot \mathbf{s})/(\mathbf{t} \cdot \mathbf{t})$$

$$\mathbf{x}_i = \mathbf{x}_{i-1} + \alpha_i\hat{\mathbf{p}} + \omega_i\hat{\mathbf{s}}$$

$$\mathbf{r}_i = \mathbf{s} - \omega_i\mathbf{t}$$

If $\|\mathbf{r}_i\|_2 < \epsilon\|\mathbf{b}\|_2$, stop iteration

end

Figure 3.15: Preconditioned biconjugate gradient stabilized (BiCG-Stab) algorithm.

of error, because [10]

$$\frac{\|\mathbf{e}_n\|}{\|\mathbf{e}_0\|} \leq \kappa(\mathbf{A}) \frac{\|\mathbf{r}_n\|}{\|\mathbf{r}_0\|} \quad (3.67)$$

and if \mathbf{A} is badly conditioned, \mathbf{x}_i may not be a very accurate estimate of the solution for a given N_i . In a practical implementation, the iteration should be stopped after the desired residual norm is obtained or a maximum number of iterations is reached.

3.4.5 Examples

Let us compare the convergence behavior of the CGNR, BiCG, CGS and BiCG-Stab algorithms for a couple of practical cases. Figures 3.16a and 3.16b depict the convergence history when solving for the currents induced by a plane wave on a sphere of diameter 2λ and cube of side length 2λ . RWG basis functions (Chapter 7) and CFIE are used, and the models comprise 7680 and 5952 edges (unknowns), respectively. Iteration is performed to a residual norm of 10^{-4} . For the sphere, the

CGS algorithm performs the best followed by BiCG-Stab and CGNR, with BiCG demonstrating the slowest convergence. For the cube, the results are much different. CGS and BiCG-Stab have a very similar rate of convergence and converge quite fast, whereas CGNR and BiCG converge much slower.

These examples show that various iterative solvers will have different performance, depending on the type of problem. In some cases a solver can demonstrate very good convergence, however it might not converge in others. As a result, it is often advisable to try different solvers on a particular problem to determine which one performs best.

3.4.5.1 Preconditioning

Previous sections have emphasized the relationship between the condition number of a matrix and the convergence of iterative solvers. In many cases the solution may be unobtainable because the iteration stagnates or diverges. In others, the solution may converge but only after many iterations and a long compute time. In these cases, especially in those where the solution does not converge, a method of improving the convergence behavior of the solver is desirable. To investigate such a method, let us modify the original linear system to create the new system

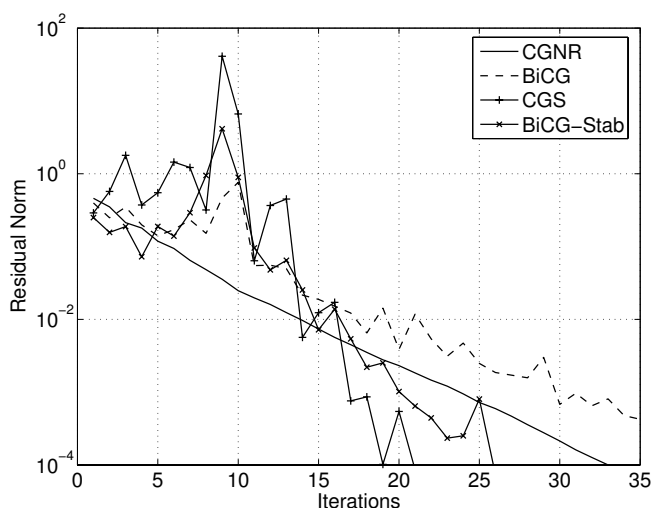
$$\mathbf{M}^{-1}\mathbf{A}\mathbf{x} = \mathbf{M}^{-1}\mathbf{b} \quad (3.68)$$

where \mathbf{M} is a *preconditioner matrix*. If \mathbf{M}^{-1} resembles \mathbf{A}^{-1} in some fashion, then the solution of the above matrix system remains the same, however the eigenvalues of $\mathbf{M}^{-1}\mathbf{A}$ may be more attractive and allow for better performance in an iterative solver. The algorithms summarized in Figures 3.12–3.15 solve the preconditioned system of (3.68) and require the solution of one or more auxiliary linear systems of the form $\mathbf{M}\mathbf{z} = \mathbf{r}$ at each iteration.

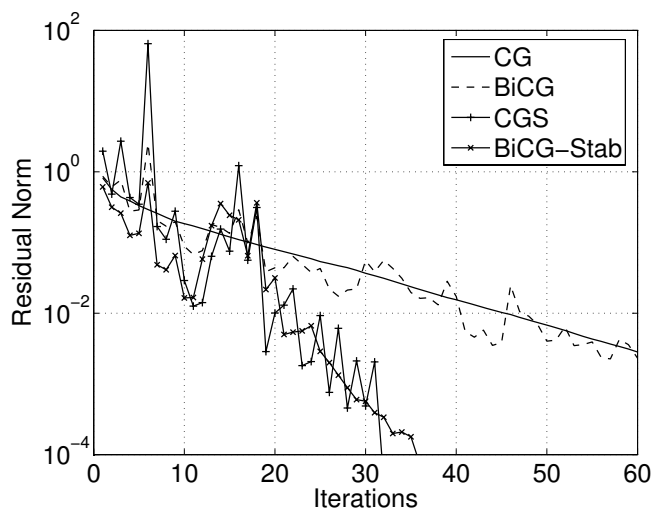
The problem we now face is finding the value of \mathbf{M}^{-1} . Obviously, if \mathbf{M}^{-1} is exactly equal to \mathbf{A}^{-1} , we have not improved the situation since this requires the complete factorization of \mathbf{A} . The key is determining a value of \mathbf{M}^{-1} that has a reasonable setup time and memory demand, and that does not impose an unacceptable overhead when solving the auxiliary problem at each iteration. In some cases, the application of a preconditioner is absolutely necessary as the original system does not converge at all. In other cases, the hope is that the improved rate of convergence of the new system will result in a significantly reduced number of iterations and therefore an overall savings in compute time. This is particularly attractive when the calculations involve multiple right-hand sides, as the preconditioner setup time can be amortized quickly. Many effective preconditioning schemes are discussed at length in [12], and we will discuss several of these in the context of the fast multipole method in Chapter 8.

3.4.6 Commonly Used Matrix Algebra Software

It is a significant advantage to have ready-made routines for solving matrix equations available without one having to “roll their own.” Fortunately, there is plenty of



(a) 2 Meter Sphere



(b) 2 Meter Cube

Figure 3.16: Iteration on sphere and cube (CFIE).

reliable software available for this task so the engineer does not have to worry about this part of the problem. Many libraries are freely available through the Web via universities and other organizations, and there are many commercial packages available as well. The software discussed in this section has been used extensively by this author for solving Moment Method problems and are highly recommended.

3.4.6.1 BLAS

The BLAS (Basic Linear Algebra Subprograms) are set of FORTRAN 77 subroutines that act as building blocks for vector and matrix operations [20]. BLAS is composed of three subsets: BLAS 1 for scalar, vector and vector-vector operations; BLAS 2 for matrix-vector operations; and BLAS 3 for matrix-matrix operations. Separate routines are supplied for real and complex arithmetic (single and double precision). The BLAS source codes are freely available via the Netlib repository at <http://www.netlib.orgblas>, and may be compiled and included in commercial applications at no cost. A popular hand-optimized BLAS library known as Goto BLAS is available from the University of Texas Advanced Computing Center at <http://www.tacc.utexas.edu/resources/software/>. Machine optimized versions of BLAS are also available from various vendors such as Intel, Apple, IBM, Sun and Cray and are included as part of their operating system or sold separately as a runtime library.

3.4.6.2 LAPACK

LAPACK is a FORTRAN 77 library for solving linear systems, least-squares solutions of linear systems of equations, eigenvalue problems, and singular value problems [21]. It is freely available via the Netlib repository at <http://www.netlib.orglapack>, and may be used in commercial applications. The routines are written to handle dense and banded matrices, but not sparse ones. LAPACK draws upon the BLAS routines and a BLAS library must be installed to use it. Like BLAS, separate versions of the routines are supplied for real and complex variables. LAPACK may also be linked with and called from programs written in C, provided that the programmer interfaces between FORTRAN and C properly.

3.4.6.3 MATLAB®

MATLAB is a popular numerical computing environment and programming language commercially available from The Mathworks, Inc. It was originally developed to aid in solving matrix problems, and many of its matrix functions use the BLAS and LAPACK libraries. The MATLAB scripting language is easy to learn, and fairly complex simulations can be written with it. Though its scripts are interpreted and less efficient than compiled code, MATLAB is accurate and can be used to reproduce many examples from this book using its built-in functions.

REFERENCES

- [1] H. Dwight, *Tables of Integrals and Other Mathematical Data*. The Macmillan Company, 1961.
- [2] *The Integrator*. Wolfram Research, <http://integrals.wolfram.com>.
- [3] R. F. Harrington, *Field Computation by Moment Methods*. IEEE Press, 1993.
- [4] J. Jin, *The Finite Element Method in Electromagnetics*. John Wiley and Sons, 1993.
- [5] N. Morita, N. Kumagai, and J. R. Mautz, *Integral Equation Methods for Electromagnetics*. Artech House, 1990.
- [6] B. D. Popovich, “Polynomial approximation of current along thin symmetrical cylindrical dipoles,” *Proc. IEE*, vol. 117, 873–878, May 1970.
- [7] L. Greengard and V. Rokhlin, “A fast algorithm for particle simulations,” *J. Comput. Phys.*, vol. 73, 325–348, 1987.
- [8] E. Bleszynski, M. Bleszynski, and T. Jaroszewicz, “AIM: Adaptive integral method for solving large-scale electromagnetic scattering and radiation problems,” *Radio Sci.*, vol. 31, 1225–1251, 1996.
- [9] W. H. Press, B. P. Flannery, S. A. Teukolsky, and W. T. Vetterling, *Numerical recipes in C: The Art of Scientific Computing*. Cambridge University Press, 1992.
- [10] A. F. Peterson, S. L. Ray, and R. Mittra, *Computational Methods for Electromagnetics*. IEEE Press, 1998.
- [11] M. Hestenes and E. Steifel, “Methods of conjugate gradients for solving linear systems,” *J. Res. Nat. Bur. Stand.*, vol. 49, 409–435, 1952.
- [12] Y. Saad, *Iterative Methods for Sparse Linear Systems*. PWS, 1st ed., 1996.
- [13] T. K. Sarkar, K. R. Siarkiewicz, and R. F. Stratton, “Survey of numerical methods for solution of large systems of linear equations for electromagnetic field problems,” *IEEE Trans. Antennas Propagat.*, vol. 29, 847–856, November 1981.
- [14] T. K. Sarkar, “The conjugate gradient method as applied to electromagnetic field problems,” *IEEE Antennas Propagat. Soc. Newsletter*, 5–14, August 1986.
- [15] A. F. Peterson and R. Mittra, “Convergence of the conjugate gradient method when applied to matrix equations representing electromagnetic scattering problems,” *IEEE Trans. Antennas Propagat.*, vol. 34, 1447–1454, December 1986.

- [16] A. F. Peterson, C. F. Smith, and R. Mittra, “Eigenvalues of the moment-method matrix and their effect on the convergence of the conjugate gradient algorithm,” *IEEE Trans. Antennas Propagat.*, vol. 36, 1177–1179, August 1988.
- [17] C. Lanczos, “Solution of systems of linear equations by minimized iterations,” *J. Res. Nat. Bur. Standards*, vol. 49, 33–53, 1952.
- [18] R. Barrett, M. Berry, T. F. Chan, J. Demmel, J. Donato, J. Dongarra, V. Eijkhout, R. Pozo, C. Romine, and H. V. der Vorst, *Templates for the Solution of Linear Systems: Building Blocks for Iterative Methods*. SIAM, 2nd ed., 1994.
- [19] P. Sonneveld, “Cgs, a fast lanczos-type solver for nonsymmetric linear systems,” *SIAM J. Sci. Statist. Comput.*, vol. 10, 36–52, 1989.
- [20] L. S. Blackford, J. Demmel, J. Dongarra, I. Duff, S. Hammarling, G. Henry, M. Heroux, L. Kaufman, A. Lumsdaine, A. Petitet, R. Pozo, K. Remington, and R. C. Whaley, “An updated set of Basic Linear Algebra Subprograms (BLAS),” *ACM Transactions on Mathematical Software*, vol. 28, 135–151, June 2002.
- [21] E. Anderson, Z. Bai, C. Bischof, S. Blackford, J. Demmel, J. Dongarra, J. Du Croz, A. Greenbaum, S. Hammarling, A. McKenney, and D. Sorensen, *LAPACK Users’ Guide*. Society for Industrial and Applied Mathematics, 3rd ed., 1999.

Chapter 4

Thin Wires

In this chapter we will use the method of moments to analyze radiation and scattering by thin wires. This is an area of great practical interest, as realistic antennas can be modeled by wires whose radius is smaller than their length and the wavelength. We will first derive a thin wire approximation in the magnetic vector potential and then look at the well-known Hallén and Pocklington integral equations for thin, straight wires. We next discuss modeling of the feed system at the antenna terminals, a thin wire model for wires of arbitrary shape, and then compare the effectiveness of each model using several examples.

4.1 THIN WIRE APPROXIMATION

To begin, we first develop the *thin wire kernel*, an approximation we will use in integral equation formulations for thin wires. Consider a perfectly conducting long, $\hat{\mathbf{z}}$ -oriented thin wire of length L whose radius a is much less than L and λ . An incident electric field $\mathbf{E}^i(\mathbf{r})$ excites on this wire a surface current $\mathbf{J}(\mathbf{r})$. Since the wire is very thin, we will assume that $\mathbf{J}(\mathbf{r})$ can be written in terms of a $\hat{\mathbf{z}}$ -oriented filamentary current $I_z(\mathbf{r})$ as

$$\mathbf{J}(\mathbf{r}) = \frac{I_z(z)}{2\pi a} \hat{\mathbf{z}} \quad (4.1)$$

where there is no dependence on wire azimuthal angle ϕ . We also assume that the current goes to zero at the ends of a wire without any current flow onto the wire end-caps. In cylindrical coordinates, we can write the corresponding magnetic vector potential A_z in terms of the surface integral

$$A_z(\rho, \phi, z) = \mu \int_{-L/2}^{L/2} \int_0^{2\pi} \frac{I_z(z')}{2\pi} \frac{e^{-jk r}}{4\pi r} d\phi' dz' \quad (4.2)$$

where

$$r = |\mathbf{r} - \mathbf{r}'| = \sqrt{(z - z')^2 + |\boldsymbol{\rho} - \boldsymbol{\rho}'|^2} \quad (4.3)$$

Using the fact that $\rho' = a$, we write

$$|\boldsymbol{\rho} - \boldsymbol{\rho}'| = \rho^2 + a^2 - 2\boldsymbol{\rho} \cdot \boldsymbol{\rho}' = \rho^2 + a^2 - 2\rho a \cos(\phi' - \phi) \quad (4.4)$$

Since the above is a function of $\phi' - \phi$, the result is cylindrically symmetric. Therefore, we can replace $\phi' - \phi$ by just ϕ' and write

$$A_z(\rho, z) = \mu \int_{-L/2}^{L/2} \frac{I_z(z')}{2\pi} \int_0^{2\pi} \frac{e^{-jkr}}{4\pi r} d\phi' dz' \quad (4.5)$$

with $r = \sqrt{(z - z')^2 + \rho^2 + a^2 - 2\rho a \cos \phi'}$. The integral

$$\int_0^{2\pi} \frac{e^{-jkr}}{4\pi r} d\phi' \quad (4.6)$$

is referred to as the cylindrical wire kernel in the literature [1, 2]. If we assume a to be very small, r can be approximated as

$$r = \sqrt{(z - z')^2 + \rho^2} \quad (4.7)$$

and the innermost integral is no longer a function of ϕ' , resulting in

$$A_z(\rho, z) = \mu \int_{-L/2}^{L/2} I_z(z') \frac{e^{-jkr}}{4\pi r} dz' \quad (4.8)$$

The above is often referred to as a *thin wire approximation* with reduced kernel. The original surface integral has now been effectively replaced by a line integral along the axis of the wire. In cases where the dimensions of the problem invalidates the assumptions of the reduced kernel, the cylindrical wire kernel should be evaluated by more exact means such as that of [3].

The radiated field can be obtained via (2.65) and is

$$E_z^s = -j\omega A_z - \frac{j}{\omega\mu\epsilon} \frac{\partial^2}{\partial z^2} A_z \quad (4.9)$$

By enforcing the boundary condition of zero tangential electric field on the surface of the wire, we can now write a *thin wire* EFIE in terms of the incident field E_z^i :

$$E_z^i = \frac{j}{\omega\mu\epsilon} \left[\frac{\partial^2}{\partial z^2} + k^2 \right] A_z \quad (4.10)$$

where the distance from the source to the observation point is $r = \sqrt{(z - z')^2 + a^2}$. When solving the thin wire equations in this chapter, we will assume the testing points to be located on the axis of the wire and the source points to be on the surface.

There are two common forms by which (4.10) is commonly written. The first retains the differential operator outside the integral in (4.10), which is

$$E_z^i(z) = \frac{j}{\omega \mu \epsilon} \left[\frac{\partial^2}{\partial z^2} + k^2 \right] A_z = \frac{j}{\omega \epsilon} \left[\frac{\partial^2}{\partial z^2} + k^2 \right] \int_{-L/2}^{L/2} I_z(z') \frac{e^{-jkr}}{4\pi r} dz' \quad (4.11)$$

which is called *Hallén's integral equation* [4]. We may also move the differential operator under the integral sign,

$$E_z^i(z) = \frac{j}{\omega \epsilon} \int_{-L/2}^{L/2} I_z(z') \left[\frac{\partial^2}{\partial z^2} + k^2 \right] \frac{e^{-jkr}}{4\pi r} dz' \quad (4.12)$$

which is called *Pocklington's integral equation* [5]. Pocklington's equation is not as well behaved as Hallén's, since the differential operator acts directly on the Green's function. As we will see, the results obtained by it typically exhibit slower convergence and less accuracy than those obtained from Hallén's.

4.2 THIN WIRE EXCITATIONS

In most antenna problems, the key variables of interest are typically the input impedance at a particular feed location and the resulting radiation pattern, directivity and gain. The easiest way to compute these is to consider the antenna in its transmitting mode, requiring a reasonable model of the feed system at the input terminals. In the real world, an antenna might be fed by an open-wire transmission line, or by a coaxial feed through a ground plane. These various feed systems impact the antenna impedance characteristics in different ways. With this in mind, we need a way to effectively model a feed method without having to model the feed itself. In this section we consider two common feed methods used in thin wire problems, the delta-gap source and the magnetic frill. The delta-gap source treats the feed as if the electric field impressed by the feedline exists only in the gap between the antenna terminals and is zero outside, i.e., no fringing. This method typically produces less accurate results for input impedance though it still performs very well for computing radiation patterns. The magnetic frill models the feed as a coaxial line that terminates into a monopole over a ground plane. Use of the frill results in more accurate input impedance values at the expense of increased computations in computing the excitation vector elements.

4.2.1 Delta-Gap Source

The delta-gap source model assumes that the impressed electric field in the thin gap between the antenna terminals can be expressed as

$$\mathbf{E}^i = \frac{V_o}{\Delta_z} \hat{\mathbf{z}} \quad (4.13)$$

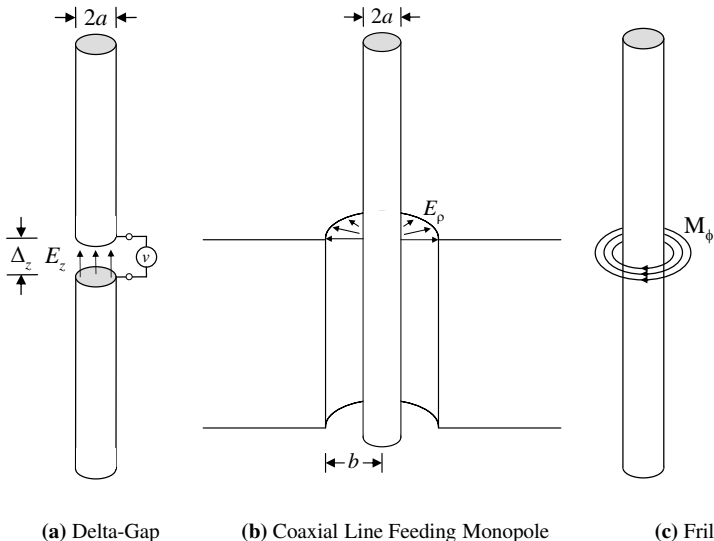


Figure 4.1: Thin wire excitation models.

where Δ_z is the width of the gap, and V_0 is usually set to unity. This is illustrated in Figure 4.1a. In our numerical simulation, we will assume that this field exists inside one wire segment and is zero outside. The resulting excitation vector will have nonzero elements only for basis functions having support on that segment.

4.2.2 Magnetic Frill

In Figure 4.1b, we depict a coaxial line feeding a monopole antenna over an infinite ground plane. If we assume the field distribution in the aperture to be purely TEM, we can use the method of images and replace the ground plane and aperture with the magnetic frill shown in Figure 4.1c. With an aperture electric field given by

$$\mathbf{E}(\rho) = \frac{1}{2\rho \log(b/a)} \hat{\rho} \quad (4.14)$$

the equivalent magnetic current density is

$$\mathbf{M}(\rho) = -2\hat{\mathbf{n}} \times \mathbf{E}(\rho) = \frac{-1}{\rho \log(b/a)} \hat{\phi} \quad a \leq \rho \leq b \quad (4.15)$$

This current generates an electric field along the wire. For a frill centered at the origin, the field intensity on the axis of the wire ($\rho = 0$) is [6]

$$E_z^i(z) = \frac{1}{2 \log(b/a)} \left(\frac{e^{-jkR_1}}{R_1} - \frac{e^{-jkR_2}}{R_2} \right) \quad (4.16)$$

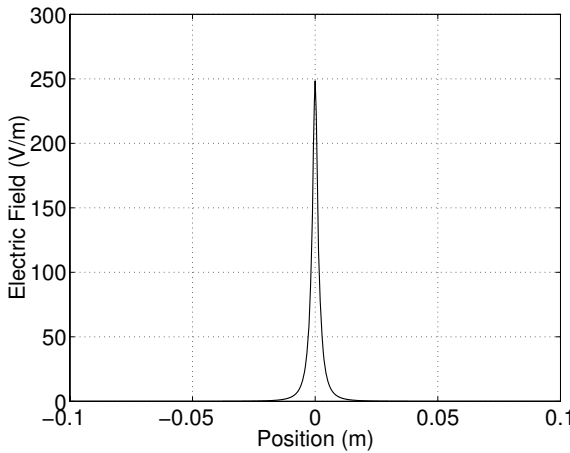


Figure 4.2: Field intensity due to frill.

where

$$R_1 = \sqrt{z^2 + a^2} \quad (4.17)$$

$$R_2 = \sqrt{z^2 + b^2} \quad (4.18)$$

The $\hat{\mathbf{z}}$ -directed field of (4.16) becomes the new incident field used as the excitation. Note that by using this model, we are effectively modeling a dipole with the feed system of a monopole. A true monopole will have an input impedance only half that of the dipole as it only radiates into the half space above the ground. A plot of the axis electric field intensity due to a frill with $a = 1\text{mm}$, $b = 5\text{mm}$ and $\lambda = 1\text{m}$ is shown in Figure 4.2. Because of the sharp dropoff of the field, special care should be given to the numerical integrations used to compute excitation vector elements to ensure their accuracy.

4.2.3 Plane Wave

The tangential electric field intensity on a filamentary wire is given by

$$E_{tan}(\mathbf{r}) = \hat{\mathbf{t}}(\mathbf{r}) \cdot \mathbf{E}(\mathbf{r}) \quad (4.19)$$

where $\hat{\mathbf{t}}$ is tangent to the wire at \mathbf{r} . For a $\hat{\mathbf{z}}$ -oriented wire illuminated by a $\hat{\theta}$ -oriented plane wave of unit amplitude, the above becomes

$$E_{tan}\mathbf{r} = \sin \theta^i e^{jkz \cos \theta^i} \quad (4.20)$$

Because the thin wire approximation assumes there are no azimuthally-excited currents, an incident wave of $\hat{\phi}$ -polarization wave will induce no currents on the wire.

4.3 SOLVING HALLÉN'S EQUATION

Hallén's equation

$$\left[\frac{\partial^2}{\partial z^2} + k^2 \right] A_z(z) = -j\omega\mu\epsilon E_z^i(z) \quad (4.21)$$

is an inhomogeneous scalar Helmholtz equation for $A_z(z)$, which we can solve by the Green's function method. The general solution to the homogeneous equation

$$\left[\frac{\partial^2}{\partial z^2} + k^2 \right] A_z(z) = 0 \quad (4.22)$$

is

$$A_z(z) = C_1 e^{jkz} + C_2 e^{-jkz} \quad (4.23)$$

To obtain a particular solution we must obtain the Green's function $F(z)$ that satisfies the equation

$$\left[k^2 + \frac{\partial^2}{\partial z^2} \right] F(z) = \delta(z) \quad (4.24)$$

Once $F(z)$ is known, the solution for $A_z(z)$ can be obtained by

$$A_z(z) = C_1 e^{jkz} + C_2 e^{-jkz} - j\omega\mu\epsilon \int_{-L/2}^{L/2} F(z, z') E_z^i(z') dz' \quad (4.25)$$

To obtain the Green's function let us use the trial function

$$F(z) = C \sin(k|z|) \quad (4.26)$$

which is continuous at $z = 0$ with discontinuous derivative at $z = 0$ as required for a Green's function [7]. To determine the constant C , let us integrate (4.24) from $-\epsilon$ to ϵ , yielding

$$k^2 C \int_{-\epsilon}^{\epsilon} \sin(k|z|) dz - [Ck \cos(-kz)] \Big|_{-\epsilon}^0 + [Ck \cos(kz)] \Big|_0^{\epsilon} = 1 \quad (4.27)$$

If in the above we allow ϵ to approach zero, the first term goes to zero and after evaluating the remaining terms we get

$$C = \frac{1}{2k} \quad (4.28)$$

hence

$$F(z) = \frac{1}{2k} \sin(k|z|) \quad (4.29)$$

and the solution for $A_z(z)$ is

$$A_z(z) = C_1 e^{jkz} + C_2 e^{-jkz} - \frac{j\mu}{2\eta} \int_{-L/2}^{L/2} \sin(k|z - z'|) E_z^i(z') dz' \quad (4.30)$$

Substituting the original expression for A_z on the left-hand side of the above yields

$$\int_{-L/2}^{L/2} I_z(z') \frac{e^{-jkr}}{4\pi r} dz' = C_1 e^{jkz} + C_2 e^{-jkz} - \frac{j}{2\eta} \int_{-L/2}^{L/2} \sin(k|z-z'|) E_z^i(z') dz' \quad (4.31)$$

By similar reasoning, a second solution for the Green's Function is found to be

$$F_z(z) = \frac{j}{2k} e^{-jk|z|} \quad (4.32)$$

which leads to a second expression for A_z

$$\int_{-L/2}^{L/2} I_z(z') \frac{e^{-jkr}}{4\pi r} dz' = C_1 e^{jkz} + C_2 e^{-jkz} + \frac{1}{2\eta} \int_{-L/2}^{L/2} e^{-jk|z-z'|} E_z^i(z') dz' \quad (4.33)$$

Note also that the two homogeneous terms in the above can also be written as

$$C_1 e^{jkz} + C_2 e^{-jkz} = D_1 \cos(kz) + D_2 \sin(kz) \quad (4.34)$$

where D_1 and D_2 are complex. The form we use will depend on the symmetry of the problem.

4.3.1 Symmetric Problems

Let us solve Hallén's equation for symmetric problems such as the induced current and input impedance of a center-fed dipole antenna. We first expand the left-hand side of (4.31) using N weighted subdomain basis functions yielding

$$\sum_{n=1}^N a_n \int_{f_n} f_n(z') \frac{e^{-jkr}}{4\pi r} dz' \quad (4.35)$$

Testing by N functions f_m yields matrix elements z_{mn} given by

$$z_{mn} = \int_{f_m} f_m(z) \int_{f_n} f_n(z') \frac{e^{-jkr}}{4\pi r} dz' dz \quad (4.36)$$

The choice of the right-hand side depends on the symmetry of the problem being considered. Since we are feeding the antenna at its center, we expect that the induced current will be symmetric. Therefore, let us retain the right-hand side of (4.31) but rewrite the homogeneous terms following (4.34):

$$D_1 \cos(kz) + D_2 \sin(kz) - \frac{j}{2\eta} \int_{-L/2}^{L/2} \sin(k|z-z'|) E_z^i(z') dz' \quad (4.37)$$

Since we expect the solution to be symmetric, we set D_2 in the above to zero. Applying the testing functions yields

$$D_1 \int_{f_m} f_m(z) \cos(kz) dz - \frac{j}{2\eta} \int_{f_m} f_m(z) \int_{-L/2}^{L/2} \sin(k|z - z'|) E_z^i(z') dz' dz \quad (4.38)$$

The above expressions result in the following matrix equation:

$$\mathbf{Z}\mathbf{a} = D_1\mathbf{s} + \mathbf{b} \quad (4.39)$$

To obtain the solution vector \mathbf{a} we must determine the constant D_1 , which can be done by enforcing the boundary conditions at the ends of the wire, i.e., $I_z(-L/2) = I_z(L/2) = 0$. We will do this in our discretized version by forcing the basis function coefficient at each end to be zero [8]. This can be expressed vectorially as $\mathbf{u}^T \mathbf{a} = 0$, where $\mathbf{u}^T = [1, 0, \dots, 0, 1]$. Solving (4.39) for \mathbf{a} we obtain

$$\mathbf{a} = D_1[\mathbf{Z}]^{-1}\mathbf{s} + [\mathbf{Z}]^{-1}\mathbf{b} \quad (4.40)$$

and multiplying both sides by \mathbf{u}^T we obtain

$$\mathbf{u}^T \mathbf{a} = D_1 \mathbf{u}^T [\mathbf{Z}]^{-1} \mathbf{s} + \mathbf{u}^T [\mathbf{Z}]^{-1} \mathbf{b} = 0 \quad (4.41)$$

and solving for D_1 yields

$$D_1 = -\frac{\mathbf{u}^T [\mathbf{Z}]^{-1} \mathbf{b}}{\mathbf{u}^T [\mathbf{Z}]^{-1} \mathbf{s}} \quad (4.42)$$

The complete right-hand side vector can now be built from \mathbf{s} and \mathbf{b} using D_1 .

4.3.1.1 Solution by Pulse Functions and Point Matching

To solve the symmetric Hallén's equation with pulse basis functions and point matching, we subdivide the wire into N equally spaced segments of length L/N . The matrix elements of (4.36) become

$$z_{mn} = \int_{z_n - \Delta_z/2}^{z_n + \Delta_z/2} \frac{e^{-jkR}}{4\pi R} dz' \quad (4.43)$$

where matching is done at the center of each segment z_m , and $R = \sqrt{(z_m - z')^2 + a^2}$. We will compute the non-self terms via an M -point numerical quadrature yielding

$$z_{mn} = \sum_{q=1}^M w_q \frac{e^{-jkR_{mq}}}{4\pi R_{mq}} \quad (4.44)$$

where $R_{mq} = \sqrt{(z_m - z_q)^2 + a^2}$. For the self terms ($m = n$), we will use a small-argument approximation to the Green's function to write

$$z_{mm} = \int_{-\Delta_z/2}^{\Delta_z/2} \frac{e^{-jkR}}{4\pi R} dz' \approx \int_{-\Delta_z/2}^{\Delta_z/2} \frac{1 - jkR}{4\pi R} dz' \quad (4.45)$$

which evaluates to [9] (Equation 200.01)

$$z_{mm} = \frac{1}{4\pi} \log \left[\frac{\sqrt{1+4a^2/\Delta_z^2} + 1}{\sqrt{1+4a^2/\Delta_z^2} - 1} \right] - \frac{jk\Delta_z}{4\pi} \quad (4.46)$$

We assume that the approximation in (4.46) will remain valid if the segment is small compared to the wavelength. The right-hand side vector elements are

$$s_m = \cos(kz_m) \quad (4.47)$$

and

$$b_m = -\frac{j}{2\eta} \int_{-L/2}^{L/2} \sin(k|z_m - z'|) E_z^i(z') dz' \quad (4.48)$$

where we have not yet specified the excitation field $E_z^i(z')$. If we use a delta-gap source located at the center of the wire, $E_z^i(z') = \delta(z')$, the above simplifies to

$$b_m = -\frac{j}{2\eta} \sin(k|z_m|) \quad (4.49)$$

If we use the magnetic frill of (4.16), the convolution in (4.48) must be performed numerically for each z_m . Because of the sharp dropoff of the frill field, special care should be given to this integral to ensure its accuracy.

4.3.2 Asymmetric Problems

When the feedpoint is not at the center of the antenna or the wire is excited by an incident wave, we can no longer assume the solution to be symmetric. In this case, the elements of the impedance matrix remain the same as in (4.36), however we will use the more general right-hand side of (4.33). Applying the testing function f_m to the right-hand side yields

$$\begin{aligned} & C_1 \int_{f_m} f_m(z) e^{jkz} dz + C_2 \int_{f_m} f_m(z) e^{-jkz} dz + \\ & \frac{1}{2\eta} \int_{f_m} f_m(z) \int_{-L/2}^{L/2} e^{-jk|z_m-z'|} E_z^i(z') dz' dz \end{aligned} \quad (4.50)$$

The resulting matrix equation is of the form

$$\mathbf{Z}\mathbf{a} = C_1 \mathbf{s}_1 + C_2 \mathbf{s}_2 + \mathbf{b} \quad (4.51)$$

which we can rewrite as

$$\mathbf{Z}\mathbf{a} = [\mathbf{s}_1, \mathbf{s}_2] [C_1, C_2]^T + \mathbf{b} \quad (4.52)$$

Solving for \mathbf{a} , we obtain

$$\mathbf{a} = [\mathbf{Z}]^{-1}[\mathbf{s}_1, \mathbf{s}_2] [C_1, C_2]^T + [\mathbf{A}]^{-1}\mathbf{b} \quad (4.53)$$

We must solve for the constants C_1 and C_2 to obtain \mathbf{a} , which can be done by a method similar to the symmetric case [8]. Let us define the matrix $[\mathbf{U}] = [\mathbf{u}_1^T, \mathbf{u}_2^T]$, where the vectors $\mathbf{u}_1^T = [1, 0, \dots, 0, 0]$ and $\mathbf{u}_2^T = [0, 0, \dots, 0, 1]$ select the elements on the end of the wire and enforce the condition

$$[\mathbf{U}]^T \mathbf{a} = 0 \quad (4.54)$$

Applying this to the above yields

$$[\mathbf{U}]^T \mathbf{a} = [\mathbf{U}]^T [\mathbf{Z}]^{-1}[\mathbf{s}_1, \mathbf{s}_2] [C_1, C_2]^T + [\mathbf{U}]^T [\mathbf{Z}]^{-1}\mathbf{b} = 0 \quad (4.55)$$

Solving for $[C_1, C_2]^T$ yields

$$[C_1, C_2]^T = \left[[\mathbf{U}]^T [\mathbf{Z}]^{-1}[\mathbf{s}_1, \mathbf{s}_2] \right]^{-1} [\mathbf{U}]^T [\mathbf{Z}]^{-1}\mathbf{b} \quad (4.56)$$

The asymmetric Hallén's equation can be solved numerically by the same method used in the symmetric case, so we will not repeat the process here.

4.4 SOLVING POCKLINGTON'S EQUATION

Pocklington's equation,

$$-j\omega\epsilon E_z^i(z) = \int_{-L/2}^{L/2} I_z(z') \left[\frac{\partial^2}{\partial z^2} + k^2 \right] \frac{e^{-jkr}}{4\pi r} dz' \quad (4.57)$$

can be solved by a straightforward application of the moment method, since the differential operator is inside the integral and acts on the Green's function only. Expanding the current into a sum of N weighted basis functions and applying N testing functions we obtain a linear system with matrix elements

$$z_{mn} = \int_{f_m} f_m(z) \int_{f_n} f_n(z') \left[\frac{\partial^2}{\partial z^2} + k^2 \right] \frac{e^{-jkr}}{4\pi r} dz' dz \quad (4.58)$$

and excitation vector elements b_m given by

$$b_m = -j\omega\epsilon \int_{f_m} f_m(z) E_z^i(z) dz \quad (4.59)$$

4.4.1 Solution by Pulse Functions and Point Matching

Using pulse basis functions for the current and point matching for testing, we obtain the following excitation vector elements:

$$b_m = -j\omega\epsilon E_z^i(z_m) \quad (4.60)$$

The impedance matrix elements can be written as

$$z_{mn} = \frac{k^2}{4\pi} \int_{z_n-\Delta_z/2}^{z_n+\Delta_z/2} \frac{e^{-jkR}}{R} dz' + \left[\frac{\partial}{\partial z'} \frac{e^{-jkR}}{R} \right] \Bigg|_{z'=z_n-\Delta_z/2}^{z'=z_n+\Delta_z/2} \quad (4.61)$$

where $R = \sqrt{(z_m - z')^2 + a^2}$, and $\partial/\partial z$ has been replaced by $\partial/\partial z'$. Evaluating the derivative in the second term yields

$$\frac{\partial}{\partial z'} \frac{e^{-jkR}}{R} = (z_m - z') \frac{1 + jkR}{R^3} e^{-jkR} \quad (4.62)$$

allowing us to write

$$z_{mn} = \frac{k^2}{4\pi} \int_{z_n-\Delta_z/2}^{z_n+\Delta_z/2} \frac{e^{-jkR}}{R} dz' + \left[(z_m - z') \frac{1 + jkR}{R^3} e^{-jkR} \right] \Bigg|_{z'=z_n-\Delta_z/2}^{z'=z_n+\Delta_z/2} \quad (4.63)$$

The first term is of the same form as (4.43) and is computed the same way. The second term is analytic and may be used as-is for all matrix elements. Due to the strongly singular $1/R^3$ term, we will find our results to converge less quickly than those obtained using Hallén's equation for the same problem.

4.5 THIN WIRES OF ARBITRARY SHAPE

Because there are many antennas with bend and wire-to-wire junctions, we need to consider the thin wire EFIE in a form appropriate for these geometries. In this form, the wire current will be a vector function of position; therefore, the basis and testing functions will also be vectors. Let us retain the thin wire kernel of (4.8) but make the line current a vector valued function of position

$$\mathbf{I}(\mathbf{r}) = I(\mathbf{r}) \hat{\mathbf{t}}(\mathbf{r}) \quad (4.64)$$

where $\hat{\mathbf{t}}(\mathbf{r})$ is the tangent to the wire at \mathbf{r} . Substituting the above into the EFIE of (2.120) results in

$$-\frac{j}{\omega\mu} [\hat{\mathbf{t}}(\mathbf{r}) \cdot \mathbf{E}^i(\mathbf{r})] = \left[1 + \frac{1}{k^2} \nabla \nabla \cdot \right] \int_L I(\mathbf{r}') \hat{\mathbf{t}}(\mathbf{r}') G(\mathbf{r}, \mathbf{r}') d\mathbf{r}' \quad (4.65)$$

which we will refer to as the EFIE for arbitrarily shaped thin wires (ATW). We next approximate the current as a sum of N weighted vector basis functions:

$$I(\mathbf{r}')\hat{\mathbf{t}}(\mathbf{r}) \approx \sum_{n=1}^N a_n \mathbf{f}_n(\mathbf{r}) \quad (4.66)$$

where $\mathbf{f}(\mathbf{r})$ is everywhere tangent to the wire. Substituting the above in the EFIE yields

$$-\frac{j}{\omega\mu} [\hat{\mathbf{t}}(\mathbf{r}) \cdot \mathbf{E}^i(\mathbf{r})] = \left[1 + \frac{1}{k^2} \nabla \nabla \cdot \right] \sum_{n=1}^N a_n \int_{\mathbf{f}_n} \mathbf{f}_n(\mathbf{r}') G(\mathbf{r}, \mathbf{r}') d\mathbf{r}' \quad (4.67)$$

Testing the above by N testing functions $\mathbf{f}_m(\mathbf{r})$ yields a linear system with matrix elements given by

$$\begin{aligned} z_{mn} &= \int_{\mathbf{f}_m} \mathbf{f}_m(\mathbf{r}) \cdot \int_{\mathbf{f}_n} \mathbf{f}_n(\mathbf{r}') G(\mathbf{r}, \mathbf{r}') d\mathbf{r}' d\mathbf{r} \\ &+ \frac{1}{k^2} \int_{\mathbf{f}_m} \mathbf{f}_m(\mathbf{r}) \cdot \left[\nabla \nabla \cdot \int_{\mathbf{f}_n} \mathbf{f}_n(\mathbf{r}') G(\mathbf{r}, \mathbf{r}') d\mathbf{r}' \right] d\mathbf{r} \end{aligned} \quad (4.68)$$

and excitation vector elements b_m given by

$$b_m = -\frac{j}{\omega\mu} \int_{\mathbf{f}_m} \mathbf{f}_m(\mathbf{r}) \cdot \mathbf{E}^i(\mathbf{r}) d\mathbf{r} \quad (4.69)$$

Let us now focus on the second term on the right-hand side of (4.68). If we redistribute the differential operators so they operate on the basis and testing functions, it will simplify the calculation of the matrix elements.

4.5.1 Redistribution of EFIE Differential Operators

Let us focus on the term

$$\int_{\mathbf{f}_m} \mathbf{f}_m(\mathbf{r}) \cdot \left[\nabla \nabla \cdot \int_{\mathbf{f}_n} \mathbf{f}_n(\mathbf{r}') G(\mathbf{r}, \mathbf{r}') d\mathbf{r}' \right] d\mathbf{r} \quad (4.70)$$

Following the discussion in Section 2.4.3, this can be rewritten as

$$\int_{\mathbf{f}_m} \mathbf{f}_m(\mathbf{r}) \cdot \nabla S(\mathbf{r}) d\mathbf{r} = \int_{\mathbf{f}_m} \mathbf{f}_m(\mathbf{r}) \cdot \left[\nabla \int_{\mathbf{f}_n} \nabla' \cdot \mathbf{f}(\mathbf{r}') G(\mathbf{r}, \mathbf{r}') d\mathbf{r}' \right] d\mathbf{r} \quad (4.71)$$

Using the vector identity

$$\mathbf{f}(\mathbf{r}) \cdot \nabla S(\mathbf{r}) = \nabla \cdot [\mathbf{f}(\mathbf{r})S(\mathbf{r})] - [\nabla \cdot \mathbf{f}(\mathbf{r})]S(\mathbf{r}) \quad (4.72)$$

we can write the above as

$$\int_{\mathbf{f}_m} \mathbf{f}_m(\mathbf{r}) \cdot \nabla S(\mathbf{r}) d\mathbf{r} = \int_{\mathbf{f}_m} \nabla \cdot [\mathbf{f}_m(\mathbf{r}) S(\mathbf{r})] d\mathbf{r} - \int_{\mathbf{f}_m} [\nabla \cdot \mathbf{f}_m(\mathbf{r})] S(\mathbf{r}) d\mathbf{r} \quad (4.73)$$

We convert the first term on the right-hand side to a surface integral using the divergence theorem:

$$\iiint_V \nabla \cdot [\mathbf{f}_m(\mathbf{r}) S(\mathbf{r})] d\mathbf{r} = \iint_S \hat{\mathbf{n}} \cdot [\mathbf{f}_m(\mathbf{r}) S(\mathbf{r})] d\mathbf{r} \quad (4.74)$$

Since the bounding surface can be made large enough that $\mathbf{f}_m(\mathbf{r})$ vanishes, the above goes to zero leaving only the second term which is

$$\int_{\mathbf{f}_m} \mathbf{f}_m(\mathbf{r}) \cdot \nabla S(\mathbf{r}) d\mathbf{r} = - \int_{\mathbf{f}_m} \nabla \cdot \mathbf{f}_m(\mathbf{r}) \int_n \nabla' \cdot \mathbf{f}(\mathbf{r}') G(\mathbf{r}, \mathbf{r}') d\mathbf{r}' d\mathbf{r} \quad (4.75)$$

Substituting the above into (4.68) results in the following new expression for the EFIE matrix elements:

$$\begin{aligned} z_{mn} &= \int_{\mathbf{f}_m} \mathbf{f}_m(\mathbf{r}) \cdot \int_{\mathbf{f}_n} \mathbf{f}_n(\mathbf{r}') G(\mathbf{r}, \mathbf{r}') d\mathbf{r}' d\mathbf{r} \\ &\quad - \frac{1}{k^2} \int_{\mathbf{f}_m} \nabla \cdot \mathbf{f}_m(\mathbf{r}) \int_{\mathbf{f}_n} \nabla' \cdot \mathbf{f}(\mathbf{r}') G(\mathbf{r}, \mathbf{r}') d\mathbf{r}' d\mathbf{r} \end{aligned} \quad (4.76)$$

The above avoids the differential operators acting on the Green's function provided that the basis and testing functions have a well-behaved divergence. Therefore, we will use triangular or sinusoidal basis and testing functions to solve the EFIE in this form.

4.5.2 Solution Using Triangle Basis and Testing Functions

To solve the ATW EFIE using triangle functions, we use the configuration of Figure 3.9 since the current must go to zero at the ends of the wire. We subdivide the wire into N segments of length Δ_l resulting in $N - 1$ basis and testing functions. The matrix elements are

$$\begin{aligned} z_{mn} &= \int_{\mathbf{f}_m} f_m(l) \hat{\mathbf{t}}(l) \cdot \int_{\mathbf{f}_n} f_n(l') \hat{\mathbf{t}}(l') G(\mathbf{r}, \mathbf{r}') dl' dl \\ &\quad - \frac{1}{k^2} \int_{\mathbf{f}_m} \dot{f}_m(l) \int_{\mathbf{f}_n} \dot{f}_n(l') G(\mathbf{r}, \mathbf{r}') dl' dl \end{aligned} \quad (4.77)$$

where $f_m(l)$ and $f_n(l')$ are the scalar triangle functions expressed in terms of parametrized wire location l , and $\hat{\mathbf{t}}(l)$ and $\hat{\mathbf{t}}(l')$ are the associated wire tangent vectors. For ascending and descending triangle functions of the form l/Δ_l and $(\Delta_l - l)/\Delta_l$, the derivatives are $1/\Delta_l$ and $-1/\Delta_l$, respectively. When the source

and testing triangles have no overlapping segments, the elements can be computed via an M -point numerical quadrature yielding

$$\begin{aligned} z_{mn} = & \frac{1}{4\pi} \sum_{p=1}^M \sum_{q=1}^M w_p(l_p) w_q(l'_q) \left[f_m(l_p) f_n(l'_q) \hat{\mathbf{t}}(l_p) \cdot \hat{\mathbf{t}}(l'_q) \right. \\ & \left. - \frac{1}{k^2} \dot{f}_m(l_p) \dot{f}_n(l'_q) \right] \frac{e^{-jkR_{pq}}}{R_{pq}} \end{aligned} \quad (4.78)$$

For segments that are not close together, we will use the distance between quadrature points along the wire axis, $R_{pq} = |\mathbf{r}_p - \mathbf{r}'_q|$. For segments close together, we will retain the original expression $R_{pq} = \sqrt{|\mathbf{r}_p - \mathbf{r}'_q| + a^2}$. The excitation vector elements b_m are

$$b_m = -\frac{j}{\omega\mu} \int_{\mathbf{f}_m} f_m(l) \hat{\mathbf{t}}(l) \cdot \mathbf{E}^i(l) dl \quad (4.79)$$

4.5.2.1 Self Terms

For overlapping segments we will evaluate the innermost integral analytically and the outermost integral numerically. To calculate the first term on the right in (4.77), consider the following innermost integral with the ascending triangle function x'/Δ_l :

$$S_1(x) = \int_0^{\Delta_l} \frac{x'}{\Delta_l} \frac{e^{-jkr}}{r} dx' \quad (4.80)$$

where $r = \sqrt{(x - x')^2 + a^2}$. Using the small-argument approximation to the Green's function this becomes

$$\int_0^{\Delta_l} \frac{x'}{\Delta_l} \frac{e^{-jkr}}{r} dx' \approx \int_0^{\Delta_l} \frac{x'}{\Delta_l} \frac{1 - jkr}{r} dx' \quad (4.81)$$

which is

$$\int_0^{\Delta_l} \frac{x'}{\Delta_l} \frac{1 - jkr}{r} dx' = \frac{1}{\Delta_l} \int_0^{\Delta_l} \frac{x'}{r} dx' - \frac{jk\Delta_l}{2} \quad (4.82)$$

The first term on the right then evaluates to [10]

$$\frac{1}{\Delta_l} \sqrt{a^2 + (x - \Delta_l)^2} - \frac{1}{\Delta_l} \sqrt{a^2 + x^2} + \frac{x}{\Delta_l} \log \left[\frac{x + \sqrt{a^2 + x^2}}{x - \Delta_l + \sqrt{a^2 + (x - \Delta_l)^2}} \right]$$

resulting in

$$\begin{aligned} S_1(x) = & \frac{1}{\Delta_l} \sqrt{a^2 + (x - \Delta_l)^2} - \frac{1}{\Delta_l} \sqrt{a^2 + x^2} \\ & + \frac{x}{\Delta_l} \log \left[\frac{x + \sqrt{a^2 + x^2}}{x - \Delta_l + \sqrt{a^2 + (x - \Delta_l)^2}} \right] - \frac{jk\Delta_l}{2} \end{aligned} \quad (4.83)$$

The integral involving the ascending triangle is sufficient to obtain all the self terms because of symmetry. We will compute the second term on the right in (4.77) the same way as the first term. The innermost integral is

$$S_2(x) = \pm \frac{1}{\Delta_l^2} \int_0^{\Delta_l} \frac{1 - jkr}{r} dx' \quad (4.84)$$

where we have again used the small-argument approximation to the Green's function, and the sign of the integral depends on whether the derivatives of the source and testing functions are of opposing sign. The above evaluates to [10]

$$S_2(x) = \pm \frac{1}{\Delta_l^2} \left[\log \left[\frac{x + \sqrt{a^2 + x^2}}{x - \Delta_l + \sqrt{a^2 + (x - \Delta_l)^2}} \right] - jk\Delta_l \right] \quad (4.85)$$

The contributions from overlapping segments to (4.77) can then be obtained via the sum

$$\frac{1}{4\pi} \sum_{p=1}^M w_p(x_p) \left[f_m(x_p) S_1(x_p) - \frac{1}{k^2} S_2(x_p) \right] \quad (4.86)$$

4.5.3 Solution Using Sinusoidal Basis and Testing Functions

Solving (4.76) using sinusoidal basis and testing functions is virtually the same as with triangle functions. The difference lies in the near and self terms, which we compute using numerical outer and analytic inner integrations as before.

4.5.3.1 Self Terms

To calculate the first term on the right in (4.77), consider the following innermost integral with the ascending sinusoid function:

$$S_1(x_p) = \frac{1}{\sin(k\Delta_l)} \int_0^{\Delta_l} \sin(kx') \frac{e^{-jkr}}{r} dx' \quad (4.87)$$

Again using the small-argument approximation to the Green's function, this becomes

$$\int_0^{\Delta_l} \sin(kx') \frac{e^{-jkr}}{r} dx' \approx \int_0^{\Delta_l} \sin(kx') \left[\frac{1 - jkr}{r} \right] dx' \quad (4.88)$$

which is

$$\int_0^{\Delta_l} \sin(kx') \left[\frac{1 - jkr}{r} \right] dx' = \int_0^{\Delta_l} \frac{\sin(kx')}{r} dx' + j[\cos(k\Delta_l) - 1] \quad (4.89)$$

The first term on the right is not tractable in its present form, so we will approximate the sine by its third-order polynomial approximation. This yields

$$\int_0^{\Delta_l} \frac{\sin(kx')}{r} dx' \approx \int_0^{\Delta_l} \frac{kx' - (kx')^3/6}{\sqrt{(x' - x_p)^2 + a^2}} dx' \quad (4.90)$$

Evaluating the above results in [10]

$$\begin{aligned} S_1(x_p) = & C \frac{kx_p}{12} \left(\left[-3a^2k^2 + 2x_p^2k^2 - 12 \right] \cdot \log \left[x_p - x' + \sqrt{a^2 + (x_p - x')^2} \right] \right. \\ & - \frac{k}{36} \left[-4a^2k^2 + k^2(11x_p^2 + 5x'x_p - 2(x')^2) - 36 \right] \\ & \left. \cdot \sqrt{a^2 + (x_p - x')^2} \right) \Big|_0^{\Delta_l} + jC[\cos(k\Delta_l) - 1] \end{aligned} \quad (4.91)$$

where $C = 1 / \sin(k\Delta_l)$. This result is lengthy but can be evaluated numerically in a straightforward manner. We compute the second term on the right of (4.77) the same way. Under the small-argument approximation to the Green's function, the innermost integral in this case is

$$S_2(x_p) = \frac{k}{\sin(k\Delta_l)} \int_0^{\Delta_l} \frac{\cos(kx')}{r} dx' - jk \quad (4.92)$$

We approximate the cosine by its second-order approximation, yielding the integral

$$\int_0^{\Delta_l} \frac{\cos(kx')}{r} dx' \approx \int_0^{\Delta_l} \frac{1 - (kx')^2/2}{\sqrt{(x' - x_p)^2 + a^2}} dx' \quad (4.93)$$

The above evaluates to [10]

$$\begin{aligned} S_2(x_p) = & -\frac{C}{4} \left(k^2[3x_p + x'] \sqrt{a^2 + (x_p - x')^2} + (a^2k^2 - 2x_p^2k^2 + 4) \right. \\ & \left. \cdot \log \left[x_p - x' + \sqrt{a^2 + (x_p - x')^2} \right] \right) \Big|_0^{\Delta_l} - jk \end{aligned} \quad (4.94)$$

The contributions to the self terms are then computed as

$$\frac{1}{4\pi} \sum_{p=1}^M w_p(x_p) \left[f_m(x_p)S_1(x_p) - \frac{1}{k^2} \dot{f}_m(x_p)S_2(x_p) \right] \quad (4.95)$$

4.5.4 Lumped and Distributed Impedances

In some cases it may be desirable to place an impedance on an antenna to change its characteristics. Feedpoint matching is one of the more common modifications, and can be done by placing an impedance in parallel at the feedpoint, or by inserting a coil or capacitor at a point along the wire. To model impedances in our thin wire integral equation, we must modify the boundary conditions on the segment(s) where

the load(s) exists. Given a complex impedance Z_l on a segment of length Δ_l , the new condition on this segment is

$$E_{tan}^i + E_{tan}^s = E_{load} = \frac{V_l}{\Delta_l} = \frac{Z_l I_s}{\Delta_l} \quad (4.96)$$

The right-hand side of the EFIE now becomes

$$\frac{j}{\omega \mu} \left(\frac{Z_l I_l}{\Delta_l} - E_{tan}^i \right) \quad (4.97)$$

where the current I_l on the segment is due to one or more basis functions. If we use the thin wire formulation of Section 4.5 with triangle basis functions, the testing operation with the basis function f_m will create a “self term” on the right-hand side of the form

$$z_m = \frac{j}{2\omega\mu} Z_l \quad (4.98)$$

which would then be moved to the left-hand side and subtracted from the diagonal element z_{mm} . Any basis function having support on the segment will have its diagonal term modified in a similar manner.

4.6 EXAMPLES

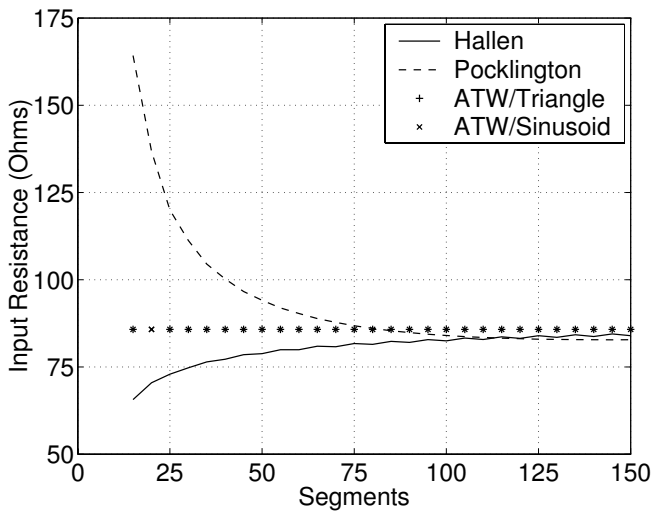
In this section we consider several thin wire antenna problems. We will first compare the performance of the Hallén, Pocklington and arbitrary thin wire models. We will then compute the input impedance of several common antenna types such as the loop, folded dipole, and Yagi. For each, we will apply the ATW formulation with triangular basis functions.

4.6.1 Comparison of Thin Wire Models

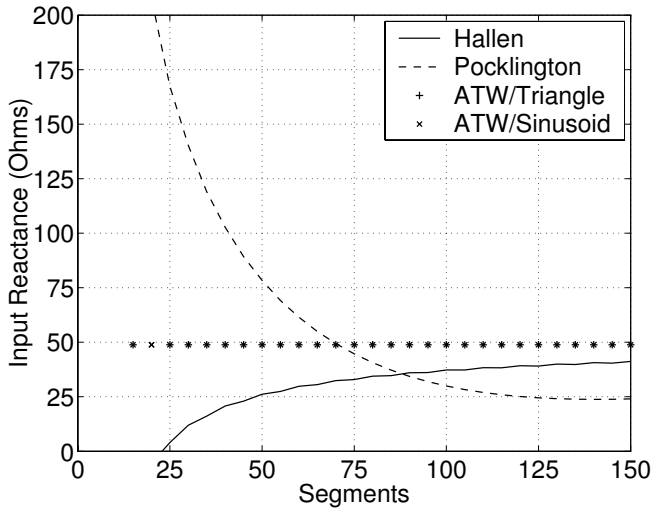
For our comparison, we will compute the input impedance and induced current distribution on center-fed dipole antennas. To judge the effectiveness of each method, we will compare the rates of convergence versus the number of wire segments used in the discretization. We use the delta-gap voltage source and an odd number of wire segments so the source lies at the center of the antenna. For numerical integrations, a five-point Gaussian quadrature per segment is used. The dipoles are given a radius of $10^{-3}\lambda$, and for induced current distributions, the magnitude of the applied voltage is unity.

4.6.1.1 Input Impedance

We first compare the convergence of the input impedance versus the number of wire segments used. Figure 4.3 shows the relative rates of convergence for a $\lambda/2$ dipole. Hallén’s equation is seen to converge somewhat faster than Pocklington’s equation

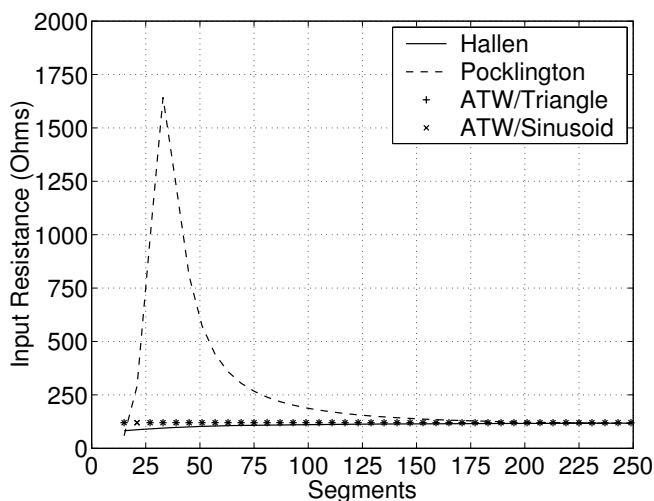


(a) Input Resistance

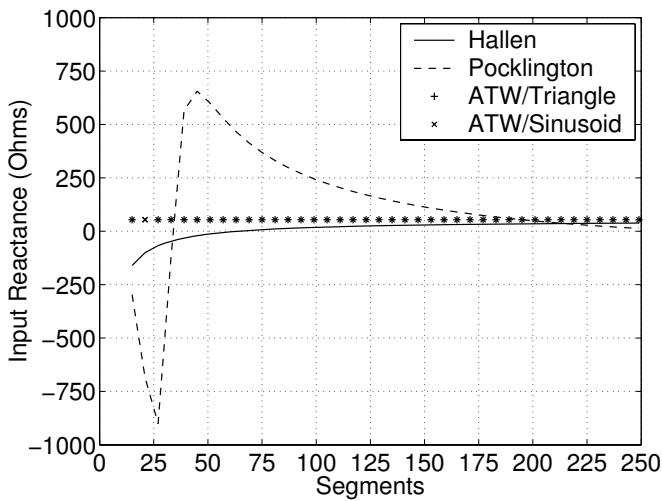


(b) Input Reactance

Figure 4.3: Input impedance of a $\lambda/2$ dipole.

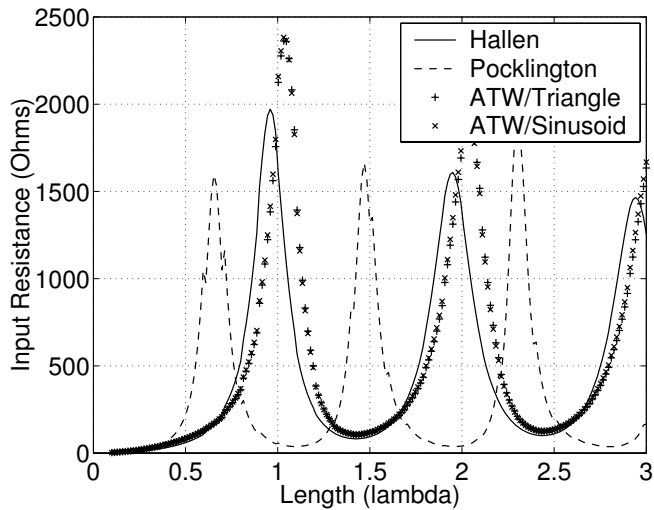


(a) Input Resistance

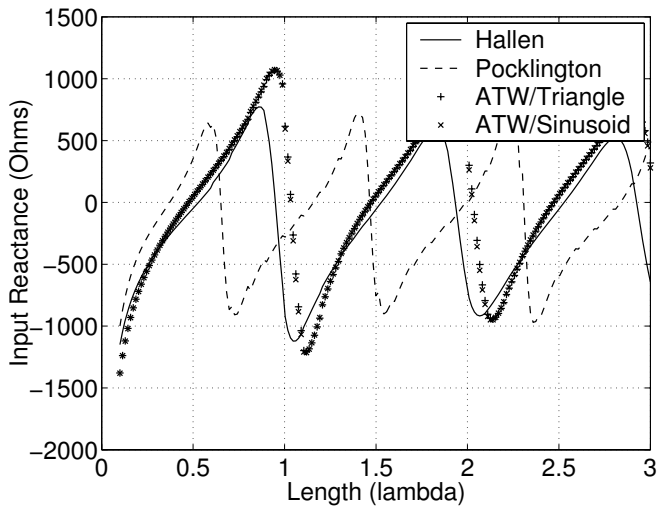


(b) Input Reactance

Figure 4.4: Input impedance of a $3\lambda/2$ dipole.



(a) Input Resistance



(b) Input Reactance

Figure 4.5: Input impedance versus dipole length.

for this case, and fairly good convergence for each is seen at around 100 segments (200 segments per wavelength). The solutions obtained using the ATW model with triangles and sinusoids appear converged and are nearly indistinguishable. This is not surprising since these basis functions model the current distribution much better than pulses. Figure 4.4 shows the convergence for a $3\lambda/2$ dipole. The results from Hallén's equation converge somewhat faster in this case. The results obtained by Pocklington's equation are again not very good, and demonstrate the undesirable convergence properties of the $1/R^3$ term in its integrand. The results obtained using triangles and sinusoids are again excellent.

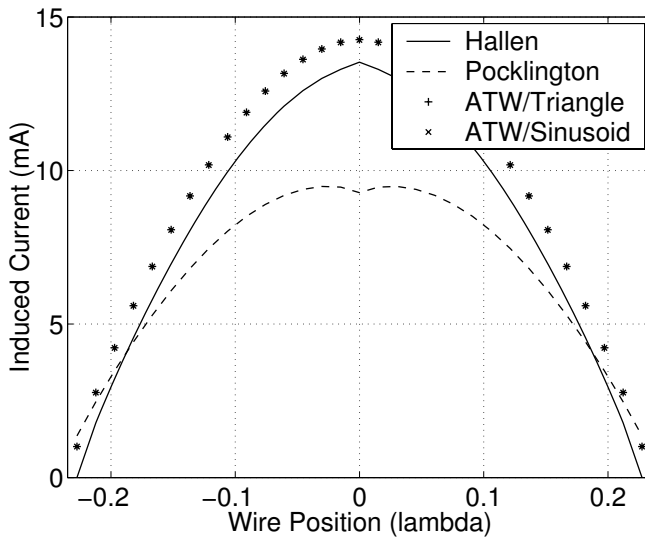
We next fix the number of segments per wavelength at approximately 20 and vary the dipole length over the range 0.1 to 3λ . The results are shown in Figure 4.5. The ATW models agree very well at almost every data point, suggesting that triangles and sinusoids will perform much the same for thin wire problems. The impedances obtained from Hallén's and Pocklington's equations do not compare very well for this level of discretization, as expected.

4.6.1.2 Current Distribution

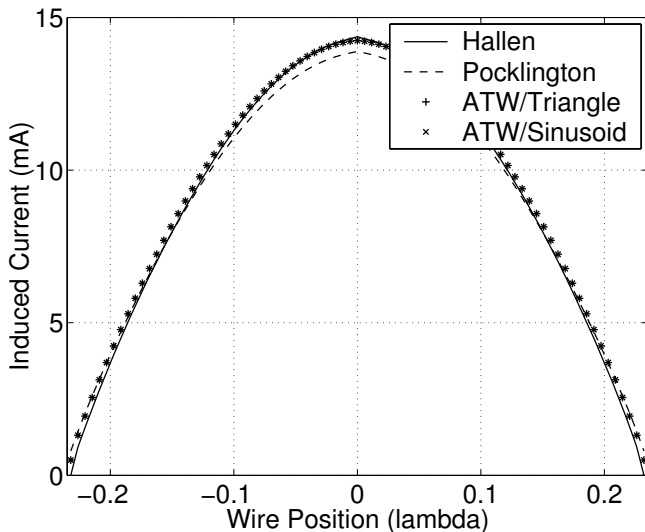
We next compare the induced current calculations. Hallén's equation will be zero on the end segments as it is set to that value explicitly. Figures 4.6a and 4.6b depict the induced current on a 0.47λ dipole computed using 31 and 81 wire segments, respectively. The ATW models show practically no change between the two figures, indicating excellent convergence. The current from Hallén's equation changes slightly between the two figures, indicating a fair level of convergence, however that of Pocklington's equation exhibits large variation. Results for a 2λ dipole are shown in Figures 4.7a and 4.7b, computed using 81 and 181 segments, respectively. The convergence of the various methods is again very similar to the previous case. The ATW methods again demonstrate superior performance, whereas Pocklington's equation performs the worst.

4.6.2 Circular Loop Antenna

We next consider the input impedance of a closed circular loop antenna. We vary the circumference of the loop from a very small value up to 2.5λ , and fix the radius of the wire to $10^{-4}\lambda$ at each step. At each point, we subdivide the loop into approximately 10 segments per wavelength, and use no fewer than 36 segments at the smallest electrical length. This ensures that the model retains the shape of a circle at the lowest frequency. The real and imaginary parts of the input impedance are shown in Figure 4.8. For lengths below 0.5λ , the loop presents a high inductance with virtually no radiation resistance. At approximately $\lambda/2$, the loop acts as an open circuit at the antenna terminals. We observe the first resonance is at a length just over 1λ , where the input resistance is approximately 140Ω .

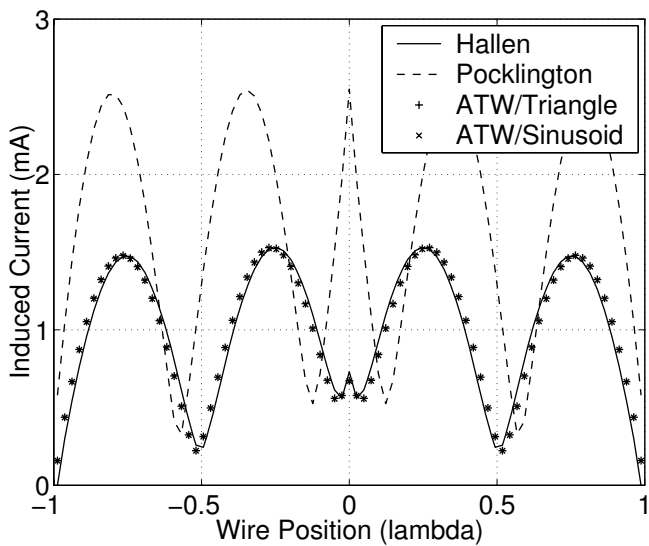


(a) 31 Segments

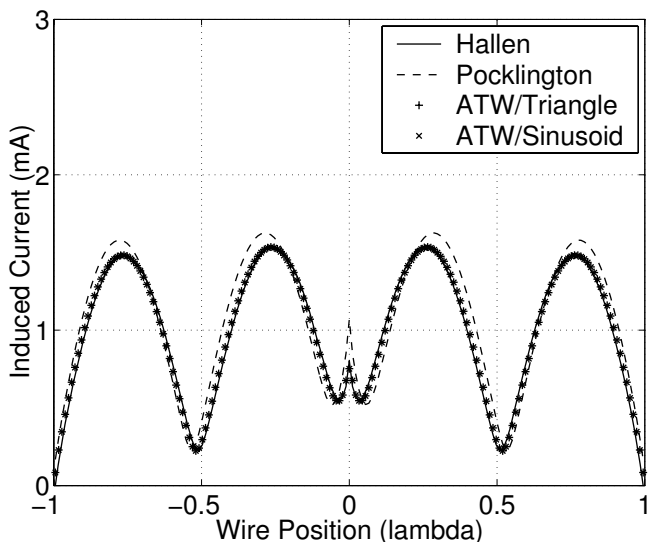


(b) 81 Segments

Figure 4.6: Induced current on a 0.47λ dipole.



(a) 81 Segments



(b) 181 Segments

Figure 4.7: Induced current on a 2λ dipole.

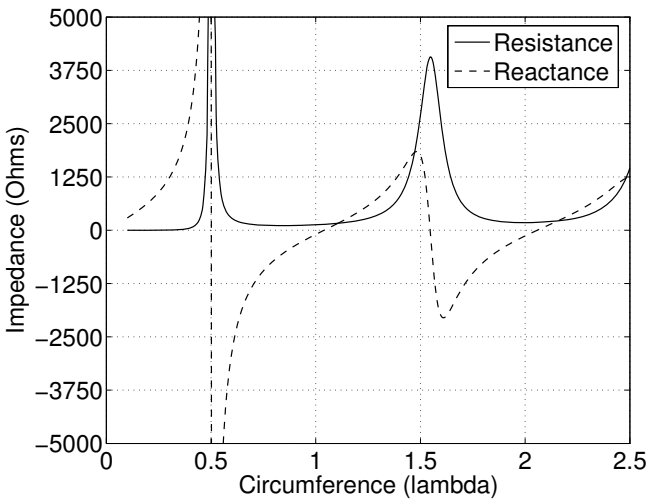


Figure 4.8: Circular loop input impedance.

4.6.3 Folded Dipole Antenna

The folded dipole is an antenna commonly used in HF and VHF systems. It takes the name from a dipole antenna that is “folded over on itself,” and comprises a square loop that is very short in one dimension. This is illustrated in Figure 4.9a, where the main conductors are offset by a small distance s . At DC, this antenna is a short circuit, but with increasing length the current distribution changes and assumes the characteristics of Figure 4.9b when L approaches $\lambda/2$. In this case, the currents on the secondary conductor take on the same magnitude and phase as those on the primary. Because the conductors are so closely spaced, the far-zone radiated field remains much the same, however the current is divided evenly between the two halves. Therefore, the input impedance of the folded dipole will be four times that of an ordinary dipole, or approximately $4 \cdot 72 = 288 \Omega$. Folded dipoles are often used because of this property, as they can be matched to open-wire feed lines that usually have a higher intrinsic impedance than coaxial cable.

In Figure 4.10 we plot the input impedance of a folded dipole for lengths $L \leq 1\lambda$. At each step, the separation distance is $s = L/20$ and the wire radius is $a = 10^{-4}\lambda$. We use 30 segments for each long conductor and 5 segments for the short ends. We see that when the dipole is electrically small it is similar to the circular loop and has virtually no radiation resistance. It becomes an open circuit at the antenna terminals at approximately 0.3λ . The first resonance occurs at about $.45\lambda$ with an input resistance of 283Ω , very close to the expected value.

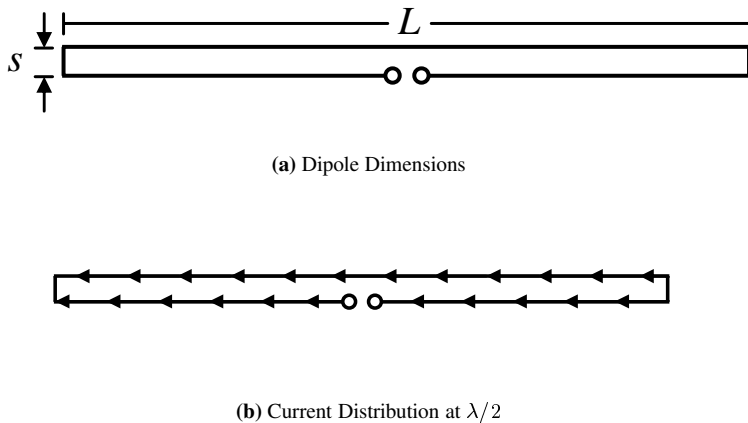


Figure 4.9: Folded dipole antenna.

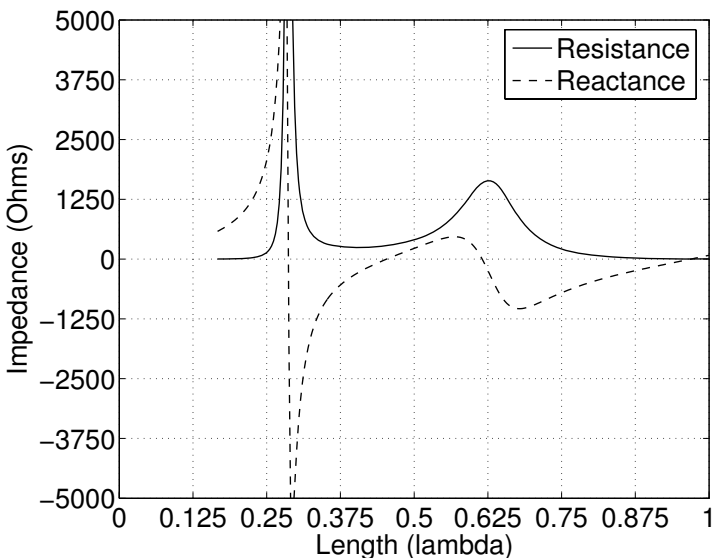


Figure 4.10: Folded dipole input impedance.

4.6.4 Two-Wire Transmission Line

As transmission lines are implicit to virtually all antenna problems, let us use the MOM to simulate the behavior of a common two-wire transmission line or “ladder line,” illustrated in Figure 4.11. For the purposes of our simulation, we treat the transmission line in an identical manner to the folded dipole of Section 4.6.3, except

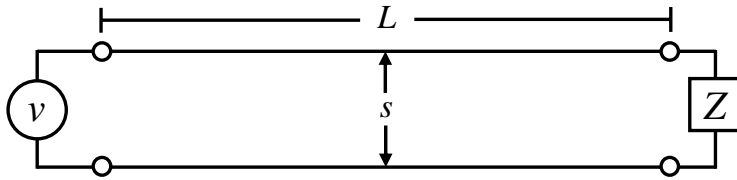


Figure 4.11: Two-wire transmission line.

that the feedpoint and load are placed at the short ends. We will analyze a two-wire line 2.5 meters long, constructed from wires 1 mm in radius with a separation distance of 3 cm. Thirty segments are used for each of the main wires and 5 segments for each end.

Our first task is to determine the characteristic impedance of the line. The theoretical value for a two-wire line is obtained from transmission line theory and is

$$Z_o = \sqrt{L/C} \quad (4.99)$$

where L is the inductance per unit length,

$$L = \frac{\mu}{\pi} \cosh^{-1} \left(\frac{s}{2a} \right) \quad (4.100)$$

and C is the capacitance per unit length,

$$C = (\pi\epsilon) / \cosh^{-1} \left(\frac{s}{2a} \right) \quad (4.101)$$

Using (4.99)–(4.101), we find the impedance of the line to be approximately $Z_o = 407 \Omega$. The true impedance can be determined numerically via the expression

$$Z_o = \sqrt{Z_{oc}Z_{sc}} \quad (4.102)$$

where Z_{oc} and Z_{sc} are the input impedances with an opened and shorted load end, respectively. We must be careful, however, that we do not make the measurement at a frequency where the length of the line results in an extremely small or large impedance at the driving end, or numerical problems will result. We therefore make the measurement at a frequency of 15 MHz, where the length of the line is approximately $\lambda/8$. This results in a value of $Z_o = 405 \Omega$, very close to the theoretical value.

We next compare the input impedance obtained from the MOM to that of the ideal lossless transmission line, given by the well-known equation

$$Z_{in} = Z_o \frac{Z_l + jZ_o \tan(kl)}{Z_o + jZ_l \tan(kl)} \quad (4.103)$$

where Z_l is the load impedance and Z_{in} is the impedance measured a distance l from the load. For this comparison we use a pure resistance of 200 Ω . The results

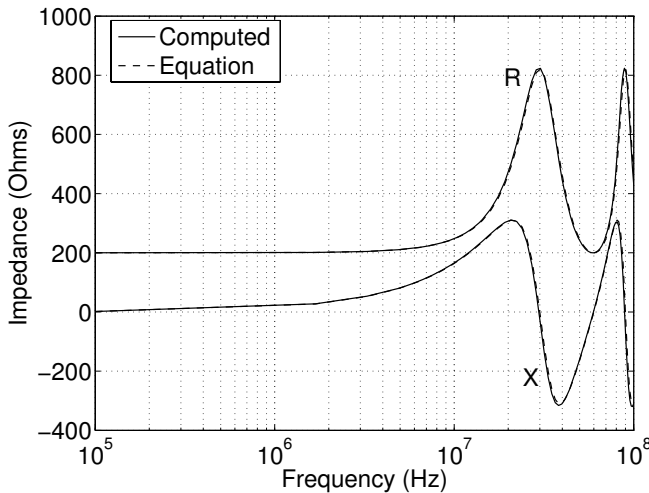


Figure 4.12: Two-wire line input impedance.

are plotted in Figure 4.12 for frequencies between 100 kHz and 100 MHz. The comparison is quite good. At lower frequencies, the input impedance tends towards its DC value, as expected.

4.6.5 Matching a Yagi Antenna

Let us use this method of loading to match a thin wire Yagi antenna at its feedpoint. We use the ATW formulation with triangular basis and testing functions. The dimensions of a nine-element thin wire Yagi antenna for the 2-meter amateur radio band (144–148 MHz) are summarized in Table 4.1 [11]. The diameter of all antenna elements is 1/4 inch (0.635 cm). The input resistance and reactance of the unmatched antenna over the band are shown in Figures 4.14a and 4.14b, respectively. The antenna has a feedpoint resistance between 15 and 35 Ω over most of the frequency range, a typical value for parasitic Yagi antennas. This antenna can be matched to a 50 Ω coaxial feed using a lumped inductive element at the feedpoint (a coil) or a tuning stub such as the hairpin match [12] and a 2:1 balun. We choose to match this antenna at about 146.5 MHz, where its reactance is approximately $-j18.8 \Omega$. To achieve the match we will place an inductance of about 20 nH at the feedpoint to

Table 4.1: 2 Meter Yagi Dimensions

Element	REF	DE	D1	D2	D3	D4	D5	D6	D7
Length (mm)	1038	955	956	932	916	906	897	891	887
Position (mm)	0	312	447	699	1050	1482	1986	2553	3168

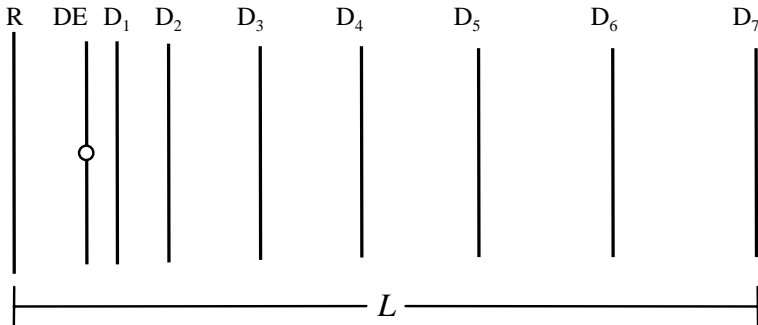
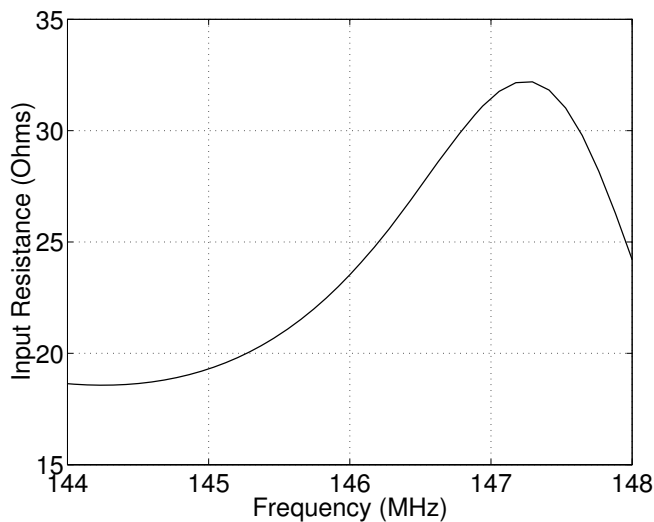
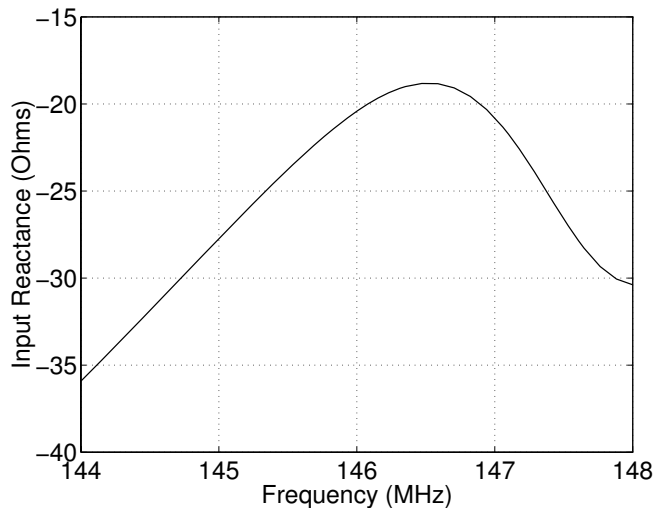


Figure 4.13: Yagi antenna for the two meter amateur radio band.

tune out the capacitive reactance. The reactance after matching is shown in Figure 4.15a and the standing wave ratio (SWR) in Figure 4.15b. The front-to-back ratio and the forward gain (in dBd) are shown in Figures 4.16a and 4.16b, respectively.

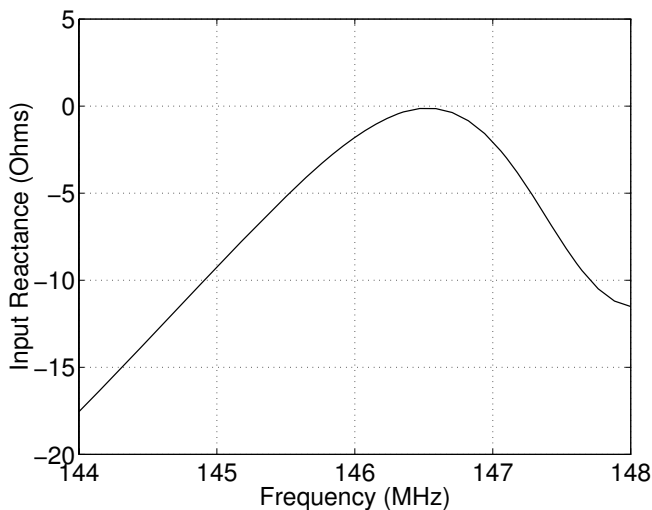


(a) Input Resistance

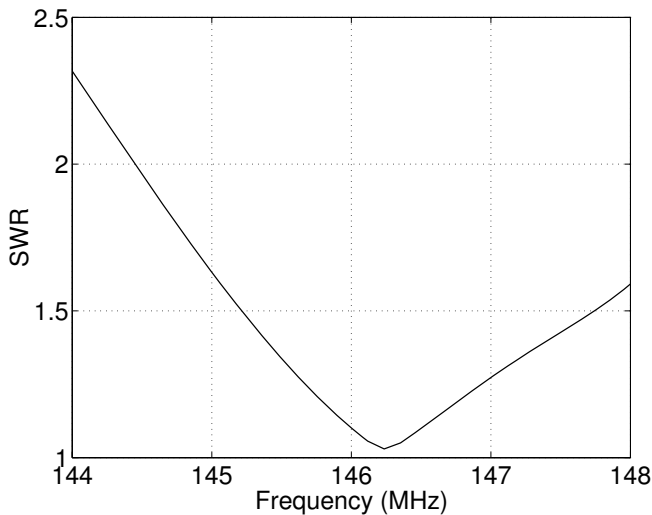


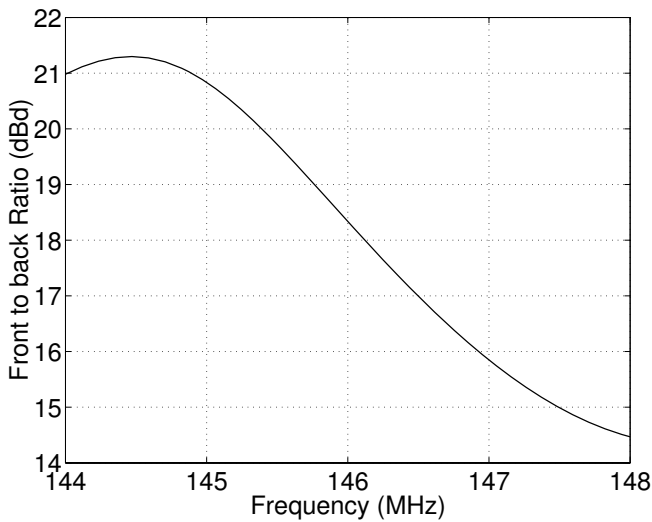
(b) Input Reactance

Figure 4.14: Unmatched Yagi input impedance.

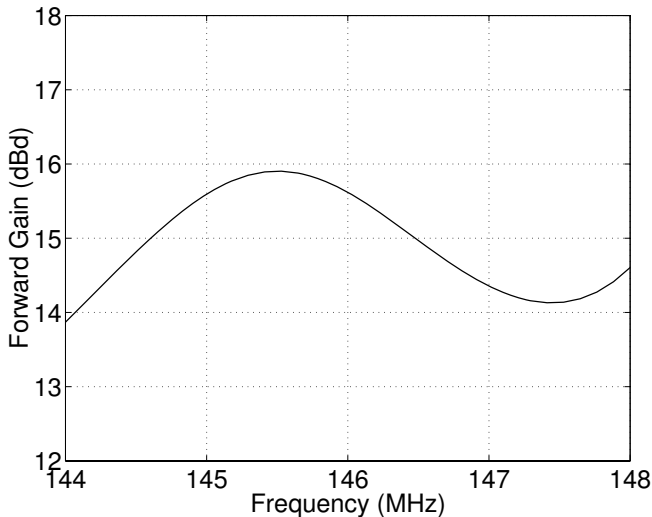


(a) Matched Reactance

(b) Matched SWR ($Z_o = 50 \Omega$)**Figure 4.15:** Matched reactance and SWR.



(a) Front to Back Ratio



(b) Forward Gain

Figure 4.16: Matched front to back ratio and gain.

REFERENCES

- [1] R. W. P. King, “The linear antenna—eighty years of progress,” *Proc. IEEE*, vol. 55, 2–26, January 1967.
- [2] W. Wang, “The exact kernel for cylindrical antenna,” *IEEE Trans. Antennas Propagat.*, vol. 39, 434–435, April 1991.
- [3] D. R. Wilton and N. J. Champagne, “Evaluation and integration of the thin wire kernel,” *IEEE Trans. Antennas Propagat.*, vol. 54, 1200–1206, April 2006.
- [4] E. Hallen, “Theoretical investigations into the transmitting and receiving qualities of antennae,” *Nova Acta (Uppsala)*, vol. 11, 1–44, 1938.
- [5] H. C. Pocklington, “Electrical oscillations in wires,” *Proc. Camb. Phil. Soc.*, vol. 9, 1897.
- [6] W. Stutzman and G. Thiele, *Antenna Theory and Design*. John Wiley and Sons, 1981.
- [7] C. A. Balanis, *Advanced Engineering Electromagnetics*. John Wiley and Sons, 1989.
- [8] S. J. Orfanidis, “Electromagnetic waves and antennas.” Electronic version: <http://www.ece.rutgers.edu/orfanidi/ewa/>.
- [9] H. Dwight, *Tables of Integrals and Other Mathematical Data*. The Macmillan Company, 1961.
- [10] *The Integrator*. Wolfram Research, <http://integrals.wolfram.com>.
- [11] *The ARRL Antenna Book*. The Amateur Radio Relay League, 17th ed., 1994.
- [12] W. Orr, *Radio Handbook*. Sams, 1992.

Chapter 5

Two-Dimensional Problems

Now having covered the basics of the moment method, we apply it to some two-dimensional scattering and radiation problems. These examples will further illustrate the manipulation of the EFIE and MFIE, making them suitable for each problem, as well as the proper evaluation of matrix elements given the choice of basis and testing functions.

5.1 TWO-DIMENSIONAL EFIE

We first apply the EFIE to two-dimensional problems of TM (perpendicular) and TE (parallel) polarization. We will consider the problem of scattering by a finite strip and then present expressions for radiation and scattering by two-dimensional boundaries of arbitrary shape.

5.1.1 EFIE for a Strip: TM Polarization

Consider a thin, perfectly conducting strip illuminated by a uniform plane wave of TM polarization, illustrated in Figure 5.1. An incident electric field of unit magnitude is given by

$$\mathbf{E}^i(\rho) = e^{jk\hat{\rho}_i \cdot \rho} \hat{\mathbf{z}} = e^{jk(x \cos \phi^i + y \sin \phi^i)} \hat{\mathbf{z}} \quad (5.1)$$

and the corresponding magnetic field is

$$\mathbf{H}^i(\rho) = -\hat{\rho}_i \times \frac{\mathbf{E}^i}{\eta} = \frac{1}{\eta} (-\sin \phi^i \hat{\mathbf{x}} + \cos \phi^i \hat{\mathbf{y}}) e^{jk(x \cos \phi^i + y \sin \phi^i)} \quad (5.2)$$

where $\eta = \sqrt{\mu/\epsilon}$ and $\hat{\mathbf{r}}^i = \cos \phi^i \hat{\mathbf{x}} + \sin \phi^i \hat{\mathbf{y}}$. Since the incident field has a component only along $\hat{\mathbf{z}}$, we expect that the induced surface current density \mathbf{J} will have only a $\hat{\mathbf{z}}$ component. The EFIE of (2.119) can then be simplified to

$$E_z^i(x) = j\omega\mu \int_0^L G(\rho, \rho') \left[J_z(x') + \frac{1}{k^2} \nabla' \nabla' \cdot J_z(x') \right] dx' \quad (5.3)$$

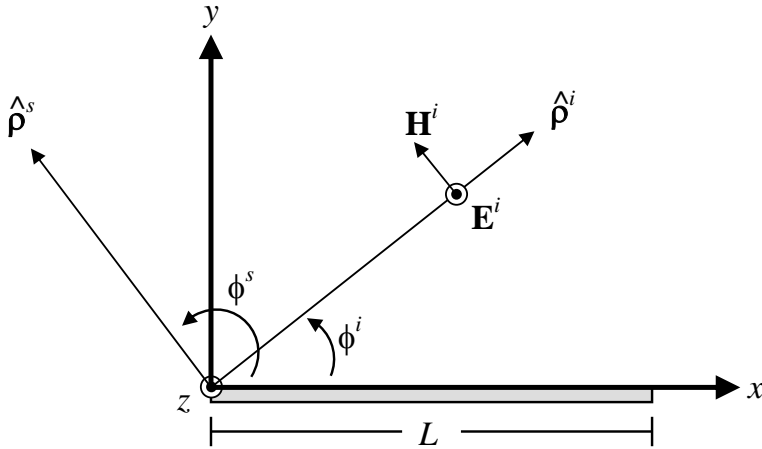


Figure 5.1: Thin strip: perpendicular polarization.

where the functions vary only along x because the strip is extremely thin. Since by inspection $\nabla' \cdot J_z(x') = 0$, the above reduces to

$$E_z^i(x) = j\omega\mu \int_0^L G(\rho, \rho') J_z(x') dx' \quad (5.4)$$

Substituting the two-dimensional Green's function $G(\rho, \rho') = -\frac{j}{4}H_0^{(2)}(k|x-x'|)$ from (2.52) we get

$$\frac{4}{\omega\mu} e^{jkx \cos \phi_i} = \int_0^L J_z(x') H_0^{(2)}(k|x-x'|) dx' \quad (5.5)$$

where we have evaluated $\mathbf{E}^i(\rho)$ and $G(\rho, \rho')$ on the surface of the strip ($y=0$). After we solve this equation for the current J_z , the scattered electric field is given by

$$E_z^s(\rho) = -\frac{\omega\mu}{4} \int_0^L J_z(x') H_0^{(2)}(k|x-x'|) dx' \quad (5.6)$$

Using (2.106), the scattered far field can be written as

$$E_z^s(\rho) = -\omega\mu\sqrt{\frac{j}{8\pi k}} \frac{e^{-jk\rho}}{\sqrt{\rho}} \int_0^L J_z(x') e^{jkx' \cos \phi^s} dx' \quad r \rightarrow \infty \quad (5.7)$$

The corresponding physical optics current density for this problem is $\mathbf{J}(\rho) = 2\hat{\mathbf{n}}(\rho) \times \mathbf{H}^i(\rho)$, which is

$$\mathbf{J}(\rho) = 2\hat{\mathbf{y}} \times \left[-\hat{\rho}^i \times \frac{\mathbf{E}^i(\rho)}{\eta} \right] = \frac{2}{\eta} \sin \phi^i e^{jkx \cos \phi^i} \hat{\mathbf{z}} \quad (5.8)$$

which we will compare to the results of the EFIE.

5.1.1.1 Solution Using Pulse Functions

Let us first solve this problem using pulse basis functions and point matching for testing. We subdivide the strip into N segments of width $\Delta_x = L/N$, resulting in N basis functions. The matrix elements z_{mn} are given by

$$z_{mn} = \int_{x_n}^{x_{n+1}} H_0^{(2)}(k|x_m - x'|) dx' \quad (5.9)$$

and the excitation vector elements b_m are

$$b_m = \frac{4}{\omega\mu} e^{j k x_m \cos \phi_i} \quad (5.10)$$

We position the testing and source points x_m, x_n at the center of each segment. To evaluate the non-self terms we will use a simple centroidal approximation to the integral, which is

$$z_{mn} = H_0^{(2)}(k|x_m - x_n|) \Delta_x \quad (5.11)$$

For the self terms, we will use the small argument approximation to the Hankel function

$$H_0^{(2)}(kx) \approx 1 - j \frac{2}{\pi} \log\left(\frac{\gamma k x}{2}\right) \quad x \rightarrow 0 \quad (5.12)$$

where $\gamma = 1.781$. This results in the following integral for the self terms:

$$I = \int_0^{\Delta_x} \left[1 - j \frac{2}{\pi} \log\left(\frac{\gamma|x-x'|}{2}\right) \right] dx' \quad (5.13)$$

The logarithmic part of this integral has a singularity, so we must integrate it carefully. To do so we make use of [1], which summarizes the solution for potential integrals of the form $\log x$ and $x \log x$. Performing the integration yields

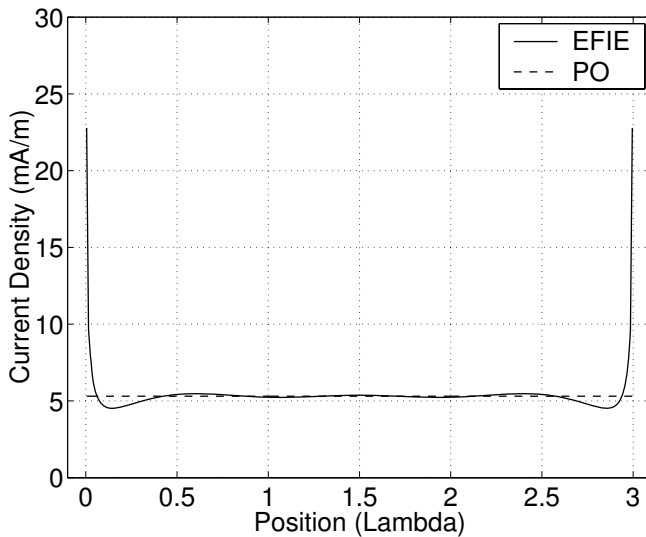
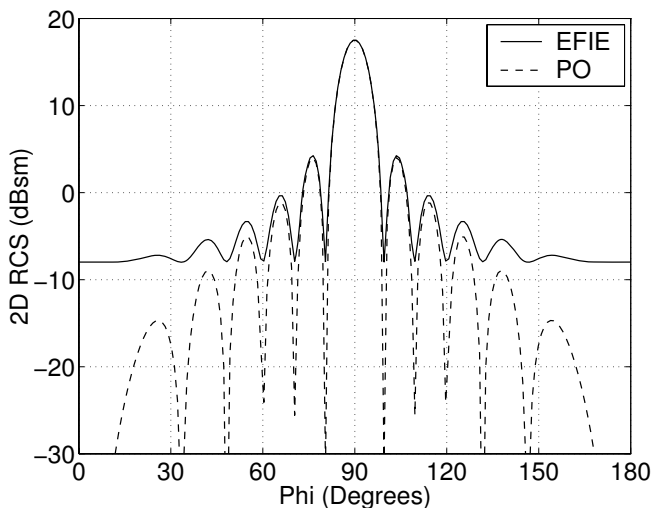
$$I = \Delta_x - j \frac{2}{\pi} \left[\Delta_x \log\left(\frac{\gamma k \Delta_x}{2e}\right) + x \log\left(\frac{x}{\Delta_x - x}\right) \right] \quad (5.14)$$

and substituting the value $x = \Delta_l/2$, the self terms z_{mm} are

$$z_{mm} = \Delta_x \left[1 - j \frac{2}{\pi} \log\left(\frac{\gamma k \Delta_x}{4e}\right) \right] \quad (5.15)$$

When the segments are adjacent but not overlapping, the integrand may still exhibit a strong singular behavior that can lead to inaccurate matrix elements if a centroidal approximation is used. For these near terms ($|m - n| = 1$), we will evaluate the integral analytically using the same method used for the self terms. The result is

$$z_{mn} = \Delta_x - j \frac{\Delta_x}{\pi} \left[3 \log\left(\frac{3\gamma k \Delta_x}{4}\right) - \log\left(\frac{\gamma k \Delta_x}{4}\right) - 2 \right] \quad |m - n| = 1 \quad (5.16)$$

(a) Induced Surface Current ($\phi^i = \pi/2$)(b) Two-Dimensional Monostatic RCS ($0 \leq \phi^i \leq \pi$)**Figure 5.2:** Strip with pulse functions: TM polarization.

Note that the resulting matrix will be symmetric Toeplitz due to the choice of basis functions and the linear geometry of the strip.

Consider a strip of width 3λ , which we subdivide into 300 segments. In Figure 5.2a we plot the induced surface current intensity at broadside incidence ($\phi^i = 90^\circ$). The current is singular near the edges, however the magnitude falls off quickly with distance from each edge. The numerically computed EFIE current (solid line) is compared to the PO current (dashed line). The PO current matches the EFIE fairly well near the center of the strip, but badly near the edges. In Figure 5.2b is shown the two-dimensional RCS for incident angles ranging from 0 to 180 degrees. The PO compares to the EFIE well at angles near broadside and within the first mainlobe, but does poorly beyond that.

5.1.1.2 Solution Using Triangle Functions

We now solve this problem using triangle basis and testing functions. Since we know the current will be nonzero at the ends of the strip, we use the configuration of Figure 3.10. The strip is again divided into N segments of width $\Delta_x = L/N$, with N triangle functions ($N - 2$ whole triangles, 2 half triangles). The matrix elements z_{mn} are given by

$$z_{mn} = \int_{f_m} f_m(x) \cdot \int_{f_n} f_n(x') H_0^{(2)}(k|x - x'|) dx' dx \quad (5.17)$$

To evaluate the above integral we will use an M -point quadrature rule over the source and testing triangles, resulting in

$$z_{mn} = \sum_{p=1}^M w_m(x_p) f_m(x_p) \sum_{q=1}^M w_n(x_q) f_n(x_q) H_0^{(2)}(k|x_p - x_q|) \quad (5.18)$$

where p and q refer to the testing and source locations, respectively. When the source and observation triangles have no overlapping segments, the above expression can be implemented as written. If the triangles partially or completely overlap (in this case, whenever $|m - n| < 2$), the Hankel function will have singularities on the overlapping segments. To solve this, we will evaluate the innermost integral in (5.17) analytically and the outermost integral numerically. Again using the small-argument approximation to the Hankel function, the innermost integral becomes

$$I = \int_0^{\Delta_x} f_n(x') \left[1 - j \frac{2}{\pi} \log \left(\frac{\gamma k |x_p - x'|}{2} \right) \right] dx' \quad (5.19)$$

The observation point x_p lies within the limits of integration, and the function $f_n(x')$ represents the ascending or descending half of the source triangle. This integral can be decomposed into a sum of integrals involving $x \log x$ and $\log x$, the solutions to which are summarized in [1]. For the ascending triangle $f_n(x') = x'/\Delta_x$, the result

is

$$I = \frac{\Delta_x}{2} - j \frac{2}{\pi} \left[\frac{x_p^2}{2\Delta_x} \log \left(\frac{x_p}{\Delta_x - x_p} \right) + \frac{\Delta_x}{2} \log \left(b[\Delta_x - x_p] \right) - \frac{x_p}{2} - \frac{\Delta_x}{4} \right] \quad (5.20)$$

where $b = \gamma k/2$. The result for the ascending triangle is sufficient for computing all singular terms for itself and the descending triangle because of their symmetry. The singular portions of the matrix element z_{mn} can then be obtained via the sum

$$P = \Delta_s \sum_{p=1}^M f_m(x_p) I(x_p) \quad (5.21)$$

When either of the triangles is the half-triangle at the ends of the strip, (5.18) should still be used, however the sum over the half triangle is modified to take into account the fact that it is over a single segment only. The excitation vector elements are computed by numerical quadrature and are

$$b_m = \frac{4}{\omega\mu} \int_{f_m} f_m(x) e^{j k x \cos \phi^i} dx = \frac{4}{\omega\mu} \sum_{p=1}^M w_m(x_p) f_m(x_p) e^{j k x_p \cos \phi^i} \quad (5.22)$$

We again subdivide the 3λ strip into 300 segments. For integration over the testing segments, we use a five-point Gaussian quadrature. Figure 5.3a shows the computed surface current intensity at broadside incidence. The EFIE current is seen to take on a higher value at the edges than it did with pulse functions, however the difference is slight. Figure 5.3b depicts the two-dimensional RCS, which appears identical to the RCS obtained using pulse functions. This suggests that pulse functions may be sufficient to accurately characterize this problem, though the large number of segments used is likely a contributor to the agreement.

5.1.2 Generalized EFIE: TM Polarization

We can easily generalize (5.4) to a two-dimensional contour C of arbitrary shape. Doing so yields

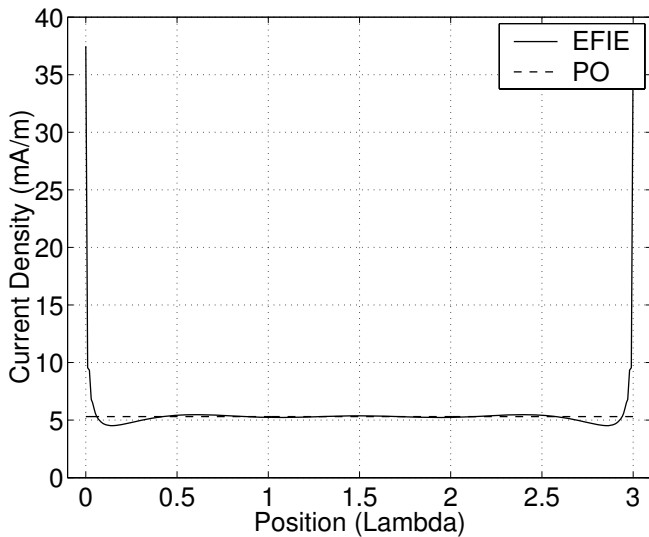
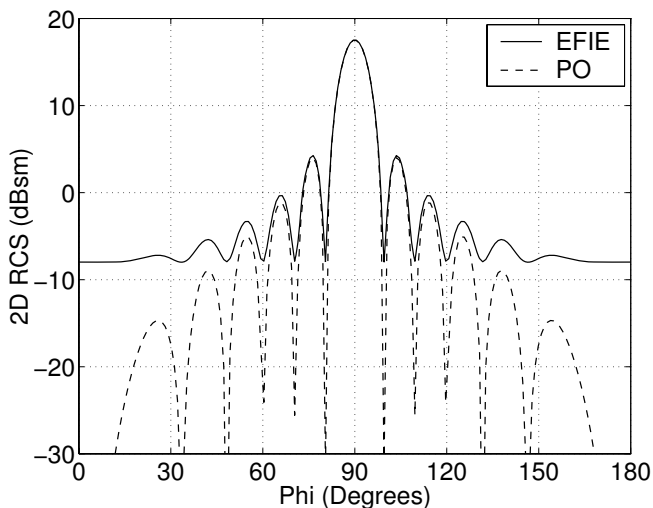
$$\frac{4}{\omega\mu} E_z^i(\boldsymbol{\rho}) = \int_C J_z(\boldsymbol{\rho}') H_0^{(2)}(k|\boldsymbol{\rho} - \boldsymbol{\rho}'|) d\boldsymbol{\rho}' \quad (5.23)$$

Applying basis and testing functions f_n and f_m , respectively, yields an MOM matrix with elements given by

$$z_{mn} = \int_{f_m} f_m(\boldsymbol{\rho}) \int_{f_n} f_n(\boldsymbol{\rho}') H_0^{(2)}(k|\boldsymbol{\rho} - \boldsymbol{\rho}'|) d\boldsymbol{\rho}' d\boldsymbol{\rho} \quad (5.24)$$

and excitation vector elements

$$b_m = \frac{4}{\omega\mu} \int_{f_m} f_m(\boldsymbol{\rho}) E_z^i(\boldsymbol{\rho}) d\boldsymbol{\rho} \quad (5.25)$$

(a) Induced Surface Current ($\phi^i = \pi/2$)(b) Two-Dimensional Monostatic RCS ($0 \leq \phi^i \leq \pi$)**Figure 5.3:** Strip with triangle functions: TM polarization.

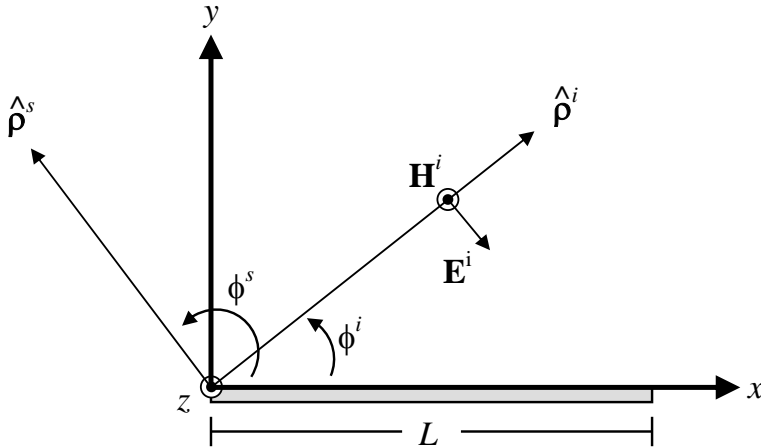


Figure 5.4: Thin strip: parallel polarization.

5.1.3 EFIE for a Strip: TE Polarization

We next consider the TE polarized case, as illustrated in Figure 5.4. The incident electric field of unit magnitude is given by

$$\mathbf{E}^i(\rho) = (\sin \phi^i \hat{\mathbf{x}} - \cos \phi^i \hat{\mathbf{y}}) e^{jk(x \cos \phi^i + y \sin \phi^i)} \quad (5.26)$$

and the incident magnetic field is

$$\mathbf{H}^i(\rho) = -\hat{\rho}^i \times \frac{\mathbf{E}^i}{\eta} = \frac{1}{\eta} e^{jk(x \cos \phi^i + y \sin \phi^i)} \hat{\mathbf{z}} \quad (5.27)$$

On the surface of a conducting strip, the total tangential electric field must be zero, hence

$$\hat{\mathbf{y}} \times (\mathbf{E}^i + \mathbf{E}^s) = \hat{\mathbf{y}} \times [(E_x^i + E_x^s) \hat{\mathbf{x}} + (E_y^i + E_y^s) \hat{\mathbf{y}}] = 0 \quad (5.28)$$

leading to

$$E_x^s = -E_x^i \quad (y = 0) \quad (5.29)$$

or

$$E_x^s = -\sin \phi^i e^{jkx \cos \phi^i} \quad (y = 0) \quad (5.30)$$

where all observations are made on the strip ($y = 0$). Since the incident field has $\hat{\mathbf{x}}$ and $\hat{\mathbf{y}}$ components, we expect that the induced currents will as well. Since $\hat{\mathbf{y}}$ -directed currents (normal to the strip) are not possible in this case, we are left with an induced current with only an $\hat{\mathbf{x}}$ component. Using the vector potential EFIE (2.120) we now write

$$E_x^s(x) = -j\omega A_x - \frac{j}{\omega\mu\epsilon} \frac{\partial^2 A_x}{\partial x^2} = -\frac{j}{\omega\mu\epsilon} \left[k^2 + \frac{\partial^2}{\partial x^2} \right] A_x \quad (5.31)$$

and

$$E_y^s(x) = -\frac{j}{\omega\mu\epsilon} \frac{\partial^2 A_x}{\partial x \partial y} \quad (5.32)$$

where A_x is

$$A_x(x) = -\frac{j\mu}{4} \int_0^L J_x(x') H_0^{(2)}(k\rho) dx' \quad (5.33)$$

with $\rho = \sqrt{(x-x')^2 + (y-y')^2}$. Substituting in the above expression for A_x yields

$$E_x^s(x) = -\frac{1}{4\omega\epsilon} \left[k^2 + \frac{\partial^2}{\partial x^2} \right] \int_0^L J_x(x') H_0^{(2)}(k\rho) dx' \quad (5.34)$$

and

$$E_y^s(x) = -\frac{1}{4\omega\epsilon} \frac{\partial^2}{\partial x \partial y} \int_0^L J_x(x') H_0^{(2)}(k\rho) dx' \quad (5.35)$$

Exchanging the differentiation and integration operators, we get

$$E_x^s(x) = -\frac{1}{4\omega\epsilon} \int_0^L J_x(x') \left[k^2 + \frac{\partial^2}{\partial x^2} \right] H_0^{(2)}(k\rho) dx' \quad (5.36)$$

and

$$E_y^s(x) = -\frac{1}{4\omega\epsilon} \int_0^L J_x(x') \left[\frac{\partial^2}{\partial x \partial y} H_0^{(2)}(k\rho) \right] dx' \quad (5.37)$$

Let us evaluate the expression

$$\left[k^2 + \frac{\partial^2}{\partial x^2} \right] H_0^{(2)}(k\rho) \quad (5.38)$$

To begin, we note that [2]

$$\frac{d}{du} H_n^{(2)}(u) = -H_{n+1}^{(2)}(u) + \frac{n}{u} H_n^{(2)}(u) \quad (5.39)$$

and

$$\frac{\partial}{\partial x} H_n^{(2)}(k\rho) = \frac{d}{du} [H_n^{(2)}(u)] \frac{\partial u}{\partial x} \quad (5.40)$$

where $u = k\rho$. Therefore,

$$\frac{\partial u}{\partial x} = \frac{\partial(k\rho)}{\partial x} = \frac{k(x-x')}{\sqrt{(x-x')^2 + (y-y')^2}} \quad (5.41)$$

and so

$$\frac{\partial}{\partial x} H_0^{(2)}(k\rho) = -H_1^{(2)}(k\rho) \frac{k(x-x')}{\sqrt{(x-x')^2 + (y-y')^2}} \quad (5.42)$$

Differentiating a second time yields

$$\begin{aligned} \frac{\partial^2}{\partial x^2} H_0^{(2)}(k\rho) = & -\frac{k(x-x')}{\sqrt{(x-x')^2 + (y-y')^2}} \left[\frac{\partial}{\partial x} H_1^{(2)}(k\rho) \right] \\ & - H_1^{(2)}(k\rho) \left[\frac{\partial}{\partial x} \frac{k(x-x')}{\sqrt{(x-x')^2 + (y-y')^2}} \right] \end{aligned} \quad (5.43)$$

which is

$$\begin{aligned} \frac{\partial^2}{\partial x^2} H_0^{(2)}(k\rho) = & -\frac{k^2(x-x')^2}{(x-x')^2 + (y-y')^2} \left[-H_2^{(2)}(k\rho) + \frac{1}{k\rho} H_1^{(2)}(k\rho) \right] \\ b - H_1^{(2)}(k\rho) \left[\frac{k}{(x-x')^2 + (y-y')^2} - \frac{k^2(x-x')^2}{[(x-x')^2 + (y-y')^2]^{3/2}} \right] \end{aligned} \quad (5.44)$$

The second and fourth terms cancel, leaving

$$\begin{aligned} \frac{\partial^2}{\partial x^2} H_0^{(2)}(k\rho) = & \frac{k^2(x-x')^2}{(x-x')^2 + (y-y')^2} H_2^{(2)}(k\rho) \\ & - \frac{k}{(x-x')^2 + (y-y')^2} H_1^{(2)}(k\rho) \end{aligned} \quad (5.45)$$

Using the recurrence relationship [3]

$$\frac{k}{r} H_1^{(2)}(k\rho) = \frac{k^2}{2} [H_0^{(2)}(k\rho) + H_2^{(2)}(k\rho)] \quad (5.46)$$

we can write the final result as

$$\left[k^2 + \frac{\partial^2}{\partial x^2} \right] H_0^{(2)}(k\rho) = \frac{k^2}{2} \left[\frac{2(x-x')^2}{(x-x')^2 + (y-y')^2} - 1 \right] H_2^{(2)}(k\rho) + \frac{k^2}{2} H_0^{(2)}(k\rho) \quad (5.47)$$

We note from the geometry of Figure 5.4 that

$$\cos \theta = \frac{(x-x')}{\sqrt{(x-x')^2 + (y-y')^2}} \quad (5.48)$$

where the angle θ is measured in the right-hand sense from the positive x axis. Using this we can simplify the previous expression to

$$\left[k^2 + \frac{\partial^2}{\partial x^2} \right] H_0^{(2)}(k\rho) = \frac{k^2}{2} \left[\cos(2\theta) H_2^{(2)}(k\rho) + H_0^{(2)}(k\rho) \right] \quad (5.49)$$

By a similar derivation, we arrive at

$$\frac{\partial^2}{\partial x \partial y} H_0^{(2)}(k\rho) = \frac{k^2}{2} \sin(2\theta) H_2^{(2)}(k\rho) \quad (5.50)$$

The scattered electric field is therefore

$$E_x^s = -\frac{k^2}{8\omega\epsilon} \int_0^L J_x(x') \left[\cos(2\theta) H_2^{(2)}(k\rho) + H_0^{(2)}(k\rho) \right] dx' \quad (5.51)$$

and

$$E_y^s = -\frac{k^2}{8\omega\epsilon} \int_0^L J_x(x') \sin(2\theta) H_2^{(2)}(k\rho) dx' \quad (5.52)$$

To obtain the scattered far field, we again use (2.104) and (2.106) to write the above as

$$E_x^s = -\frac{k^2}{8\omega\epsilon} \sqrt{\frac{2j}{\pi k}} \frac{e^{-jk\rho}}{\sqrt{\rho}} \int_0^L J_x(x') \left[1 - \cos(2\theta) \right] e^{jkx' \cos \phi^s} dx' \quad r \rightarrow \infty \quad (5.53)$$

and

$$E_y^s = \frac{k^2}{8\omega\epsilon} \sqrt{\frac{2j}{\pi k}} \frac{e^{-jk\rho}}{\sqrt{\rho}} \int_0^L J_x(x') \sin(2\theta) e^{jkx' \cos \phi^s} dx' \quad r \rightarrow \infty \quad (5.54)$$

To solve for the induced current on the strip, we will now enforce the boundary conditions of (5.30). Inserting this expression into (5.51) we get

$$\frac{8\omega\epsilon}{k^2} \sin \phi^i e^{jkx \cos \phi^i} = \int_0^L J_x(x') \left[\cos(2\theta) H_2^{(2)}(k\rho) + H_0^{(2)}(k\rho) \right] dx' \quad (5.55)$$

where for observations on the strip, $y = 0$ and $\rho = |x - x'|$. For any point $x \neq x'$, the values for θ are 0 and $\pi/2$, and $\cos(2\theta)$ will have a value of unity. For integrations where we encounter $x = x'$, we will need to use (5.48) in evaluating the integral.

The PO current on the strip is given by

$$\mathbf{J}(\rho) = 2\hat{\mathbf{y}} \times \mathbf{H}^i(\rho) = 2\hat{\mathbf{y}} \times \frac{\hat{\mathbf{z}}}{\eta} = \frac{2}{\eta} e^{jkx \cos \phi^i} \hat{\mathbf{x}} \quad (5.56)$$

which is equivalent in magnitude to the PO current for the TM case at broadside incidence.

5.1.3.1 Pulse Function Solution

We will approach this problem numerically as we did for the TM case. We subdivide the strip into N segments with N pulse basis functions, and point match at the center of each segment. For segments that are not “close” ($|m - n| > 2$), we will compute the matrix elements using the centroidal approximation

$$z_{mn} = 2\Delta_x \frac{H_1^{(2)}(k|x_m - x_n|)}{k|x_m - x_n|} \quad |m - n| > 2 \quad (5.57)$$

where we have again used the recurrence relationship of (5.46). Elements that are adjacent or separated by one segment we will treat as near terms and perform the integration analytically. This integral is

$$z_{mn} = \int_{-\Delta_x/2}^{\Delta_x/2} \frac{H_1^{(2)}(k|x_m - x_n| - x')}{k(|x_m - x_n| - x')} dx' \quad |m - n| = 1, 2 \quad (5.58)$$

Using the small-argument approximation to the Hankel function $H_1^{(2)}$ [3],

$$H_1^{(2)}(k\rho) \approx \frac{k\rho}{2} + \frac{2j}{\pi k\rho} \quad r \rightarrow 0 \quad (5.59)$$

this integral can be written as

$$z_{mn} = \int_{-\Delta_x/2}^{\Delta_x/2} \left[1 + \frac{4j}{\pi k^2 (|x_m - x_n| - x')^2} \right] dx' \quad (5.60)$$

which evaluates to

$$z_{mn} = \Delta_x \left[1 + \frac{4j}{\pi k^2} \frac{1}{|x_m - x_n|^2 - \Delta_x^2/4} \right] \quad |m - n| = 1, 2 \quad (5.61)$$

For the self terms, we can again use (5.15) for the portion of the integral involving $H_0^{(2)}(k\rho)$, however we must be careful with the Hankel function of order 2 as it has a non integrable singularity. To overcome this problem, we will do the integration and then apply a limiting argument as the observation point approaches the strip. The integral to be evaluated is

$$I = \int_{-\Delta_x/2}^{\Delta_x/2} H_2^{(2)}(k\rho) \cos(2\theta) dx' \quad (5.62)$$

First we will employ the small-argument approximation to the Hankel function $H_2^{(2)}$ [3]

$$H_2^{(2)}(k\rho) \approx \frac{(k\rho)^2}{8} + \frac{4j}{\pi(k\rho)^2} \quad r \rightarrow 0 \quad (5.63)$$

We next fix the observation point at $x = 0, y = \delta$, where δ is very small. The distance r is then

$$r = \sqrt{(x')^2 + \delta^2} \quad (5.64)$$

and we can write the integral as

$$I = \frac{k^2}{4} \int_0^{\Delta_x/2} (x'^2 + \delta^2) \left[\frac{2x'^2}{x'^2 + \delta^2} - 1 \right] dx' + \frac{8j}{\pi k^2} \int_0^{\Delta_x/2} \frac{1}{x'^2 + \delta^2} \left[\frac{2x'^2}{x'^2 + \delta^2} - 1 \right] dx' \quad (5.65)$$

where we have reintroduced the expression for $\cos(2\theta)$ from (5.48). The above is then

$$I = \frac{k^2}{4} \int_0^{\Delta_x/2} (x'^2 - \delta^2) dx' + \frac{8j}{\pi k^2} \int_0^{\Delta_x/2} \left[\frac{2x'^2}{(x'^2 + \delta^2)^2} - \frac{1}{x'^2 + \delta^2} \right] dx' \quad (5.66)$$

The first integral is evaluated easily and is

$$I_1 = \frac{k^2}{4} \left(\frac{\Delta_x^3}{24} - \frac{\delta^2 \Delta_x}{2} \right) \quad (5.67)$$

The second integral is obtained by way of [4] (Eqns. 120.1 and 122.2) and is

$$I_2 = \frac{8j}{\pi k^2} \left[\frac{1}{\delta} \tan^{-1} \left(\frac{\Delta_x}{2\delta} \right) - \frac{\Delta_x/2}{\delta^2 + (\Delta_x/2)^2} - \frac{1}{\delta} \tan^{-1} \left(\frac{\Delta_x}{2\delta} \right) \right] \quad (5.68)$$

which reduces to

$$I_2 = \frac{-8j}{\pi k^2} \left[\frac{\Delta_x/2}{\delta^2 + (\Delta_x/2)^2} \right] \quad (5.69)$$

If we now take the limit as the observation point approaches the strip ($\delta \rightarrow 0$), the results are

$$I_1 = k^2 \frac{\Delta_x^3}{96} \quad (5.70)$$

and

$$I_2 = \frac{-16j}{\pi k^2 \Delta_x} \quad (5.71)$$

and the resulting self term is

$$z_{mm} = \Delta_x + k^2 \frac{\Delta_x^3}{96} - \frac{j\Delta_x}{\pi} \left[2 \log \left(\frac{\gamma k \Delta_x}{4e} \right) + \frac{16}{(k\Delta_x)^2} \right] \quad (5.72)$$

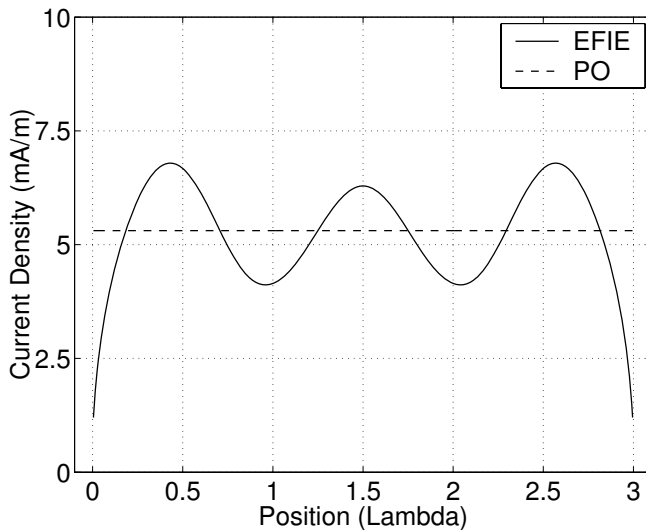
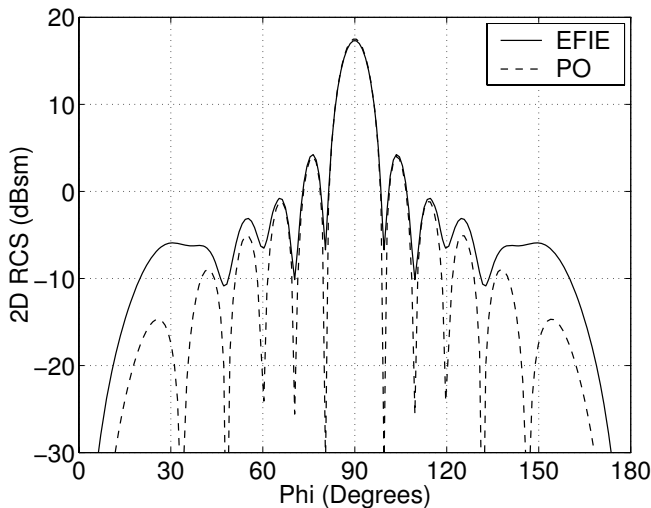
Figure 5.5a depicts the surface current intensity J_x on the 3λ strip at broadside incidence, with 300 segments as before. The EFIE current tends toward zero near the ends of the strip as expected. Figure 5.2b compares the two-dimensional RCS obtained using the EFIE and PO. Again the PO compares well to the EFIE near normal incidence, but does poorly beyond that.

5.1.4 Generalized EFIE: TE Polarization

Let us start with (2.120) and write a generalized EFIE in two dimensions. Doing so yields

$$\frac{4}{\omega\mu} \hat{\mathbf{n}}(\boldsymbol{\rho}) \times \mathbf{E}^i(\boldsymbol{\rho}) = \hat{\mathbf{n}}(\boldsymbol{\rho}) \times \int_C \left[1 + \frac{1}{k^2} \nabla \nabla \cdot \right] \mathbf{J}(\boldsymbol{\rho}') H_0^{(2)}(k|\boldsymbol{\rho} - \boldsymbol{\rho}'|) d\boldsymbol{\rho}' \quad (5.73)$$

where the current $\mathbf{J}(\boldsymbol{\rho}')$ is everywhere tangent to C . Choosing basis and testing functions that are tangent to C allows us to create a linear system with matrix

(a) Induced Surface Current ($\phi^i = \pi/2$)(b) Two-Dimensional Monostatic RCS ($0 \leq \phi^i \leq \pi$)**Figure 5.5:** Strip with pulse functions: TE polarization.

elements given by

$$\begin{aligned} z_{mn} = & \int_{\mathbf{f}_m} \mathbf{f}_m(\boldsymbol{\rho}) \cdot \int_{\mathbf{f}_n} \mathbf{f}_n(\boldsymbol{\rho}') H_0^{(2)}(k|\boldsymbol{\rho} - \boldsymbol{\rho}'|) d\boldsymbol{\rho}' d\boldsymbol{\rho} \\ & + \frac{1}{k^2} \int_{\mathbf{f}_m} \mathbf{f}_m(\boldsymbol{\rho}) \cdot \int_{\mathbf{f}_n} \nabla \nabla \cdot \mathbf{f}_n(\boldsymbol{\rho}') H_0^{(2)}(k|\boldsymbol{\rho} - \boldsymbol{\rho}'|) d\boldsymbol{\rho}' d\boldsymbol{\rho} \end{aligned} \quad (5.74)$$

As demonstrated in Section 5.1.3, solving the EFIE as written in (5.74) will be quite complicated, even for simple geometries. This difficulty originates from the location of the differential operators. If we redistribute the operators following Section 4.5.1, the TE problem will be greatly simplified. Using this method, the matrix elements of (5.74) can be rewritten as

$$\begin{aligned} z_{mn} = & \int_{\mathbf{f}_m} \mathbf{f}_m(\boldsymbol{\rho}) \cdot \int_{\mathbf{f}_n} \mathbf{f}_n(\boldsymbol{\rho}') H_0^{(2)}(k|\boldsymbol{\rho} - \boldsymbol{\rho}'|) d\boldsymbol{\rho}' d\boldsymbol{\rho} \\ & - \frac{1}{k^2} \int_{\mathbf{f}_m} \nabla \cdot \mathbf{f}_m(\boldsymbol{\rho}) \cdot \int_{\mathbf{f}_n} \nabla' \cdot \mathbf{f}_n(\boldsymbol{\rho}') H_0^{(2)}(k|\boldsymbol{\rho} - \boldsymbol{\rho}'|) d\boldsymbol{\rho}' d\boldsymbol{\rho} \end{aligned} \quad (5.75)$$

where the basis and testing functions must now have a nonzero divergence throughout their domain. If we use triangle basis and testing functions, this requirement will be satisfied. The excitation vector elements are

$$b_m = \frac{4}{\omega \mu} \int_{\mathbf{f}_m} \mathbf{f}_m(\boldsymbol{\rho}) \cdot \mathbf{E}^i(\boldsymbol{\rho}) d\boldsymbol{\rho} \quad (5.76)$$

5.2 TWO-DIMENSIONAL MFIE

As the MFIE is valid only for closed surfaces, will consider two-dimensional MFIE problems in the context of a closed, conducting boundary of arbitrary shape.

5.2.1 MFIE: TM Polarization

The geometry of a TM MFIE problem is illustrated in Figure 5.6, where the incident magnetic field induces the $\hat{\mathbf{z}}$ -directed current $J_z(\boldsymbol{\rho})$. Using (2.136), we can write the two-dimensional MFIE as

$$\hat{\mathbf{n}}(\boldsymbol{\rho}) \times \mathbf{H}_i(\boldsymbol{\rho}) = \frac{\mathbf{J}(\boldsymbol{\rho})}{2} - \frac{j}{4} \hat{\mathbf{n}}(\boldsymbol{\rho}) \times \iint_{C'} \mathbf{J}(\boldsymbol{\rho}') \times \nabla H_0^{(2)}(k\rho) d\boldsymbol{\rho}' \quad (5.77)$$

Since the induced current has only $\hat{\mathbf{z}}$ components on C , the only portion of the incident field that contributes to the current is that which is tangent to C . Therefore,

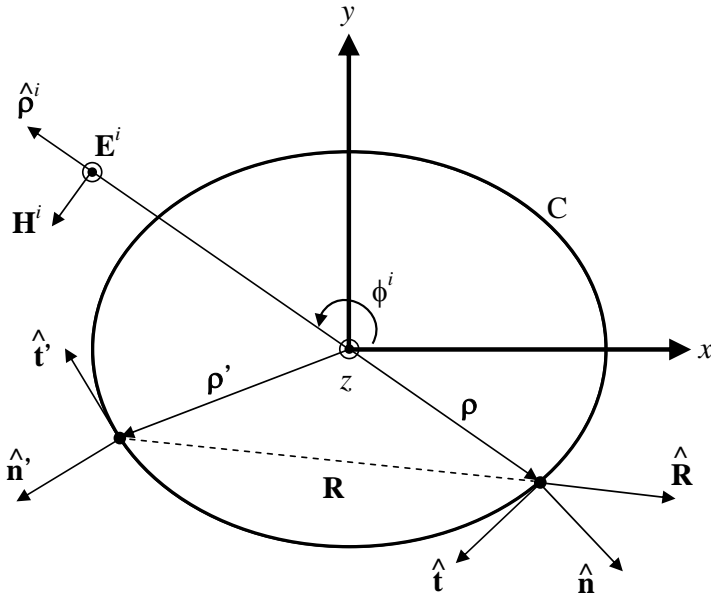


Figure 5.6: Two-Dimensional MFIE geometry: perpendicular polarization.

the above can be written as

$$\hat{\mathbf{t}}(\rho) \cdot \mathbf{H}^i(\rho) = \frac{J_z(\rho)}{2} - \frac{j}{4} \hat{\mathbf{z}} \cdot \left[\hat{\mathbf{n}}(\rho) \times \iint_{C'} J_z(\rho') \hat{\mathbf{z}} \times \nabla H_0^{(2)}(k\rho) d\rho' \right] \quad (5.78)$$

where the tangent vector $\hat{\mathbf{t}}(\rho) = \hat{\mathbf{n}}(\rho) \times \hat{\mathbf{z}}$. Applying the vector identity

$$\mathbf{A} \times \mathbf{B} \times \mathbf{C} = (\mathbf{A} \cdot \mathbf{C})\mathbf{B} - (\mathbf{A} \cdot \mathbf{B})\mathbf{C} \quad (5.79)$$

we obtain

$$\hat{\mathbf{n}}(\rho) \times \hat{\mathbf{z}} \times \nabla H_0^{(2)}(k\rho) = \hat{\mathbf{z}} \left[\hat{\mathbf{n}}(\rho) \cdot \nabla H_0^{(2)}(k\rho) \right] \quad (5.80)$$

since $\hat{\mathbf{n}} \cdot \hat{\mathbf{z}} = 0$ everywhere on C . Substituting this into (5.78) yields

$$\hat{\mathbf{t}}(\rho) \cdot \mathbf{H}^i(\rho) = \frac{J_z(\rho)}{2} - \frac{j}{4} \iint_{C'} J_z(\rho') [\hat{\mathbf{n}}(\rho) \cdot \nabla H_0^{(2)}(k\rho)] d\rho' \quad (5.81)$$

Furthermore, since

$$\nabla H_0^{(2)}(k\rho) = -k H_1^{(2)}(k\rho) \left[\frac{x - x'}{R} \hat{\mathbf{x}} + \frac{y - y'}{R} \hat{\mathbf{y}} \right] \quad (5.82)$$

the two-dimensional MFIE for TM polarization can be written as

$$\hat{\mathbf{t}}(\rho) \cdot \mathbf{H}^i(\rho) = \frac{J_z(\rho)}{2} + \frac{jk}{4} \int_{C'} [\hat{\mathbf{n}}(\rho) \cdot \hat{\mathbf{R}}] J_z(\rho') H_1^{(2)}(k\rho) d\rho' \quad (5.83)$$

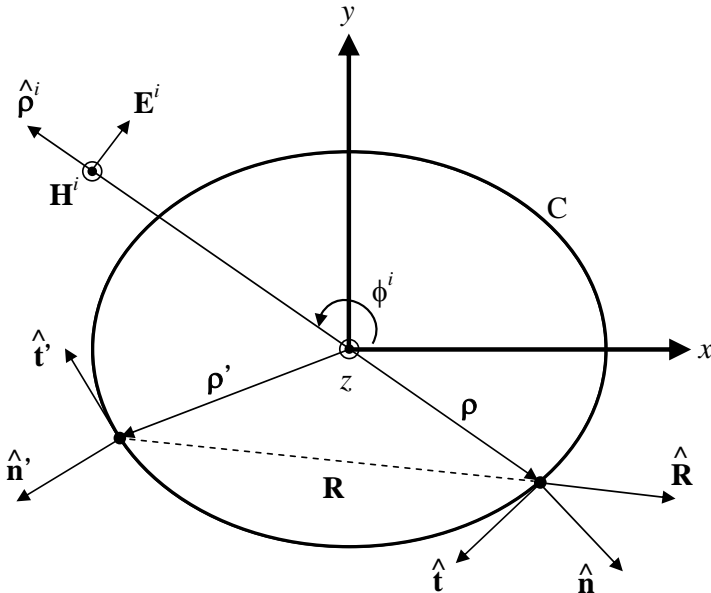


Figure 5.7: Two-Dimensional MFIE geometry: parallel polarization.

where

$$\hat{\mathbf{R}} = \frac{x - x'}{R} \hat{\mathbf{x}} + \frac{y - y'}{R} \hat{\mathbf{y}} = \frac{\rho - \rho'}{|\rho - \rho'|} \quad (5.84)$$

Once we have solved (5.83) for $J_z(\mathbf{r}')$, the scattered far field is obtained via (2.106). Applying a set of basis and testing functions to (5.83) yields a linear system with matrix elements given by

$$z_{mn} = \frac{1}{2} \int_{f_m \cup f_n} f_m(\rho) f_n(\rho) d\rho + \frac{jk}{4} \int_{f_m} f_m(\rho) \int_{f_n} f_n(\rho') [\hat{\mathbf{n}}(\rho) \cdot \hat{\mathbf{R}}] H_1^{(2)}(k\rho) d\rho' d\rho \quad (5.85)$$

where the first integration is performed over portions of the boundary where f_m and f_n overlap, and the second where they do not. The excitation vector elements are

$$b_m = \int_{f_m} f_m(\rho) [\hat{\mathbf{t}}(\rho) \cdot \mathbf{H}^i(\rho)] d\rho \quad (5.86)$$

5.2.2 MFIE: TE Polarization

The geometry of the TE MFIE problem is illustrated in Figure 5.7. Since the incident magnetic field is $\hat{\mathbf{z}}$ -directed, we know that the induced current must be aligned along

the tangent $\hat{\mathbf{t}}$ to C . Therefore, we write the two-dimensional MFIE as

$$\hat{\mathbf{t}}(\boldsymbol{\rho}) \cdot [\hat{\mathbf{n}}(\boldsymbol{\rho}) \times \mathbf{H}_i(\boldsymbol{\rho})] = \frac{J_t(\boldsymbol{\rho})}{2} - \frac{j}{4} \int_{C'} J_t(\boldsymbol{\rho}') \left(\hat{\mathbf{t}}(\boldsymbol{\rho}') \cdot \hat{\mathbf{n}}(\boldsymbol{\rho}) \times [\hat{\mathbf{t}}(\boldsymbol{\rho}') \times \nabla H_0^{(2)}(k\rho)] \right) d\boldsymbol{\rho}' \quad (5.87)$$

Let us simplify the right hand side of the above equation. Since $\hat{\mathbf{t}}(\boldsymbol{\rho}') = \hat{\mathbf{n}}(\boldsymbol{\rho}') \times \hat{\mathbf{z}}$, we can write that

$$\hat{\mathbf{t}}(\boldsymbol{\rho}') \times \nabla H_0^{(2)}(k\rho) = -\nabla H_0^{(2)}(k\rho) \times [\hat{\mathbf{n}}(\boldsymbol{\rho}') \times \hat{\mathbf{z}}] \quad (5.88)$$

Using the identity (5.79) and the fact that $\nabla H_0^{(2)}(k\rho)$ has no component along $\hat{\mathbf{z}}$, this reduces to

$$\hat{\mathbf{t}}(\boldsymbol{\rho}') \times \nabla H_0^{(2)}(k\rho) = \hat{\mathbf{z}} [\hat{\mathbf{n}}(\boldsymbol{\rho}') \cdot \nabla H_0^{(2)}(k\rho)] \quad (5.89)$$

and

$$\hat{\mathbf{t}}(\boldsymbol{\rho}) \cdot [\hat{\mathbf{n}}(\boldsymbol{\rho}) \times \hat{\mathbf{z}}] [\hat{\mathbf{n}}(\boldsymbol{\rho}') \cdot \nabla H_0^{(2)}(k\rho)] = \hat{\mathbf{n}}(\boldsymbol{\rho}') \cdot \nabla H_0^{(2)}(k\rho) \quad (5.90)$$

Therefore,

$$-H_z^i(\boldsymbol{\rho}) = \frac{J_t(\boldsymbol{\rho})}{2} - \frac{j}{4} \int_{C'} J_t(\boldsymbol{\rho}') [\hat{\mathbf{n}}(\boldsymbol{\rho}') \cdot \nabla H_0^{(2)}(k\rho)] d\boldsymbol{\rho}' \quad (5.91)$$

Combining the above with (5.82) yields the two-dimensional MFIE for TE polarization

$$-H_z^i(\boldsymbol{\rho}) = \frac{J_t(\boldsymbol{\rho})}{2} + \frac{jk}{4} \int_{C'} [\hat{\mathbf{n}}(\boldsymbol{\rho}') \cdot \hat{\mathbf{R}}] J_t(\boldsymbol{\rho}') H_1^{(2)}(k\rho) d\boldsymbol{\rho}' \quad (5.92)$$

Applying a set of basis and testing functions in the above yields a linear system with matrix elements given by

$$\begin{aligned} z_{mn} &= \frac{1}{2} \int_{f_m \cup f_n} f_m(\boldsymbol{\rho}) f_n(\boldsymbol{\rho}) d\boldsymbol{\rho} + \frac{jk}{4} \int_{f_m} f_m(\boldsymbol{\rho}) \cdot \\ &\quad \int_{f_n} f_n(\boldsymbol{\rho}') [\hat{\mathbf{n}}(\boldsymbol{\rho}') \cdot \hat{\mathbf{R}}] H_1^{(2)}(k\rho) d\boldsymbol{\rho}' d\boldsymbol{\rho} \end{aligned} \quad (5.93)$$

and excitation vector elements

$$b_m = - \int_{f_m} f_m(\boldsymbol{\rho}) H_z^i(\boldsymbol{\rho}) d\boldsymbol{\rho} \quad (5.94)$$

Note that even though we are solving for the *scalar* tangential current in (5.92), the current is still a *vector* function of position and needs to be treated as such when computing the scattered field, i.e., $\mathbf{J}(\boldsymbol{\rho}) = J_t(\boldsymbol{\rho}) \hat{\mathbf{t}}(\boldsymbol{\rho})$.

5.3 EXAMPLES

In this section we will look at practical solutions of the generalized two-dimensional EFIE and MFIE for TM and TE polarizations, and summarize expressions that can be used in computing the matrix and excitation vector elements. We will then consider examples that illustrate the implementation of each formulation.

5.3.1 Scattering by an Infinite Cylinder: TM Polarization

We first solve for the induced currents and scattered field of a two-dimensional cylinder of radius a illuminated by an incident plane wave. The exact solution for the induced current $J_z(\phi)$ is [5]

$$J_z(\phi) = \frac{2}{\pi k a \eta} \sum_{n=0}^{\infty} \frac{\epsilon_n (-j)^n \cos n\phi}{H_n^{(1)}(ka)} \quad (5.95)$$

and the bistatic scattered far field for an incident azimuthal angle $\phi^i = 0$ and observation angle ϕ^s is

$$E^s(\rho, \phi^s) = -\sqrt{\frac{2}{\pi}} \frac{e^{-j(k\rho - \pi/4)}}{\sqrt{k\rho}} \sum_{n=0}^{\infty} \epsilon_n (-1)^n \cos n\phi^s \frac{J_n(ka)}{H_n^{(1)}(ka)} \quad (5.96)$$

where $\epsilon_n = 1$ for $n = 0$, and $\epsilon_n = 2$ otherwise. For an MOM simulation, we divide the boundary of the cylinder into N segments of length $\Delta_l = 2\pi a/N$. This results in N unknowns when using pulse basis functions, and $N + 1$ unknowns when using triangles.

5.3.1.1 EFIE: Pulse Basis Functions and Point Matching

We will use the centroidal approximation to evaluate (5.24). The resulting matrix elements are

$$z_{mn} = H_0^{(2)}(k|\boldsymbol{\rho}_m - \boldsymbol{\rho}'_n|) \Delta_l \quad (5.97)$$

The corresponding self terms z_{mm} are summarized in (5.15). The excitation vector elements are

$$b_m = \frac{4}{\omega \mu} e^{jk(x_m \cos \phi_i + y_m \sin \phi_i)} \quad (5.98)$$

5.3.1.2 EFIE: Triangle Basis and Testing Functions

Applying the basis and testing functions to (5.24), the matrix elements are computed using an M -point numerical quadrature and are

$$z_{mn} = \sum_{p=1}^M w_m(\boldsymbol{\rho}_p) f_m(\boldsymbol{\rho}_p) \sum_{q=1}^M w_n(\boldsymbol{\rho}_q) f_n(\boldsymbol{\rho}_q) H_0^{(2)}(k|\boldsymbol{\rho}_p - \boldsymbol{\rho}_q|) \quad (5.99)$$

The singular portions of these elements are summarized in (5.20) and (5.21). In generating the elements, the integrations should be performed via loops over segment pairs and the resulting values placed into the corresponding matrix locations. As each segment supports two triangles, (5.99) contributes to a total of four matrix elements. The excitation vector elements (5.25) are also computed via quadrature and are

$$b_m = \frac{4}{\omega\mu} \sum_{p=1}^M w_m(\boldsymbol{\rho}_p) f_m(\boldsymbol{\rho}_p) e^{jk(x_p \cos \phi_i + y_p \sin \phi_i)} \quad (5.100)$$

5.3.1.3 MFIE: Pulse Basis Functions and Point Matching

Using pulse basis functions and point matching, only the first integral in (5.85) contributes to the matrix self terms. Evaluating this using point matching yields simply

$$z_{mm} = \frac{1}{2} \quad (5.101)$$

The second integral contributes to the off-diagonal terms, and using the centroidal approximation these elements are

$$z_{mn} = (\hat{\mathbf{n}}_m \cdot \hat{\mathbf{R}}_{mn}) \frac{jk\Delta_l}{4} H_1^{(2)}(k|\boldsymbol{\rho}_m - \boldsymbol{\rho}_n|) \quad (5.102)$$

where for the cylinder,

$$\hat{\mathbf{n}}_m \cdot \hat{\mathbf{R}}_{mn} = \frac{\boldsymbol{\rho}_m}{a} \cdot \frac{\boldsymbol{\rho}_m - \boldsymbol{\rho}_n}{|\boldsymbol{\rho}_m - \boldsymbol{\rho}_n|} \quad (5.103)$$

Using the tangent vector

$$\hat{\mathbf{t}}(\boldsymbol{\rho}) = \sin \phi \hat{\mathbf{x}} - \cos \phi \hat{\mathbf{y}} \quad (5.104)$$

and the incident magnetic field (5.2), the excitation vector elements from (5.86) are

$$b_m = -\frac{1}{\eta} [\sin \phi_m \sin \phi^i + \cos \phi_m \cos \phi^i] e^{jk(x_m \cos \phi^i + y_m \sin \phi^i)} \quad (5.105)$$

5.3.1.4 MFIE: Triangle Basis and Testing Functions

Using triangle basis and testing functions in (5.85), the matrix elements are computed via numerical quadrature and are

$$z_{mn} = \frac{1}{2} \sum_{p=1}^M w_m(\boldsymbol{\rho}_p) f_m(\boldsymbol{\rho}_p) f_n(\boldsymbol{\rho}_p) + \frac{jk}{4} \sum_{p=1}^M w_m(\boldsymbol{\rho}_p) f_m(\boldsymbol{\rho}_p) \cdot \\ \sum_{q=1}^M w_n(\boldsymbol{\rho}_q) f_n(\boldsymbol{\rho}_q) (\hat{\mathbf{n}}_p \cdot \hat{\mathbf{R}}_{pq}) H_1^{(2)}(k|\boldsymbol{\rho}_p - \boldsymbol{\rho}_q|) \quad (5.106)$$

The first term is computed only on segments where the basis functions overlap, and the second on non-overlapping segments. As with the EFIE, the above calculations are best performed by looping over boundary segments instead of triangles, and placing the integrations into the correct matrix locations. The excitation vector elements are

$$b_m = -\frac{1}{\eta} \sum_{p=1}^M w_m(\rho_p) f_m(\rho_p) [\sin \phi_p \sin \phi^i + \cos \phi_p \cos \phi^i] e^{jk(x_p \cos \phi^i + y_p \sin \phi^i)} \quad (5.107)$$

5.3.1.5 Results

We compute the induced current and bistatic radar cross section ($\phi_i = 0$) for a cylinder of radius $a = 2\lambda$. For each case, we divide the perimeter of the cylinder into 180 segments of equal length. This choice results in just over 14 segments per wavelength. Numerical integration with triangle functions uses Gaussian quadrature with six points per segment. The modal solution is terminated after 20 modes. The EFIE results using pulses and triangles are summarized in Figures 5.8 and 5.9, respectively. The results from the triangle functions are seen to be better than pulses, though the agreement with the modal solution is excellent in both cases. The corresponding MFIE results are summarized in Figures 5.10 and 5.11, respectively. Triangles again perform better than pulses, though both solutions are still very good.

5.3.2 Scattering by an Infinite Cylinder: TE Polarization

For TE-polarized waves, the exact solution for the induced tangential current J_t as a function of azimuthal angle ϕ is [5]

$$J_t(\phi) = \frac{-2j}{\pi k a \eta} \sum_{n=0}^{\infty} \frac{\epsilon_n(-j)^n \cos n\phi}{H_n^{(1)\prime}(ka)} \quad (5.108)$$

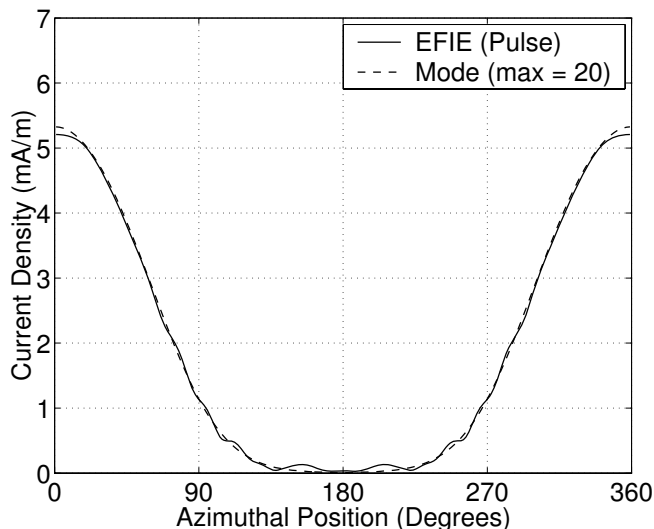
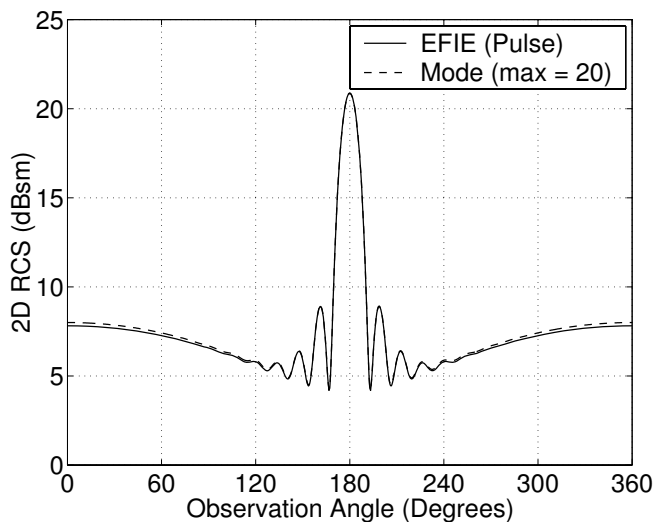
and the far-zone bistatic scattered magnetic field for an incident azimuthal angle $\phi^i = 0$ and observation angle ϕ^s is

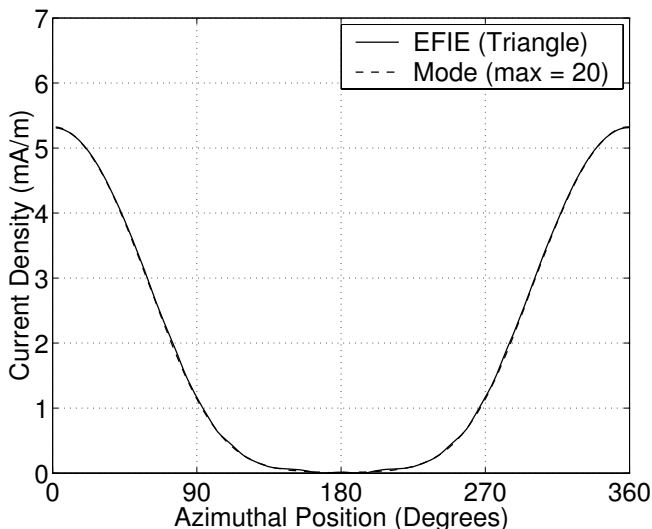
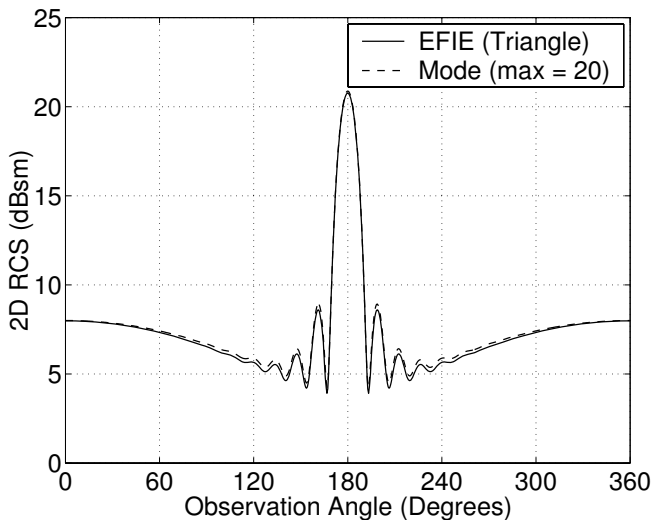
$$H^s(r, \phi^s) = -\frac{1}{\eta} \sqrt{\frac{2}{\pi}} \frac{e^{-j(k\rho - \pi/4)}}{\sqrt{k\rho}} \sum_{n=0}^{\infty} \epsilon_n (-1)^n \cos n\phi^s \frac{J'_n(ka)}{H_n^{(1)\prime}(ka)} \quad (5.109)$$

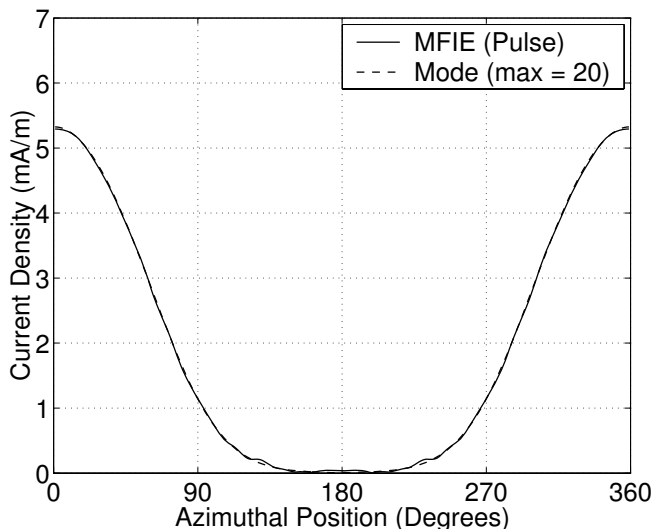
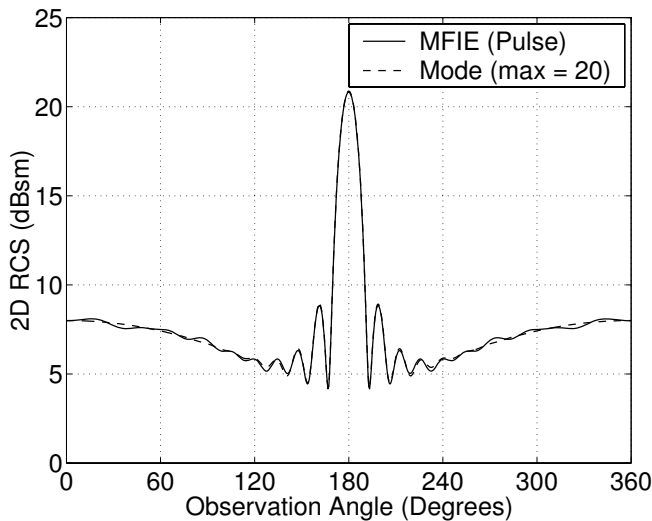
with

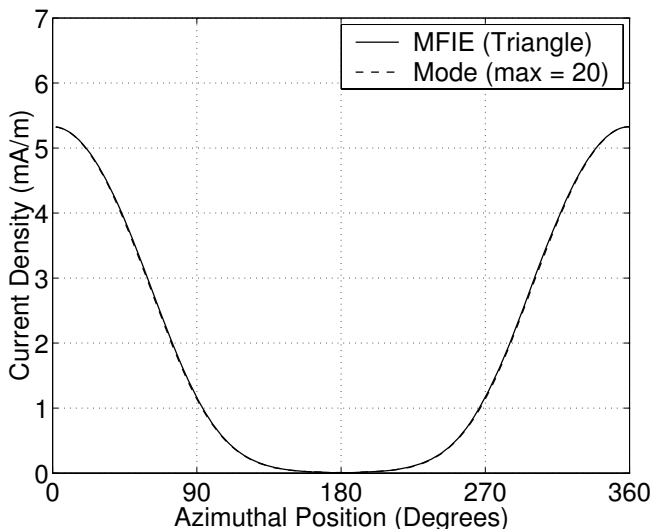
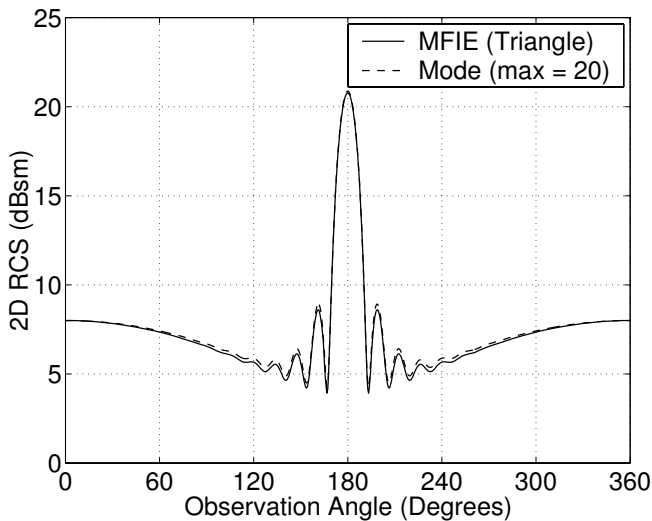
$$Z'_n(ka) = \frac{n}{ka} Z_n(ka) - Z_{n+1}(ka) \quad (5.110)$$

where $Z_n(ka)$ is either $J_n(ka)$ or $H_n^{(1)}(ka)$ [3].

(a) Induced Surface Current ($|J_z|$)(b) Two-Dimensional Monostatic RCS ($0 \leq \phi^s \leq 2\pi$)**Figure 5.8:** Infinite cylinder ($a = 2\lambda$): TM polarization (EFIE).

(a) Induced Surface Current ($|J_z|$)(b) Two-Dimensional Monostatic RCS ($0 \leq \phi^s \leq 2\pi$)**Figure 5.9:** Infinite cylinder ($a = 2\lambda$): TM polarization (EFIE).

(a) Induced Surface Current ($|J_z|$)(b) Two-Dimensional Monostatic RCS ($0 \leq \phi^s \leq 2\pi$)**Figure 5.10:** Infinite cylinder ($a = 2\lambda$): TM polarization (MFIE).

(a) Induced Surface Current ($|J_z|$)(b) Two-Dimensional Monostatic RCS ($0 \leq \phi^s \leq 2\pi$)**Figure 5.11:** Infinite cylinder ($a = 2\lambda$): TM polarization (MFIE).

5.3.2.1 EFIE: Triangle Basis and Testing Functions

Triangle functions must be used to solve the TE EFIE (5.75), as the basis and testing functions must have a well-behaved divergence. These functions are vector valued and are everywhere tangent to the boundary. Applying numerical quadrature, the matrix elements are

$$z_{mn} = \sum_{p=1}^M \sum_{q=1}^M w_m(\boldsymbol{\rho}_p) w_n(\boldsymbol{\rho}_q) \left[\mathbf{f}_m(\boldsymbol{\rho}_p) \cdot \mathbf{f}_n(\boldsymbol{\rho}_q) \pm \frac{1}{k^2 \Delta_l^2} \right] H_0^{(2)}(k|\boldsymbol{\rho}_p - \boldsymbol{\rho}_q|) \quad (5.111)$$

where we have used the fact that the divergence of each triangle function is

$$\nabla \cdot \mathbf{f}(\boldsymbol{\rho}) = \pm \frac{1}{\Delta_l} \quad (5.112)$$

and the sign of the second term in (5.111) depends on the slope of the triangle functions on each segment. For overlapping segments, the portion of the self terms involving the triangle functions may be computed via (5.20) and (5.21). This leaves us with the second integration of (5.75), which has the form

$$\int_0^{\Delta_l} \int_0^{\Delta_l} H_0^{(2)}(k|x - x'|) dx' dx \quad (5.113)$$

We will evaluate this integration using analytic inner and numerical outer integrations, where the innermost is summarized in (5.14). Using the incident electric field (5.26) and tangent vector (5.104), the excitation vector elements are

$$b_m = \frac{4}{\omega \mu} \sum_{p=1}^M w_m(\boldsymbol{\rho}_p) f_m(\boldsymbol{\rho}_p) [\sin \phi_p \sin \phi^i + \cos \phi_p \cos \phi^i] e^{jk(x_p \cos \phi^i + y_p \sin \phi^i)} \quad (5.114)$$

5.3.2.2 MFIE: Pulse Basis Functions and Point Matching

The elements that result from (5.92) are very similar to those from the TM case, so we will simply summarize the results. The matrix elements are

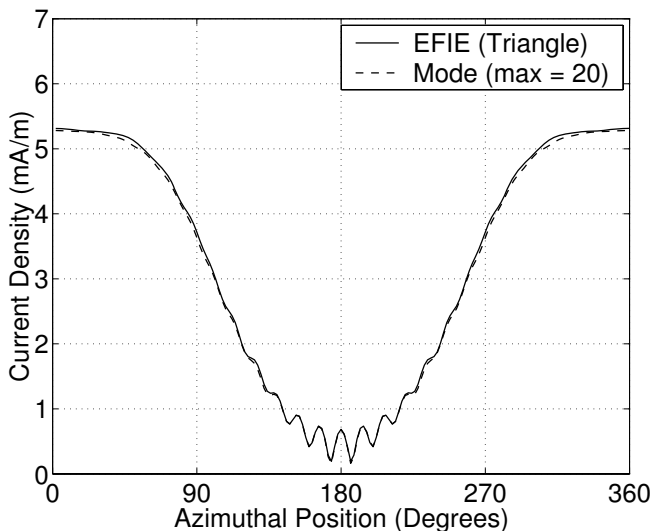
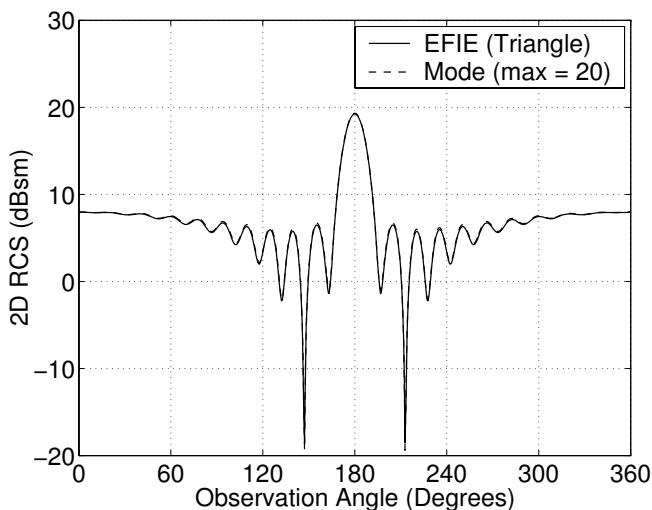
$$z_{mm} = \frac{1}{2} \quad (5.115)$$

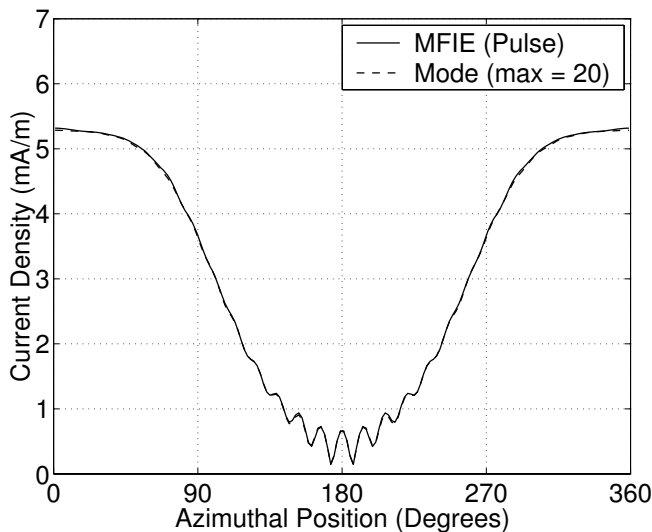
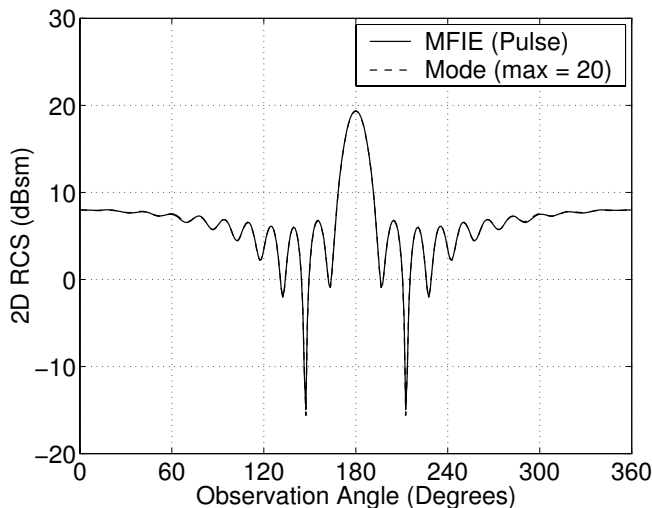
and

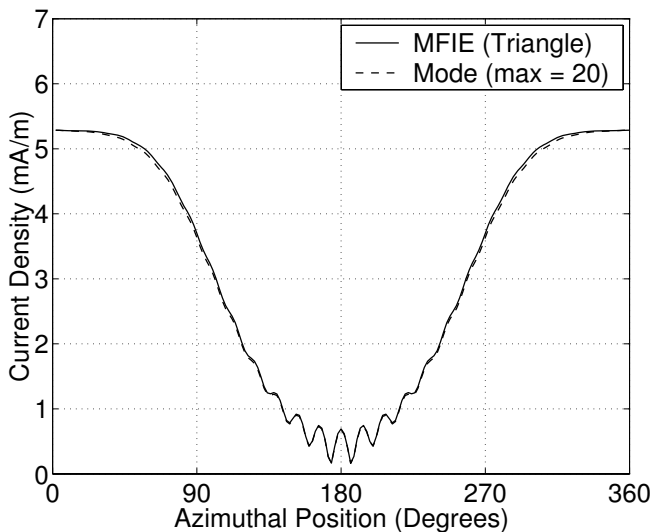
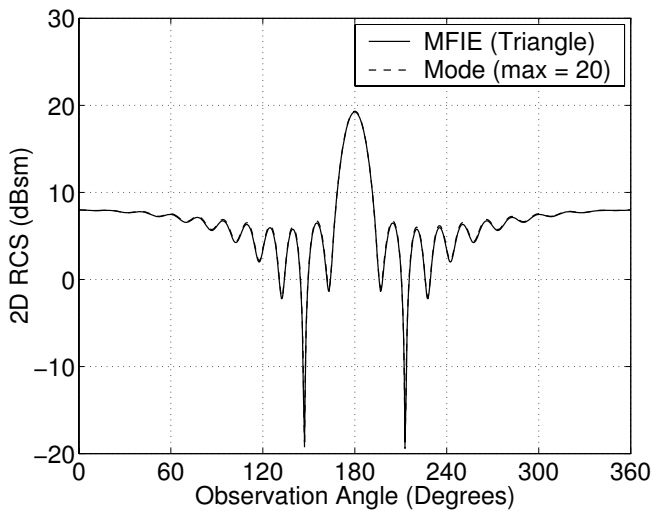
$$z_{mn} = (\hat{\mathbf{n}}_n \cdot \hat{\mathbf{R}}_{mn}) \frac{jk \Delta_l}{4} H_1^{(2)}(k|\boldsymbol{\rho}_m - \boldsymbol{\rho}_n|) \quad (5.116)$$

The excitation vector elements are

$$b_m = -\frac{1}{\eta} e^{jk(x_m \cos \phi^i + y_m \sin \phi^i)} \quad (5.117)$$

(a) Induced Surface Current ($|J_z|$)(b) Two-Dimensional Monostatic RCS ($0 \leq \phi^s \leq 2\pi$)**Figure 5.12:** Infinite cylinder ($a = 2\lambda$): TE polarization (EFIE).

(a) Induced Surface Current ($|J_z|$)(b) Two-Dimensional Monostatic RCS ($0 \leq \phi^s \leq 2\pi$)**Figure 5.13:** Infinite cylinder ($a = 2\lambda$): TE polarization (MFIE).

(a) Induced Surface Current ($|J_z|$)(b) Two-Dimensional Monostatic RCS ($0 \leq \phi^s \leq 2\pi$)**Figure 5.14:** Infinite cylinder ($a = 2\lambda$): TE polarization (MFIE).

5.3.2.3 MFIE: Triangle Basis and Testing Functions

The results in this case are also very similar to the TM case, so we will simply summarize the results. The matrix elements are

$$\begin{aligned} z_{mn} = & \frac{1}{2} \sum_{p=1}^M w_m(\boldsymbol{\rho}_p) f_m(\boldsymbol{\rho}_p) f_n(\boldsymbol{\rho}_p) + \frac{jk}{4} \sum_{p=1}^M w_m(\boldsymbol{\rho}_p) f_m(\boldsymbol{\rho}_p) \cdot \\ & \sum_{q=1}^M w_n(\boldsymbol{\rho}_q) f_n(\boldsymbol{\rho}_q) (\hat{\mathbf{n}}_q \cdot \hat{\mathbf{R}}_{pq}) H_1^{(2)}(k|\boldsymbol{\rho}_p - \boldsymbol{\rho}_q|) \end{aligned} \quad (5.118)$$

The first term is computed only on segments where the basis functions overlap, and the second on non-overlapping segments. The excitation vector elements are

$$b_m = -\frac{1}{\eta} \sum_{p=1}^M w_m(\boldsymbol{\rho}_p) f_m(\boldsymbol{\rho}_p) e^{jk(x_p \cos \phi^i + y_p \sin \phi^i)} \quad (5.119)$$

5.3.2.4 Results

We compute the same quantities as for the TM case, and again use 180 segments for the circumference of the cylinder. The EFIE results using triangles are shown in Figure 5.12 and compare very well to the exact solution. The corresponding MFIE results are summarized in Figures 5.10 and 5.11, respectively, and are also very good.

REFERENCES

- [1] D. Wilton, S. Rao, A. Glisson, D. Schaubert, M. Al-Bundak, and C. M. Butler, “Potential integrals for uniform and linear source distributions on polygonal and polyhedral domains,” *IEEE Trans. Antennas Propagat.*, vol. 32, 276–281, March 1984.
- [2] C. A. Balanis, *Advanced Engineering Electromagnetics*. John Wiley and Sons, 1989.
- [3] M. Abramowitz and I. Stegun, *Handbook of Mathematical Functions*. National Bureau of Standards, 1966.
- [4] H. Dwight, *Tables of Integrals and Other Mathematical Data*. The Macmillan Company, 1961.
- [5] G. T. Ruck, ed., *Radar Cross Section Handbook*. Plenum Press, 1970.

Chapter 6

Bodies of Revolution

In this chapter we apply the method of moments to problems involving bodies of revolution (BOR). This is of great practical interest, as scattering problems involving spheres, ellipsoids and finite cylinders are often used to benchmark new computational electromagnetics techniques and codes, as well as to calibrate equipment used to measure RCS. Furthermore, many real-world objects such as the conic reentry vehicle can be modeled as rotationally symmetric objects. The method discussed in this chapter is largely that of Harrington and Mautz [1], one of the most commonly used methods of solving BOR problems using the MOM.

The formulations in this chapter describe the surface currents on a BOR using basis functions that are piecewise linear in the longitudinal direction and a finite Fourier series in the azimuthal direction. The advantage of this method is that the basis function coefficients exist only on the boundary curve that defines the BOR, resulting in a matrix equation of compact size for each Fourier mode.

6.1 BOR SURFACE DESCRIPTION

A general BOR can be specified completely by a bounding curve revolved around an axis of symmetry. We represent this curve by a piecewise linear approximation, shown in Figure 6.1. We divide the curve into N segments, each of which describes an annulus on the BOR surface. A point on the BOR can be specified by its cylindrical coordinates (ρ, ϕ, z) , by its longitudinal distance on the curve and its azimuthal location (t, ϕ) , or by its cartesian coordinates

$$\mathbf{r} = \rho \cos \phi \hat{\mathbf{x}} + \rho \sin \phi \hat{\mathbf{y}} + z \hat{\mathbf{z}} \quad (6.1)$$

The longitudinal vector $\hat{\mathbf{t}}(\mathbf{r})$ and azimuthal vector $\hat{\phi}(\mathbf{r})$ are everywhere tangent to the surface and form the orthogonal set with the surface normal $\hat{\mathbf{n}}(\mathbf{r})$:

$$\hat{\mathbf{n}}(\mathbf{r}) = \hat{\phi}(\mathbf{r}) \times \hat{\mathbf{t}}(\mathbf{r}) \quad (6.2)$$

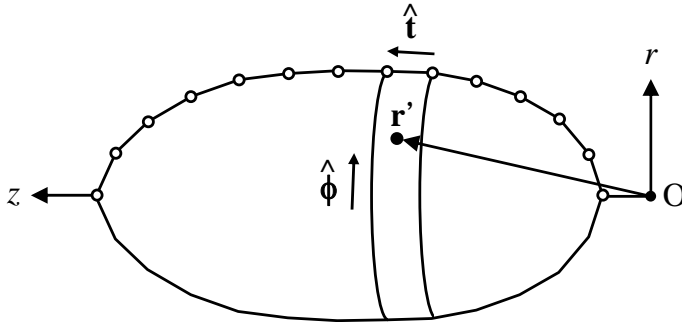


Figure 6.1: BOR surface outline.

and the distance r between any two points on the surface can be written as

$$r = |\mathbf{r} - \mathbf{r}'| = \sqrt{(\rho - \rho')^2 + (z - z')^2 + 2\rho\rho'(1 - \cos[\phi - \phi'])} \quad (6.3)$$

6.2 SURFACE CURRENT EXPANSION ON A BOR

Let us consider an efficient method of expanding surface currents on a BOR. Because of the rotational symmetry, it is possible to represent the currents by a set of basis functions that are local in the longitudinal dimension and a Fourier series in the azimuthal dimension. This can be expressed as [1]

$$\mathbf{J}(\mathbf{r}) = \sum_{\alpha=-\infty}^{\infty} \sum_{n=1}^N \left[a_{\alpha n}^t \mathbf{f}_{\alpha n}^t(\mathbf{r}) + a_{\alpha n}^\phi \mathbf{f}_{\alpha n}^\phi(\mathbf{r}) \right] \quad (6.4)$$

where $a_{\alpha n}^t$ and $a_{\alpha n}^\phi$ are the longitudinal and azimuthal expansion coefficients for mode α and basis function n , respectively, and the expansion functions $\mathbf{f}_{\alpha n}^{t,\phi}(\mathbf{r})$ are

$$\begin{aligned} \mathbf{f}_{\alpha n}^t(\mathbf{r}) &= f_n(t) e^{j\alpha\phi} \hat{\mathbf{t}}(\mathbf{r}) \\ \mathbf{f}_{\alpha n}^\phi(\mathbf{r}) &= f_n(t) e^{j\alpha\phi} \hat{\phi}(\mathbf{r}) \end{aligned} \quad (6.5)$$

where $f_n(t)$ is the expansion function in the longitudinal direction. So that several expressions will simplify later, let us define $f_m(t)$ as

$$f_m(t) = \frac{T_m(t)}{\rho(t)} \quad (6.6)$$

where $T_m(t)$ is a standard one-dimensional local basis function. For these basis functions, Harrington and Mautz use pulse approximations to the one-dimensional

triangle function of Section 3.3.2. Each full triangle spans $2d$ boundary segments with d segments per half triangle, and is assigned a constant value inside each segment. Integration in the longitudinal dimension is performed using a centroidal approximation, and integrals involving the Green's function are performed in the azimuthal dimension. This results in a set of one-dimensional numerical integrations for all matrix elements. For an open BOR or a BOR that begins and ends on the z axis, we assign half triangles to the first and last segments. For closed curves that exist entirely off the z axis, an additional triangle is added to span the first and last segments so the boundary closes on itself.

6.3 EFIE FOR A CONDUCTING BOR

Let us solve the EFIE for a conducting BOR. We first substitute the current from (6.4) into the EFIE of (2.120), yielding

$$-\frac{j}{\omega\mu} \hat{\mathbf{t}}(\mathbf{r}) \cdot \mathbf{E}^i(\mathbf{r}) = \iint_S (1 + \frac{1}{k^2} \nabla \nabla \cdot) \sum_{n=1}^N \left[a_{\alpha n}^t \mathbf{f}_{\alpha n}^t(\mathbf{r}') + a_{\alpha n}^\phi \mathbf{f}_{\alpha n}^\phi(\mathbf{r}') \right] \frac{e^{-jkr}}{4\pi r} d\mathbf{r}' \quad (6.7)$$

The above comprises one equation in $2N$ unknowns, so we will test with $2N$ testing functions $\mathbf{f}_{\beta m}^{t,\phi}(\mathbf{r})$. For the testing we choose the complex conjugates of the basis functions

$$\begin{aligned} \mathbf{f}_{\beta m}^t(\mathbf{r}) &= f_m(t) e^{-j\beta\phi} \hat{\mathbf{t}}(\mathbf{r}) \\ \mathbf{f}_{\beta m}^\phi(\mathbf{r}) &= f_m(t) e^{-j\beta\phi} \hat{\phi}(\mathbf{r}) \end{aligned} \quad (6.8)$$

Applying the testing functions and redistributing the vector differential operators according to the method in Section 4.5.1, we obtain the matrix \mathbf{Z} :

$$\mathbf{Z} = \begin{bmatrix} \mathbf{Z}^{tt} & \mathbf{Z}^{t\phi} \\ \mathbf{Z}^{\phi t} & \mathbf{Z}^{\phi\phi} \end{bmatrix} \quad (6.9)$$

where for modes α and β the sub-matrix elements are of the form

$$z_{mn}^{pq} = \iint_{\mathbf{f}_{\beta m}^{t,\phi}} \iint_{\mathbf{f}_{\alpha n}^{t,\phi}} \left(\mathbf{f}_{\beta m}^{t,\phi}(\mathbf{r}) \cdot \mathbf{f}_{\alpha n}^{t,\phi}(\mathbf{r}') - \frac{1}{k^2} [\nabla \cdot \mathbf{f}_{\beta m}^{t,\phi}(\mathbf{r})] [\nabla' \cdot \mathbf{f}_{\alpha n}^{t,\phi}(\mathbf{r}')] \right) \frac{e^{-jkr}}{4\pi r} d\mathbf{r}' d\mathbf{r} \quad (6.10)$$

6.3.1 EFIE Matrix Elements

To compute the matrix elements we first calculate the divergence of the basis and testing functions, yielding

$$\nabla \cdot \mathbf{f}_{\beta m}^t(\mathbf{r}) = \frac{1}{\rho(t)} \frac{\partial}{\partial t} [\rho(t) f_m(t)] e^{-j\beta\phi} \quad (6.11)$$

$$\nabla' \cdot \mathbf{f}_{\alpha n}^t(\mathbf{r}') = \frac{1}{\rho(t')} \frac{\partial}{\partial t'} [\rho(t') f_n(t')] e^{j\alpha\phi'} \quad (6.12)$$

$$\nabla \cdot \mathbf{f}_{\beta m}^\phi(\mathbf{r}) = \frac{f_m(t)}{\rho(t)} \frac{\partial}{\partial \phi} e^{j\beta\phi} = -j\beta \frac{f_m(t)}{\rho(t)} e^{-j\beta\phi} \quad (6.13)$$

$$\nabla' \cdot \mathbf{f}_{\alpha n}^\phi(\mathbf{r}') = \frac{f_n(t')}{\rho(t')} \frac{\partial}{\partial \phi'} e^{j\alpha\phi'} = j\alpha \frac{f_n(t')}{\rho(t')} e^{j\alpha\phi'} \quad (6.14)$$

Noting that

$$\hat{\mathbf{t}}(\mathbf{r}) = \sin \gamma \hat{\mathbf{p}} + \cos \gamma \hat{\mathbf{z}} \quad (6.15)$$

where $\gamma = \cos^{-1} [\hat{\mathbf{t}}(\mathbf{r}) \cdot \hat{\mathbf{z}}]$, we write the following dot products:

$$\hat{\mathbf{t}}(\mathbf{r}) \cdot \hat{\mathbf{t}}(\mathbf{r}') = \sin \gamma \sin \gamma' \cos(\phi' - \phi) + \cos \gamma \cos \gamma' \quad (6.16)$$

$$\hat{\mathbf{t}}(\mathbf{r}) \cdot \hat{\phi}(\mathbf{r}') = -\sin \gamma \sin(\phi' - \phi) \quad (6.17)$$

$$\hat{\phi}(\mathbf{r}) \cdot \hat{\mathbf{t}}(\mathbf{r}') = \sin \gamma' \sin(\phi' - \phi) \quad (6.18)$$

$$\hat{\phi}(\mathbf{r}) \cdot \hat{\phi}(\mathbf{r}') = \cos(\phi' - \phi) \quad (6.19)$$

Using the above and noting that the differential surface element in cylindrical coordinates is $ds = \rho d\phi dt$, the sub-matrix elements can be written as

$$z_{mn}^{tt} = \int_{t_m}^{t_n} \int_{t_n}^{2\pi} \int_0^{2\pi} \int_0^{2\pi} \left([\rho(t) f_m(t)] [\rho(t') f_n(t')] \hat{\mathbf{t}}(\mathbf{r}) \cdot \hat{\mathbf{t}}(\mathbf{r}') - \frac{1}{k^2} \frac{\partial}{\partial t} [\rho(t) f_m(t)] \right. \\ \left. \cdot \frac{\partial}{\partial t'} [\rho(t') f_n(t')] \right) e^{j(\alpha\phi' - \beta\phi)} \frac{e^{-jkr}}{4\pi r} d\phi' d\phi dt' dt \quad (6.20)$$

$$z_{mn}^{t\phi} = \int_{t_m}^{t_n} \int_{t_n}^{2\pi} \int_0^{2\pi} \int_0^{2\pi} \left([\rho(t) f_m(t)] [\rho(t') f_n(t')] \hat{\mathbf{t}}(\mathbf{r}) \cdot \hat{\phi}(\mathbf{r}') + \frac{1}{k^2} \frac{\alpha}{\rho(t')} \right. \\ \left. \cdot \frac{\partial}{\partial t} [\rho(t) f_m(t)] [\rho(t') f_n(t')] \right) e^{j(\alpha\phi' - \beta\phi)} \frac{e^{-jkr}}{4\pi r} d\phi' d\phi dt' dt \quad (6.21)$$

$$z_{mn}^{\phi t} = \int_{t_m}^{t_n} \int_{t_n}^{2\pi} \int_0^{2\pi} \int_0^{2\pi} \left([\rho(t) f_m(t)] [\rho(t') f_n(t')] \hat{\phi}(\mathbf{r}) \cdot \hat{\mathbf{t}}(\mathbf{r}') - \frac{1}{k^2} \frac{\beta}{\rho(t)} \right. \\ \left. \cdot [\rho(t) f_m(t)] \frac{\partial}{\partial t'} [\rho(t') f_n(t')] \right) e^{j(\alpha\phi' - \beta\phi)} \frac{e^{-jkr}}{4\pi r} d\phi' d\phi dt' dt \quad (6.22)$$

$$z_{mn}^{\phi\phi} = \int_{t_m}^{t_n} \int_{t_n}^{2\pi} \int_0^{2\pi} \int_0^{2\pi} [\rho(t) f_m(t)] [\rho(t') f_n(t')] \left(\hat{\phi}(\mathbf{r}) \cdot \hat{\phi}(\mathbf{r}') - \right. \\ \left. \frac{1}{k^2} \frac{j\alpha\beta}{\rho(t)\rho(t')} \right) e^{j(\alpha\phi' - \beta\phi)} \frac{e^{-jkr}}{4\pi r} d\phi' d\phi dt' dt \quad (6.23)$$

where the integrations are performed over the annuli spanned by the basis and testing functions. We note that these integrals are periodic functions of ϕ' with period 2π , therefore ϕ' can be replaced by $\phi' + \phi$ without altering their values [1]. Making this substitution allows us to write

$$\int_0^{2\pi} e^{j(\alpha\phi' - \beta\phi)} d\phi = e^{j\alpha\phi'} \int_0^{2\pi} e^{j(\alpha - \beta)\phi} d\phi \quad (6.24)$$

and noting that

$$\int_0^{2\pi} e^{j(\alpha - \beta)\phi} d\phi = \begin{cases} 0 & \alpha \neq \beta \\ 2\pi & \alpha = \beta \end{cases} \quad (6.25)$$

only those integrals where $\alpha = \beta$ remain. Combining the above with (6.6) and (6.16)–(6.19) and using the pulse approximation to the triangle functions inside each segment, the sub matrix elements can be written as

$$z_{mn}^{tt} = \sum_{p=1}^{M_p} \sum_{q=1}^{M_q} \left(T_p T_q [\sin \gamma_p \sin \gamma_q G_2 + \cos \gamma_p \cos \gamma_q G_1] - \frac{1}{k^2} \dot{T}_p \dot{T}_q G_1 \right) \quad (6.26)$$

$$z_{mn}^{t\phi} = j \sum_{p=1}^{M_p} \sum_{q=1}^{M_q} \left(\sin \gamma_p T_p T_q G_3 + \frac{1}{k^2} \frac{\alpha}{\rho_q} \dot{T}_p T_q G_1 \right) \quad (6.27)$$

$$z_{mn}^{\phi t} = j \sum_{p=1}^{M_p} \sum_{q=1}^{M_q} \left(\sin \gamma_q T_p T_q G_3 + \frac{1}{k^2} \frac{\alpha}{\rho_p} T_p \dot{T}_q G_1 \right) \quad (6.28)$$

$$z_{mn}^{\phi\phi} = - \sum_{p=1}^{M_p} \sum_{q=1}^{M_q} \left(G_2 - \frac{1}{k^2} \frac{\alpha^2}{\rho_p \rho_q} G_1 \right) T_p T_q \quad (6.29)$$

where the indices p and q represent the segments on the BOR boundary for the observation and source triangle functions T_m and T_n , respectively, and M_p and M_q are the numbers of segments per triangle. $T_{p,q}$ and $\dot{T}_{p,q}$ refer to the triangle functions and their derivatives evaluated at the center of each segment. The integrals G_n , G_{cn} and G_{sn} are

$$G_1 = \Delta_p \Delta_q \int_0^\pi \cos(\alpha\phi') \frac{e^{-jkR_{pq}}}{R_{pq}} d\phi' \quad (6.30)$$

$$G_2 = \Delta_p \Delta_q \int_0^\pi \cos(\phi') \cos(\alpha\phi') \frac{e^{-jkR_{pq}}}{R_{pq}} d\phi' \quad (6.31)$$

$$G_3 = \Delta_p \Delta_q \int_0^\pi \sin(\phi') \sin(\alpha\phi') \frac{e^{-jkR_{pq}}}{R_{pq}} d\phi' \quad (6.32)$$

where Δ_p and Δ_q are the lengths of segments p and q , respectively. These integrals can be evaluated by a one-dimensional numerical quadrature. When the source and

observation segments do not overlap we choose for R_{pq}

$$R_{pq} = \sqrt{(\rho_p - \rho_q)^2 + (z_p - z_q)^2 + 2\rho_p\rho_q(1 - \cos\phi')} \quad (6.33)$$

and for overlapping source and testing segments we choose [1]

$$R_{pq} = \sqrt{(\Delta_p/4)^2 + 2\rho_p^2(1 - \cos\phi')} \quad (6.34)$$

Inspecting (6.26)–(6.29) we observe the following relationship between positive and negative modes in the EFIE matrix

$$\begin{bmatrix} \mathbf{Z}^{tt} & \mathbf{Z}^{t\phi} \\ \mathbf{Z}^{\phi t} & \mathbf{Z}^{\phi\phi} \end{bmatrix}_{-\alpha} = \begin{bmatrix} \mathbf{Z}^{tt} & -\mathbf{Z}^{t\phi} \\ -\mathbf{Z}^{\phi t} & \mathbf{Z}^{\phi\phi} \end{bmatrix}_\alpha \quad (6.35)$$

The properties in (6.35) survive inversion.

6.3.2 Excitation

Applying the testing functions $\mathbf{f}_{\alpha m}^{t,\phi}(\mathbf{r})$ to the left-hand side of (6.7) yields a column vector of length $2N$ of the form

$$\mathbf{b} = \begin{bmatrix} \mathbf{b}^t \\ \mathbf{b}^\phi \end{bmatrix} \quad (6.36)$$

The individual excitation vector elements are given by

$$b_m^{t,\phi} = -\frac{j}{\omega\mu} \int_{t_m} \int_0^{2\pi} \mathbf{f}_{\alpha m}^{t,\phi}(\mathbf{r}) \cdot \mathbf{E}^i(\mathbf{r}) \rho d\phi dt \quad (6.37)$$

Using the pulse approximation of the triangle functions, the above can be written as

$$b_m^{t,\phi} = -\frac{j}{\omega\mu} \sum_{p=1}^{M_p} T_p \Delta_p \int_0^{2\pi} e^{-j\alpha\phi} (\hat{\mathbf{t}}, \hat{\phi}) \cdot \mathbf{E}^i(\mathbf{r}) d\phi \quad (6.38)$$

where $\mathbf{E}^i(\mathbf{r})$ is an arbitrary incident field. In general, the above integral must be evaluated numerically, however for incident plane waves it can be evaluated analytically.

6.3.2.1 Plane Wave Excitation

A plane wave of unit magnitude incident along a vector $\hat{\mathbf{r}}^i$ at the spherical angles (θ^i, ϕ^i) can be written in cartesian coordinates as

$$E^i(\mathbf{r}) = e^{jk\hat{\mathbf{r}}^i \cdot \mathbf{r}} = e^{jkz \cos\theta^i} e^{jk \sin\theta^i(x \cos\phi^i + y \sin\phi^i)} \quad (6.39)$$

The above can be written in cylindrical coordinates (ρ, ϕ, z) as

$$e^{jkz \cos \theta^i} e^{jk \sin \theta^i (x \cos \phi^i + y \sin \phi^i)} = e^{jkz \cos \theta^i} e^{jk \sin \theta^i \rho \cos(\phi - \phi^i)} \quad (6.40)$$

To obtain the complete scattering matrix we must consider $\hat{\theta}$ and $\hat{\phi}$ polarized incident waves, so we must calculate the excitation vectors

$$\mathbf{b}_{\theta^i} = -\frac{j}{\omega \mu} \begin{bmatrix} \mathbf{b}^{t\theta^i} \\ \mathbf{b}^{\phi\theta^i} \end{bmatrix} \quad (6.41)$$

and

$$\mathbf{b}_{\phi^i} = -\frac{j}{\omega \mu} \begin{bmatrix} \mathbf{b}^{t\phi^i} \\ \mathbf{b}^{\phi\phi^i} \end{bmatrix} \quad (6.42)$$

Computing the dot products

$$\hat{\mathbf{t}} \cdot \hat{\theta}^i = \cos \theta^i \sin \gamma \cos(\phi - \phi^i) - \sin \theta^i \cos \gamma \quad (6.43)$$

$$\hat{\phi} \cdot \hat{\theta}^i = -\cos \theta^i \sin(\phi - \phi^i) \quad (6.44)$$

$$\hat{\mathbf{t}} \cdot \hat{\phi}^i = \sin \gamma \sin(\phi - \phi^i) \quad (6.45)$$

$$\hat{\phi} \cdot \hat{\phi}^i = \cos(\phi - \phi^i) \quad (6.46)$$

$$(6.47)$$

allows us to write the excitation vector elements as

$$b_m^{t\theta^i} = \sum_{p=1}^{M_p} T_p \Delta_p e^{jk z_p \cos \theta^i} \int_0^{2\pi} e^{jk \rho_p \sin \theta^i \cos \phi - j\alpha \phi} \left[\cos \theta^i \sin \gamma_p \cos \phi - \sin \theta^i \cos \gamma_p \right] d\phi \quad (6.48)$$

$$b_m^{\phi\theta^i} = -\sum_{p=1}^{M_p} T_p \Delta_p e^{jk z_p \cos \theta^i} \int_0^{2\pi} e^{jk \rho_p \sin \theta^i \cos \phi - j\alpha \phi} \cos \theta^i \sin \phi d\phi \quad (6.49)$$

$$b_m^{t\phi^i} = \sum_{p=1}^{M_p} T_p \Delta_p e^{jk z_p \cos \theta^i} \int_0^{2\pi} e^{jk \rho_p \sin \theta^i \cos \phi - j\alpha \phi} \sin \gamma_p \sin \phi d\phi \quad (6.50)$$

$$b_m^{\phi\phi^i} = \sum_{p=1}^{M_p} T_p \Delta_p e^{jk z_p \cos \theta^i} \int_0^{2\pi} e^{jk \rho_p \sin \theta^i \cos \phi - j\alpha \phi} \cos \phi d\phi \quad (6.51)$$

Due to the rotational symmetry, we can set ϕ^i to zero in the above and later replace ϕ^s by $\phi^s - \phi^i$ if we need to solve a bistatic problem. Let us now consider the following integral for $b_m^{i\theta^i}$:

$$\begin{aligned} I &= \cos \theta^i \sin \gamma_p \int_0^{2\pi} \cos \phi e^{jk \sin \theta^i \rho_p \cos \phi - j\alpha \phi} d\phi \\ &\quad - \sin \theta^i \cos \gamma_p \int_0^{2\pi} e^{jk \sin \theta^i \rho_p \cos \phi - j\alpha \phi} d\phi \end{aligned} \quad (6.52)$$

Using the relationship [2]

$$\int_0^{2\pi} e^{jk \sin \theta^i \rho_p \cos \phi - j\alpha \phi} d\phi = 2\pi j^\alpha J_\alpha(k \rho_p \sin \theta_i) \quad (6.53)$$

(6.52) becomes

$$\begin{aligned} I &= \cos \theta^i \sin \gamma_p \int_0^{2\pi} \cos \phi e^{jk \sin \theta^i \rho_p \cos \phi - j\alpha \phi} d\phi \\ &\quad - 2\pi j^\alpha \sin \theta^i \cos \gamma_p J_\alpha(k \rho_p \sin \theta_i) \end{aligned} \quad (6.54)$$

To evaluate the remaining integral, we make the substitution

$$\int_0^{2\pi} \cos \phi e^{jk \sin \theta^i \rho_p \cos \phi - j\alpha \phi} d\phi = \int_0^{2\pi} (e^{j\phi} - j \sin \phi) e^{jk \sin \theta^i \rho_p \cos \phi - j\alpha \phi} d\phi \quad (6.55)$$

The first term can be evaluated as before, yielding

$$2\pi j^{\alpha-1} J_{\alpha-1}(k \rho_p \sin \theta_i) - j \int_0^{2\pi} \sin \phi e^{jk \sin \theta^i \rho_p \cos \phi - j\alpha \phi} d\phi \quad (6.56)$$

and the second term can be integrated by parts, yielding

$$2\pi j^{\alpha-1} J_{\alpha-1}(k \rho_p \sin \theta_i) + j \left[\frac{2\pi \alpha}{k \rho_p \sin \theta_i} j^\alpha J_\alpha(k \rho_p \sin \theta_i) \right] \quad (6.57)$$

Using the recurrence relationship [2]

$$\frac{2\alpha}{z} J_\alpha(z) = J_{\alpha+1}(z) + J_{\alpha-1}(z) \quad (6.58)$$

the above can be rewritten as

$$\pi j^\alpha j \left[J_{\alpha+1}(k \rho_p \sin \theta^i) - J_{\alpha-1}(k \rho_p \sin \theta^i) \right] \quad (6.59)$$

and $b_m^{t\theta^i}$ is

$$b_m^{t\theta^i} = \pi j^\alpha \sum_{p=1}^{M_p} T_p \Delta_p e^{jk z_p \cos \theta^i} \left(\cos \theta^i \sin \gamma_p j [J_{\alpha+1} - J_{\alpha-1}] - 2 \sin \theta^i \cos \gamma_p J_\alpha \right) \quad (6.60)$$

The other elements follow similarly and are

$$b_m^{\phi\theta^i} = -\pi j^\alpha \sum_{p=1}^{M_p} T_p \Delta_p e^{jk z_p \cos \theta^i} \left[J_{\alpha+1} + J_{\alpha-1} \right] \cos \theta^i \quad (6.61)$$

$$b_m^{t\phi^i} = \pi j^\alpha \sum_{p=1}^{M_p} T_p \Delta_p e^{jk z_p \sin \theta^i} \left[J_{\alpha+1} + J_{\alpha-1} \right] \sin \gamma_p \quad (6.62)$$

$$b_m^{\phi\phi^i} = \pi j^{\alpha+1} \sum_{p=1}^{M_p} T_p \Delta_p e^{jk z_p \sin \theta^i} \left[J_{\alpha+1} - J_{\alpha-1} \right] \quad (6.63)$$

where $J_\alpha = J_\alpha(k \rho_p \sin \theta^i)$.

Inspecting (6.60)–(6.63), we observe the following relationship between positive and negative modes in the plane wave excitation vectors:

$$\begin{bmatrix} \mathbf{b}^{t\theta^i} \\ \mathbf{b}^{\phi\theta^i} \end{bmatrix}_{-\alpha} = \begin{bmatrix} \mathbf{b}^{t\theta^i} \\ -\mathbf{b}^{\phi\theta^i} \end{bmatrix}_\alpha \quad (6.64)$$

and

$$\begin{bmatrix} \mathbf{b}^{t\phi^i} \\ \mathbf{b}^{\phi\phi^i} \end{bmatrix}_{-\alpha} = \begin{bmatrix} -\mathbf{b}^{t\phi^i} \\ \mathbf{b}^{\phi\phi^i} \end{bmatrix}_\alpha \quad (6.65)$$

Using (6.35), (6.64) and (6.65), the solution vectors are

$$\begin{bmatrix} \mathbf{x}^{t\theta^i} \\ \mathbf{x}^{\phi\theta^i} \end{bmatrix}_\alpha = \begin{bmatrix} \mathbf{Z}^{tt} & \mathbf{Z}^{t\phi} \\ \mathbf{Z}^{\phi t} & \mathbf{Z}^{\phi\phi} \end{bmatrix}_\alpha^{-1} \begin{bmatrix} \mathbf{b}^{t\theta^i} \\ \mathbf{b}^{\phi\theta^i} \end{bmatrix}_\alpha \quad (6.66)$$

$$\begin{bmatrix} \mathbf{x}^{t\theta^i} \\ \mathbf{x}^{\phi\theta^i} \end{bmatrix}_{-\alpha} = \begin{bmatrix} \mathbf{Z}^{tt} & -\mathbf{Z}^{t\phi} \\ -\mathbf{Z}^{\phi t} & \mathbf{Z}^{\phi\phi} \end{bmatrix}_\alpha^{-1} \begin{bmatrix} \mathbf{b}^{t\theta^i} \\ -\mathbf{b}^{\phi\theta^i} \end{bmatrix}_\alpha = \begin{bmatrix} \mathbf{x}^{t\theta^i} \\ -\mathbf{x}^{\phi\theta^i} \end{bmatrix}_\alpha \quad (6.67)$$

and

$$\begin{bmatrix} \mathbf{x}^{t\phi^i} \\ \mathbf{x}^{\phi\phi^i} \end{bmatrix}_\alpha = \begin{bmatrix} \mathbf{Z}^{tt} & \mathbf{Z}^{t\phi} \\ \mathbf{Z}^{\phi t} & \mathbf{Z}^{\phi\phi} \end{bmatrix}_\alpha^{-1} \begin{bmatrix} \mathbf{b}^{t\phi^i} \\ \mathbf{b}^{\phi\phi^i} \end{bmatrix}_\alpha \quad (6.68)$$

$$\begin{bmatrix} \mathbf{x}^{t\phi^i} \\ \mathbf{x}^{\phi\phi^i} \end{bmatrix}_{-\alpha} = \begin{bmatrix} \mathbf{Z}^{tt} & -\mathbf{Z}^{t\phi} \\ -\mathbf{Z}^{\phi t} & \mathbf{Z}^{\phi\phi} \end{bmatrix}_\alpha^{-1} \begin{bmatrix} -\mathbf{b}^{t\phi^i} \\ \mathbf{b}^{\phi\phi^i} \end{bmatrix}_\alpha = \begin{bmatrix} -\mathbf{x}^{t\phi^i} \\ \mathbf{x}^{\phi\phi^i} \end{bmatrix}_\alpha \quad (6.69)$$

The $\hat{\theta}^i$ - and $\hat{\phi}^i$ -induced currents for basis function n can now be written as

$$\mathbf{J}_n^{\theta^i}(\mathbf{r}) = \sum_{\alpha=-\infty}^{\infty} \left[x_{\alpha n}^{t\theta^i} f_n(t) \hat{\mathbf{t}}(\mathbf{r}) + x_{\alpha n}^{\phi\theta^i} f_n(t) \hat{\phi}(\mathbf{r}) \right] e^{j\alpha\phi} \quad (6.70)$$

and

$$\mathbf{J}_n^{\phi^i}(\mathbf{r}) = \sum_{\alpha=-\infty}^{\infty} \left[x_{\alpha n}^{t\phi^i} f_n(t) \hat{\mathbf{t}}(\mathbf{r}) + x_{\alpha n}^{\phi\phi^i} f_n(t) \hat{\phi}(\mathbf{r}) \right] e^{j\alpha\phi} \quad (6.71)$$

In light of (6.66)–(6.69), the above can be written in terms of only positive modes as

$$\mathbf{J}_n^{\theta^i}(\mathbf{r}) = x_{0n}^{t\theta^i} f_n(t) \hat{\mathbf{t}}(\mathbf{r}) + 2 \sum_{\alpha=1}^{\infty} \left[x_{\alpha n}^{t\theta^i} f_n(t) \cos(\alpha\phi) \hat{\mathbf{t}}(\mathbf{r}) + j x_{\alpha n}^{\phi\theta^i} f_n(t) \sin(\alpha\phi) \hat{\phi}(\mathbf{r}) \right] \quad (6.72)$$

and

$$\mathbf{J}_n^{\phi^i}(\mathbf{r}) = x_{0n}^{t\phi^i} f_n(t) \hat{\mathbf{t}}(\mathbf{r}) + 2 \sum_{\alpha=1}^{\infty} \left[j x_{\alpha n}^{t\phi^i} f_n(t) \sin(\alpha\phi) \hat{\mathbf{t}}(\mathbf{r}) + x_{\alpha n}^{\phi\phi^i} f_n(t) \cos(\alpha\phi) \hat{\phi}(\mathbf{r}) \right] \quad (6.73)$$

Therefore, a numerical implementation of the EFIE for a BOR only needs to perform a loop over modes $\alpha \geq 0$.

6.3.3 Scattered Field

The radiated far electric field due to the current of (6.4) is computed via (2.101) and is

$$\mathbf{E}^{\theta^s, \phi^s}(\mathbf{r}) = -j\omega\mu \frac{e^{-jk r}}{4\pi r} (\hat{\theta}^s, \hat{\phi}^s) \cdot \sum_{n=1}^N \int_{t_m}^{2\pi} \int_0^{\theta^s} \mathbf{J}_n^{\theta^i, \phi^i}(\mathbf{r}) e^{jk \mathbf{r}^s \cdot \mathbf{r}'} \rho d\phi dt \quad (6.74)$$

6.3.3.1 Plane Wave Scattering

Following (6.40), we can express the exponential in (6.74) as

$$e^{jk \mathbf{r}^s \cdot \mathbf{r}'} = e^{jk z \cos \theta^s} e^{jk \sin \theta^s \rho \cos(\phi - \phi^s)} \quad (6.75)$$

Applying the appropriate dot products, the $\hat{\theta}^s$ -polarized scattered field $E_{\theta\theta}^s(\mathbf{r})$ from $\mathbf{J}_n^{\theta^i}(\mathbf{r})$ for modes $\alpha > 0$ is

$$\begin{aligned} E_{\theta\theta}^s(\mathbf{r}) = & B \sum_{p=1}^{M_p} T_p \Delta_p e^{jk z_p \cos \theta^s} \left[x_{\alpha n}^{t\theta^i} \int_0^{2\pi} e^{jk \rho_p \sin \theta^s \cos \phi} \cos(\alpha\phi + \alpha\phi^s) \right. \\ & \cdot \left(\cos \theta^s \sin \gamma_m \cos \phi - \sin \theta^s \cos \gamma_m \right) d\phi \\ & - j x_{\alpha n}^{\phi\theta^i} \int_0^{2\pi} e^{jk \rho_p \sin \theta^s \cos \phi} \sin(\alpha\phi + \alpha\phi^s) \sin \phi \cos \theta^s d\phi \right] \quad (6.76) \end{aligned}$$

where we have made the substitution $\phi = \phi + \phi^s$, and

$$B = -\frac{j\omega\mu}{2\pi} \frac{e^{-jkr}}{r} \quad (6.77)$$

Let us consider the first integral in (6.76). Using the identity

$$\cos(\alpha\phi + \alpha\phi^s) = \cos(\alpha\phi)\cos(\alpha\phi^s) - \sin(\alpha\phi)\sin(\alpha\phi^s) \quad (6.78)$$

this integral becomes

$$\begin{aligned} I_1 &= \cos(\alpha\phi^s) \int_0^{2\pi} e^{jk\rho_p \sin \theta^s \cos \phi} \cos(\alpha\phi)(\cos \theta^s \sin \gamma_m \cos \phi - \sin \theta^s \cos \gamma_m) d\phi \\ &\quad - \sin(\alpha\phi^s) \int_0^{2\pi} e^{jk\rho_p \sin \theta^s \cos \phi} \sin(\alpha\phi)(\cos \theta^s \sin \gamma_m \cos \phi - \sin \theta^s \cos \gamma_m) d\phi \end{aligned} \quad (6.79)$$

The second term evaluates to zero as it is a product of orthogonal functions over the range $0 - 2\pi$. Noting that [2]

$$2\pi j^\alpha J_\alpha(z) = \int_0^{2\pi} e^{jz \cos \phi} \cos(\alpha\phi) \quad (6.80)$$

the first term is

$$I_1 = \cos(\alpha\phi^s) \pi j^\alpha \left(\cos \theta^s \sin \gamma_m j [J_{\alpha+1} - J_{\alpha-1}] - 2 \sin \theta^s \cos \gamma_m J_\alpha \right) \quad (6.81)$$

where $J_\alpha = J_\alpha(k\rho_p \sin \theta^s)$. Using the identity

$$\sin(\alpha\phi + \alpha\phi^s) = \sin(\alpha\phi)\cos(\alpha\phi^s) + \cos(\alpha\phi)\sin(\alpha\phi^s) \quad (6.82)$$

the second integral becomes

$$\begin{aligned} I_2 &= \cos(\alpha\phi^s) \cos \theta^s \int_0^{2\pi} j e^{jk\rho_p \sin \theta^s \cos \phi} \sin(\alpha\phi) \sin \phi d\phi \\ &\quad + \sin(\alpha\phi^s) \cos \theta^s \int_0^{2\pi} j e^{jk\rho_p \sin \theta^s \cos \phi} \cos(\alpha\phi) \sin \phi d\phi \end{aligned} \quad (6.83)$$

The second term is a product of orthogonal functions in the range $0 - 2\pi$ and is zero. The first term can be integrated by parts, yielding

$$I_2 = \cos(\alpha\phi^s) \cos \theta^s \pi j^\alpha \frac{2\alpha}{k\rho_p \sin \theta^s} J_\alpha(k\rho_p \sin \theta^s) \quad (6.84)$$

and again using (6.58) this becomes

$$I_2 = \cos(\alpha\phi^s) \pi j^\alpha [J_{\alpha+1} + J_{\alpha-1}] \cos \theta^s \quad (6.85)$$

Combining the results and noting that the above integrals are of the form $b_n^{t\theta^s}$ and $b_n^{\phi\theta^s}$, the scattered field $E_{\theta\theta}^s(\mathbf{r})$ summed over all modes is

$$E_{\theta\theta}^s(\mathbf{r}) = \frac{B}{2} x_{0n}^{t\theta^i} b_0^{t\theta^s} + B \sum_{\alpha=1}^{\infty} \left[x_{\alpha n}^{t\theta^i} b_{\alpha}^{t\theta^s} + x_{\alpha n}^{\phi\theta^i} b_{\alpha}^{\phi\theta^s} \right] \cos(\alpha\phi^s) \quad (6.86)$$

The other terms follow via similar calculations and are

$$E_{\phi\theta}^s(\mathbf{r}) = jB \sum_{\alpha=1}^{\infty} \left[x_{\alpha n}^{t\theta^i} b_{\alpha}^{t\phi^s} + x_{\alpha n}^{\phi\theta^i} b_{\alpha}^{\phi\phi^s} \right] \sin(\alpha\phi^s) \quad (6.87)$$

$$E_{\theta\phi}^s(\mathbf{r}) = jB \sum_{\alpha=1}^{\infty} \left[x_{\alpha n}^{t\phi^i} b_{\alpha}^{t\theta^s} + x_{\alpha n}^{\phi\phi^i} b_{\alpha}^{\phi\theta^s} \right] \sin(\alpha\phi^s) \quad (6.88)$$

$$E_{\phi\phi}^s(\mathbf{r}) = \frac{B}{2} x_{0n}^{t\phi^i} b_0^{t\phi^s} + B \sum_{\alpha=1}^{\infty} \left[x_{\alpha n}^{t\phi^i} b_{\alpha}^{t\phi^s} + x_{\alpha n}^{\phi\phi^i} b_{\alpha}^{\phi\phi^s} \right] \cos(\alpha\phi^s) \quad (6.89)$$

For monostatic calculations, the elements of the excitation vectors \mathbf{b}^{θ^i} and \mathbf{b}^{ϕ^i} only need to be computed once per right-hand side, and can be used in the induced current and scattered field calculations.

6.4 MFIE FOR A CONDUCTING BOR

Let us apply the MFIE to a conducting BOR. Computing the gradient of the Green's function yields

$$\nabla' G(\mathbf{r}, \mathbf{r}') = \nabla' \frac{e^{-jkr}}{4\pi r} = (\mathbf{r} - \mathbf{r}') \left[1 + jkr \right] \frac{e^{-jkr}}{4\pi r^3} \quad (6.90)$$

with $r = |\mathbf{r} - \mathbf{r}'| = \sqrt{(x - x')^2 - (y - y')^2 - (z - z')^2}$. Substitution of the above into (2.136) yields

$$\hat{\mathbf{n}}(\mathbf{r}) \times \mathbf{H}^i(\mathbf{r}) = \frac{\mathbf{J}(\mathbf{r})}{2} + \frac{1}{4\pi} \iint_{S-\delta S} \hat{\mathbf{n}}(\mathbf{r}) \times [(\mathbf{r} - \mathbf{r}') \times \mathbf{J}(\mathbf{r}')] \left[1 + jkr \right] \frac{e^{-jkr}}{r^3} d\mathbf{r}' \quad (6.91)$$

We will again use the representation of the surface current from (6.4). Substituting this into the above yields for mode α ,

$$\begin{aligned} \hat{\mathbf{n}}(\mathbf{r}) \times \mathbf{H}^i(\mathbf{r}) &= \frac{1}{2} \sum_{n=1}^N \left[a_{\alpha n}^t \mathbf{f}_{\alpha n}^t(\mathbf{r}) + a_{\alpha n}^\phi \mathbf{f}_{\alpha n}^\phi(\mathbf{r}) \right] + \frac{1}{4\pi} \sum_{n=1}^N \iint_{\mathbf{f}_n^{t,\phi}} \hat{\mathbf{n}}(\mathbf{r}) \times \\ &\quad \left\{ (\mathbf{r} - \mathbf{r}') \times \left[a_{\alpha n}^t \mathbf{f}_{\alpha n}^t(\mathbf{r}') + a_{\alpha n}^\phi \mathbf{f}_{\alpha n}^\phi(\mathbf{r}') \right] \right\} \left[1 + jkr \right] \frac{e^{-jkr}}{r^3} d\mathbf{r}' \end{aligned} \quad (6.92)$$

Testing the right-hand side in the above by the functions $\mathbf{f}_{\beta m}^{t,\phi}(\mathbf{r})$, we obtain

$$\mathbf{Z} = \begin{bmatrix} \mathbf{Z}^{tt} & \mathbf{Z}^{t\phi} \\ \mathbf{Z}^{\phi t} & \mathbf{Z}^{\phi\phi} \end{bmatrix} \quad (6.93)$$

where for modes α and β the sub-matrix elements are of the form

$$\begin{aligned} z_{mn}^{pq} = & \frac{1}{2} \iint_{\mathbf{f}_{\beta m}^{t,\phi}} \mathbf{f}_{\beta m}^{t,\phi}(\mathbf{r}) \cdot \mathbf{f}_{\alpha n}^{t,\phi}(\mathbf{r}) d\mathbf{r} + \frac{1}{4\pi} \iint_{\mathbf{f}_m^{t,\phi}} \iint_{\mathbf{f}_{\alpha n}^{t,\phi}} \mathbf{f}_{\beta m}^{t,\phi}(\mathbf{r}) \cdot \hat{\mathbf{n}}(\mathbf{r}) \\ & \times \left[(\mathbf{r} - \mathbf{r}') \times \mathbf{f}_{\alpha n}^{t,\phi}(\mathbf{r}') \right] \cdot \left[1 + jkr \right] \frac{e^{-jkr}}{r^3} d\mathbf{r}' d\mathbf{r} \end{aligned} \quad (6.94)$$

According to the definition of the MFIE, the first integral on the right-hand side in (6.94) is computed only where the basis and testing functions overlap. The second integral is computed only where they do not.

6.4.1 MFIE Matrix Elements

To evaluate the matrix elements we will first compute $(\mathbf{r} - \mathbf{r}') \times \mathbf{f}_{\alpha n}^{t,\phi}(\mathbf{r}')$, which requires only the vector components $\hat{\mathbf{t}}(\mathbf{r}')$ and $\hat{\phi}(\mathbf{r}')$. We first define the vectors

$$\mathbf{r} = \rho \hat{\rho} + z \hat{\mathbf{z}} \quad (6.95)$$

$$\mathbf{r}' = \rho' \cos(\phi' - \phi) \hat{\rho} + \rho' \sin(\phi' - \phi) \hat{\phi} + z' \hat{\mathbf{z}} \quad (6.96)$$

$$\hat{\mathbf{t}}(\mathbf{r}') = \sin \gamma' \left[\cos(\phi' - \phi) \hat{\rho} + \sin(\phi' - \phi) \hat{\phi} \right] + \cos \gamma' \hat{\mathbf{z}} \quad (6.97)$$

$$\hat{\phi}(\mathbf{r}') = -\sin(\phi' - \phi) \hat{\rho} + \cos(\phi' - \phi) \hat{\phi} \quad (6.98)$$

Using the above to evaluate the cross products yields

$$\begin{aligned} (\mathbf{r} - \mathbf{r}') \times \hat{\mathbf{t}}(\mathbf{r}') = & \sin(\phi' - \phi) \left[(z' - z) \sin \gamma' - \rho' \cos \gamma' \right] \hat{\rho} \\ & - \left[(\rho - \rho' \cos(\phi' - \phi)) \cos \gamma' + (z' - z) \sin \gamma' \cos(\phi' - \phi) \right] \hat{\phi} \\ & + \rho \sin \gamma' \sin(\phi' - \phi) \hat{\mathbf{z}} \end{aligned} \quad (6.99)$$

and

$$\begin{aligned} (\mathbf{r} - \mathbf{r}') \times \hat{\phi}(\mathbf{r}') = & (z' - z) \cos(\phi' - \phi) \hat{\rho} + (z' - z) \sin(\phi' - \phi) \hat{\phi} \\ & + \left[-\rho' + \rho \cos(\phi' - \phi) \right] \hat{\mathbf{z}} \end{aligned} \quad (6.100)$$

Next we must evaluate the dot products of the above with the testing functions. Using (6.15) and noting that

$$\hat{\mathbf{t}}(\mathbf{r}) \cdot \hat{\mathbf{n}}(\mathbf{r}) \times \left[(\mathbf{r} - \mathbf{r}') \times \mathbf{f}(\mathbf{r}') \right] = \hat{\phi}(\mathbf{r}) \cdot \left[(\mathbf{r} - \mathbf{r}') \times \mathbf{f}(\mathbf{r}') \right] \quad (6.101)$$

and

$$\hat{\phi}(\mathbf{r}) \cdot \hat{\mathbf{n}}(\mathbf{r}) \times [(\mathbf{r} - \mathbf{r}') \times \mathbf{f}(\mathbf{r}')] = -\hat{\mathbf{t}}(\mathbf{r}) \cdot [(\mathbf{r} - \mathbf{r}') \times \mathbf{f}(\mathbf{r}')] \quad (6.102)$$

allows us to write

$$\begin{aligned} \hat{\mathbf{t}}(\mathbf{r}) \cdot \hat{\mathbf{n}}(\mathbf{r}) \times [(\mathbf{r} - \mathbf{r}') \times \hat{\mathbf{t}}(\mathbf{r}')] &= [(\rho' - \rho) \cos \gamma' - (z' - z) \sin \gamma'] \\ &\cdot \cos(\phi' - \phi) - 2\rho \cos \gamma' \sin^2 [(\phi' - \phi)/2] \end{aligned} \quad (6.103)$$

$$\hat{\mathbf{t}}(\mathbf{r}) \cdot \hat{\mathbf{n}}(\mathbf{r}) \times [(\mathbf{r} - \mathbf{r}') \times \hat{\phi}(\mathbf{r}')] = (z' - z) \sin(\phi' - \phi) \quad (6.104)$$

$$\begin{aligned} \hat{\phi}(\mathbf{r}) \cdot \hat{\mathbf{n}}(\mathbf{r}) \times [(\mathbf{r} - \mathbf{r}') \times \hat{\mathbf{t}}(\mathbf{r}')] &= [\rho' \sin \gamma \cos \gamma' - \rho \sin \gamma' \cos \gamma \\ &- (z' - z) \sin \gamma \sin \gamma'] \sin(\phi' - \phi) \end{aligned} \quad (6.105)$$

$$\begin{aligned} \hat{\phi}(\mathbf{r}) \cdot \hat{\mathbf{n}}(\mathbf{r}) \times [(\mathbf{r} - \mathbf{r}') \times \hat{\phi}(\mathbf{r}')] &= [(\rho' - \rho) \cos \gamma - (z' - z) \sin \gamma] \\ &\cdot \cos(\phi' - \phi) + 2\rho' \cos \gamma \sin^2 [(\phi' - \phi)/2] \end{aligned} \quad (6.106)$$

Using the above, we can write each of the sub-matrix elements as

$$\begin{aligned} z_{mn}^{tt} &= \frac{1}{2} \int_{t_m} \int_0^{2\pi} \rho f_m(t) f_n(t) e^{j\phi(\alpha-\beta)} d\phi dt \\ &+ \frac{1}{4\pi} \int_{t_m} \int_{t_n} \int_0^{2\pi} \int_0^{2\pi} f_m(t) f_n(t) e^{j(\alpha\phi'-\beta\phi)} \left\{ \begin{aligned} &[(\rho' - \rho) \cos \gamma' \\ &- (z' - z) \sin \gamma'] \cos(\phi' - \phi) - 2\rho \cos \gamma' \sin^2 [(\phi' - \phi)/2] \end{aligned} \right\} \\ &\cdot \left[1 + jkr \right] \frac{e^{-jkr}}{r^3} d\phi' d\phi dt' dt \end{aligned} \quad (6.107)$$

$$\begin{aligned} z_{mn}^{t\phi} &= \frac{1}{4\pi} \int_{t_m} \int_{t_n} \int_0^{2\pi} \int_0^{2\pi} f_m(t) f_n(t) e^{j(\alpha\phi'-\beta\phi)} (z' - z) \sin(\phi' - \phi) \\ &\cdot \left[1 + jkr \right] \frac{e^{-jkr}}{r^3} d\phi' d\phi dt' dt \end{aligned} \quad (6.108)$$

$$\begin{aligned}
z_{mn}^{\phi t} = & \frac{1}{4\pi} \int_{t_m} \int_{t_n} \int_0^{2\pi} \int_0^{2\pi} f_m(t) f_n(t) e^{j(\alpha\phi' - \beta\phi)} \left[\rho' \sin \gamma \cos \gamma' \right. \\
& - \left. \rho \sin \gamma' \cos \gamma - (z' - z) \sin \gamma \sin \gamma' \right] \sin(\phi' - \phi) \\
& \cdot \left[1 + jkr \right] \frac{e^{-jkr}}{r^3} d\phi' d\phi dt' dt
\end{aligned} \tag{6.109}$$

$$\begin{aligned}
z_{mn}^{\phi\phi} = & \frac{1}{2} \int_{t_m} \int_0^{2\pi} \rho(t) f_m(t) f_n(t) e^{j\phi(\alpha-\beta)} d\phi dt \\
& + \frac{1}{4\pi} \int_{t_m} \int_{t_n} \int_0^{2\pi} \int_0^{2\pi} f_m(t) f_n(t) e^{j(\alpha\phi' - \beta\phi)} \left\{ \left[(\rho' - \rho) \cos \gamma \right. \right. \\
& - \left. \left. (z' - z) \sin \gamma \right] \cos(\phi' - \phi) + 2\rho' \cos \gamma \sin^2 [(\phi' - \phi)/2] \right\} \\
& \cdot \left[1 + jkr \right] \frac{e^{-jkr}}{r^3} d\phi' d\phi dt' dt
\end{aligned} \tag{6.110}$$

As we did for the EFIE, we use a pulse approximation to the triangle functions inside each segment, and replace $\phi' - \phi$ with ϕ' because of 2π periodicity. This again eliminates all elements where $\alpha \neq \beta$. Using (6.24), we can write the following expressions for the sub-matrix elements for mode α :

$$\begin{aligned}
z_{mn}^{tt} = & \sum_{p=1}^{M_p} \frac{\pi}{\rho_p} T_{mp} T_{np} \Delta_p \\
& + \sum_{p=1}^{M_p} \sum_{q=1}^{M_q} T_{mp} T_{nq} \left[\left[(\rho_q - \rho_p) \cos \gamma_q - (z_q - z_p) \sin \gamma_q \right] G_5 - \rho_p \cos \gamma_q G_4 \right]
\end{aligned} \tag{6.111}$$

$$z_{mn}^{t\phi} = j \sum_{p=1}^{M_p} \sum_{q=1}^{M_q} T_p T_q (z_q - z_p) G_6 \tag{6.112}$$

$$\begin{aligned}
z_{mn}^{\phi t} = & j \sum_{p=1}^{M_p} \sum_{q=1}^{M_q} T_p T_q \left[\rho_q \sin \gamma_p \cos \gamma_q - \rho_p \sin \gamma_q \cos \gamma_p \right. \\
& \left. - (z_q - z_p) \sin \gamma_p \sin \gamma_q \right] G_6
\end{aligned} \tag{6.113}$$

$$\begin{aligned} z_{mn}^{\phi\phi} &= \sum_{p=1}^{M_p} \frac{\pi}{\rho_p} T_{mp} T_{np} \Delta_p \\ &+ \sum_{p=1}^{M_p} \sum_{q=1}^{M_q} T_{mp} T_{nq} \left[[(\rho_q - \rho_p) \cos \gamma_p - (z_q - z_p) \sin \gamma_p] G_5 + \rho_q \cos \gamma_p G_4 \right] \end{aligned} \quad (6.114)$$

The integrals G_4 , G_5 and G_6 are given by

$$G_4 = 2\Delta_p \Delta_q \int_0^\pi \sin^2(\phi'/2) \cos(\alpha\phi') \left[1 + jkR_{pq} \right] \frac{e^{-jkR_{pq}}}{R_{pq}^3} d\phi' \quad (6.115)$$

$$G_5 = \Delta_p \Delta_q \int_0^\pi \cos(\phi') \cos(\alpha\phi') \left[1 + jkR_{pq} \right] \frac{e^{-jkR_{pq}}}{R_{pq}^3} d\phi' \quad (6.116)$$

$$G_6 = \Delta_p \Delta_q \int_0^\pi \sin(\phi') \sin(\alpha\phi') \left[1 + jkR_{pq} \right] \frac{e^{-jkR_{pq}}}{R_{pq}^3} d\phi' \quad (6.117)$$

where R_{pq} is given by (6.33). These integrals can be evaluated via a one-dimensional numerical quadrature.

Inspecting (6.107)–(6.110) we observe the following relationship between positive and negative modes in the MFIE matrix:

$$\begin{bmatrix} \mathbf{Z}^{tt} & \mathbf{Z}^{t\phi} \\ \mathbf{Z}^{\phi t} & \mathbf{Z}^{\phi\phi} \end{bmatrix}_{-\alpha} = \begin{bmatrix} \mathbf{Z}^{tt} & -\mathbf{Z}^{t\phi} \\ -\mathbf{Z}^{\phi t} & \mathbf{Z}^{\phi\phi} \end{bmatrix}_\alpha \quad (6.118)$$

The relationship in (6.118) is the same as was observed for the EFIE matrix.

6.4.2 Excitation

Applying the testing functions $\mathbf{f}_{\alpha m}^{t,\phi}(\mathbf{r})$ to the left hand side of 6.92 yields a column vector of length $2N$ of the form

$$\mathbf{b} = \begin{bmatrix} \mathbf{b}^t \\ \mathbf{b}^\phi \end{bmatrix} \quad (6.119)$$

The individual excitation vector elements are given by

$$b_m^{t,\phi} = \int_{t_m}^{2\pi} \int_0^\pi \mathbf{f}_{\alpha m}^{t,\phi}(\mathbf{r}) \cdot [\hat{\mathbf{n}}(\mathbf{r}) \times \mathbf{H}^i(\mathbf{r})] \rho d\phi dt \quad (6.120)$$

Using the pulse approximation of the triangle functions, the above can be written as

$$b_m^{t,\phi} = \sum_{p=1}^{M_p} T_p \Delta_p \int_0^{2\pi} e^{-j\alpha\phi} (\hat{\mathbf{t}}, \hat{\phi}) \cdot [\hat{\mathbf{n}}(\mathbf{r}) \times \mathbf{H}^i(\mathbf{r})] d\phi \quad (6.121)$$

where $\mathbf{H}^i(\mathbf{r})$ is an arbitrary incident magnetic field. In general, the above integral must be evaluated numerically, however for incident plane waves it can be evaluated analytically.

6.4.2.1 Plane Wave Excitation

To obtain the complete scattering matrix we must consider waves with $\hat{\theta}$ and $\hat{\phi}$ polarized electric fields. The corresponding magnetic fields are

$$\mathbf{H}_\theta^i(\mathbf{r}) = -\frac{1}{\eta} \hat{\mathbf{r}}^i \times \mathbf{E}_\theta^i(\mathbf{r}) = -\frac{E^i}{\eta} \hat{\mathbf{r}}^i \times \hat{\theta} = -\frac{E^i}{\eta} \hat{\phi} \quad (6.122)$$

and

$$\mathbf{H}_\phi^i(\mathbf{r}) = -\frac{1}{\eta} \hat{\mathbf{r}}^i \times \mathbf{E}_\phi^i(\mathbf{r}) = -\frac{E^i}{\eta} \hat{\mathbf{r}}^i \times \hat{\phi} = \frac{E^i}{\eta} \hat{\theta} \quad (6.123)$$

Since $\hat{\mathbf{n}}(\mathbf{r}) \times \mathbf{H}^i(\mathbf{r})$ represents a vector tangent to the surface, the excitation vectors \mathbf{b}_{θ^i} and \mathbf{b}_{ϕ^i} can be written in terms of the excitation vectors of the EFIE case:

$$\mathbf{b}_{\theta^i} = -\frac{1}{\eta} \begin{bmatrix} \mathbf{b}^{t\phi^i} \\ \mathbf{b}^{\phi\phi^i} \end{bmatrix} \quad (6.124)$$

and

$$\mathbf{b}_{\phi^i} = \frac{1}{\eta} \begin{bmatrix} \mathbf{b}^{t\theta^i} \\ \mathbf{b}^{\phi\theta^i} \end{bmatrix} \quad (6.125)$$

When applying the CFIE, the components of the EFIE excitation vector elements can be used to obtain those for the MFIE, so only the EFIE terms need to be computed for each incident direction. Following the discussion in Section 6.3.2.1, only a loop over modes $\alpha/g\epsilon 0$ is required for the MFIE as well.

6.4.3 Scattered Field

The scattered field for the MFIE is obtained in an identical manner to that of the EFIE in Section 6.3.3.

6.5 NOTES ON SOFTWARE IMPLEMENTATION

6.5.1 Parallelization

Because of the relatively modest matrix size of the MOM-BOR formulation, it is generally convenient to allocate matrix storage space for each of the compute

threads in a multiprocessor configuration. An efficient parallelization scheme will then divide calculations on a per-mode basis for each frequency, with each thread performing a matrix fill, factorization and calculation of the fields for all excitations and scattering angles. The fields from each mode are then added to a master field array. Because the calculation of one mode does not depend on the others, there is minimal inter-process communication between threads except for assigning of mode and frequency and reporting of results. This scheme is equally well suited for shared memory and distributed memory (MPI) systems.

6.5.2 Convergence

While it is simple to set a maximum mode number and allow the code to calculate the fields for each mode, it is likely that the calculation may converge to an accurate solution at a lower mode number. One way to determine this convergence is to set a threshold on the amplitude of the radiated/scattered field for each angle. The software tracks the magnitude for each angle, and when this threshold is reached, calculations are terminated at that angle for all subsequent modes. If all angles converge before the highest mode number is reached, the sum over modes is stopped and the code then moves on to the next frequency. This method is especially useful in monostatic RCS computations due to the many right-hand side operations that can be skipped, increasing the efficiency of the code for larger problems.

6.6 EXAMPLES

In this section we use the MOM-BOR technique to compute the radar cross section of several conducting test objects, such as the sphere and benchmark targets measured by the Electromagnetic Code Consortium (EMCC) [3].

6.6.1 Galaxy

The numerical results in this section are computed using the Tripoint Industries, Inc. code *Galaxy*, an MOM-BOR radar cross section code implementing the procedures described in this chapter. This code is written in the C programming language and uses double precision complex for computing and storing the MOM matrix. *Galaxy* is part of Tripoint Industries' *lucernhammer* suite of radar cross section codes.

6.6.2 Conducting Sphere

The conducting sphere is an excellent test object as its scattering behavior is known analytically by Mie theory and comprises specular reflection as well as creeping waves. Assuming an \hat{x} -oriented electric field incident along the \hat{z} axis, the scattered far electric field is [4]

$$\mathbf{E}^s(\theta^s, \phi^s) = \frac{e^{jkr}}{kr} \left[\cos \phi^s S_1(\theta^s) \hat{\theta} - \sin \phi^s S_2(\theta^s) \hat{\phi} \right] \quad (6.126)$$

where

$$S_1(\theta) = \sum_{n=1}^{\infty} (-j)^{n+1} \left[A_n \frac{P_n^1(\cos \theta)}{\sin \theta} + j B_n \frac{d}{d\theta} P_n^1(\cos \theta) \right] \quad (6.127)$$

and

$$S_2(\theta) = \sum_{n=1}^{\infty} (-j)^{n+1} \left[A_n \frac{d}{d\theta} P_n^1(\cos \theta) + j B_n \frac{P_n^1(\cos \theta)}{\sin \theta} \right] \quad (6.128)$$

where $P_n^1(\cos \theta)$ is the associated Legendre polynomial of degree 1 and order n . The coefficients A_n and B_n are given by

$$A_n = -(-j)^n \frac{2n+1}{n(n+1)} \frac{j_n(ka)}{h_n^{(1)}(ka)} \quad (6.129)$$

and

$$B_n = -(-j)^{n+1} \frac{2n+1}{n(n+1)} \frac{[ka j_n(ka)]'}{[ka h_n^{(1)}(ka)]'} \quad (6.130)$$

where $j_n(ka)$ and $h_n^{(1)}(ka)$ are spherical Bessel and Hankel functions of the first kind of order n , and the primes indicate differentiation with respect to ka [4]. In practice, the sums in (6.127) and (6.128) are truncated after a finite number of modes. The recurrence relationships in [2] can be used to compute higher-order associated Legendre polynomials and derivatives of Bessel functions.

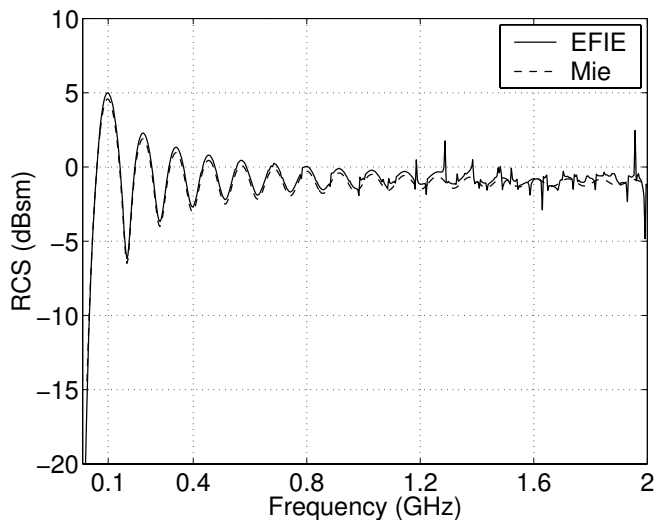
6.6.2.1 Monostatic RCS Versus Frequency

We first compute the monostatic RCS versus frequency of a 1-meter sphere for frequencies up to 2 GHz. For the Mie series of (6.126) we truncate the computation after 50 modes. Figures 6.2a and 6.2b compare the RCS from the Mie series to the EFIE and MFIE, respectively. The comparisons are good at lower frequencies, though at higher ones discrepancies begin to appear. These correspond to internal resonances of the discretized BOR, similar to what is observed for the cube in Figure 2.8. Figure 6.3a depicts the results obtained using the CFIE ($\alpha = 0.5$), and the resonance problems have been eliminated.

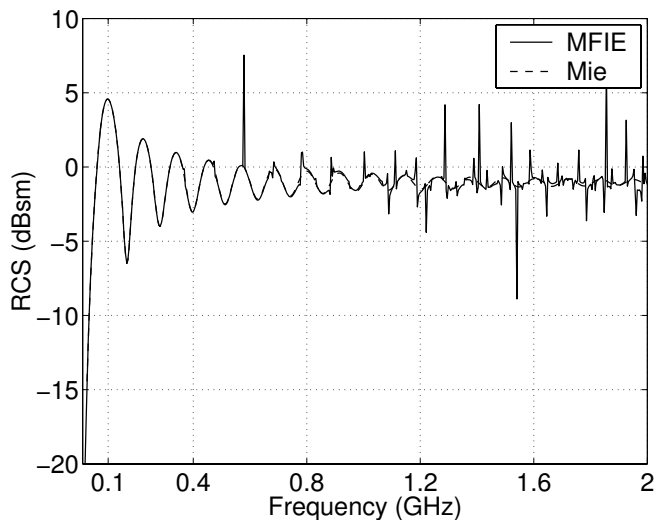
We next compare the *range profiles* of the CFIE and Mie series. The range profile is a time-domain representation of the electromagnetic signature and can be used to localize the scattering centers of a target in the down-range dimension. Given an array of complex-valued scattered electric fields \mathbf{S} over a range of evenly spaced frequencies f_{min} to f_{max} , the range profile \mathbf{R} can be computed as

$$\mathbf{R} = \text{IFFT}(\mathbf{S}) \quad (6.131)$$

which is also known as *pulse compression* or *matched filtering* [5]. This method increases the effective range resolution by linearly modulating the frequency of the



(a) EFIE vs. Mie: RCS vs. Frequency



(b) MFIE vs. Mie: RCS vs. Frequency

Figure 6.2: 1-meter sphere: EFIE and MFIE.

transmitted waveform, and is a key technique in radar signal processing. The range resolution of a pulse-compressed waveform is

$$\Delta_R = \frac{c}{2B} \quad (6.132)$$

where B is the modulated bandwidth. A window function is typically applied to the array before performing the FFT to reduce the sidelobes in the range domain. A commonly used window function is the *Hamming window*, which comprises the N -element array \mathbf{w} with elements given by

$$w_{k+1} = 0.54 - 0.46 \cos \left[\frac{2\pi k}{N-1} \right] \quad k = 0, \dots, N-1 \quad (6.133)$$

The windowing operation decreases the sidelobes at the expense of decreased range resolution.

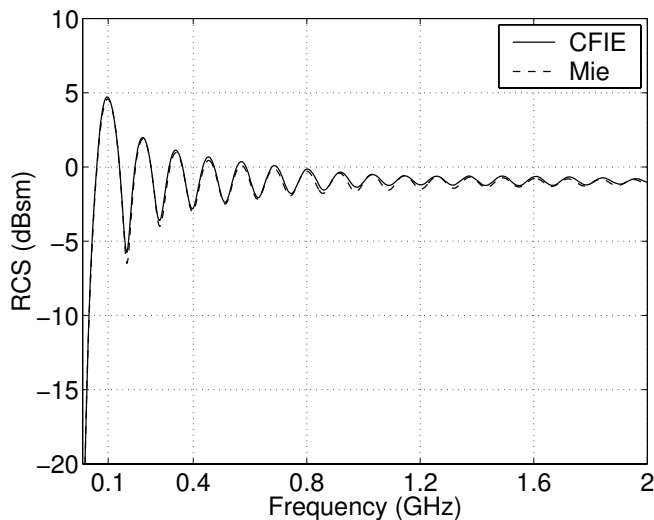
Figure 6.3b depicts the monostatic range profiles of the CFIE and Mie series computed from 32 evenly spaced data points from 1 to 2 GHz. The 1 GHz of bandwidth results in a range resolution of approximately 15 cm. A Hamming window is applied to the data, which decreases the range resolution by approximately 50 percent. Positive range in this figure represents the distance away from the transmitter. Immediately seen at -0.5m is the very bright specular reflection of the sphere. Slightly further down-range is the well-known creeping wave response, caused by electromagnetic energy that originates from the shadow boundary and travels around the shadowed side of the sphere, eventually coming back toward the transmitter. The comparison is excellent.

6.6.2.2 Bistatic RCS

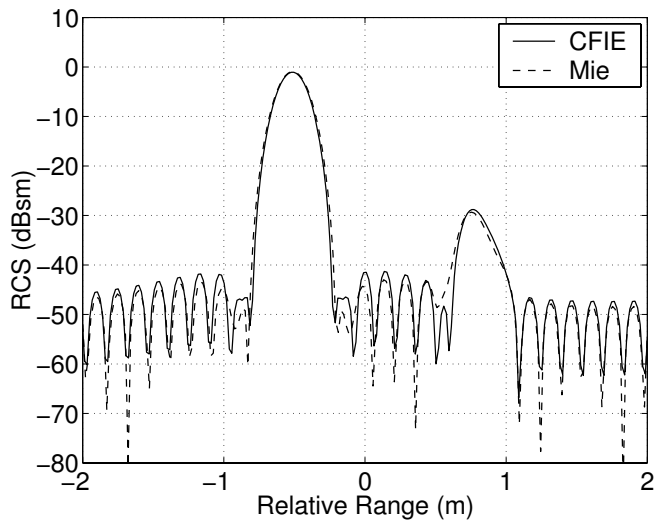
The bistatic cross section of the sphere is another commonly used benchmark. We retain the same simulation parameters used in Section 6.6.2.1, but fix the frequency at 2 GHz. The results from the CFIE are compared to the Mie series in Figures 6.4a and 6.4b for vertical and horizontal polarizations, respectively. The comparison is again very good.

6.6.3 EMCC Benchmark Targets

We next compute the RCS of several EMCC benchmark radar targets described and measured in [6]. The objects considered are the ogive, double ogive, cone-sphere and cone-sphere with gap, and are illustrated in Figure 6.5. The test articles used for the measurements were fabricated from aluminum using a numerically-controlled mill. In the plots that follow, the measurement data are shifted slightly in angle to better align them with the computed results. The comparisons are made at 9.0 GHz, and *Galaxy* uses the CFIE ($\alpha = 0.5$).

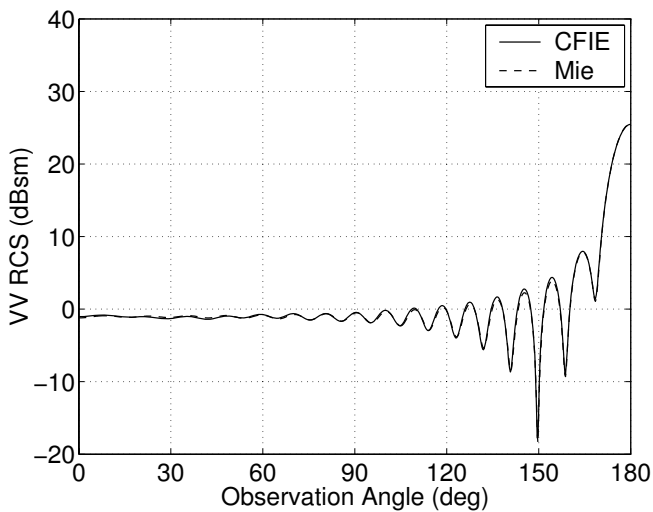


(a) CFIE vs. Mie: RCS vs. Frequency

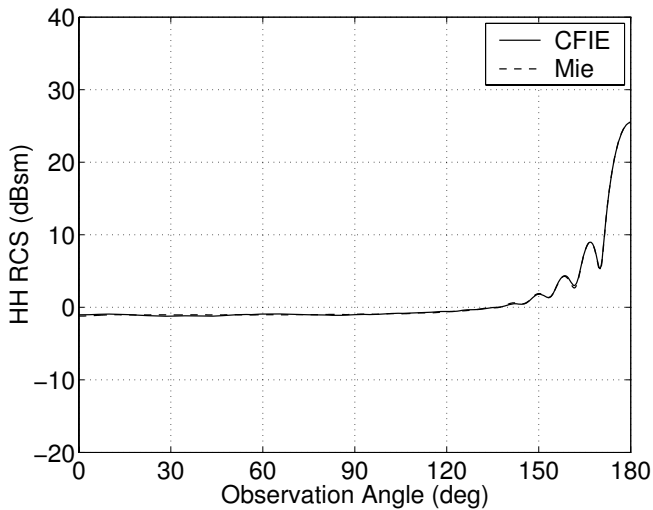


(b) Range Profile

Figure 6.3: 1-meter sphere: CFIE.



(a) Vertical Polarization



(b) Horizontal Polarization

Figure 6.4: 1-meter sphere: bistatic RCS.

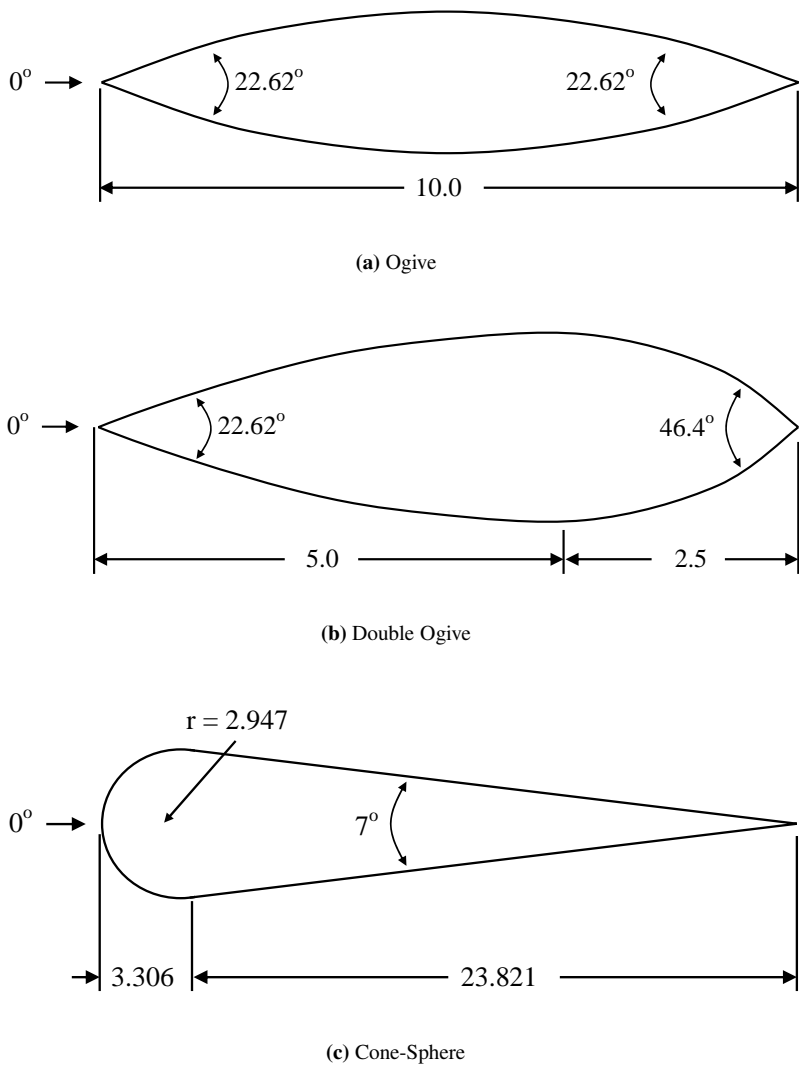


Figure 6.5: EMCC BOR targets.

6.6.3.1 EMCC Ogive

The 10-inch EMCC ogive of Figure 6.5a can be expressed for $0 < \phi < 2\pi$ as [6]

$$f(x) = \left[\sqrt{1 - \left(\frac{x}{5.0} \right)^2 \sin^2(22.62^\circ)} - \cos(22.62^\circ) \right] \quad (6.134)$$

$$y(x) = \frac{f(x) \cos \phi}{1 - \cos(22.62^\circ)} \quad (6.135)$$

$$z(x) = \frac{f(x) \sin \phi}{1 - \cos(22.62^\circ)} \quad (6.136)$$

for $-5 < x < 5$ inches. The numerical results are compared to the EMCC measurements in Figures 6.6a and 6.6b for vertical and horizontal polarizations, respectively. The agreement is excellent, even at aspect angles near tip-on where the cross section is very low.

6.6.3.2 EMCC Double Ogive

The 7.5-inch EMCC double ogive of Figure 6.5b can be expressed for $0 < \phi < 2\pi$ as [6]

$$g(x) = \left[\sqrt{1 - \left(\frac{x}{2.5} \right)^2 \sin^2(46.6^\circ)} - \cos(46.6^\circ) \right] \quad (6.137)$$

$$y(x) = \frac{g(x) \cos \phi}{1 - \cos(46.4^\circ)} \quad (6.138)$$

$$z(x) = \frac{g(x) \sin \phi}{1 - \cos(46.4^\circ)} \quad (6.139)$$

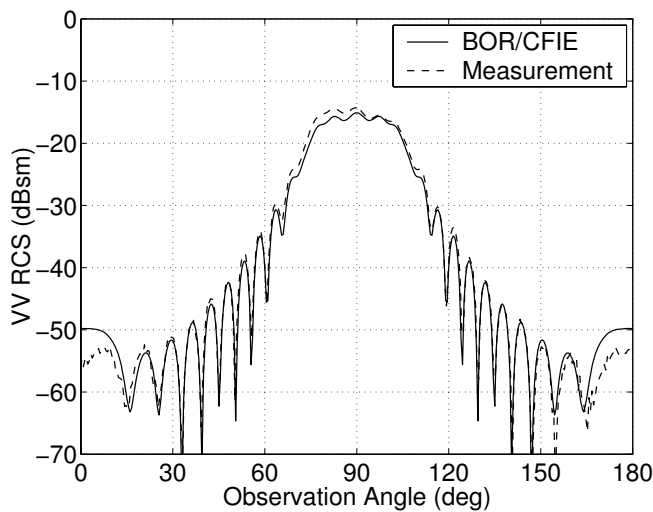
for $-2.5 < x < 0$ inches, and

$$f(x) = \left[\sqrt{1 - \left(\frac{x}{5.0} \right)^2 \sin^2(22.62^\circ)} - \cos(22.62^\circ) \right] \quad (6.140)$$

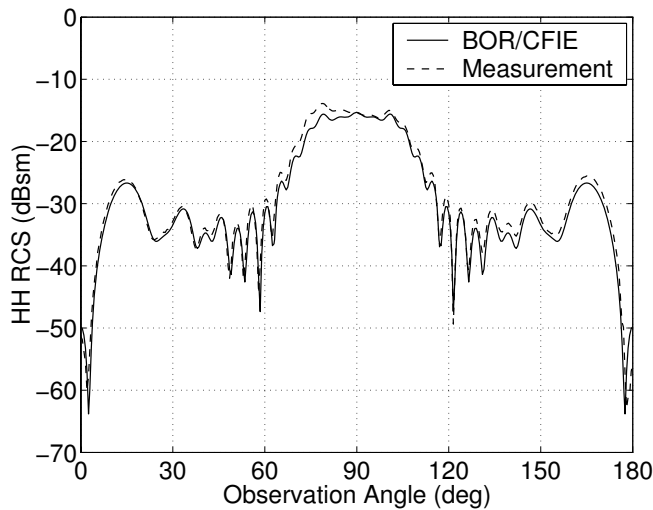
$$y(x) = \frac{f(x) \cos \phi}{1 - \cos(22.62^\circ)} \quad (6.141)$$

$$z(x) = \frac{f(x) \sin \phi}{1 - \cos(22.62^\circ)} \quad (6.142)$$

for $0 < x < 5$ inches. The numerical results are compared to the EMCC measurements in Figures 6.7a and 6.7b for vertical and horizontal polarizations, respectively. The agreement is again excellent.

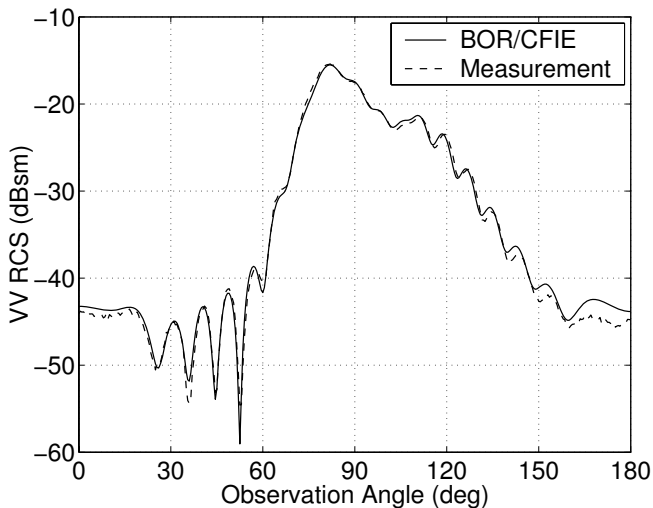


(a) Vertical Polarization

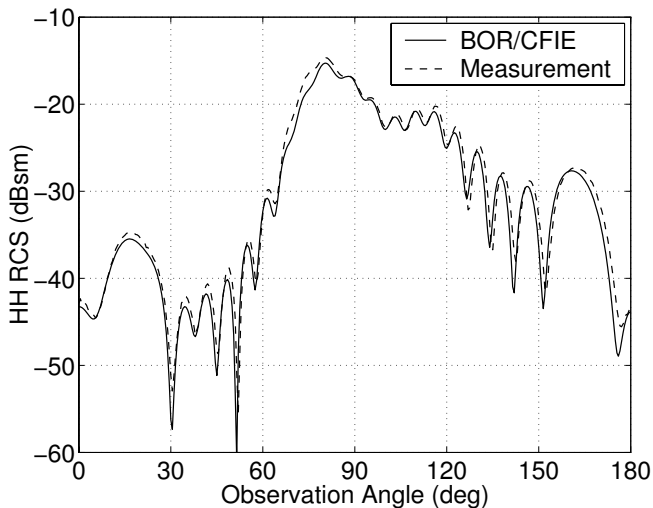


(b) Horizontal Polarization

Figure 6.6: EMCC ogive: BOR versus measurement at 9.0 GHz.



(a) Vertical Polarization



(b) Horizontal Polarization

Figure 6.7: EMCC double ogive: BOR versus measurement at 9.0 GHz.

6.6.3.3 EMCC Cone-Sphere

The 27-inch EMCC cone-sphere of Figure 6.5c can be expressed for $0 < \phi < 2\pi$ as [6]

$$y(x) = 0.87145(x + 23.821) \cos \phi \quad (6.143)$$

$$z(x) = 0.87145(x + 23.821) \sin \phi \quad (6.144)$$

for $-23.821 < x < 0$ inches, and

$$y(x) = 2.947 \sqrt{1 - \left(\frac{x - 0.359}{2.947} \right)^2} \cos \phi \quad (6.145)$$

$$z(x) = 2.947 \sqrt{1 - \left(\frac{x - 0.359}{2.947} \right)^2} \sin \phi \quad (6.146)$$

for $0 < x < 3.306$ inches. The numerical results are compared to the EMCC measurements in Figures 6.8a and 6.8b for vertical and horizontal polarizations, respectively. The agreement is quite good at all aspect angles.

6.6.3.4 EMCC Cone-Sphere with Gap

The EMCC cone-sphere with gap is identical to the cone-sphere of Section 6.6.3.3, except that a square groove $1/4$ inch deep is cut into the target near the cone-sphere junction point. The gap can be expressed for $0 < \phi < 2\pi$ as [6]

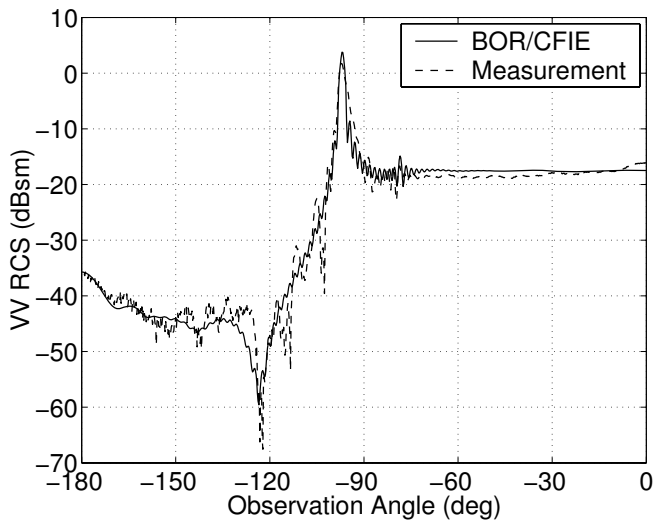
$$y(x) = 2.697 \cos \phi \quad (6.147)$$

$$z(x) = 2.697 \sin \phi \quad (6.148)$$

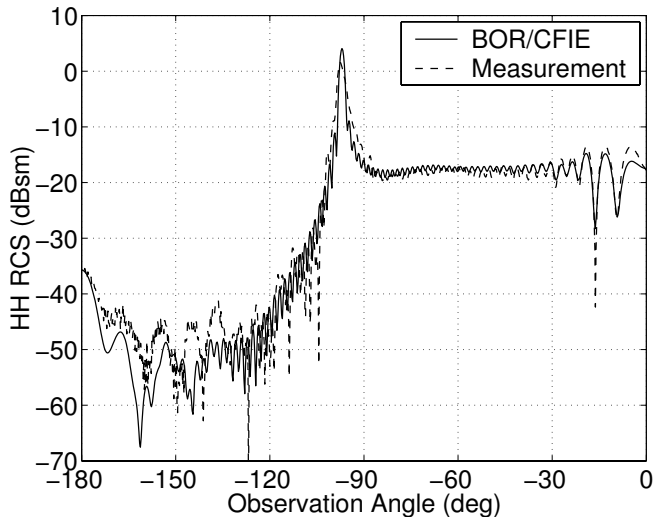
for $0 < x < 0.25$ inches. At 9.0 GHz, the dimensions of the gap are approximately $\lambda/5$. The numerical results are compared to the EMCC measurements in Figures 6.9a and 6.9b for vertical and horizontal polarizations, respectively. The agreement is excellent. The presence of the gap has a significant effect on the backscattered field, especially for horizontal polarization.

6.6.4 Biconic Reentry Vehicle

We next compute the monostatic RCS of a biconic reentry vehicle (RV) whose dimensions are outlined in Figure 6.10a. The RV has a blunt nose as well as a deeply recessed rear cavity that are expected to be significant sources of backscatter. The three-dimensional shape of the RV is illustrated at forward and rear aspects in Figures 6.10b and 6.10c, respectively. The length of the RV boundary curve is approximately 3.2 m.

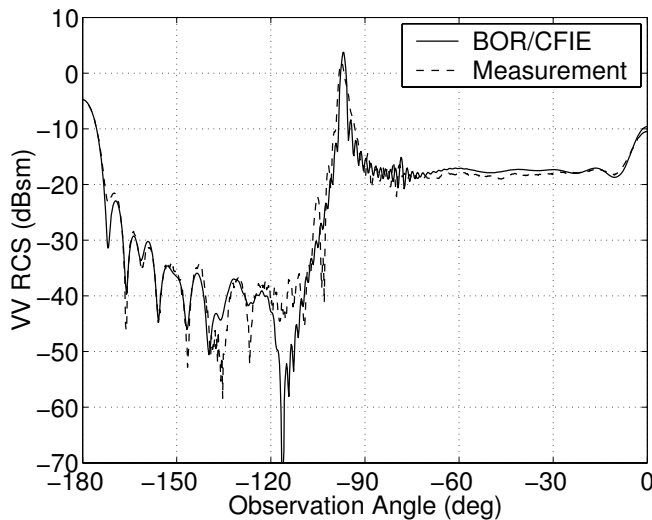


(a) Vertical Polarization

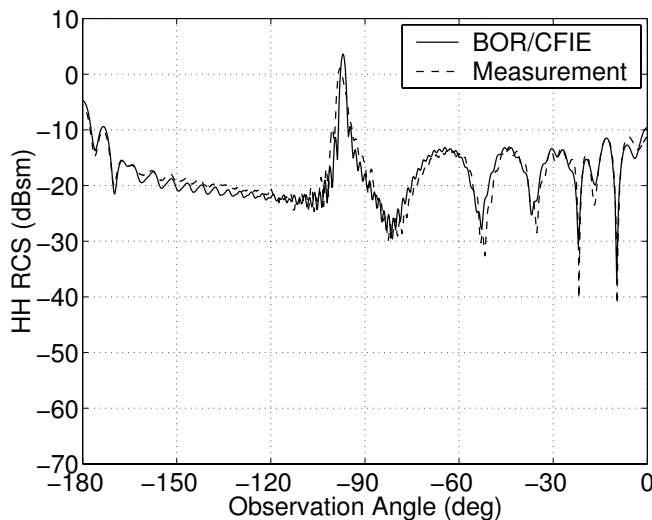


(b) Horizontal Polarization

Figure 6.8: EMCC cone-sphere: BOR versus measurement at 9.0 GHz.

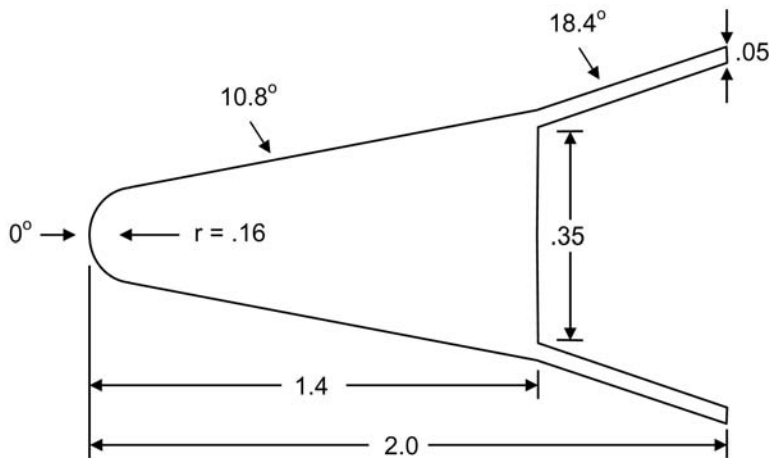


(a) Vertical Polarization

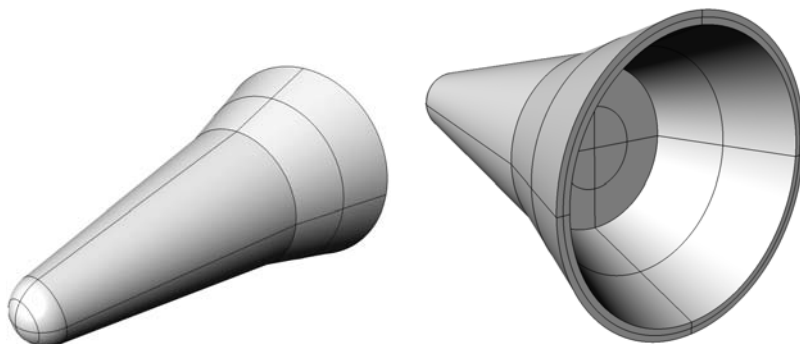


(b) Horizontal Polarization

Figure 6.9: EMCC cone-sphere with gap: BOR versus measurement at 9.0 GHz.



(a) Biconic Reentry Vehicle Dimensions



(b) Front View

(c) Rear View

Figure 6.10: Biconic reentry vehicle.

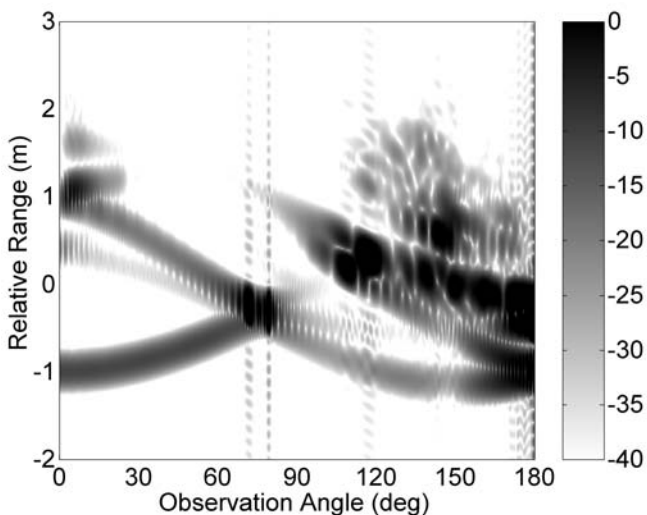
In studying a target's backscattering behavior, it is often useful to consider its range profile over a wide range of incident angles. This allows for the isolation of target scattering features over a wide range of viewing geometries. Therefore, let us compute the backscattered field of the RV for frequencies ranging from 5 to 6 GHz (C-Band), for observation angles from 0 to 180 degrees. At 6 GHz, the perimeter of the RV is approximately 64 wavelengths in length. Our numerical model uses 944 boundary segments, yielding approximately 15 segments per wavelength.

We compute the range profile for each incident angle and generate a two-dimensional figure known as a *range-aspect-intensity* (RAI) plot. Plots for vertical and horizontal polarizations are shown in Figures 6.11a and 6.11b, respectively. The choice of bandwidth results in a down-range resolution of approximately 15 centimeters, and a Hamming window is used to reduce the sidelobes. Clearly visible in the forward scattering angles are the large responses of the RV nose as well as its base edge. In rear aspects, the multi-bounce inside the cavity clearly dominates, giving rise to significant down-range returns.

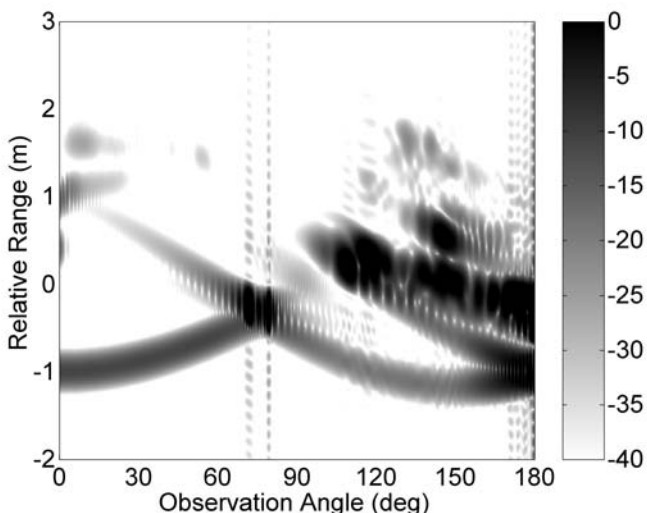
We can further isolate the scattering centers of the target by generating a two-dimensional *range-Doppler* (ISAR) image. Such an image is generated by computing the FFT of each range bin over a small range of angles. If we assume that the Doppler frequency of each bin remains constant across the integration interval, then we can achieve a cross-range resolution given by [7]

$$\Delta_{cr} = \frac{\lambda_o}{2\Delta_\theta} \quad (6.149)$$

where λ_o is the center wavelength and Δ_θ is the angular extent of the integration interval. If we integrate over approximately 6 degrees, the cross-range resolution will be approximately 0.26 meter at 5.5 GHz. Range-Doppler images centered at 3 and 138 degrees are shown in Figures 6.12a and 6.12b, respectively, for vertical polarization. A Hamming window is used in the cross-range dimension to reduce sidelobes. Superimposed onto each image is the two-dimensional outline of the RV, allowing us to register the scattering features. In the forward aspect, the scattering centers at the nose and stationary phase-points of the base edge (sometimes referred to as slipping scatterers) are clearly visible. The joint between the two frustums is also visible, as well as the faint double-diffraction term located slightly beyond the target. At rear aspects, the delayed returns again dominate the image. These scattering centers appear to originate from off-body locations, obscuring the true shape of the target. Such features are often detrimental to automated target recognition (ATR) algorithms that use length as a discrimination feature. Real-world reentry vehicles would have hoses, gas bottles, wiring and assorted electronics inside the rear cavity that would create even greater multiple-bounce behavior. As a result, radar observations of such a target could result in an apparent wideband length several times that of the actual object.

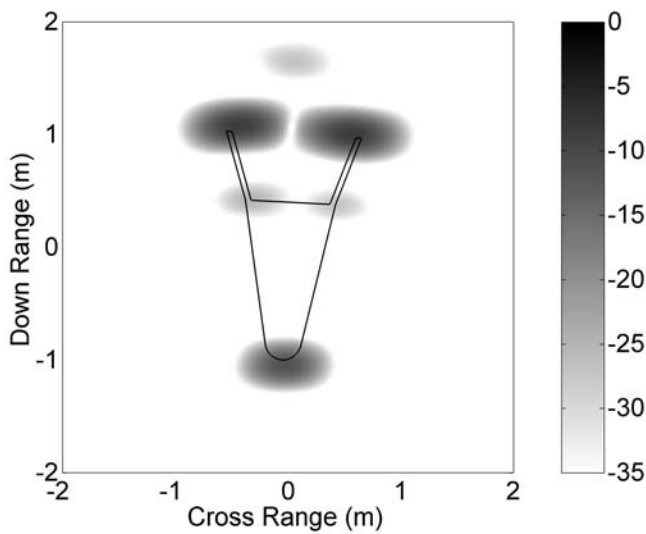


(a) Vertical Polarization

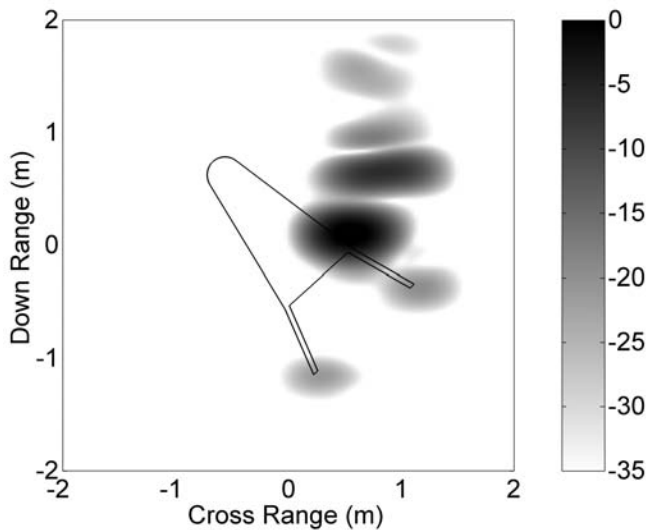


(b) Horizontal Polarization

Figure 6.11: Biconic reentry vehicle: C-band range profiles (dBsm).



(a) Center Aspect = 3 Degrees



(b) Center Aspect = 138 Degrees

Figure 6.12: Biconic reentry vehicle: C-band range-Doppler images (dBsm).

Table 6.1: Summary of Examples

Object	Segments	N	α_{max}	RAM
Sphere	181	89	30	0.120
Ogive	450	224	30	0.766
Double Ogive	450	224	30	0.766
Cone-Sphere	756	377	40	2.17
Cone-Sphere with Gap	754	376	40	2.16
Biconic RV	944	471	70	3.39

6.6.5 Summary of Examples

The run metrics for each case are summarized in Table 6.1. Shown are the number of boundary segments, number of unknowns, maximum mode, and memory (in MB) required for the MOM-BOR matrix.

REFERENCES

- [1] R. Mautz and R. Harrington, “H-field, e-field and combined solutions for bodies of revolution,” Tech. Rep. Report RADC-TR-77-109, Rome Air Development Center, Griffiss AFB, NY, March 1977.
- [2] M. Abramowitz and I. Stegun, *Handbook of Mathematical Functions*. National Bureau of Standards, 1966.
- [3] K. Faison, “The electromagnetics code consortium,” *IEEE Antennas Propagat. Magazine*, vol. 30, 19–23, February 1990.
- [4] G. T. Ruck, ed., *Radar Cross Section Handbook*. Plenum Press, 1970.
- [5] B. R. Mahafza, *Introduction to Radar Analysis*. CRC Press, 1998.
- [6] A. C. Woo, H. T. G. Wang, M. J. Schuh, and M. L. Sanders, “Benchmark radar targets for the validation of computational electromagnetics programs,” *IEEE Antennas Propagat. Magazine*, vol. 35, 84–89, February 1993.
- [7] A. Ausherman, A. Kozma, J. Waker, H. M. Jones, and E. C. Poggio, “Developments in radar imaging,” *IEEE Trans. Aerospace Electron. Syst.*, vol. 20, 363–400, July 1984.

Chapter 7

Three-Dimensional Problems

In this chapter we use the method of moments to analyze radiation and scattering by three-dimensional surfaces of arbitrary shape. Problems of this kind appear in many areas of practical interest such as electromagnetic interference (EMI), electronic packaging, radar cross section, and antenna design. This area has received significant attention in the literature in the last thirty years, and many different methods of treating three-dimensional surfaces have been considered. Until recently, most three-dimensional problems were limited to a relatively small electrical size, given the limitations of commonly available computers and system memory. Solving larger problems typically required access to supercomputer-class equipment, which was not readily available to most people. With the advances in processing speed, memory and operating systems in the last 10 years, larger problems can now be solved on modest desktop computers. This has opened up areas of study that were not attempted or even considered before. The development of the fast multipole method has further increased the tractability of the larger problems, and we discuss its application to MOM problems in detail in Chapter 8.

7.1 REPRESENTATION OF THREE-DIMENSIONAL SURFACES

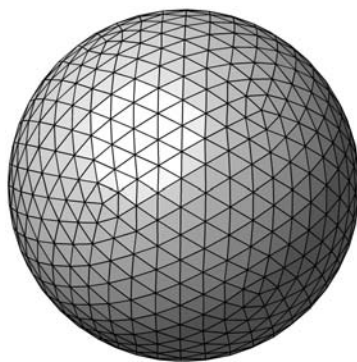
We first need to consider how to numerically represent three-dimensional objects in the computer. The basic approach is to first develop a detailed model of the object using computer aided design (CAD) software. Modern modeling programs such as Rhinoceros 3D [1] represent free-form objects using a mathematically-exact description such as non uniform rational B-splines (NURBS) [2]. This approach preserves necessary information such as the surface normal and radii of curvature at every point. NURBS is a part of many industry-wide standard CAD file formats and modeling engines such as IGES, STEP, ACIS and Parasolid. Once the curved surface model has been developed, it must be discretized or reduced to a set of geometric primitives that can be processed further. The most commonly used primitive for this purpose is the planar triangle, which has the ability to conform to the surface curvature of virtually any realistic shape [3]. Highly efficient integration rules have been developed for the triangle (Chapter 9) as well as analytic solutions to

9	
-1.0 1.0 0.0	
0.0 1.0 0.0	
1.0 1.0 0.0	
-1.0 0.0 0.0	
0.0 0.0 0.0	
1.0 0.0 0.0	
-1.0 -1.0 0.0	
0.0 -1.0 0.0	
1.0 -1.0 0.0	
8	
4 2 1	
4 5 2	
5 3 2	
5 6 3	
7 5 4	
7 8 5	
8 6 5	
8 9 6	

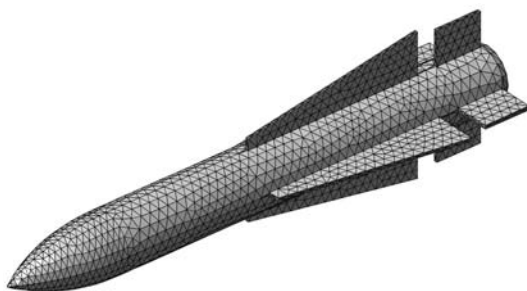
Figure 7.1: Example connectivity list.

potential integrals over triangular domains [4, 5, 6, 7], making them an attractive choice for electromagnetic modeling. Triangles are also the de facto standard in computer graphics, and most CAD programs have the ability to generate meshes of exceptionally high quality.

A common way to describe a surface using triangles is the finite element connectivity file [8], an example of which is illustrated in Figure 7.1. This file comprises a *node list* containing the cartesian positions of all triangle nodes, and a *facet list* that assembles individual triangles by referencing three vertexes from the node list. The example in Figure 7.1 contains 9 nodes and 8 facets. Many different formats for storing these data have been developed, such as the popular 3D Studio (.3ds), Stereolithography (.stl), and Lightwave (.obj) files. Because these are used by computer graphics and animation tools, they often contain information concerning camera placement, lighting and textures in addition to the geometry. For our purposes, we will use the format described in Table 7.1, which we call a *facet file*. Figures 7.2a, 7.2b and 7.2c depict a sphere, a missile and a main battle tank represented entirely by triangular facets. Because of the flexibility of this format, very complex shapes such as ground and air vehicles can be represented with great precision by a facet model, provided that enough triangles are used and sufficient care is given to their construction.



(a) Sphere



(b) Simple Missile



(c) Main Battle Tank

Figure 7.2: Example three-dimensional facet models.

7.2 SURFACE CURRENTS ON A TRIANGLE

We next investigate an efficient means of representing the currents on a surface described by planar triangles. As before, we expand the current $\mathbf{J}(\mathbf{r})$ via a sum of weighted basis functions:

$$\mathbf{J}(\mathbf{r}) = \sum_{n=1}^N a_n \mathbf{f}_n(\mathbf{r}) \quad (7.1)$$

Undoubtedly the most successful basis function used in this role in the past 25 years is the Rao-Wilton-Glisson (RWG) triangular basis function [9]. This function is defined as

$$\mathbf{f}_n(\mathbf{r}) = \frac{L_n}{2A_n^+} \rho_n^+(\mathbf{r}) \quad \mathbf{r} \text{ in } T_n^+ \quad (7.2)$$

$$\mathbf{f}_n(\mathbf{r}) = \frac{L_n}{2A_n^-} \rho_n^-(\mathbf{r}) \quad \mathbf{r} \text{ in } T_n^- \quad (7.3)$$

$$\mathbf{f}_n(\mathbf{r}) = 0 \quad \text{otherwise} \quad (7.4)$$

where T_n^+ and T_n^- are the triangles that share edge n , and L_n is the length of the edge. On T_n^+ , the vector $\rho_n^+(\mathbf{r})$ points *toward* the vertex \mathbf{v}^+ opposite the edge and is

$$\rho_n^+(\mathbf{r}) = \mathbf{v}^+ - \mathbf{r} \quad \mathbf{r} \text{ in } T_n^+ \quad (7.5)$$

and on the T_n^- , $\rho_n^-(\mathbf{r})$ points *away* from the opposite vertex \mathbf{v}^- and is

$$\rho_n^-(\mathbf{r}) = \mathbf{r} - \mathbf{v}^- \quad \mathbf{r} \text{ in } T_n^- \quad (7.6)$$

The RWG basis function is illustrated in Figure 7.3. By their definition, RWG functions are assigned only to *interior* edges in the model, which are edges shared by two adjacent triangles. Boundary edges are not assigned basis functions. The RWG function has no component normal to any edge other than the one it is assigned

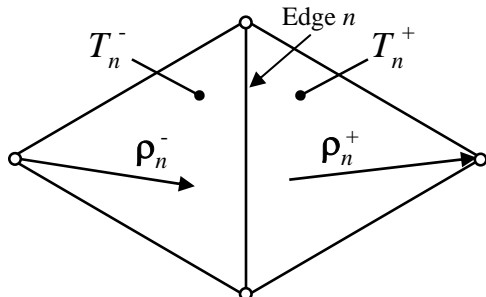


Figure 7.3: RWG basis function.

to, and the component of function normal to this edge is unity. Taking the surface divergence of $\mathbf{f}_n(\mathbf{r})$ yields

$$\nabla_s \cdot \mathbf{f}_n(\mathbf{r}) = -\frac{L_n}{A_n^+} \quad \mathbf{r} \text{ in } T_n^+ \quad (7.7)$$

$$\nabla_s \cdot \mathbf{f}_n(\mathbf{r}) = \frac{L_n}{A_n^-} \quad \mathbf{r} \text{ in } T_n^- \quad (7.8)$$

$$\nabla_s \cdot \mathbf{f}_n(\mathbf{r}) = 0 \quad \text{otherwise} \quad (7.9)$$

Since the divergence of the current is proportional to the surface charge density through the equation of continuity, we see from (7.7)–(7.9) that the total charge density associated with adjacent triangle pairs is zero. As there is no accumulation of charges on an edge, the RWG function is said to be *divergence conforming*. *Curl conforming* as well as higher-order basis functions are also used in computational electromagnetic problems, and they are described further in [10].

7.2.1 Edge Finding Algorithm

Once we have the facet model, we need an algorithm for identifying and registering all unique edges. To illustrate an edge finding algorithm, we use the geometry outlined in Figure 7.1, which comprises a simple flat plate in the xy plane. The numbering of nodes and facets in this model is illustrated in Figures 7.4a, and 7.4b, respectively. Our first task is to identify the connections between each node and the facet(s) it is part of. This will allow us to identify unique edges and determine

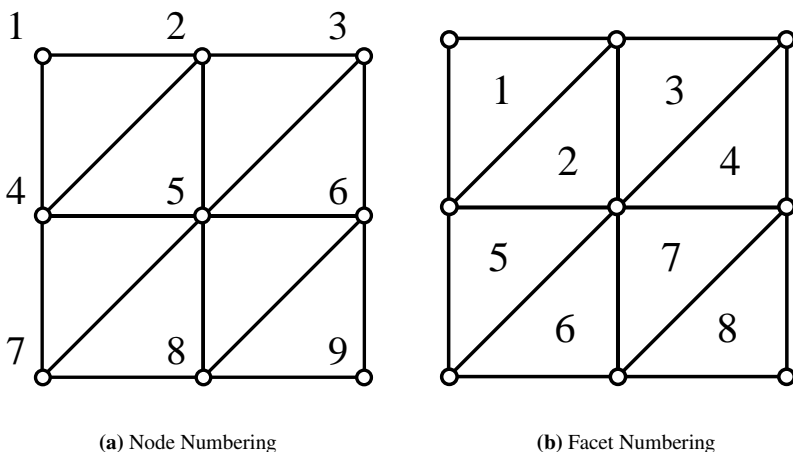


Figure 7.4: Simple flat plate geometry.

Table 7.1: Node and Facet Connectivity Lists

Node #	Connected Nodes	Connected Facets
1	2 4	1
2	4 5 3	1 2 3
3	5 6	3 4
4	5 7	1 2 5
5	6 7 8	2 3 4 5 6 7
6	8 9	4 7 8
7	8	5 6
8	9	6 7 8
9	-	8

what facets share each edge. To do this, we create two lists for each node, a *node connectivity list* and a *facet connectivity list*. The node connectivity list contains all unique connections between a node and other nodes, and the facet connectivity list contains the facets a node is referenced by. We next loop over each individual triangle and identify the nodes that make up the triangle and sort them into ascending order. We then add the index of the current facet to the facet connectivity list of each node. For the node of lowest index, we add to its list the two higher node indexes if they are not already in the list. For the second node, the index of the third node is added to its list if not already present, and nothing is done for the third node. After this operation is completed, the node and facet connectivity lists are as shown in Table 7.1. Note that the node connectivity list contains no redundant links; this results in an empty list for node 9 since it is already referenced in the list for nodes 6 and 8.

At this point, the connectivity lists contain all the information regarding unique edges in the model. The remaining task is to go through the connectivity list for each node and create an edge for each entry. The facets common to the endpoints of each edge are recorded. If the edge belongs to only one triangle, it is a boundary edge and is not assigned a basis function. Edges touching two triangles are interior edges, and they will be assigned basis functions. We will not consider geometries with edges touching three or more triangles. Additional information regarding each edge can be stored by the programmer at this step, such as its length, the facets it touches, and its endpoints. The vertex opposite the edge on each triangle might also be stored so that basis function vectors can be quickly computed later.

7.2.1.1 Shared Nodes

The algorithm of Section 7.2.1 requires that facets connected to each other use the same node indexes, otherwise no edges will be found. Some three-dimensional modeling tools will generate separate nodes for each triangle, resulting in a loss of logical connectivity between triangles at an edge. The modeler should exert care that these redundant nodes are collapsed into single elements in their geometry file. Most

packages have a function to *join* or *weld* meshes that will remove coincident nodes; these functions should be exercised before saving the geometry to a disk file or other media.

7.3 EFIE FOR THREE-DIMENSIONAL CONDUCTING SURFACES

Let us now solve the EFIE for a conducting surface of arbitrary shape. Substituting the current of (7.1) into (2.120) yields

$$-\frac{j}{\omega\mu}\hat{\mathbf{t}}(\mathbf{r}) \cdot \mathbf{E}^i(\mathbf{r}) = \iint_S (1 + \frac{1}{k^2}\nabla\nabla \cdot) \sum_{n=1}^N a_n \mathbf{f}_n(\mathbf{r}') \frac{e^{-jk r}}{4\pi r} d\mathbf{r}' \quad (7.10)$$

which is one equation in N unknowns. Applying N testing functions and redistributing the vector differential operators following Section 4.5.1, we obtain the matrix \mathbf{Z} with elements given by

$$z_{mn} = \iint_{\mathbf{f}_m} \iint_{\mathbf{f}_n} \left(\mathbf{f}_m(\mathbf{r}) \cdot \mathbf{f}_n(\mathbf{r}') - \frac{1}{k^2} [\nabla \cdot \mathbf{f}_m(\mathbf{r})] [\nabla' \cdot \mathbf{f}_n(\mathbf{r}')] \right) \frac{e^{-jk r}}{4\pi r} d\mathbf{r}' d\mathbf{r} \quad (7.11)$$

and excitation vector elements b_m given by

$$b_m = -\frac{j}{\omega\mu} \iint_{\mathbf{f}_m} \mathbf{f}_m(\mathbf{r}) \cdot \mathbf{E}^i(\mathbf{r}) d\mathbf{r} \quad (7.12)$$

The source and testing integrals in (7.11) are performed over two RWG functions, which span two triangles each. As each triangle supports at most three RWG functions, integration over a source and observation triangle contributes to a maximum of nine matrix elements. Therefore, it is more efficient to perform outer loops over source and testing triangles and inner loops over basis functions, and add the results to the appropriate matrix locations.

7.3.1 EFIE Matrix Elements

Using (7.2), (7.3), (7.7) and (7.8) in (7.11) we write

$$I = \frac{L_m L_n}{A_m A_n} \iint_{T_m} \iint_{T_n} \left[\frac{1}{4} \boldsymbol{\rho}_m^\pm(\mathbf{r}) \cdot \boldsymbol{\rho}_n^\pm(\mathbf{r}') \pm \frac{1}{k^2} \right] \frac{e^{-jk r}}{4\pi r} d\mathbf{r}' d\mathbf{r} \quad (7.13)$$

where we have restricted the integral to a single source and testing triangle for simplicity. The variable sign depends on whether each triangle is T^+ or T^- for the respective basis function. Applying an M -point numerical quadrature rule over the source and testing triangles yields

$$I \approx \frac{L_m L_n}{4\pi} \sum_{p=1}^M \sum_{q=1}^M w_p w_q \left[\frac{1}{4} \boldsymbol{\rho}_m^\pm(\mathbf{r}_p) \cdot \boldsymbol{\rho}_n^\pm(\mathbf{r}_q) \pm \frac{1}{k^2} \right] \frac{e^{-jk R_{pq}}}{R_{pq}} \quad (7.14)$$

where the quadrature weights w_p and w_q are normalized with respect to triangle area, and

$$R_{pq} = \sqrt{(x_p - x_q)^2 + (y_p - y_q)^2 + (z_p - z_q)^2} \quad (7.15)$$

When the source and testing triangles are separated by a sufficient distance, (7.14) can be implemented as written. When they are relatively close together or overlapping, the integration must be treated carefully to obtain accurate results.

7.3.2 Singular Matrix Element Evaluation

One of the more challenging aspects of computing (7.14) is when the source and testing triangles are close together or overlapping. One of the methods we used in previous chapters was to replace the Green's function by a small-argument approximation and compute the resulting integral analytically. This method yielded reasonable results because the small size of the integration domain was small and inside the valid range of the approximation. On the other hand, triangular subdomains may be large enough to invalidate such an approximation and we must apply a different method. The one most often used is the following rewrite of the Green's function:

$$\frac{e^{-jkr}}{r} = \left[\frac{e^{-jkr}}{r} - \frac{1}{r} \right] + \frac{1}{r} \quad (7.16)$$

which is referred to as a *singularity extraction*. The first term on the right-hand side can be used in the numerical quadrature of (7.14) as it is well behaved for all values of r with the limit

$$\lim_{r \rightarrow 0} \left[\frac{e^{-jkr}}{r} - \frac{1}{r} \right] = -jk \quad (7.17)$$

Inserting the second term on the right-hand side of (7.16) into (7.13) yields integrals of the form

$$I_1 = \iint_T \rho_m^\pm(\mathbf{r}) \cdot \iint_{T'} \rho_n^\pm(\mathbf{r}') \frac{1}{r} d\mathbf{r}' d\mathbf{r} \quad (7.18)$$

and

$$I_2 = \iint_T \iint_{T'} \frac{1}{r} d\mathbf{r}' d\mathbf{r} \quad (7.19)$$

where T and T' are close together or overlapping. We will now discuss several methods for computing these integrals.

7.3.2.1 Analytic Integration

When T and T' overlap, we can compute the inner and outer integrations analytically. We first convert the basis function vector $\rho_{m,n}(\mathbf{r})$ to simplex coordinates (Section 9.2.1), yielding

$$\rho_{m,n}(\mathbf{r}) = (1 - \lambda_1 - \lambda_2)\mathbf{v}_1 + \lambda_1\mathbf{v}_2 + \lambda_2\mathbf{v}_3 - \mathbf{v}_{m,n} \quad (7.20)$$

where $\mathbf{v}_1, \mathbf{v}_2$ and \mathbf{v}_3 are the triangle vertices and $\mathbf{v}_{m,n}$ is the vertex opposite edge m, n on the triangle. The above represents the basis function $\rho^-(\mathbf{r})$ on T^- , and the results that follow may be used by changing the sign of the vector appropriately. Substituting the above into (7.18) yields

$$I_1 = \iint_T \iint_{T'} \left[(1 - \lambda_1 - \lambda_2) \mathbf{v}_1 + \lambda_1 \mathbf{v}_2 + \lambda_2 \mathbf{v}_3 - \mathbf{v}_m \right] \\ \cdot \left[(1 - \lambda'_1 - \lambda'_2) \mathbf{v}_1 + \lambda'_1 \mathbf{v}_2 + \lambda'_2 \mathbf{v}_3 - \mathbf{v}_n \right] \frac{1}{r} d\lambda'_1 d\lambda'_2 d\lambda_1 d\lambda_2 \quad (7.21)$$

Multiplying together all the above terms and performing some lengthy term collection yields the integrand

$$\left[\lambda_1 \lambda'_1 (\mathbf{r}_3 \cdot \mathbf{v}_3 - 2\mathbf{v}_3 \cdot \mathbf{v}_1 + \mathbf{v}_1 \cdot \mathbf{v}_1) + \lambda_1 \lambda'_2 (\mathbf{v}_3 \cdot \mathbf{v}_2 - \mathbf{v}_3 \cdot \mathbf{v}_1 - \mathbf{v}_2 \cdot \mathbf{v}_1 + \mathbf{v}_1 \cdot \mathbf{v}_1) \right. \\ + \lambda_1 (\mathbf{v}_3 \cdot \mathbf{v}_1 - \mathbf{v}_3 \cdot \mathbf{v}_n + \mathbf{v}_1 \cdot \mathbf{v}_n - \mathbf{v}_1 \cdot \mathbf{v}_1) + \lambda_2 \lambda'_1 (\mathbf{v}_3 \cdot \mathbf{v}_2 - \mathbf{v}_2 \cdot \mathbf{v}_1 - \mathbf{v}_3 \cdot \mathbf{v}_1 + \mathbf{v}_1 \cdot \mathbf{v}_1) \\ + \lambda_2 \lambda'_2 (\mathbf{v}_2 \cdot \mathbf{v}_2 - 2\mathbf{v}_2 \cdot \mathbf{v}_1 + \mathbf{v}_1 \cdot \mathbf{v}_1) + \lambda_2 (\mathbf{v}_2 \cdot \mathbf{v}_1 - \mathbf{v}_2 \cdot \mathbf{v}_n + \mathbf{v}_1 \cdot \mathbf{v}_n - \mathbf{v}_1 \cdot \mathbf{v}_1) \\ + \lambda'_1 (\mathbf{v}_1 \cdot \mathbf{v}_m + \mathbf{v}_3 \cdot \mathbf{v}_1 - \mathbf{r}_3 \cdot \mathbf{v}_m - \mathbf{v}_1 \cdot \mathbf{v}_1) + \lambda'_2 (\mathbf{v}_2 \cdot \mathbf{v}_1 - \mathbf{v}_2 \cdot \mathbf{v}_m + \mathbf{v}_1 \cdot \mathbf{v}_m - \mathbf{v}_1 \cdot \mathbf{v}_1) \\ \left. - \mathbf{v}_1 \cdot \mathbf{v}_n + \mathbf{v}_m \cdot \mathbf{v}_n - \mathbf{v}_1 \cdot \mathbf{v}_m + \mathbf{v}_1 \cdot \mathbf{v}_1 \right] \frac{1}{r} \quad (7.22)$$

resulting in a set of integrals of the form

$$\iint_T \iint_{T'} \lambda_i \lambda'_j \frac{1}{|\mathbf{r} - \mathbf{r}'|} d\lambda'_1 d\lambda'_2 d\lambda_1 d\lambda_2 \quad (7.23)$$

The various permutations of this integral have been evaluated analytically by Eibert and Hansen in [7] and are

$$\frac{1}{4A^2} \iint_T \iint_{T'} \lambda_1 \lambda'_1 \frac{1}{|\mathbf{r} - \mathbf{r}'|} dT dT' = \frac{\log \left[\frac{b + \sqrt{a}\sqrt{c}}{b - c + \sqrt{c}\sqrt{a - 2b + c}} \right]}{40\sqrt{c}} \\ + \frac{\log \left[\frac{-b + c + \sqrt{c}\sqrt{a - 2b + c}}{-b + \sqrt{a}\sqrt{c}} \right]}{40\sqrt{c}} + \frac{\sqrt{a}\sqrt{a - 2b + c} - \sqrt{c}\sqrt{a - 2b + c}}{120(a - 2b + c)^{\frac{3}{2}}} \\ + \frac{(2a - 5b + 3c) \log \left[\frac{(a - b + \sqrt{a}\sqrt{a - 2b + c})(c - b + \sqrt{c}\sqrt{a - 2b + c})}{(b - a + \sqrt{a}\sqrt{a - 2b + c})(b - c + \sqrt{c}\sqrt{a - 2b + c})} \right]}{120(a - 2b + c)^{\frac{3}{2}}} \\ + \frac{-\sqrt{a}\sqrt{c} + \sqrt{a}\sqrt{a - 2b + c}}{120a^{\frac{3}{2}}} + \frac{(2a + b) \log \left[\frac{(b + \sqrt{a}\sqrt{c})(a - b + \sqrt{a}\sqrt{a - 2b + c})}{(-b + \sqrt{a}\sqrt{c})(-a + b + \sqrt{a}\sqrt{a - 2b + c})} \right]}{120a^{\frac{3}{2}}} \quad (7.24)$$

$$\begin{aligned}
& \frac{1}{4A^2} \iint_T \iint_{T'} \lambda_1 \lambda'_2 \frac{1}{|\mathbf{r} - \mathbf{r}'|} dT dT' = \frac{\log \left[\frac{b + \sqrt{a} \sqrt{c}}{b - c + \sqrt{c} \sqrt{a - 2b + c}} \right]}{120\sqrt{c}} \\
& + \frac{\log \left[\frac{a - b + \sqrt{a} \sqrt{a - 2b + c}}{-b + \sqrt{a} \sqrt{c}} \right]}{120\sqrt{a}} + \frac{-\sqrt{a} \sqrt{a - 2b + c} + \sqrt{c} \sqrt{a - 2b + c}}{120(a - 2b + c)^{\frac{3}{2}}} \\
& + \frac{(2a - 3b + c) \log \left[\frac{a - b + \sqrt{a} \sqrt{a - 2b + c}}{b - c + \sqrt{c} \sqrt{a - 2b + c}} \right]}{120(a - 2b + c)^{\frac{3}{2}}} + \frac{\sqrt{a} \sqrt{a - 2b + c} - \sqrt{c} \sqrt{a - 2b + c}}{120(a - 2b + c)^{\frac{3}{2}}} \\
& + \frac{(a - 3b + 2c) \log \left[\frac{-b + c + \sqrt{c} \sqrt{a - 2b + c}}{-a + b + \sqrt{a} \sqrt{a - 2b + c}} \right]}{120(a - 2b + c)^{\frac{3}{2}}} + \frac{-3\sqrt{a} \sqrt{c} + 3\sqrt{c} \sqrt{a - 2b + c}}{120c^{\frac{3}{2}}} \\
& + \frac{(3b + 2c) \log \left[\frac{-b + c + \sqrt{c} \sqrt{a - 2b + c}}{-b + \sqrt{a} \sqrt{c}} \right]}{120c^{\frac{3}{2}}} + \frac{-3\sqrt{a} \sqrt{c} + 3\sqrt{a} \sqrt{a - 2b + c}}{120a^{\frac{3}{2}}} \\
& + \frac{(2a + 3b) \log \left[\frac{b + \sqrt{a} \sqrt{c}}{-a + b + \sqrt{a} \sqrt{a - 2b + c}} \right]}{120a^{\frac{3}{2}}} \tag{7.25}
\end{aligned}$$

$$\begin{aligned}
& \frac{1}{4A^2} \iint_T \iint_{T'} \lambda'_1 \frac{1}{|\mathbf{r} - \mathbf{r}'|} dT dT' = \frac{-\log \left[\frac{-b + \sqrt{a} \sqrt{c}}{a - b + \sqrt{a} \sqrt{a - 2b + c}} \right]}{24\sqrt{a}} \\
& + \frac{\log \left[\frac{b + \sqrt{a} \sqrt{c}}{b - c + \sqrt{c} \sqrt{a - 2b + c}} \right]}{24\sqrt{c}} + \frac{-\sqrt{a} \sqrt{c} + \sqrt{a} \sqrt{a - 2b + c}}{24a^{\frac{3}{2}}} \\
& + \frac{(a + b) \log \left[\frac{b + \sqrt{a} \sqrt{c}}{-a + b + \sqrt{a} \sqrt{a - 2b + c}} \right]}{24a^{\frac{3}{2}}} + \frac{\log \left(\frac{a - b + \sqrt{a} \sqrt{a - 2b + c}}{b - c + \sqrt{c} \sqrt{a - 2b + c}} \right)}{24\sqrt{a - 2b + c}} \\
& - \frac{\log \left[\frac{b + \sqrt{a} \sqrt{c}}{-b + c + \sqrt{c} \sqrt{a - 2b + c}} \right]}{12\sqrt{c}} + \frac{\sqrt{a} \sqrt{a - 2b + c} - \sqrt{c} \sqrt{a - 2b + c}}{24(a - 2b + c)^{\frac{3}{2}}} \\
& + \frac{(a - 3b + 2c) \log \left[\frac{-b + c + \sqrt{c} \sqrt{a - 2b + c}}{-a + b + \sqrt{a} \sqrt{a - 2b + c}} \right]}{24(a - 2b + c)^{\frac{3}{2}}} \tag{7.26}
\end{aligned}$$

where

$$\begin{aligned}
a &= (\mathbf{v}_1 - \mathbf{v}_3) \cdot (\mathbf{v}_1 - \mathbf{v}_3) \\
b &= (\mathbf{v}_1 - \mathbf{v}_3) \cdot (\mathbf{v}_1 - \mathbf{v}_2) \\
c &= (\mathbf{v}_1 - \mathbf{v}_2) \cdot (\mathbf{v}_1 - \mathbf{v}_2) \tag{7.27}
\end{aligned}$$

All integrals involving terms in the integrand of (7.22) can be obtained via (7.24), (7.25) and (7.26) by permuting the vertex indices appropriately.

Converting (7.19) to simplex coordinates yields an integral of the form

$$\frac{1}{4A^2} \iint_T \iint_{T'} \frac{1}{r} d\lambda'_1 d\lambda'_2 d\lambda_1 d\lambda_2 \tag{7.28}$$

that when evaluated analytically yields [7]

$$\begin{aligned} \frac{1}{4A^2} \iint_T \iint_{T'} \frac{1}{|\mathbf{r} - \mathbf{r}'|} dT dT' &= \frac{\log \left[\frac{(a-b+\sqrt{a}\sqrt{a-2b+c})(b+\sqrt{a}\sqrt{c})}{(-b+\sqrt{a}\sqrt{c})(-a+b+\sqrt{a}\sqrt{a-2b+c})} \right]}{6\sqrt{a}} \\ &+ \frac{\log \left[\frac{(b+\sqrt{a}\sqrt{c})(-b+c+\sqrt{c}\sqrt{a-2b+c})}{(b-c+\sqrt{c}\sqrt{a-2b+c})(-b+\sqrt{a}\sqrt{c})} \right]}{6\sqrt{c}} \\ &+ \frac{\log \left[\frac{(a-b+\sqrt{a}\sqrt{a-2b+c})(-b+c+\sqrt{c}\sqrt{a-2b+c})}{(b-c+\sqrt{c}\sqrt{a-2b+c})(-a+b+\sqrt{a}\sqrt{a-2b+c})} \right]}{6\sqrt{a-2b+c}} \end{aligned} \quad (7.29)$$

where a, b and c are defined in (7.27). Note that (7.29) does not depend on any basis function so it only needs to be calculated once per triangle.

7.3.2.2 Analytic and Numerical Integration

When T and T' are close together or overlapping, we can evaluate (7.18) and (7.19) by computing the outermost integral numerically and the innermost analytically following [4]. This method can be applied to N -sided planar polygons of arbitrary shape and is summarized in terms of individual polygon edges. Therefore, let us consider the line segment C with endpoints \mathbf{r}^- and \mathbf{r}^+ located in S (the plane of the polygon) as illustrated in Figure 7.5. The projections of source and observation vectors \mathbf{r}' and \mathbf{r} onto S are ρ' and ρ , respectively. The quantities in the figure are computed as follows:

$$\rho^\pm = \mathbf{r}^\pm - \hat{\mathbf{n}}(\hat{\mathbf{n}} \cdot \mathbf{r}^\pm) \quad (7.30)$$

$$\hat{\mathbf{l}} = \frac{\rho^+ - \rho^-}{|\rho^+ - \rho^-|} \quad (7.31)$$

$$\hat{\mathbf{u}} = \hat{\mathbf{l}} \times \hat{\mathbf{n}} \quad (7.32)$$

$$l^\pm = (\rho^\pm - \rho) \cdot \hat{\mathbf{l}} \quad (7.33)$$

$$P^0 = |(\rho^\pm - \rho) \cdot \hat{\mathbf{u}}| \quad (7.34)$$

$$P^\pm = |(\rho^\pm - \rho)| = \sqrt{(P^0)^2 + (l^\pm)^2} \quad (7.35)$$

$$\hat{\mathbf{P}}^0 = \frac{(\rho^\pm - \rho) - l^\pm \hat{\mathbf{l}}}{P^0} \quad (7.36)$$

$$R^0 = \sqrt{(P^0)^2 + d^2} \quad (7.37)$$

$$R^\pm = \sqrt{(P^\pm)^2 + d^2} \quad (7.38)$$

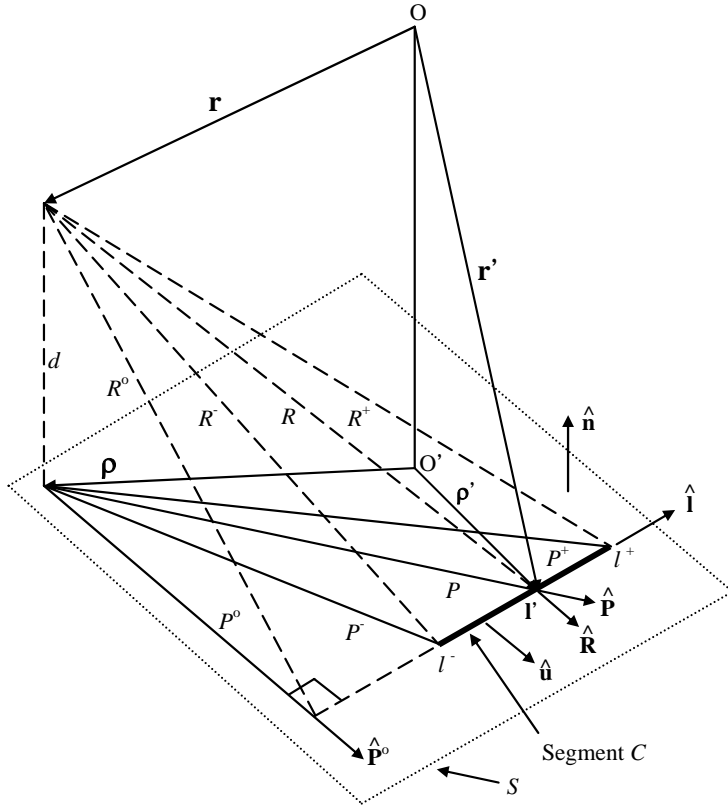


Figure 7.5: Geometric quantities for polygon segment C .

The distance d from the observation point to S is

$$d = \hat{\mathbf{n}} \cdot (\mathbf{r} - \mathbf{r}^\pm) \quad (7.39)$$

Using the above, integrals of the form

$$I_1 = \iint_{T'} \frac{\rho' - \rho}{r} d\mathbf{r}' \quad (7.40)$$

can be evaluated via the following sum over N polygon edges [4]:

$$I_1 = \frac{1}{2} \sum_{i=1}^N \hat{\mathbf{u}}_i \left[(R_i^0)^2 \log \frac{R_i^+ + l_i^+}{R_i^- + l_i^-} + l_i^+ R_i^+ - l_i^- R_i^- \right] \quad (7.41)$$

and the integral

$$I_2 = \iint_{T'} \frac{1}{r} d\mathbf{r}' \quad (7.42)$$

can be evaluated as

$$I_2 = \sum_{i=1}^N \hat{\mathbf{P}}_i^0 \cdot \hat{\mathbf{u}}_i \left[P_i^0 \log \frac{R_i^+ + l_i^+}{R_i^- + l_i^-} - |d| \left(\tan^{-1} \frac{P_i^0 l_i^+}{(R_i^0)^2 + |d|R_i^+} - \tan^{-1} \frac{P_i^0 l_i^-}{(R_i^0)^2 + |d|R_i^-} \right) \right] \quad (7.43)$$

Note that if the observation point ρ lies anywhere along an edge, the contribution from that edge to (7.41) is zero. In addition, (7.41) and (7.43) suffer from numerical problems when \mathbf{r} lies in S along the extension of an edge ($R_i^0 = 0$). In such cases one should move the observation point a very small distance away from the edge, i.e.,

$$\mathbf{r} = \mathbf{r} + \epsilon \hat{\mathbf{u}} \quad (7.44)$$

To evaluate the innermost integral of (7.18), let us write the basis function $\rho_n(\mathbf{r}')$ as

$$\rho_n(\mathbf{r}') = \rho' - \rho_n \quad (7.45)$$

where ρ_n is the projection of \mathbf{v}_n on S and we have again restricted ourselves to $\rho_n(\mathbf{r}')$ on T_n^- for simplicity. Let us now write

$$\rho' - \rho_n = (\rho' - \rho) + (\rho - \rho_n) \quad (7.46)$$

which leads to

$$\iint_{T'} \frac{\rho_n(\mathbf{r}')}{r} d\mathbf{r}' = \iint_{T'} \frac{\rho' - \rho}{r} d\mathbf{r}' + (\rho - \rho_n) \iint_{T'} \frac{1}{r} d\mathbf{r}' \quad (7.47)$$

The two integrals on the right can now be evaluated via (7.41) and (7.43), and the innermost integral of (7.19) can be computed directly via (7.43). Because this method can also be used for non overlapping triangles, it is highly recommended for all near-term integrations to obtain maximum accuracy.

7.3.2.3 Duffy Transform

The Duffy transform [11, 12, 13, 14] is a method of regularizing integrals over a triangle with a $1/r$ singularity at a vertex, allowing numerical quadrature to be employed. This technique converts the region of integration from a triangle to a rectangle following the transformation

$$\iint_T \frac{f(\mathbf{r}')}{r(\mathbf{r}')} d\mathbf{r}' = \int_0^1 \int_0^1 \frac{f(u, \gamma)}{r(u, \gamma)} |J(u, \gamma)| du d\gamma \quad (7.48)$$

where $J(u, \gamma)$ is the Jacobian. Given triangle vertices \mathbf{v}_1 , \mathbf{v}_2 , and \mathbf{v}_3 , the position vector \mathbf{r}' on T becomes

$$\mathbf{r}' = (1-u)(1-\gamma)\mathbf{v}_1 + u\mathbf{v}_2 + \gamma(1-u)\mathbf{v}_3 \quad (7.49)$$

Let us apply the transform to the integral

$$\iint_T \frac{1}{r} d\mathbf{r}' = \int_0^1 \int_0^1 \frac{|J(u, \gamma)|}{r(u, \gamma)} du d\gamma \quad (7.50)$$

where the triangle is defined by the points $\mathbf{v}_1 = (x_1, y_1)$, $\mathbf{v}_2 = (x_2, y_2)$, and $\mathbf{v}_3 = (x_3, y_3)$. The Jacobian is

$$\begin{aligned} J(u, \gamma) = & (1-u) \left[(x_2 - x_1 + \gamma[x_1 - x_3])(y_3 - y_1) \right. \\ & \left. - (y_2 - y_1 + \gamma[y_1 - y_3])(x_3 - x_1) \right] \end{aligned} \quad (7.51)$$

and fixing the observation (singular) point \mathbf{r} at (x_1, y_1) , r is

$$r(x, y) = \sqrt{(x_1 - x)^2 + (y_1 - y)^2} = \sqrt{a(u, \gamma) + b(u, \gamma)} = r(u, \gamma) \quad (7.52)$$

with

$$\begin{aligned} a(u, \gamma) = & x_1^2 + ux_1x_2 + u^2x_2^2 + 2(1-u)(ux_2 - x_1) \left[(1-\gamma)x_1 + \gamma x_3 \right] \\ & + (1-u)^2 \left[(1-\gamma)x_1 + \gamma x_3 \right]^2 \end{aligned} \quad (7.53)$$

and

$$\begin{aligned} b(u, \gamma) = & y_1^2 + uy_1y_2 + u^2y_2^2 + 2(1-u)(uy_2 - y_1) \left[(1-\gamma)y_1 + \gamma y_3 \right] \\ & + (1-u)^2 \left[(1-\gamma)y_1 + \gamma y_3 \right]^2 \end{aligned} \quad (7.54)$$

The resulting $(1-u)$ term in the numerator acts to cancel the singularity in the denominator, allowing the integral to be performed using an M -point quadrature rule for a rectangle. When the observation point is located in the interior of the triangle, it can be divided into three sub-triangles with the new vertex placed at the singular point.

This method does suffer from some disadvantages. Since it is still a purely numerical method, the compute time will be higher due to the number of numerical computations required at each quadrature point. The transformation is accurate only for triangles with reasonably good aspect ratios, with thinner triangles requiring increasing numbers of quadrature points to retain the same level of accuracy [14]. In spite of these drawbacks, the method remains attractive in cases where the function $f(\mathbf{r})$ is not integrable analytically.

7.3.2.4 Alternative Singularity Extraction

It is suggested in [14] that because the first term in (7.16) has a discontinuous derivative at $r = 0$, its integration via standard Gaussian quadrature will produce

inaccurate results. They suggest an alternative singularity extraction of the form

$$\frac{e^{-jkr}}{r} = \left[\frac{e^{-jkr}}{r} - \frac{1}{r} + \frac{k^2 r}{2} \right] + \frac{1}{r} - \frac{k^2 r}{2} \quad (7.55)$$

where the first term now has two continuous derivatives. Their results conclude that applying (7.55) results in more accurate results than (7.16) for the same number of quadrature points. It is this author's opinion that the singularity extraction of (7.16) remains accurate enough for many three-dimensional problems, and we will use it for the examples in this chapter and those in Chapter 8. It is worth noting that expressions to evaluate integrals of the form

$$\iint_T r^n d\mathbf{r}' \quad (7.56)$$

$$\iint_T r^n [\mathbf{r}' - \mathbf{q}] d\mathbf{r}' \quad (7.57)$$

$$\iint_T \nabla r^n d\mathbf{r}' \quad \mathbf{r} \notin T \quad (7.58)$$

$$\iint_T [\nabla r^n] [\mathbf{r}' \times \mathbf{q}] d\mathbf{r}' \quad \mathbf{r} \notin T \quad (7.59)$$

are summarized in the appendix of [14].

7.3.2.5 Integration Examples

Let us compute the value of (7.19) using the double integration formula of (7.29) and the single integration formula (7.43). For the latter case we apply a Gaussian quadrature rule of order P (Section 9.2.4) to compute the outermost integral. The integration domain is an equilateral triangle with sides of length 1. The results are summarized in Table 7.2. The comparison matches to two significant digits at higher quadrature orders, however the results demonstrate that for overlapping triangles (7.29) is the superior choice.

We next calculate the double integration of $1/r$ over a pair of co-planar equilateral triangles of side length 1 that share a common edge. For this task we use Gaussian quadrature to compute both inner and outer integrals, and then (7.43) to compute the innermost integral, leaving the outer integration unchanged. The results

Table 7.2: Overlapping Equilateral Triangle Double Integration

Order 1	Order 2	Order 3	Order 4	Order 5	Eqn. (7.29)
0.98767	0.85005	0.84709	0.83107	0.82830	0.82392

Table 7.3: Near Equilateral Triangle Double Integration (Co-planar)

Integration Method	Order 1	Order 2	Order 3	Order 4	Order 5
All Quadrature	0.32475	0.34364	0.34724	0.35330	0.35794
Quadrature + (7.43)	0.32922	0.34331	0.34553	0.34903	0.35009

Table 7.4: Near Equilateral Triangle Double Integration (Non Co-planar)

Integration Method	Order 1	Order 2	Order 3	Order 4	Order 5
All Quadrature	3.7357	2.1169	4.4860	1.5794	1.4878
Quadrature + (7.43)	0.86129	0.73681	0.73302	0.72283	0.72166

are summarized in Table 7.3. The comparison is fairly good, suggesting that either method may be sufficient in this case. Let us now make the internal angle between triangle faces much smaller. For this case we choose an angle of 10 degrees, the results of which are summarized in Table 7.4. The results from quadrature alone compare poorly to those using the analytic inner integration. It is obvious from this example that analytic inner integrations should be used to calculate all near matrix elements. To determine when to apply the near-integration formulas, the programmer can compare the distances between triangle centroids. A reasonable threshold might be some fraction of a wavelength, such as 0.1 to 0.2 λ .

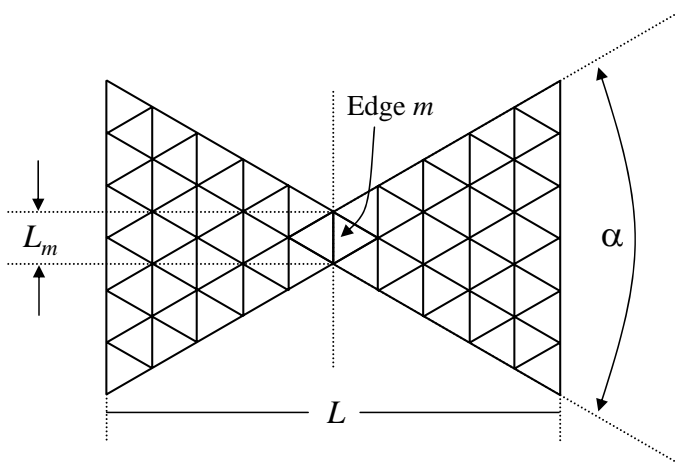
7.3.3 EFIE Excitation Vector Elements

The calculation of the EFIE excitation vector should also be performed as a loop over individual triangles. Using numerical quadrature, the contribution from each triangle and basis function can be written as

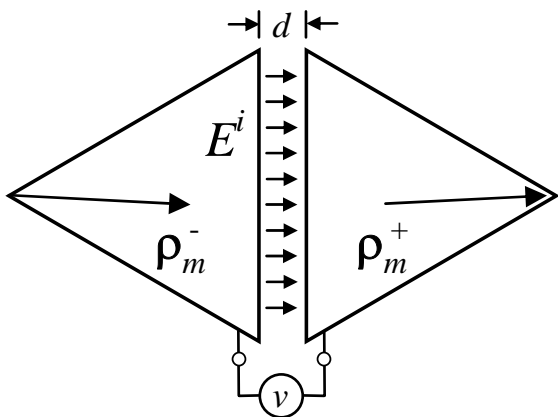
$$I_m = \frac{L_m}{2A_m} \iint_{T_m} \rho_m^\pm(\mathbf{r}) \cdot \mathbf{E}^i(\mathbf{r}) d\mathbf{r} \approx \frac{L_m}{2} \sum_{p=1}^M w_p \rho_m^\pm(\mathbf{r}_p) \cdot \mathbf{E}^i(\mathbf{r}_p) \quad (7.60)$$

7.3.3.1 Excitation of Planar Antennas

Because planar antennas are of great interest in many applications, the excitation at the antenna terminals must be modeled. In certain applications, a high fidelity feed model may be needed to obtain accurate results. While such specialized models are beyond the scope of this text, the delta-gap model remains useful in computing impedance and radiation patterns in many cases. To develop a delta-gap model, consider the planar bowtie antenna illustrated in Figure 7.6a. We partition the antenna into two halves along edge m and connect a voltage generator of amplitude V_{in} to the triangles sharing the edge, as shown in Figure 7.6b. If we assume a very small gap between the two triangles of width d , the electric field exists only in the gap and



(a) Bowtie Antenna



(b) Delta Gap at an Edge

Figure 7.6: Delta-gap feed model.

is

$$\mathbf{E}^i = \frac{V_{in}}{d} \hat{\mathbf{u}}_m \quad (7.61)$$

where $\hat{\mathbf{u}}_m$ is the vector normal to edge m in the plane. Using the above and the fact that the normal component of the RWG function is unity along the edge, the integration of (7.12) reduces to the area of the gap and evaluates to

$$b_m = -\frac{j}{\omega\mu} L_m V_{in} \quad (7.62)$$

Once we have solved the matrix system $\mathbf{Z}\mathbf{a} = \mathbf{b}$, we may wish to obtain the input impedance. As the current vector element a_m represents the linear current density flowing across edge m , the total input current I_{in} is

$$I_{in} = L_m a_m \quad (7.63)$$

and the input impedance can then be obtained as

$$Z_{in} = \frac{V_{in}}{I_{in}} = \frac{V_{in}}{L_m a_m} \quad (7.64)$$

where V_{in} is usually assigned a value of unity for convenience.

7.3.4 Radiated Field

Once the matrix system $\mathbf{Z}\mathbf{a} = \mathbf{b}$ has been solved for the coefficient vector \mathbf{a} , the contribution to the radiated electric far-field from each triangle and basis function can be written as

$$\mathbf{E}_m(\mathbf{r}) = -\frac{j\omega\mu}{4\pi} \frac{e^{-jkr}}{r} \frac{a_m L_m}{2A_m} \iint_{T_m} \rho_m^\pm(\mathbf{r}') e^{jk\mathbf{r}' \cdot \hat{\mathbf{r}}} d\mathbf{r}' \quad (7.65)$$

This can be evaluated analytically using (9.58) and is

$$\mathbf{E}_m(\mathbf{r}) = -\frac{j\omega\mu}{4\pi} \frac{e^{-jkr}}{r} \frac{a_m L_m}{2A_m} \pm \mathbf{I}(\mathbf{s}) \quad (7.66)$$

where $\mathbf{s} = k\hat{\mathbf{r}}$ and the triangle vertexes are permuted so that $\mathbf{v}_m = \mathbf{v}_1$ in (9.59). We can also evaluate (7.65) via an M -point quadrature, yielding

$$\mathbf{E}_m(\mathbf{r}) \approx -\frac{j\omega\mu}{4\pi} \frac{e^{-jkr}}{r} \frac{a_m L_m}{2A_m} \sum_{p=1}^M w_p \rho_m^\pm(\mathbf{r}'_p) e^{jk\mathbf{r}'_p \cdot \hat{\mathbf{r}}} \quad (7.67)$$

For triangles whose edges are only a fraction of a wavelength, the results of (7.66) and (7.67) should not differ significantly.

7.3.4.1 Plane Wave Incidence

For incident plane waves of $\hat{\theta}^i$ or $\hat{\phi}^i$ polarization, the integral in (7.60) will be of the form

$$\mathbf{I} = \frac{L_m}{2A_m} (\hat{\theta}^i, \hat{\phi}^i) \cdot \iint \rho_m^\pm(\mathbf{r}') e^{jkr' \cdot \mathbf{r}'} d\mathbf{r}' \quad (7.68)$$

which can be evaluated analytically in a similar manner to (7.66) using (9.58). For monostatic scattering, the $\hat{\theta}^s$ and $\hat{\phi}^s$ components of (7.65) will be of the same form. Therefore, the excitation vector elements can be stored and reused to compute the scattered field using \mathbf{a} and the appropriate constants.

7.4 MFIE FOR THREE-DIMENSIONAL CONDUCTING SURFACES

To solve the MFIE for a conducting surface of arbitrary shape, we substitute (7.1) into (6.91) to yield

$$\begin{aligned} \hat{\mathbf{n}}(\mathbf{r}) \times \mathbf{H}^i(\mathbf{r}) &= \frac{1}{2} \sum_{n=1}^N a_n \mathbf{f}_n(\mathbf{r}) + \frac{1}{4\pi} \iint_{S-\delta S} \hat{\mathbf{n}}(\mathbf{r}) \times \left[(\mathbf{r} - \mathbf{r}') \times \sum_{n=1}^N a_n \mathbf{f}_n(\mathbf{r}') \right] \\ &\quad \cdot \left[1 + jkr \right] \frac{e^{-jkr}}{r^3} d\mathbf{r}' \end{aligned} \quad (7.69)$$

Testing the above by N functions $\mathbf{f}_m(\mathbf{r})$, we obtain a matrix \mathbf{Z} with elements given by

$$\begin{aligned} z_{mn} &= \frac{1}{2} \iint_{\mathbf{f}_m = \mathbf{f}_n} \mathbf{f}_m(\mathbf{r}) \cdot \mathbf{f}_n(\mathbf{r}) d\mathbf{r} + \frac{1}{4\pi} \iint_{\mathbf{f}_m} \mathbf{f}_m(\mathbf{r}) \cdot \hat{\mathbf{n}}(\mathbf{r}) \\ &\quad \times \iint_{\mathbf{f}_n} \left[(\mathbf{r} - \mathbf{r}') \times \mathbf{f}_n(\mathbf{r}') \right] \left[1 + jkr \right] \frac{e^{-jkr}}{r^3} d\mathbf{r}' d\mathbf{r} \end{aligned} \quad (7.70)$$

The first term in (7.70) above is computed when triangles overlap, and the second term when they do not. The excitation vector elements are given by

$$b_m = \iint_{\mathbf{f}_m} \mathbf{f}_m(\mathbf{r}) \cdot \left[\hat{\mathbf{n}}(\mathbf{r}) \times \mathbf{H}^i(\mathbf{r}) \right] d\mathbf{r} \quad (7.71)$$

7.4.1 MFIE Matrix Elements

Inserting the RWG basis function (7.2, 7.3) into (7.70) allows us to write

$$\begin{aligned} I &= \frac{L_m L_n}{8A_m A_n} \iint_{T_m} \rho_m^\pm(\mathbf{r}) \cdot \rho_n^\pm(\mathbf{r}) d\mathbf{r} + \frac{L_m L_n}{16\pi A_m A_n} \iint_{T_m} \rho_m^\pm(\mathbf{r}) \cdot \hat{\mathbf{n}}(\mathbf{r}) \\ &\quad \times \iint_{T_n} \left[(\mathbf{r} - \mathbf{r}') \times \rho_n^\pm(\mathbf{r}') \right] \left[1 + jkr \right] \frac{e^{-jkr}}{r^3} d\mathbf{r}' d\mathbf{r} \end{aligned} \quad (7.72)$$

where we have restricted the integral to a single source and testing triangle. Applying an M -point numerical quadrature rule yields

$$I = \frac{L_m L_n}{8A_m} \sum_{p=1}^M w_p \rho_m^\pm(\mathbf{r}_p) \cdot \rho_n^\pm(\mathbf{r}_p) + \frac{L_m L_n}{16\pi} \sum_{p=1}^M \sum_{q=1}^M w_p w_q \rho_m^\pm(\mathbf{r}_p) \cdot \left[\hat{\mathbf{n}}(\mathbf{r}_p) \times (\mathbf{r}_p - \mathbf{r}'_q) \times \rho_n^\pm(\mathbf{r}'_q) \right] \left[1 + jkR_{pq} \right] \frac{e^{-jkr_{pq}}}{R_{pq}^3} \quad (7.73)$$

where R_{pq} is given by (7.15) and we have assumed the quadrature weights to be normalized with respect to the triangle area. For triangle pairs with adequate separation distances, (7.73) can be implemented as written. For closer interactions, the second term in the above can exhibit strongly singular behavior that results in inaccurate matrix elements if computed by quadrature alone. We will consider the evaluation of these near-MFIE terms in Section 7.4.1.1.

Because we use planar triangles to model our geometry, the surface normal $\hat{\mathbf{n}}(\mathbf{r})$ in (7.72) is a constant and the second term is zero for all co-planar triangle pairs. This would *not* be the case if higher-order basis functions and curvilinear elements were used.

7.4.1.1 MFIE Near-Matrix Element Evaluation

To improve the accuracy of MFIE near-integrations, we will apply a technique similar to what was done for the EFIE. Following [15], we rewrite the innermost integral for each element, perform a singularity extraction and evaluate the singular terms analytically. In addition to the quantities defined in Figure 7.5, we define additional quantities as shown in Figure 7.7. For basis function $\rho_n(\mathbf{r}')$, we define the vector

$$\mathbf{R}_n = \mathbf{r} - \mathbf{v}_n \quad (7.74)$$

where \mathbf{v}_n is the vertex opposite edge n on triangle T_n^\pm . Noting that

$$\mathbf{r} - \mathbf{r}' = \mathbf{R}_n - \rho_n(\mathbf{r}') \quad (7.75)$$

we can write

$$(\mathbf{r} - \mathbf{r}') \times \rho_n(\mathbf{r}') = \mathbf{R}_n \times \rho_n(\mathbf{r}') \quad (7.76)$$

and since \mathbf{R}_n is a constant vector, we can write the innermost integral in the second part of (7.72) as

$$\iint_{T_n} \left[(\mathbf{r} - \mathbf{r}') \times \rho_n(\mathbf{r}') \right] \left[1 + jkr \right] \frac{e^{-jkr}}{r^3} d\mathbf{r}' = \mathbf{R}_n \times \iint_{T_n} \rho_n(\mathbf{r}') \left[1 + jkr \right] \frac{e^{-jkr}}{r^3} d\mathbf{r}' \quad (7.77)$$

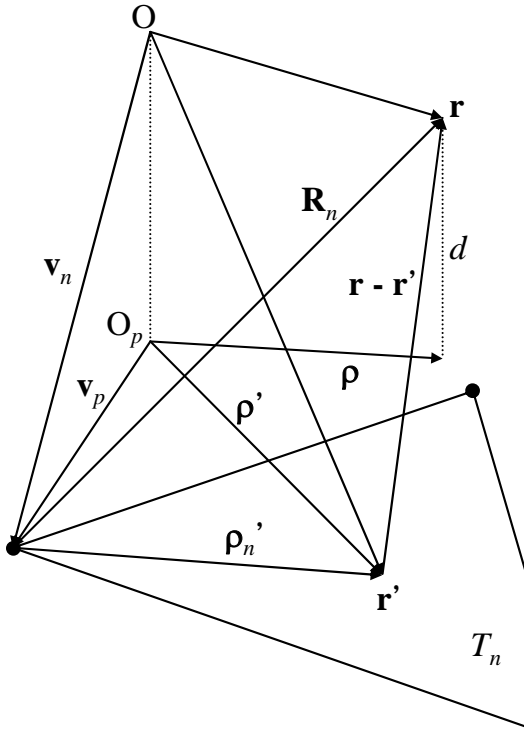


Figure 7.7: Geometric quantities for MFIE singularity extraction.

According to [15], we now perform the following singularity extraction

$$\mathbf{R}_n \times \iint_{T_n} \rho_n(\mathbf{r}') \left[1 + jkr \right] \frac{e^{-jkr}}{r^3} d\mathbf{r}' = \mathbf{R}_n \times \left[\iint_{T_n} \rho_n(\mathbf{r}') \cdot \frac{(1 + jkr)e^{-jkr} - (1 + \frac{1}{2}k^2r^2)}{r^3} + \mathbf{a}_n(\mathbf{r}) + \frac{k^2}{2} \mathbf{b}_n(\mathbf{r}) \right] \quad (7.78)$$

where

$$\mathbf{a}_n(\mathbf{r}) = \iint_{T'} \frac{\rho_n(\mathbf{r}')}{r^3} d\mathbf{r}' \quad (7.79)$$

and

$$\mathbf{b}_n(\mathbf{r}) = \iint_{T'} \frac{\rho_n(\mathbf{r}')}{r} d\mathbf{r}' \quad (7.80)$$

The first term on the right-hand side in (7.78) is well behaved and can be evaluated via numerical quadrature. The remaining two integrals $\mathbf{a}_n(\mathbf{r})$ and $\mathbf{b}_n(\mathbf{r})$ are the singular contributions and will be evaluated analytically. The integral $\mathbf{b}_n(\mathbf{r})$ can be

computed via (7.47). The integral $\mathbf{a}_n(\mathbf{r})$ can be computed by rewriting it according to (7.46), leading to

$$\iint_{T'} \frac{\rho_n(\mathbf{r}')}{r^3} d\mathbf{r}' = \iint_{T'} \frac{\rho' - \rho}{r^3} d\mathbf{r}' + (\rho - \rho_n) \iint_{T'} \frac{1}{r^3} d\mathbf{r}' \quad (7.81)$$

These integrals are [15]

$$\iint_{T'} \frac{\rho' - \rho}{r^3} d\mathbf{r}' = - \sum_{i=1}^N \hat{\mathbf{u}}_i \log \frac{R_i^+ + l_i^+}{R_i^- + l_i^-} \quad (7.82)$$

and

$$\begin{aligned} \iint_{T'} \frac{1}{r^3} d\mathbf{r}' &= \sum_{i=1}^N \hat{\mathbf{P}}_i^0 \cdot \hat{\mathbf{u}}_i \frac{1}{|d|} \left[\tan^{-1} \frac{P_i^0 l_i^+}{(R_i^0)^2 - |d|R_i^+} \right. \\ &\quad \left. - \tan^{-1} \frac{P_i^0 l_i^-}{(R_i^0)^2 - |d|R_i^-} \right] \quad (d \neq 0) \end{aligned} \quad (7.83)$$

$$\iint_{T'} \frac{1}{r^3} d\mathbf{r}' = - \sum_{i=1}^N \hat{\mathbf{P}}_i^0 \cdot \hat{\mathbf{u}}_i \left[\frac{l_i^+}{P_i^0 R_i^+} - \frac{l_i^-}{P_i^0 R_i^-} \right] \quad (d = 0) \quad (7.84)$$

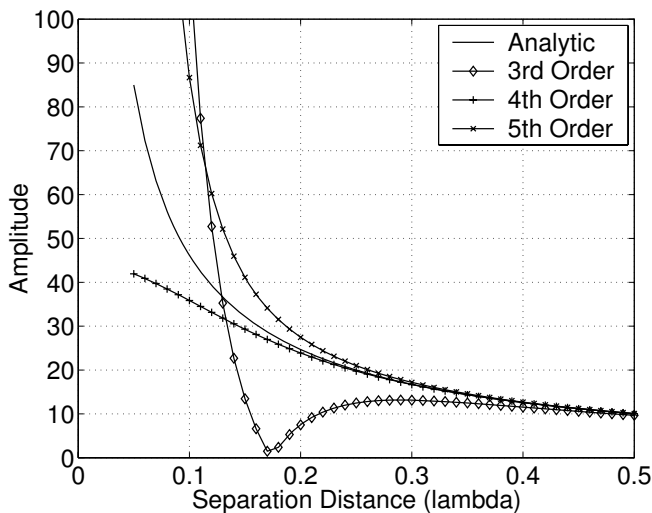
The sums in (7.82) and (7.84) may also have numerical problems when \mathbf{r} lies in S along the extension of an edge. In these cases, the observation point can again be slightly modified according to (7.44).

7.4.1.2 Integration Examples

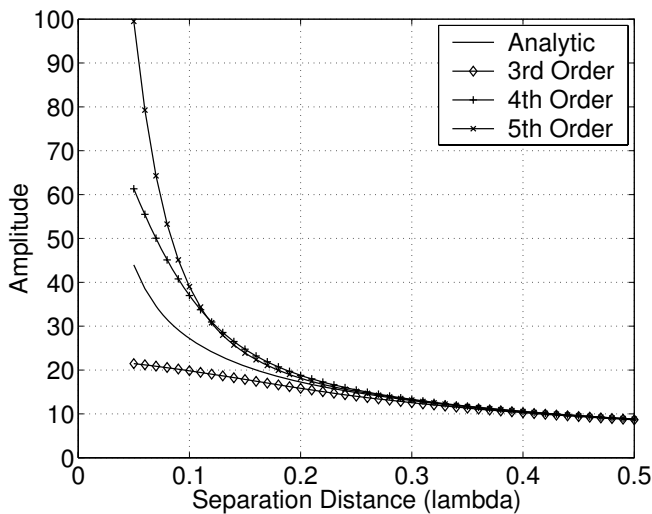
Let us evaluate the singular portion of (7.78) using a Gaussian quadrature rule of order P and the analytic method described in Section 7.4.1.1. For this comparison, we compute the scalar quantity

$$I = \left| \mathbf{a}_n(\mathbf{r}) + \frac{k^2}{2} \mathbf{b}_n(\mathbf{r}) \right| \quad (7.85)$$

The integration is performed over an equilateral triangle with sides of length $1/\lambda$. In Figure 7.8 we compare the results obtained from quadrature rules of orders 3, 4 and 5 to the analytic expression. In Figure 7.8a, the observation point is placed over the center of the triangle and the separation distance is varied. Figure 7.8b is similar, but the observation point is placed at the midpoint of an edge. In both cases the comparison is good at larger distances but increasingly poor at shorter ones, as expected. These results suggest that the singularity extraction method for the MFIE should be applied for triangle pairs separated by 0.2 – 0.3λ or less.



(a) Center of Triangle



(b) Center of Edge

Figure 7.8: MFIE singular integration.

7.4.2 MFIE Excitation Vector Elements

The calculation of the MFIE excitation vector should also be performed as a loop over individual triangles. Using an M -point numerical quadrature, the contribution from each triangle and basis function can be written as

$$I_m = \frac{L_m}{2A_m} \iint_{T_m} \rho_m^\pm(\mathbf{r}) \cdot [\hat{\mathbf{n}}(\mathbf{r}) \times \mathbf{H}^i(\mathbf{r})] d\mathbf{r} \approx \frac{L_m}{2} \sum_{p=1}^M w_p \rho_m^\pm(\mathbf{r}_p) \cdot [\hat{\mathbf{n}}(\mathbf{r}_p) \times \mathbf{H}^i(\mathbf{r}_p)] \quad (7.86)$$

7.4.2.1 Plane Wave Incidence

For incident plane waves of $\hat{\theta}^i$ - or $\hat{\phi}^i$ polarization, the integral in (7.86) will be of the form

$$\mathbf{I} = \frac{L_m}{2A_m \eta} (-\hat{\phi}^i, \hat{\theta}^i) \cdot \iint \rho_m^\pm(\mathbf{r}') e^{jkr' \cdot \hat{\mathbf{r}}^i} d\mathbf{r}' \quad (7.87)$$

which is of the same form as (7.68). Following the discussion in Section 6.4.2.1, the expression for the $\hat{\theta}$ and $\hat{\phi}$ -polarized EFIE vectors can be combined with the appropriate constants to obtain the MFIE vectors.

7.4.3 Radiated Field

The radiated field of the MFIE current is calculated in an identical manner to that of Section 7.3.4. The shortcut outlined in Section 7.3.4.1 remains valid as well.

7.4.4 Accuracy of RWG Functions in MFIE

RWG functions have been used for many years to solve the EFIE and MFIE for three-dimensional objects. We have also done so in this chapter because it presents a consistent picture to the student who is new to these concepts. We should point out that the MFIE as solved using RWG basis functions is known to possess inaccuracies that render it somewhat less accurate than the EFIE for the same problem [16]. This stems from issues such as numerical integration [14, 17], the choice of the solid-angle factor (2.138) [18, 19], and the overall choice of basis and testing functions. It has been shown that the RWG function itself is the cause of much of this inaccuracy [20], and that this can be improved by moving to a more suitable basis function such as the curl-conforming type [21, 22], or the linear-linear basis functions introduced in [23, 24].

Object	Edges/Unknowns	Double	Float
$\lambda/4$ Cube	336	1764 kB	882 kB
$\lambda/2$ Sphere	1920	56.25 MB	28.125 MB
1λ Almond	19848	5.86	2.93 GB
2λ Sphere	31260	16.56 GB	7.28 GB
8.5λ Almond	70476	74.0 GB	37.28 GB

Table 7.5: Full Matrix Memory Requirements

7.5 NOTES ON SOFTWARE IMPLEMENTATION

7.5.1 Memory Management

When applying the MOM to three-dimensional surfaces, the total number of unknowns is proportional to the square of the operating frequency. Because many objects of practical interest are electrically large, the resulting demands on system memory can be quite high. In Table 7.5 we summarize the memory requirements of the full MOM matrix for several objects of increasing size. The requirements for double and single precision complex elements (16 and 8 bytes, respectively) are shown. The geometry of each object has at least 10 edges per wavelength, or approximately 100 edges per square wavelength. We immediately see that the memory demand increases exponentially with problem size. The 8.5λ almond ($N=70476$) presents a rather formidable challenge, with its requirement of 74 GB outstripping the capabilities of virtually all consumer-level computer systems currently available. The resulting tendency is to reduce the complexity of the object, or to reduce the number of unknowns per wavelength used. This often forces one to strike a balance between model complexity and available computing resources. The scattered field of this 8.5λ almond can be computed far more easily using the FMM, which is discussed in Section 8.8.2.1.

7.5.1.1 EFIE

Because the EFIE results in a symmetric matrix, only the upper triangle and diagonal must be stored. This reduces the total number of matrix elements from N^2 to $N(N + 1)/2$, effectively halving the memory requirements. If the upper triangle of the EFIE matrix is stored in a packed column format, the LAPACK functions **csptrf** and **csptrs** can be used to factor and solve the linear system [25].

7.5.2 Parallelization

Many parts of a three-dimensional moment method program can be parallelized effectively. The subroutines that compute the system matrix and right-hand side vectors are obvious candidates. While some elements of the matrix factorization

can be parallelized, that is beyond the scope of this text and we will assume this factorization to be limited to a single processing thread.

7.5.2.1 Shared Memory Systems

In a shared memory system, all geometry information as well as system matrix and right-hand side vectors will be available to each thread. To parallelize the matrix fill, each processing thread should be assigned a unique facet pair and the mutex-protected memory space for the matrix. One effective scheme would create a separate mutex for each matrix row. When a thread needs to add to matrix element z_{mn} , it locks mutex m and prevents any access to that row until its writes are finished. Right-hand sides can be parallelized several ways. If there are many right-hand side vectors, such as a monostatic radar cross section calculation with multiple incident angles, each thread can be allocated its own right-hand side vector space and work on unique angles independently. If that number is small, a single right-hand side vector can be used and each thread assigned a unique triangle list, again with mutex protection on writes. If there are many observation angles for each right-hand side, the programmer could use either method depending on the overall number of right-hand sides.

7.5.2.2 Distributed Memory Systems

The overall design and implementation of a moment method software on distributed memory systems will depend on several factors. The more important considerations are the maximum size of the problem to be attempted, the type of processor and total memory installed on each node, and the speed and topology of the network connections. If the problem is small enough that it can be solved on a single node, one could simply utilize all the available processors to decrease the matrix fill time. In this case, each node can load the geometry into local memory and create the needed edge list and any other information, then compute and transmit its system matrix and right-hand side vector contributions to the master node.

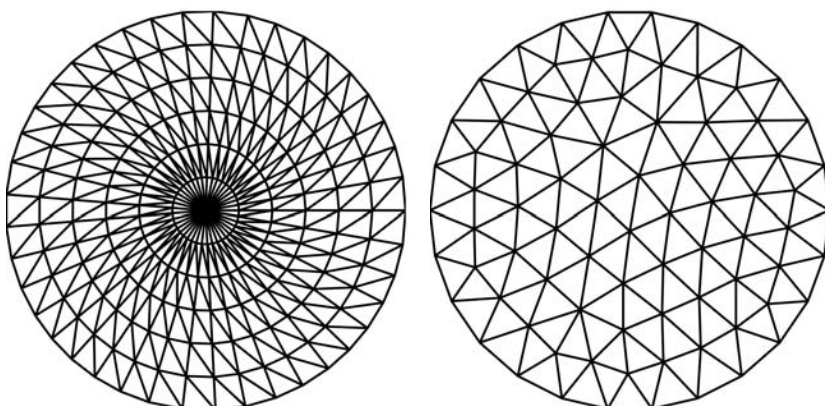
If the geometry and system matrix are too large to be stored on a single node, they must be efficiently divided among the available nodes. A mechanism must be devised that allows each node to obtain portions of the geometry it needs but does not store locally. While it may not be difficult to store unique parts of the system matrix on different nodes, the required distributed matrix factorization may be more difficult and is again beyond the scope of this text. A distributed iterative solver algorithm may be a more attractive choice in this case, as each node only needs to compute the portion of the matrix-vector product involving what it stores locally. The results from each node can then be transmitted to a master node and added to the global result vector at each iteration.

7.6 CONSIDERATIONS FOR MODELING WITH TRIANGLES

One of the most important parts of any simulation is the model input to the code. We have discussed several times the importance of the integrations that produce accurate matrix elements, however the model itself is also key to obtaining a good solution. Indeed, a significant amount of time may be spent generating a model that accurately represents the object being modeled, as well as generating a watertight mesh with reasonably shaped triangles free of t-junctions or other issues.

7.6.1 Triangle Aspect Ratios

Most geometry modeling tools have the capability to generate a triangular mesh on a surface, however the quality of these meshes can vary. Foremost when generating a mesh is to ensure that all triangles have a reasonable aspect ratio and do not contain small internal angles. An example of such a mesh is shown in Figure 7.9a, where a circular plate is meshed using a simple radial algorithm. The triangles in this mesh grow progressively smaller and thinner as they grow closer to the center. It is well known that models containing triangles of poor aspect ratios will result in a more poorly conditioned moment method matrix. While it is not always possible to create a model with equilateral triangles across the entire surface, many meshing tools allow the user to analyze the distribution of aspect ratios in a mesh. In areas where the triangles are deemed to be too thin, these tools allow for restructuring the triangles to improve their condition. A better mesh is illustrated in Figure 7.9b, where each triangle has a much better shape.



(a) Triangles with Poor Aspect Ratio

(b) Triangles with Better Aspect Ratio

Figure 7.9: Examples of triangle mesh aspect ratio.

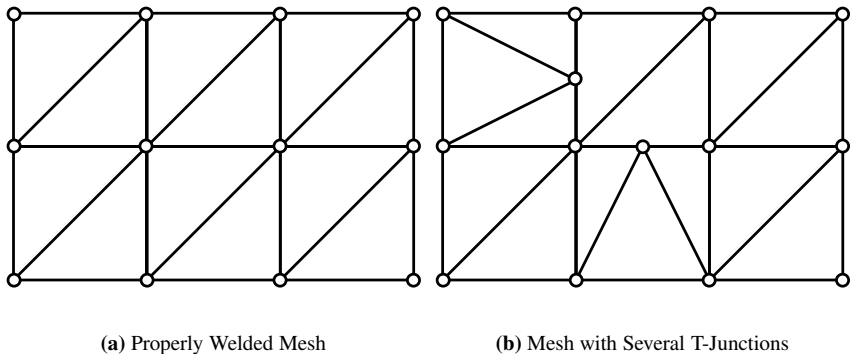


Figure 7.10: Triangle mesh connectivities.

7.6.2 Watertight Meshes and T-Junctions

We have already discussed the importance of shared nodes between triangles. If nodes are not joined together along an edge, the surface is not logically connected at that edge and no current can flow across it. When a surface mesh encloses a volume, it must be “watertight,” with no boundary edges anywhere. This is critically important when applying the MFIE, as it is only valid for a closed surface.

Some modeling tools may generate meshes where nodes of one triangle are not co-located with those of adjacent triangles. Consider the meshes shown in Figure 7.10. The mesh of Figure 7.10a is properly aligned, however that of Figure 7.10b contains many disjoint intersections called *T-junctions*. These joints cannot be logically resolved through the connectivity list and represent a tear or hole in the surface. It is imperative that the engineer ensure their model is free of these junctions. Many modeling packages will search for unjoined or *naked* edges, which may lie along these seams. When the number of triangles in the model grows to be quite high T-junctions can become difficult to find and eliminate. While sometimes it may be necessary to remove junctions manually, a good meshing tool can automatically locate and heal the junctions with little or no user intervention.

7.7 EXAMPLES

In this section we will demonstrate the efficacy of the three-dimensional MOM formulations of this chapter in solving several scattering and radiation problems. We consider the conducting sphere, several benchmark plate radar targets measured by the EMCC, and the input impedance of several antennas including the well-known bowtie and archimedean spiral.

7.7.1 Serenity

The examples in this chapter are computed using the Tripoint Industries code *Serenity*, a Moment Method software for solving radar cross section problems of three-dimensional conducting objects. *Serenity* implements the EFIE and MFIE using RWG basis functions, and contains automatic edge finding algorithms, adjustable Gaussian quadrature integration density, and near and singular integration routines following Sections 7.3.2 and 7.4.1.1. It supports a full-matrix approach with direct factorization and iterative solvers, as well as an MLFMA-accelerated iterative solver using the techniques in Chapter 8. It is written in the C programming language and uses double precision complex for computing the MOM matrix and single precision for its storage and factorization. *Serenity* is part of the Tripoint Industries *lucernhammer* suite of radar cross section codes.

7.7.2 RCS of a Sphere

We first consider a conducting sphere with a diameter of 2 meters. CFIE is used with $\alpha = 0.5$.

7.7.2.1 Monostatic RCS versus Frequency

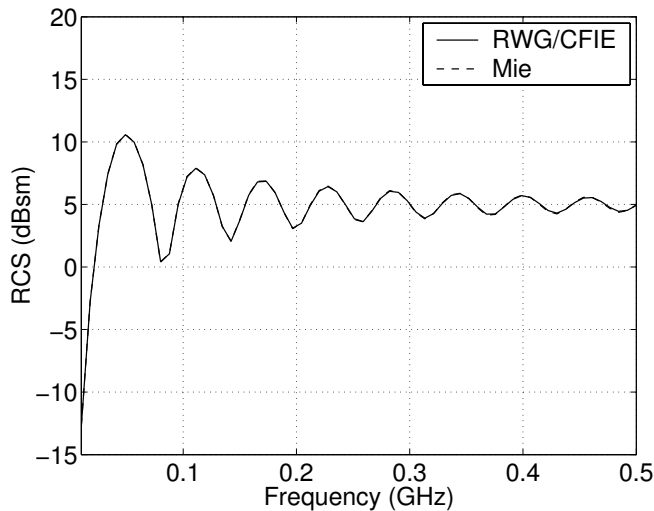
In Figure 7.11a we compare the monostatic RCS from the CFIE and Mie series for frequencies between 10 MHz and 500 MHz. The comparison is excellent, and it is difficult to differentiate the two results. In Figure 7.11b we plot the difference between the results. The overall difference is less than 0.1 dB, which is usually considered excellent for numerical RCS predictions.

7.7.2.2 Bistatic RCS

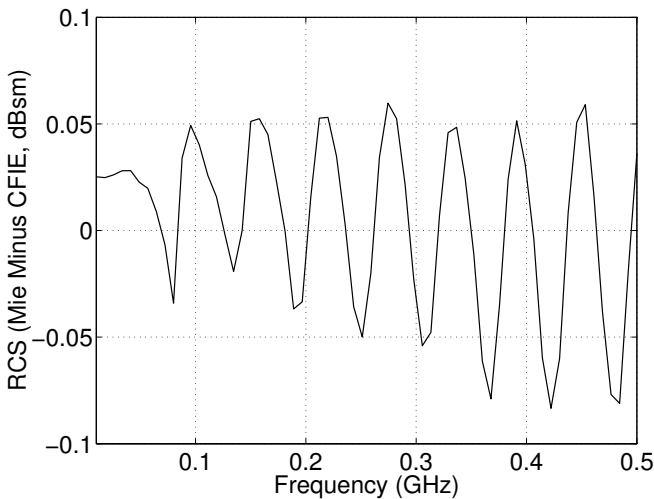
We next compute the bistatic RCS of the sphere at 300 MHz. At this frequency, the sphere is 2λ in diameter. The results are summarized in Figures 7.12a and 7.12b for vertical and horizontal polarizations, respectively. The comparison is again excellent, with the CFIE results nearly indistinguishable from the Mie series.

7.7.3 EMCC Plate Benchmark Targets

We now compute the RCS of the EMCC benchmark plate radar targets measured and described in [26]. Because edge and tip diffractions were of primary interest in this article, the measurements were performed using a conical cut 10 degrees from the plane of each target. The test articles were fabricated from aluminum foil or thin pieces of high-density foam coated with conducting paint. Our facet models comprise flat faceted surfaces, and the EFIE is used. In the plots that follow, the measurement data are shifted slightly in angle to align them with the numerical results.

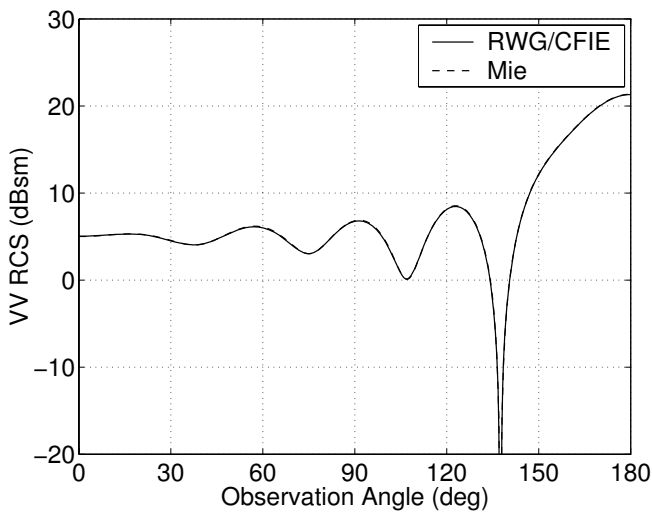


(a) Mie vs. CFIE

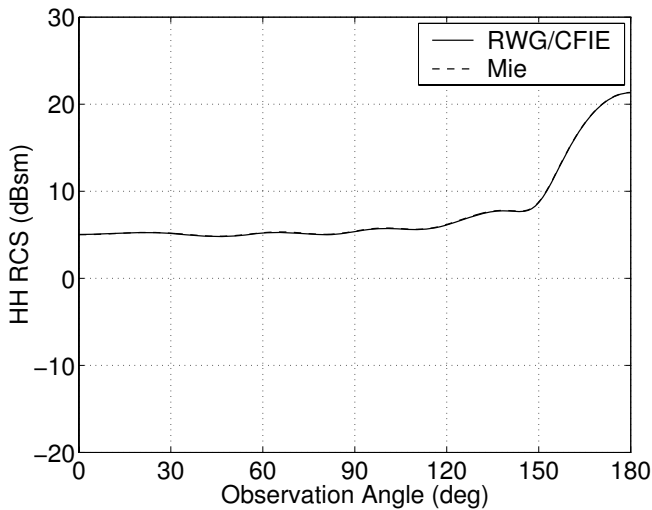


(b) Mie Minus CFIE

Figure 7.11: 2 Meter sphere: monostatic RCS versus frequency.

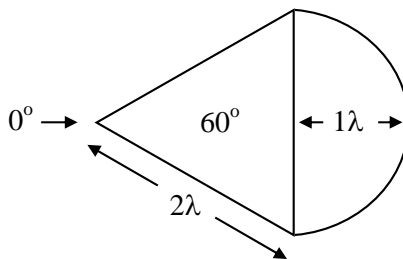


(a) Vertical Polarization

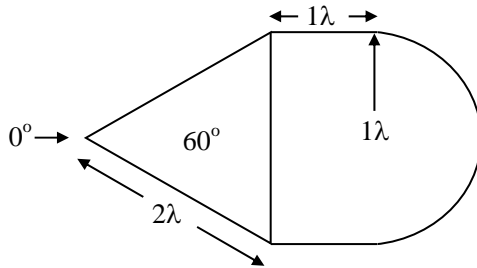


(b) Horizontal Polarization

Figure 7.12: 2 Meter sphere: bistatic RCS.



(a) Wedge Cylinder



(b) Wedge-Plate Cylinder

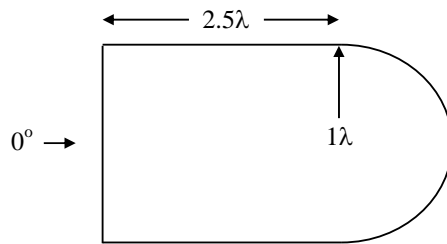
Figure 7.13: EMCC plate benchmark targets.

7.7.3.1 Wedge Cylinder

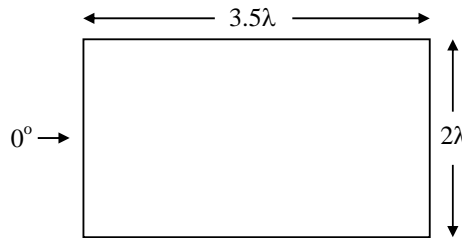
The geometry of the wedge-cylinder is shown in Figure 7.13a. The RCS computed using *Serenity* is compared to the EMCC measurements in Figures 7.15a and 7.15b for vertical and horizontal polarizations, respectively. The comparisons are very good for both polarizations, but are noticeably better in the horizontal case. In [26] the measurements were adjusted by 2 dB during plotting; however, no adjustments are made in these figures.

7.7.3.2 Wedge-Plate Cylinder

The geometry of the wedge-plate cylinder is shown in Figure 7.13b. The RCS computed using *Serenity* is compared to the EMCC measurements in Figures 7.16a and 7.16b for vertical and horizontal polarizations, respectively. The comparisons are very good for both polarizations, but are again slightly better in the horizontal case.



(a) Plate Cylinder



(b) Business Card

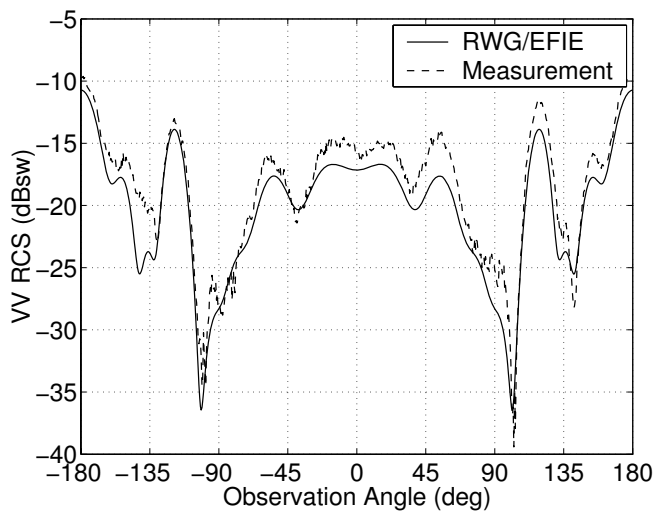
Figure 7.14: EMCC plate benchmark targets.

7.7.3.3 Plate Cylinder

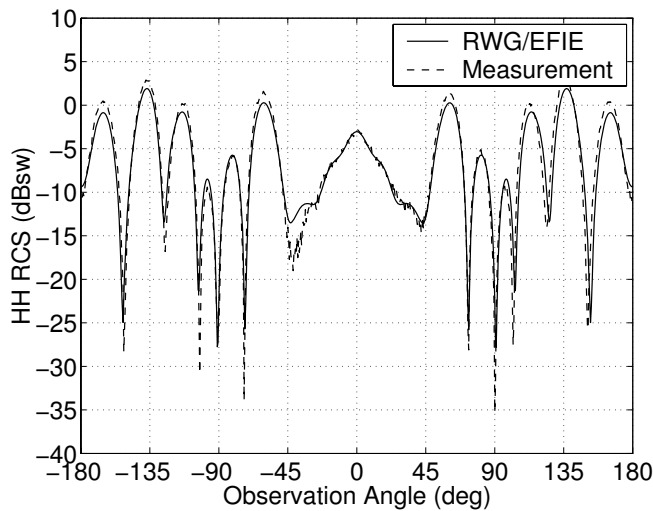
The geometry of the plate cylinder is shown in Figure 7.14a. The RCS computed using *Serenity* is compared to the EMCC measurements in Figures 7.17a and 7.17b for vertical and horizontal polarizations, respectively. The overall comparison is quite good, however measurement has a much higher magnitude than expected from 100 to 160 degrees in Figure 7.17a, the cause of which is not known.

7.7.3.4 Business Card

The geometry of the “business card” target is shown in Figure 7.14b. The RCS computed using *Serenity* is compared to the EMCC measurements in Figures 7.18a and 7.18b for vertical and horizontal polarizations, respectively. The comparison is very good for horizontal polarization, though the computed results are lower than the measurement for vertical polarization. A similar observation was made in [26].

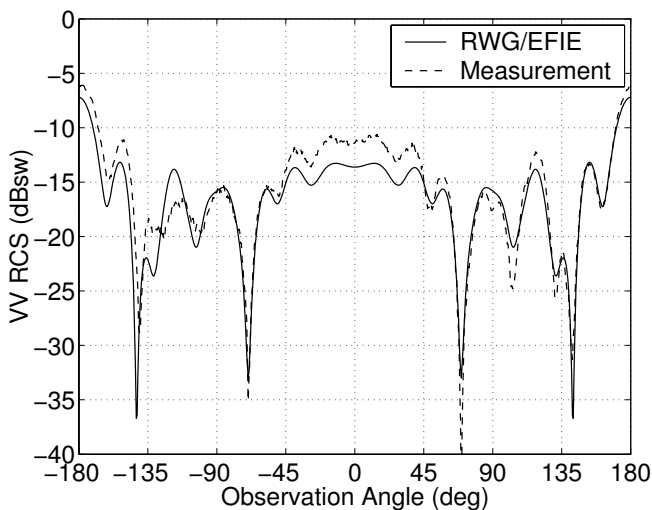


(a) Vertical Polarization

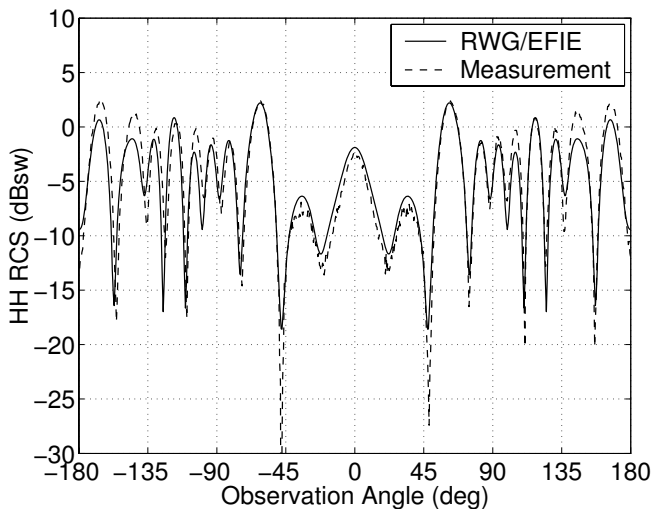


(b) Horizontal Polarization

Figure 7.15: EMCC wedge cylinder: EFIE versus measurement.

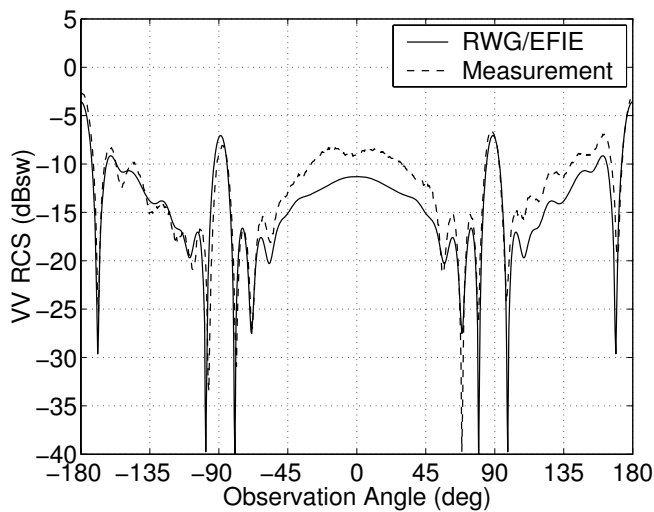


(a) Vertical Polarization

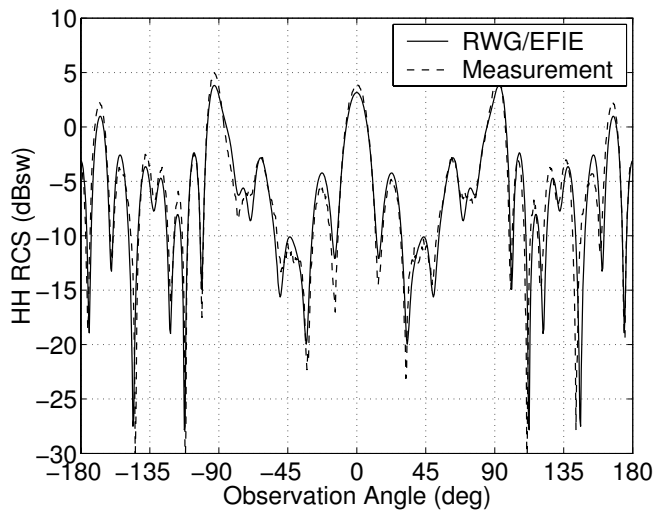


(b) Horizontal Polarization

Figure 7.16: EMCC wedge-plate cylinder: EFIE versus measurement.

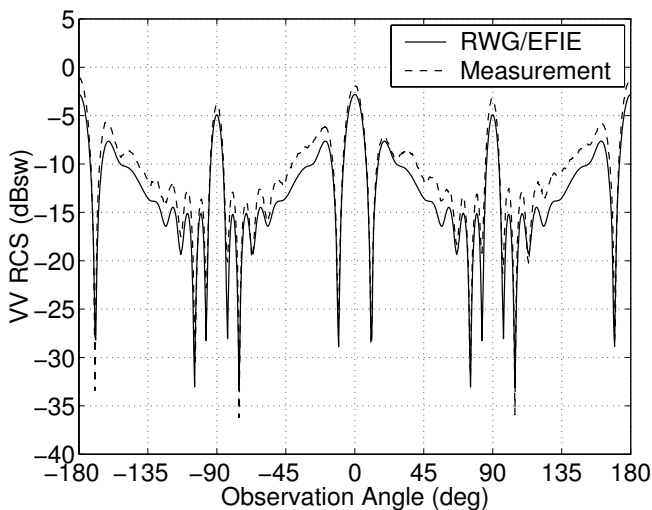


(a) Vertical Polarization

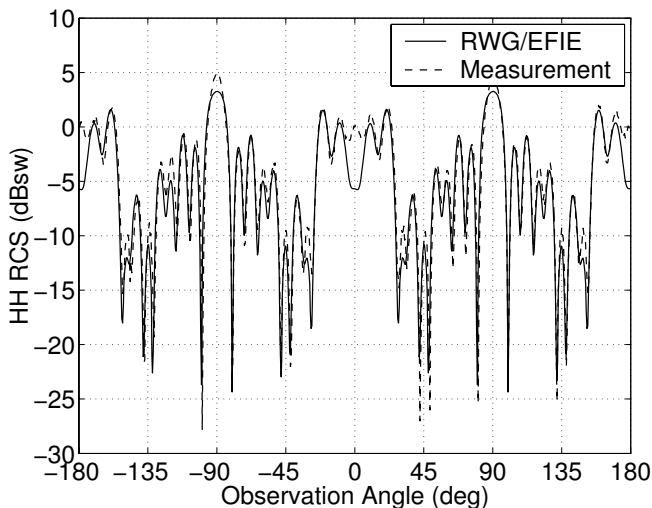


(b) Horizontal Polarization

Figure 7.17: EMCC plate cylinder: EFIE versus measurement.

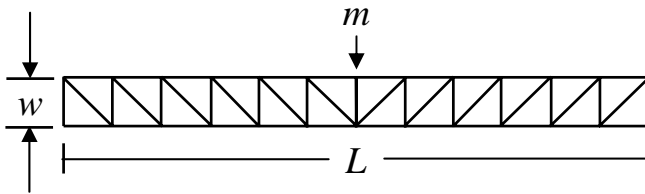


(a) Vertical Polarization

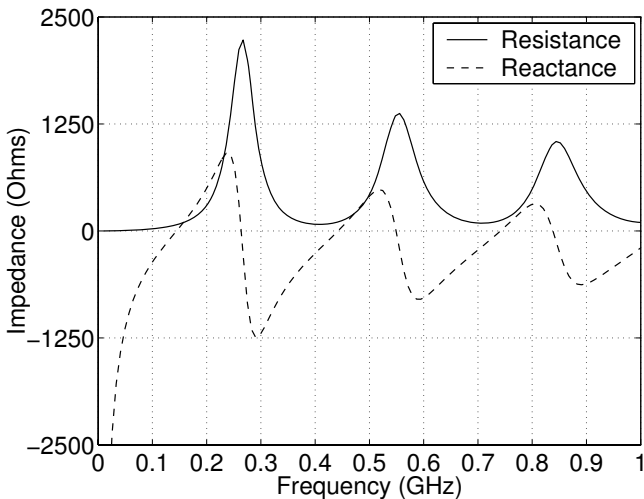


(b) Horizontal Polarization

Figure 7.18: EMCC business card: EFIE versus measurement.



(a) Strip Dipole Dimensions



(b) Input Impedance

Figure 7.19: Thin strip dipole.

7.7.4 Strip Dipole Antenna

We next consider the input impedance of a thin strip dipole antenna as illustrated in Figure 7.19a. The dipole has a length $L = 1$ meter and width $w = 3$ mm, so the figure is not drawn to scale. Such a strip is representative of thin foil chaff that might be used in a aircraft or space-vehicle radar countermeasure. The strip is center fed using the delta-gap model of Section 7.3.3.1. The input resistance and reactance are shown in Figure 7.19b for 128 frequencies ranging from 10 MHz to 1 GHz.

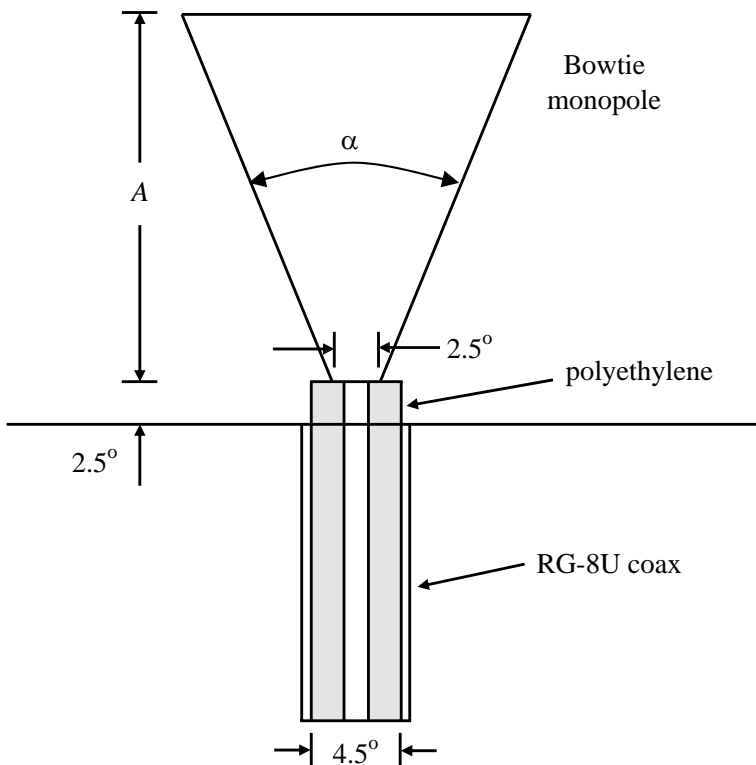


Figure 7.20: Bowtie monopole measurement setup.

7.7.5 Bowtie Antenna

The bowtie-shaped planar antenna of Figure 7.6a is used extensively in wide-bandwidth radiation and receiving applications. A study of the input impedance and radiation characteristics of the bowtie was presented in [27] for various flare angles and lengths. Their measurement setup is illustrated in Figure 7.20, where a bowtie monopole was fed and measured against a conducting disk 8 feet in diameter. The feed utilized an RG-8U coaxial cable that was trimmed and inserted through a small hole in the disk. The fed end of the bowtie was truncated to facilitate attachment to the center conductor of the coax. Measurements were obtained at a fixed frequency of 500 MHz using a slotted line with sliding probe and transmission line charts. Each antenna was fabricated to the maximum electrical length and physically cut down as the measurements were made. Therefore, the electrical dimensions at the feedpoint remained constant.

In Figures 7.21a and 7.21b we compare the input resistance and reactance obtained from the EFIE and a delta-gap feed to the measurements of [27] for flare angles of 10, 30, 50 and 90 degrees. Whereas the measurements were given in

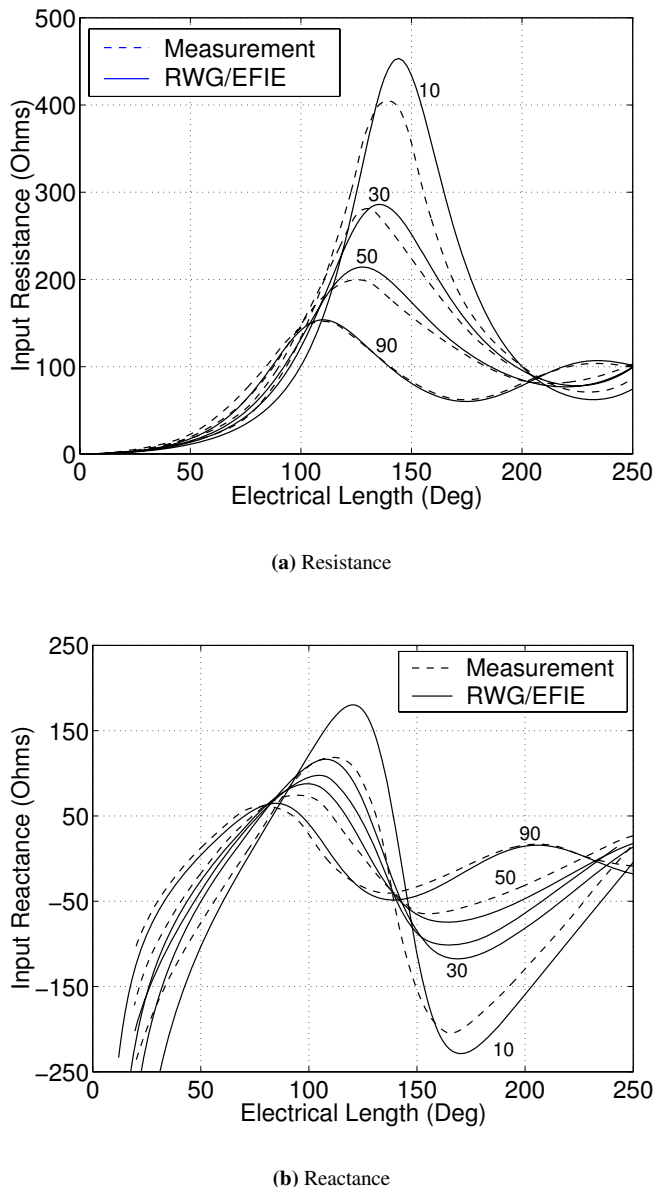


Figure 7.21: Bowtie input impedance: EFIE versus measurement.

terms of the electrical length in degrees, we fix the dimensions of the antenna and sweep across frequency. Our model is of a dipole in free space, and we take into account that the input impedance will be twice that of a monopole over a ground plane. Each antenna is assigned a half-length of 1 meter and an edge length of 2 cm at the feedpoint (Figure 7.6a). The comparison is fair, considering the differences between the physical and computer models. The disparity between feedpoint models is an obvious difference, and likely contributes to the observed offset between the resonant frequencies as well as the impedance amplitudes. A similar observation was noted in [28]. If we had instead used the magnetic frill of Section 4.2.2 and reduced the physical length of the model rather than changing the frequency, the comparison might be better, though it would be more time intensive in terms of setup and execution. This illustrates the trade-offs encountered between a “quick and dirty” result and a more accurate but time-consuming one.

7.7.6 Archimedean Spiral Antenna

We next consider the characteristics of the Archimedean spiral antenna [29, 30]. This antenna is known to have desirable broadband performance in terms of input impedance as well as a circularly polarized radiation pattern. The dimensions of this antenna are illustrated in Figure 7.22a. The radius of each arm is linearly proportional to the angle and can be written as

$$r = b\phi + r_1 \quad (7.88)$$

and

$$r = b(\phi + \pi) + r_1 \quad (7.89)$$

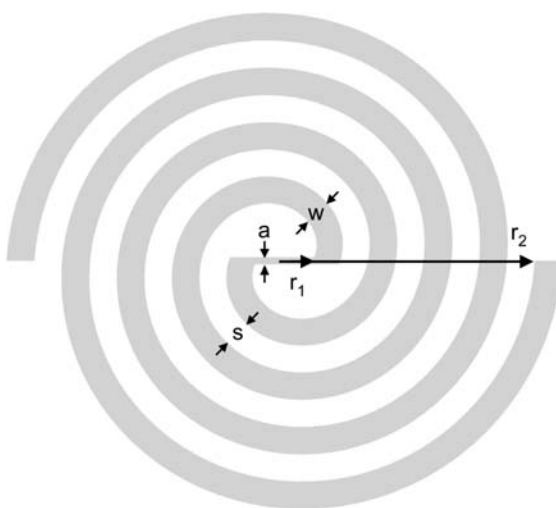
where r_1 is a starting radius and b is a constant that depends on the width w and spacing s of the arms of the antenna. If we choose a self-complementary spiral with $s = w$, then

$$b = \frac{2w}{\pi} \quad (7.90)$$

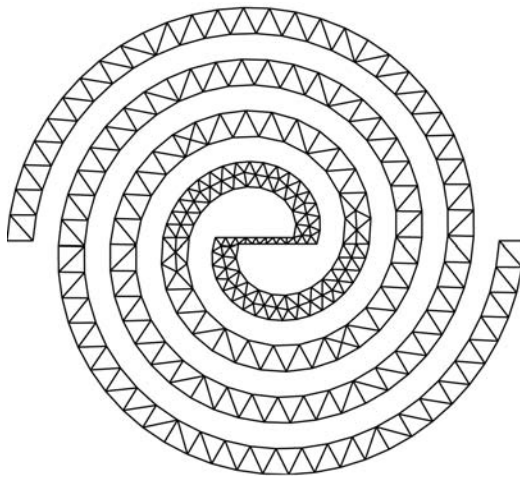
and if the spiral has an infinite number of turns, then by Babinet’s Principle the input impedance of the antenna should be approximately half that of the surrounding medium. If the medium is free space, then

$$Z_{in} = \frac{\eta}{2} \approx 188.4\Omega \quad (7.91)$$

When a voltage is applied to the center terminals of this antenna, it behaves in a manner similar to a two-wire transmission line and gradually transitions into a radiating structure where the circumference of the spiral is one wavelength [30]. In theory, an antenna with the largest number of turns should have the broadest bandwidth, however the available space and size will limit its maximum size. A way to connect a feedline to the antenna must be devised as well. These considerations will determine the final input impedance, which we do not expect will match the

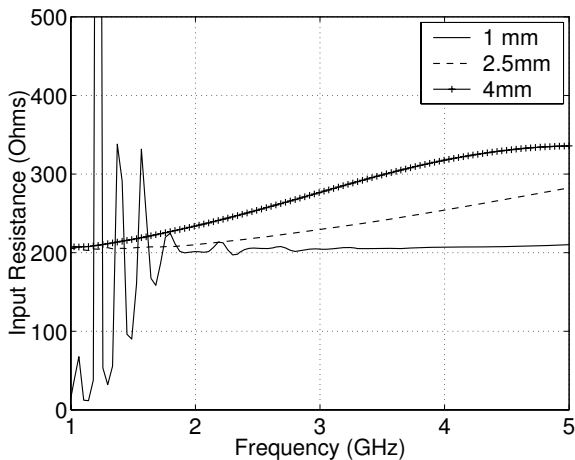


(a) Spiral Antenna Dimensions

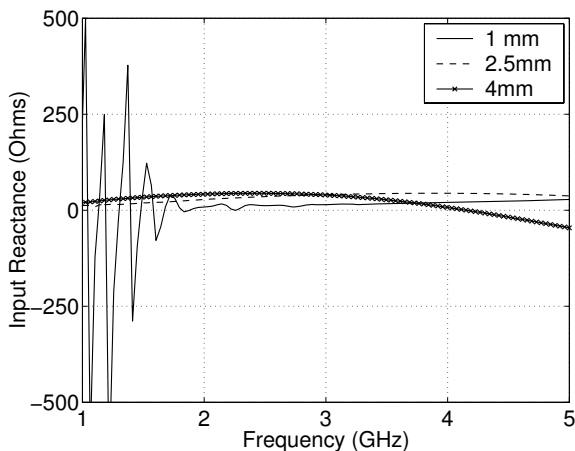


(b) Example Spiral Antenna Mesh

Figure 7.22: Archimedean spiral antenna.



(a) Input Resistance



(b) Input Reactance

Figure 7.23: Input impedances of spiral antennas versus frequency.

theoretical value of Z_{in} . For our numerical model, we choose a starting radius $r_1 = w$ and bridge the arms of the spiral at its center using a flat strip of width $a = w/2$. So that the feed area of the antenna is accurately modeled, we apply heavier triangulation near the center and a lower density in the arms. This tessellation scheme is illustrated in Figure 7.22b.

Let us determine the dimensions of a spiral antenna that has the best broadband impedance between 1 and 5 GHz. To do so, we construct three spiral antennas of widths w of 1, 2.5 and 4 mm and a total of 16 turns each. The delta-gap voltage model is used to excite the edge at the center of the strip connecting the arms.

The input resistance and reactance of each antenna are shown in Figures 7.23a and 7.23, respectively. The antenna with 1mm arms has a nearly constant input resistance of approximately 210 Ohms between 2 and 5 GHz, and an input reactance of around 20 Ohms. The other two antennas have a much wider variation throughout this range, though their performance appears to remain smooth at lower frequencies. We expect that by adding additional turns to the 1mm antenna, its flat impedance curve could be extended down to 1 GHz with little impact on its higher frequency performance. Using the 1mm design as a starting point, a laboratory model could now be fabricated and a more accurate estimate of the impedance measured using a vector network analyzer (VNA).

7.7.7 Summary of Examples

The run metrics for the examples in this chapter are summarized in Table 7.6. Provided are the number of facets and unknowns, the number of right-hand sides, the memory requirements (in MB) and the compute time for each case. The compute times comprise the entire runtime including matrix fill, factorization and scattered field calculation. For cases involving multiple frequencies, the compute time shown

Table 7.6: Summary of Examples

Object	Facets	N	NRHS	RAM	CPU
2m Sphere	5120	7680	1	450.0	62m
Wedge Cylinder	2997	4424	720	74.68	35m
Wedge-Plate Cylinder	4864	7205	720	198.1	54m
Plate Cylinder	6002	8902	720	302.3	88m
Business Card	5600	8290	720	262.2	79m
Strip Dipole	664	663	128	1.67	2.2m
10° Bowtie	260	335	1	0.43	1s
30° Bowtie	630	879	1	2.95	6s
50° Bowtie	1138	1627	1	10.1	27s
90° Bowtie	2432	3527	1	47.47	3.5m
Spirals	3176	3259	1	40.53	3.1m

is the average time for a single frequency point. Runs were performed on an AMD Athlon MP 2600 (at 2 GHz) with 2 GB memory under Red Hat Linux 7.3.

The number of unknowns used for our benchmark plate targets is higher than what was used in [26]. This was done to ensure a reasonably dense level of facetization near the edges of each object. The spiral antennas in Section 7.7.6 have slightly different dimensions with an identical facet and unknown count. Because the resulting runtimes differ very little, the average of the three cases is shown.

REFERENCES

- [1] *Rhinoceros 3D*. Robert McNeel and Associates, <http://www.rhino3d.com>.
- [2] L. Piegl and W. Tiller, *The NURBS Book*. Springer, 1995.
- [3] J. Foley, A. van Dam, S. Feiner, and J. Hughes, *Computer Graphics: Principles and Practice*. Addison-Wesley, 1996.
- [4] D. Wilton, S. Rao, A. Glisson, D. Schaubert, M. Al-Bundak, and C. M. Butler, “Potential integrals for uniform and linear source distributions on polygonal and polyhedral domains,” *IEEE Trans. Antennas Propagat.*, vol. 32, 276–281, March 1984.
- [5] S. Caorsi, D. Moreno, and F. Sidoti, “Theoretical and numerical treatment of surface integrals involving the free-space green’s function,” *IEEE Trans. Antennas Propagat.*, vol. 41, 1296–1301, September 1993.
- [6] R. D. Graglia, “On the numerical integration of the linear shape functions times the 3-d green’s function or its gradient on a plane triangle,” *IEEE Trans. Antennas Propagat.*, vol. 41, 1448–1454, October 1993.
- [7] T. F. Eibert and V. Hansen, “On the calculation of potential integrals for linear source distributions on triangular domains,” *IEEE Trans. Antennas Propagat.*, vol. 43, 1499–1502, December 1995.
- [8] J. Jin, *The Finite Element Method in Electromagnetics*. John Wiley and Sons, 1993.
- [9] S. Rao, D. Wilton, and A. Glisson, “Electromagnetic scattering by surfaces of arbitrary shape,” *IEEE Trans. Antennas Propagat.*, vol. 30, 409–418, May 1982.
- [10] R. D. Graglia, D. R. Wilton, and A. F. Peterson, “Higher order interpolatory vector bases for computational electromagnetics,” *IEEE Trans. Antennas Propagat.*, vol. 45, 329–342, March 1997.
- [11] M. G. Duffy, “Quadrature over a pyramide or cube of integrands with a singularity at a vertex,” *SIAM J. Numer. Anal.*, vol. 19, 1260–1262, December 1982.

- [12] A. Tzoulis and T. Eibert, “Review of singular potential integrals for method of moments solutions of surface integral equations,” *Advances in Radio Science*, vol. 2, 97–99, 2004.
- [13] W. C. Chew, J. M. Jin, E. Michielssen, and J. Song, *Fast and Efficient Algorithms in Computational Electromagnetics*. Artech House, 2001.
- [14] P. Ylä-Oijala and M. Taskinen, “Calculation of CFIE impedance matrix elements with RWG and $n \times$ RWG functions,” *IEEE Trans. Antennas Propagat.*, vol. 51, 1837–1846, August 2003.
- [15] R. E. Hodges and Y. Rahmat-Samii, “The evaluation of MFIE integrals with the use of vector triangle basis functions,” *Micro. Opt. Tech. Lett.*, vol. 14, 9–14, January 1997.
- [16] O. Ergül and L. Gürel, “Investigation of the inaccuracy of the MFIE discretized with the RWG basis functions,” *Proc. IEEE Antennas and Propagation Soc. Int. Symp.*, vol. 3, 3393–3396, 2004.
- [17] L. Gürel and O. Ergül, “Singularity of the magnetic-field integral equation and its extraction,” *IEEE Antennas Wireless Propag. Lett.*, vol. 4, 229–232, 2005.
- [18] J. M. Rius, E. Úbeda, and J. Parrón, “On the testing of the magnetic field integral equation with RWG basis functions in the method of moments,” *IEEE Trans. Antennas Propagat.*, vol. 49, 1550–1553, November 2001.
- [19] O. Ergül and L. Gürel, “Solid-angle factor in the magnetic-field integral equation,” *Microw. Opt. Technol. Lett.*, vol. 45, 452–456, June 2005.
- [20] O. Ergül and L. Gürel, “Improving the accuracy of the MFIE with the choice of basis functions,” *Proc. IEEE Antennas and Propagation Soc. Int. Symp.*, vol. 3, 3389–2292, 2004.
- [21] O. Ergül and L. Gürel, “The use of curl-conforming basis functions for the magnetic-field integral equation,” *IEEE Trans. Antennas Propagat.*, vol. 54, 1917–1926, July 2006.
- [22] E. Úbeda and J. M. Rius, “MFIE MoM-formulation with curl-conforming basis functions and accurate kernel integration in the analysis of perfectly conducting sharp-edged objects,” *Microw. Opt. Technol. Lett.*, vol. 44, 354–358, February 2005.
- [23] O. Ergül and L. Gürel, “Improving the accuracy of the magnetic field integral equation with the linear-linear basis function,” *Radio Sci.*, vol. 41, 2006.
- [24] O. Ergül and L. Gürel, “Linear-linear basis functions for MLFMA solutions of magnetic-field and combined-field integral equations,” *IEEE Trans. Antennas Propagat.*, vol. 55, 1103–1110, April 2007.

- [25] E. Anderson, Z. Bai, C. Bischof, S. Blackford, J. Demmel, J. Dongarra, J. Du Croz, A. Greenbaum, S. Hammarling, A. McKenney, and D. Sorensen, *LAPACK Users' Guide*. Society for Industrial and Applied Mathematics, 3rd ed., 1999.
- [26] A. C. Woo, H. T. G. Wang, M. J. Schuh, and M. L. Sanders, "Benchmark plate radar targets for the validation of computational electromagnetics programs," *IEEE Antennas Propagat. Magazine*, vol. 34, 52–56, December 1992.
- [27] G. H. Brown and J. O. M. Woodward, "Experimentally determined radiation characteristics of conical and triangular antennas," *RCA Review*, 425–452, 1952.
- [28] C. Leat, N. Shuley, and G. Stickley, "Triangular-patch model of bowtie antennas: validation against Brown and Woodward," *IEE Proc.-Microw. Antennas Propag.*, vol. 145, 465–470, December 1998.
- [29] W. L. Curtis, "Spiral antennas," *IRE Trans. Antennas Propagat.*, vol. 8, 298–306, May 1960.
- [30] J. A. Kaiser, "The archimedean two-wire spiral antenna," *IRE Trans. Antennas Propagat.*, vol. 8, 312–323, May 1960.

Chapter 8

The Fast Multipole Method

In previous chapters we discussed the computational complexities encountered in applying the method of moments to large problems. Foremost among these are storage of the MOM matrix and the potentially long compute time of the matrix factorization. Application of the iterative solvers of Section 3.4.4 can yield a shorter compute time for a small number of right-hand sides, however the runtime may still be high due to the required number of matrix-vector products. If the matrix does not fit into memory, one has few options besides modifying the problem to reduce the number of unknowns or the use of virtual memory, which may make the problem intractable because of the slow access time of swap space. This motivates the search for a technique that can reduce or eliminate many of these difficulties.

At its core, the MOM comprises the calculation of forces on a particle by many other particles. This belongs to the class of N -body problems, which are often encountered in areas of applied physics. As an example, if the motion of a star in space is desired, the gravitational forces on it due to all other stars must be computed at each time step. In a similar fashion, all other stars are also in motion and the forces on them must also be computed, resulting in an $N \times N$ problem at each point in time. When the relative number of objects is small, a brute-force pairwise calculation can be carried out for all time steps. When the number of particles grows to be large, however, the required number of calculations may be so large that they cannot be carried out in the available time. The fast multipole method (FMM) is a numerical algorithm introduced by Greengard and Rokhlin [1] for reducing the computational complexity of this problem. The FMM applies an error-controlled approximation to the system Green's function allowing the force due to a group of particles to be computed as if they were a single particle. When applied to vector electromagnetic problems, the interactions between well-separated groups of basis functions can be evaluated very quickly. This allows for a rapid calculation of the matrix-vector product in an iterative solver without needing to store many of the matrix elements. This increase in speed and reduction in memory allows us to solve existing problems much faster, as well as solve problems that could not have been attempted before.

8.1 THE MATRIX-VECTOR PRODUCT

To show how the FMM works together with the moment method, we will first look at the matrix-vector product inside an iterative solver. The MOM matrix \mathbf{Z} represents the interactions between all basis functions in the system, and the right-hand side vector \mathbf{b} represents the excitation of each basis function. When we compute the matrix-vector product $\mathbf{c} = \mathbf{Z}\mathbf{b}$, we are effectively computing the field received by each basis function due to radiation from all other basis functions. While the organization of basis functions in a given geometry is somewhat arbitrary, a pair of basis functions can be said to lie in each other's *near* or *far* region, as shown in Figure 8.1a. The basis functions in region A are considered to be "near" to the one in the center whereas those in region B are considered to be "far."

Consider now row m of \mathbf{Z} , which we label \mathbf{z}_{m*} . The product of this row with vector \mathbf{b} represents the field received by basis function m from all basis functions and can be written as

$$c_m = \mathbf{z}_{m*} \cdot \mathbf{b} = [z_{m1}, z_{m2}, z_{m3}, \dots, z_{mN}] \cdot [b_1, b_2, b_3, \dots, b_N] \quad (8.1)$$

Because some of the basis functions are in the "near" region of basis function m and others are in the "far" region, this dot product can be rewritten as

$$\mathbf{z}_{m*} \cdot \mathbf{b} = [\mathbf{z}_{m*}^{near} \ \mathbf{z}_{m*}^{far}] \cdot [\mathbf{b}^{near} \ \mathbf{b}^{far}] = \mathbf{z}_{m*}^{near} \cdot \mathbf{b}^{near} + \mathbf{z}_{m*}^{far} \cdot \mathbf{b}^{far} \quad (8.2)$$

where the elements in the sub-vectors \mathbf{z}_{m*}^{near} and \mathbf{b}^{near} contain only the source functions in the region near to basis function m , and \mathbf{z}_{m*}^{far} and \mathbf{b}^{far} contain only those in the far region. What the fast multipole method allows us to do is group together basis functions in the far region, and then quickly compute the value of $\mathbf{z}_m^{far} \cdot \mathbf{b}^{far}$ using multipole expansions of those groups. The value of $\mathbf{z}_{m*}^{near} \cdot \mathbf{b}^{near}$ is still computed using a straightforward moment method technique. As a result, the matrix elements that normally comprise \mathbf{z}_{m*}^{far} are no longer explicitly stored in memory, only those that lie in the \mathbf{z}_{m*}^{near} are actually computed and stored in the usual way. The matrix-vector product now comprises a *near multiply* step using the near MOM matrix and a *far multiply* using the FMM. We will discuss the practical implementation of these steps in this chapter.

8.2 ADDITION THEOREM

Consider again the three dimensional Green's function (without the $1/(4\pi)$ constant)

$$G(\mathbf{r}, \mathbf{r}') = \frac{e^{-jkr}}{r} = \frac{e^{-jk|\mathbf{r}-\mathbf{r}'|}}{|\mathbf{r}-\mathbf{r}'|} \quad (8.3)$$

where \mathbf{r}' and \mathbf{r} are the source and observation points, respectively. Let us now modify this expression by adding a small offset \mathbf{d} to the source location. The expression now

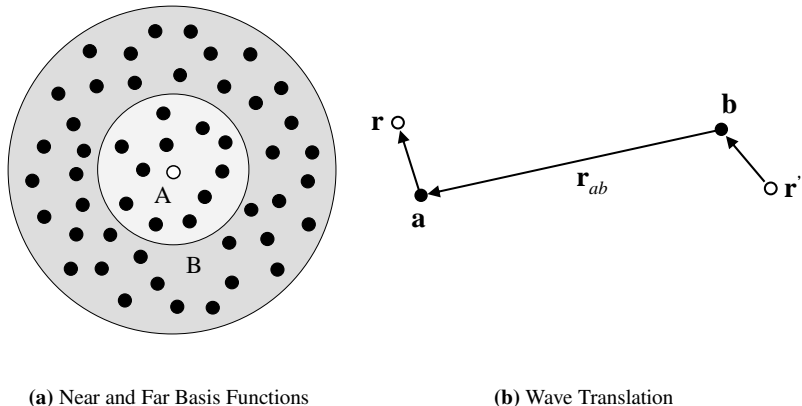


Figure 8.1: Basic FMM concepts.

reads

$$\frac{e^{-jk|\mathbf{r}-\mathbf{r}'+\mathbf{d}|}}{|\mathbf{r}-\mathbf{r}'+\mathbf{d}|} = \frac{e^{-jk|\mathbf{D}+\mathbf{d}|}}{|\mathbf{D}+\mathbf{d}|} \quad (8.4)$$

where $\mathbf{D} = \mathbf{r} - \mathbf{r}'$. We now define the *addition theorem* for spherical waves [2, 3]:

$$\frac{e^{-jk|\mathbf{D}+\mathbf{d}|}}{|\mathbf{D}+\mathbf{d}|} = -jk \sum_{l=0}^{\infty} (-1)^l (2l+1) j_1(k|\mathbf{d}|) h_l^{(2)}(k|\mathbf{D}|) P_l(\hat{\mathbf{d}} \cdot \hat{\mathbf{D}}) \quad (8.5)$$

where $j_1(x)$ is the spherical Bessel function of the first kind, and $P_l(x)$ is a Legendre polynomial of order l . $h_l^{(2)}(x)$ is a spherical Hankel function of the second kind, i.e.

$$h_l^{(2)}(x) = \sqrt{\frac{\pi}{2x}} H_{l+1/2}^{(2)}(x) = j_l(x) - j n_l(x) \quad (8.6)$$

where $j_l(x)$ and $n_l(x)$ are spherical Bessel functions of the first and second kinds, respectively. If we look closely at (8.5), we see that it is a way of writing a wave radiating from a point as if it was radiating from a different point nearby. This expansion remains valid provided that $|\mathbf{d}| < |\mathbf{D}|$.

Using Stratton [4], (8.5) can be converted to a surface integral on the unit sphere via the relationship

$$4\pi(-j^l) j_l(k|\mathbf{d}|) P_l(\hat{\mathbf{d}} \cdot \hat{\mathbf{D}}) = \iint_1 e^{-jk\hat{\mathbf{k}} \cdot \mathbf{d}} P_l(\hat{\mathbf{k}} \cdot \hat{\mathbf{D}}) dS \quad (8.7)$$

where $\hat{\mathbf{k}}$ is the unit direction (radial) vector on the sphere. Using this expression we can now write

$$\frac{e^{-jk|\mathbf{D}+\mathbf{d}|}}{|\mathbf{D}+\mathbf{d}|} = \frac{k}{4\pi} \iint_1 e^{-jk\hat{\mathbf{k}} \cdot \mathbf{d}} \sum_{l=0}^{\infty} (-j)^{l+1} (2l+1) h_l^{(2)}(k|\mathbf{D}|) P_l(\hat{\mathbf{k}} \cdot \hat{\mathbf{D}}) dS \quad (8.8)$$

where the integration and summation have been exchanged. This exchange will be legitimate provided that we truncate the summation at some finite order L , which we will do later. This truncation will also limit the acceptable values for \mathbf{D} and \mathbf{d} . Applying this truncation, we then write

$$\frac{e^{-jk|\mathbf{D}+\mathbf{d}|}}{|\mathbf{D}+\mathbf{d}|} = \iint_1 e^{-jk\hat{\mathbf{k}} \cdot \mathbf{d}} T_L(k, \hat{\mathbf{k}}, \mathbf{D}) dS \quad (8.9)$$

with

$$T_L(k, \hat{\mathbf{k}}, \mathbf{D}) = \frac{k}{4\pi} \sum_{l=0}^L (-j)^{l+1} (2l+1) h_l^{(2)}(k|\mathbf{D}|) P_l(\hat{\mathbf{k}} \cdot \hat{\mathbf{D}}) \quad (8.10)$$

which we refer to as the *transfer function*. This allows us to convert outgoing spherical waves emanating from a source point to a set of incoming spherical waves at an observation point.

8.2.1 Wave Translation

Let us use the addition theorem to calculate the Green's function between a source point \mathbf{r}' and observation point \mathbf{r} . Consider the vector

$$\mathbf{v} = \mathbf{r} - \mathbf{r}' \quad (8.11)$$

Let us now introduce a pair of points \mathbf{a} and \mathbf{b} that lie in close proximity to \mathbf{r} and \mathbf{r}' , respectively, as shown in Figure 8.1b. The above can now be written as

$$\mathbf{v} = (\mathbf{r} - \mathbf{a}) + (\mathbf{a} - \mathbf{b}) - (\mathbf{r}' - \mathbf{b}) \quad (8.12)$$

or

$$\mathbf{v} = \mathbf{r}_{ra} + \mathbf{r}_{ab} - \mathbf{r}_{r'b} \quad (8.13)$$

Using the above, we can rewrite the Green's function as

$$\frac{e^{-jk|\mathbf{r}-\mathbf{r}'|}}{|\mathbf{r}-\mathbf{r}'|} = \iint_1 e^{-jk\hat{\mathbf{k}}_s \cdot (\mathbf{r}_{ra} - \mathbf{r}_{r'b})} T_L(k, \hat{\mathbf{k}}, \mathbf{r}_{ab}) dS \quad (8.14)$$

where

$$T_L(k, \hat{\mathbf{k}}, \mathbf{r}_{ab}) = \frac{k}{4\pi} \sum_{l=0}^L (-j)^l (2l+1) h_l^{(2)}(k|\mathbf{r}_{ab}|) P_l(\hat{\mathbf{k}} \cdot \hat{\mathbf{r}}_{ab}) \quad (8.15)$$

This is an important result as the transfer function depends only on \mathbf{r}_{ab} . If we decide to move \mathbf{r} and \mathbf{r}' a small distance from their previous location, the transfer function remains unchanged. This allows us to compute the interaction between *any* two points near **a** and **b** using the *same* transfer function. If we now want to compute the sum of Green's functions evaluated between observation point \mathbf{r} and *many* source points \mathbf{r}_n located close to **b**, we can use the expression

$$\sum_{n=1}^N \frac{e^{-jk|\mathbf{r}-\mathbf{r}_n|}}{|\mathbf{r}-\mathbf{r}_n|} = \iint_1 e^{-jk\hat{\mathbf{k}} \cdot \mathbf{r}_{ra}} T_L(k, \hat{\mathbf{k}}, \mathbf{r}_{ab}) \sum_{n=1}^N e^{jk\hat{\mathbf{k}} \cdot \mathbf{r}_{rnb}} dS \quad (8.16)$$

The result in (8.16) is what allows us to quickly compute a matrix-vector product. For each source point we calculate the value of $e^{jk\hat{\mathbf{k}} \cdot \mathbf{r}_{brn}}$, which we call the *radiation function*. The radiation functions for all source points are next added coherently or *aggregated* to create a local field at **b**. This field is then *transmitted* using the transfer function, yielding a local field at **a**. This local field is then multiplied with the *receive function* of the observation point and integrated on the sphere (*disaggregation*), yielding the desired sum. In performing an FMM far multiply, we will sort all basis functions into local groups. The radiation and receive functions for all basis functions are precomputed, as well as the transfer functions linking together all group pairs. The far multiply then comprises aggregations, transfers and disaggregations of these functions between groups.

8.3 FMM MATRIX ELEMENTS

Now that we have covered the addition theorem and wave translation, we will use these results to derive radiation and receive functions used to compute the far EFIE and MFIE matrix elements. It is important to note that the following expressions are used to compute *individual* radiation and receive functions. Because the FMM operates on *aggregations* of these functions, the individual matrix elements are not explicitly available in practice. We also leave the points **a** and **b** undefined for now, and define them later when we discuss how the basis functions are sorted into groups.

8.3.1 EFIE Matrix Elements

Consider the EFIE matrix elements as written in (7.11). If we redistribute the differential operators so they work on the Green's function (Section 2.4.3), the elements can be written as

$$z_{mn}^E = \frac{1}{4\pi} \iint_{\mathbf{f}_m} \mathbf{f}_m(\mathbf{r}) \cdot \iint_{\mathbf{f}_n} \mathbf{f}_n(\mathbf{r}') \left[1 - \frac{1}{k^2} \nabla \nabla' \right] \frac{e^{-jkr}}{r} d\mathbf{r}' d\mathbf{r} \quad (8.17)$$

Applying the vector differential operations to the Green's function in (8.14) yields

$$\left[1 - \frac{1}{k^2} \nabla \nabla' \right] \frac{e^{-jkr}}{r} = \iint_1 [\bar{\mathbf{I}} - \hat{\mathbf{k}}\hat{\mathbf{k}}] e^{-jk\hat{\mathbf{k}} \cdot (\mathbf{r}_{ra} - \mathbf{r}_{rb})} T_L(k, \hat{\mathbf{k}}, \mathbf{r}_{ab}) dS \quad (8.18)$$

and inserting the above into (8.17) we can then write

$$z_{mn}^E = \frac{1}{4\pi} \iint_1 \mathbf{R}_{ra}^E(\hat{\mathbf{k}}) \cdot T_L(k, \hat{\mathbf{k}}, \mathbf{r}_{ab}) \mathbf{T}_{br'}^E(\hat{\mathbf{k}}) dS \quad (8.19)$$

where the **receive function** for testing function $\mathbf{f}_m(\mathbf{r})$ is

$$\mathbf{R}_{ra}^E(\hat{\mathbf{k}}) = [\bar{\mathbf{I}} - \hat{\mathbf{k}}\hat{\mathbf{k}}] \cdot \iint_{\mathbf{f}_m} e^{-jk\hat{\mathbf{k}} \cdot \mathbf{r}_{ra}} \mathbf{f}_m(\mathbf{r}) d\mathbf{r} \quad (8.20)$$

and the **radiation function** for basis function $\mathbf{f}_n(\mathbf{r}')$ is

$$\mathbf{T}_{br'}^E(\hat{\mathbf{k}}) = [\bar{\mathbf{I}} - \hat{\mathbf{k}}\hat{\mathbf{k}}] \cdot \iint_{\mathbf{f}_n} e^{jk\hat{\mathbf{k}} \cdot \mathbf{r}_{r'b}} \mathbf{f}_n(\mathbf{r}') d\mathbf{r}' \quad (8.21)$$

If RWG functions are used, the integrals in (8.20) and (8.21) can be evaluated analytically using (9.58). We next note that the expression

$$[\bar{\mathbf{I}} - \hat{\mathbf{k}}\hat{\mathbf{k}}] \cdot \mathbf{f}_{m,n}(\mathbf{r}, \mathbf{r}') \quad (8.22)$$

removes the components of $\mathbf{f}_{m,n}$ along $\hat{\mathbf{k}}$, preserving only the components along the spherical vectors $\hat{\theta}_s$ and $\hat{\phi}_s$. Only these two components need to be stored for each quadrature point on the unit sphere. Because the radiation, receive and transfer functions are uncoupled from one another, they can be computed separately.

8.3.2 MFIE Matrix Elements

Consider next the MFIE as written in (6.91). Because the FMM is used for basis functions that are not close to each other, we only need to consider the second term in this expression. Before taking the gradient, this term can be written as

$$z_{mn}^H = -\frac{1}{4\pi} \iint_{\mathbf{f}_m} \mathbf{f}_m(\mathbf{r}) \cdot \hat{\mathbf{n}}(\mathbf{r}) \times \iint_{\mathbf{f}_n} \mathbf{f}_n(\mathbf{r}') \times \mathbf{J}(\mathbf{r}') \left[\nabla' \frac{e^{-jkr}}{r} \right] d\mathbf{r}' d\mathbf{r} \quad (8.23)$$

Computing the gradient of (8.14) yields

$$\nabla' \frac{e^{-jkr}}{r} = jk \iint_1 \hat{\mathbf{k}} e^{-jk\hat{\mathbf{k}} \cdot (\mathbf{r}_{ra} - \mathbf{r}_{r'b})} T_L(k, \hat{\mathbf{k}}, \mathbf{r}_{ab}) dS \quad (8.24)$$

and substituting the above into (8.23) allows us to write

$$z_{mn}^H = -\frac{jk}{4\pi} \iint_1 \mathbf{R}_{ra}^H(\hat{\mathbf{k}}) \cdot T_L(k, \hat{\mathbf{k}}, \mathbf{r}_{ab}) \mathbf{T}_{br'}^H(\hat{\mathbf{k}}) dS \quad (8.25)$$

where the **receive function** for testing function \mathbf{f}_m is

$$\mathbf{R}_{ra}^H(\hat{\mathbf{k}}) = -\hat{\mathbf{k}} \times \iint_{\mathbf{f}_m} e^{-jk\hat{\mathbf{k}} \cdot \mathbf{r}_{ra}} [\mathbf{f}_m(\mathbf{r}) \times \hat{\mathbf{n}}(\mathbf{r})] d\mathbf{r} \quad (8.26)$$

and the **radiation function** for basis function \mathbf{f}_n is

$$\mathbf{T}_{br'}^H(\hat{\mathbf{k}}) = \iint_{\mathbf{f}_n} e^{j k \hat{\mathbf{k}} \cdot \mathbf{r}_{r'b}} \mathbf{f}_n(\mathbf{r}') d\mathbf{r}' \quad (8.27)$$

Note that the cross product with $\hat{\mathbf{k}}$ in (8.26) also has the effect of preserving only the $\hat{\theta}$ and $\hat{\phi}$ components of $\mathbf{R}_{ma}^H(\hat{\mathbf{k}})$. Therefore, only these components $\mathbf{T}_{bn}^H(\hat{\mathbf{k}})$ need to be computed, and, as a result, $\mathbf{T}_{br'}^H(\hat{\mathbf{k}}) = \mathbf{T}_{br'}^E(\hat{\mathbf{k}})$, which we will refer to as simply $\mathbf{T}_{br'}(\hat{\mathbf{k}})$.

8.3.3 CFIE Matrix Elements

Combining the radiation and receive functions for the EFIE and MFIE allows for a straightforward calculation of CFIE matrix elements via (2.139). These are

$$z_{mn}^C = \frac{1}{4\pi} \iint_1 \mathbf{R}_{ra}^C(\hat{\mathbf{k}}) \cdot T_L(k, \hat{\mathbf{k}}, \mathbf{r}_{ab}) \mathbf{T}_{br'}(\hat{\mathbf{k}}) dS \quad (8.28)$$

where

$$\mathbf{R}_{ra}^C(\hat{\mathbf{k}}) = \alpha \mathbf{R}_{ra}^E(\hat{\mathbf{k}}) + (1 - \alpha) \mathbf{R}_{ra}^H(\hat{\mathbf{k}}) \quad (8.29)$$

8.3.4 Matrix Transpose

Many of the iterative solvers discussed in Section 3.4.4 require products using the original matrix \mathbf{Z} as well as its transpose. If using the MFIE or CFIE, it is necessary to *interchange* the radiation and receive functions to obtain the transpose. This is not typically mentioned in the literature.

8.4 ONE-LEVEL FAST MULTIPOLE ALGORITHM

We are now ready to look at how the FMM and the moment method can be used together. We consider a one-level fast multipole algorithm and the practical issues involved in its numerical implementation. While the FMM is not limited to a particular geometry or basis function, we will focus on facet geometry and RWG functions as these are commonly used in MOM applications. We will then use many elements of the one-level FMM to develop the multi-level fast multipole algorithm in the next section.

8.4.1 Grouping of Basis Functions

Our first task is to group together basis functions, so we subdivide the object's bounding box into M small equally sized cubes with sides and diagonals of length w and $\sqrt{3w}$, respectively. The length w is usually set to some fraction of the wavelength, such as $\lambda/2$ or $\lambda/4$. We next assign basis functions to individual cubes

by testing the center of each edge against the bounding box of a cube, and any empty cubes that remain are discarded. Once this process is complete, we are left with a set of groups as shown in Figure 8.2a (shown in two-dimensions for simplicity), where each cube has a bounding sphere of diameter $d = \sqrt{3}w$.

8.4.2 Near and Far Groups

Now that we have created groups of basis functions, we can compute the Green's function between points in two groups via (8.14), assuming these groups are far enough apart. To do this we now assign the points \mathbf{a} and \mathbf{b} to be the center of each bounding sphere. Whether two groups lie near or far from each other is now a measure of the relative separation of these spheres. If we wish (8.5) to remain valid, then strictly speaking, the distance $|\mathbf{r}_{ab}|$ between groups must be greater than or equal to one diameter. If we use a grid of equally-sized bounding cubes, this requirement is satisfied if the groups are separated by at least one box. If separated in one of the key directions as shown in Figure 8.2b, the minimum separation distance between centers is $2w$. Therefore, for each group, we create a list of near and far groups. The list of near groups references the group itself and all directly adjacent groups, and the remaining groups are added to the list of far groups.

8.4.3 Number of Multipoles

To compute the transfer function (8.10) we must set the truncation limit L , referred to as the number of *multipoles*. It is a function of the diameter of the bounding spheres as well as the wavenumber, and expressions for its computation have been determined empirically. For single precision calculations, Rokhlin suggests the following formula [2]:

$$L = kd + 5 \log(kd + \pi) \quad (8.30)$$

and for double precision,

$$L = kd + 10 \log(kd + \pi) \quad (8.31)$$

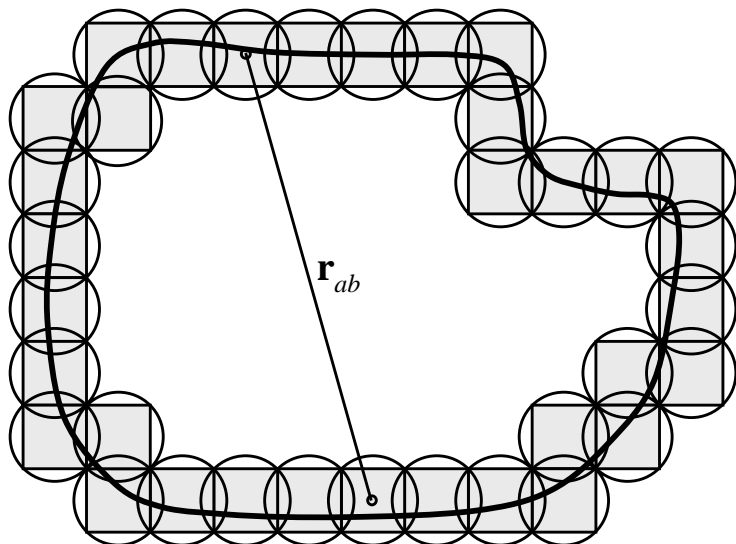
The following revised expression was later suggested by Chew and Song [5]:

$$L = kd + \beta(kd)^{1/3} \quad (8.32)$$

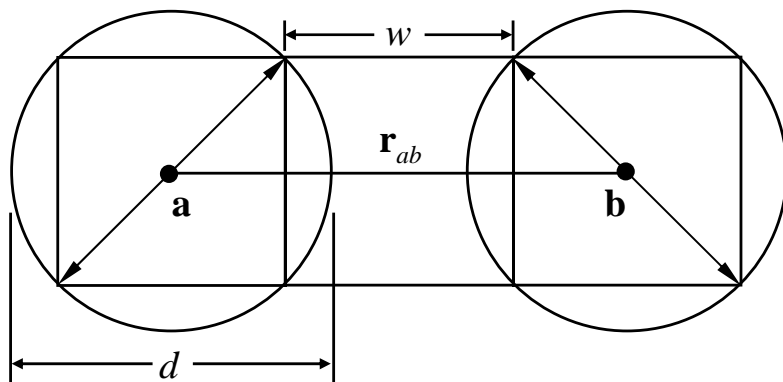
where β is the number of digits of required accuracy. It is suggested that $\beta = 6$ is sufficient for reasonable accuracy.

8.4.3.1 Limiting the Number of Multipoles

Grouping by cubes results in variable distances $|\mathbf{r}_{ab}|$ between groups. This leads to numerical problems if we use (8.32) to obtain a single value of L . This is because the spherical Hankel function $h_l^{(2)}(x)$ becomes highly oscillatory for fixed x and increasing l . As a result, we cannot take L to be much larger than the argument of



(a) Cubes and Bounding Spheres



(b) Cube Dimensions and Separation

Figure 8.2: One-level FMM grouping.

the Hankel function, $k|\mathbf{r}_{ab}|$. Therefore, we suggest limiting the value of L to the minimum of (8.32) and $k|\mathbf{r}_{ab}|$. This has the effect of reducing the accuracy of the expansion for the groups with smallest separations, but in practice this does not have a significant impact on the results.

8.4.4 Sampling Rates and Integration

For numerical integration, the radiation, receive and transfer functions must be computed and stored for a number of discrete directions on the unit sphere. We must choose the sampling rate to efficiently utilize the available system memory while still meeting the Nyquist rate. Because these functions are of finite (or *quasi-finite*) bandwidth [6], we need to investigate an efficient means of integrating the products of these functions on the sphere.

Consider a function $f_1(x)$ with bandwidth A , which we sample at a rate N_1 . Consider a similar function $f_2(x)$ of bandwidth B sampled at rate N_2 . To compute the integral of the product of these functions

$$\int_{x_1}^{x_2} f_1(x)f_2(x) dx \quad (8.33)$$

we use the quadrature formula

$$\int_{x_1}^{x_2} f_1(x)f_2(x) dx = \sum_{i=1}^{N_3} w(x_i)f_1(x_i)f_2(x_i) \quad (8.34)$$

where we have used a new sampling rate N_3 . Because the bandwidth of the product $f_1(x)f_2(x)$ is the sum of the individual bandwidths, the sample rate N_3 must be sufficiently high to represent the bandwidth of the product. This presents us with a dilemma, as the sampling rate required for integration on the sphere is greater than what is needed to store the radiation, receive and transfer functions individually. While a brute-force approach would simply compute all functions at this high sampling rate, this is wasteful in terms of memory. It is more efficient to store the individual functions at a lower sampling rate and interpolate or *upsample* them to the higher sampling rate before computing the products. Interpolation has consequences in terms of additional compute time required to upsample functions, as well as errors introduced by the interpolation itself. To simplify the present discussion, we will assume that all functions are sampled at the rate required for integration. We will then return to the subject of interpolation in Section 8.5.

8.4.4.1 Harmonic Representation

To determine the sampling rates required for numerical integration, let us write the transfer and exponential functions as a sum of band-limited spherical harmonic

functions. We note first that

$$P_l(\hat{\mathbf{a}} \cdot \hat{\mathbf{b}}) = \frac{4\pi}{2l+1} \sum_{m=-l}^l Y_l^{m*}(\hat{\mathbf{a}}) Y_l^m(\hat{\mathbf{b}}) \quad (8.35)$$

where Y_l^m are the spherical harmonics

$$Y_l^m(\theta, \phi) = P_l^{|m|}(\cos \theta) e^{jm\phi} \quad (8.36)$$

$P_l^m(\cos \theta)$ is the normalized associated Legendre polynomial given by

$$P_l^m(x) = \sqrt{\frac{2l+1}{4\pi} \frac{(l-m)!}{(l+m)!}} (1-x^2)^{m/2} \frac{d^m}{dx^m} P_l(x) \quad (8.37)$$

and $\hat{\mathbf{a}}$ and $\hat{\mathbf{b}}$ are functions of θ and ϕ . Using the Gegenbauer theorem,

$$e^{-j\mathbf{a}\cdot\mathbf{k}} = \sum_{l=0}^{\infty} (-j)^l (2l+1) j_l(|\mathbf{a}||\mathbf{k}|) P_l(\hat{\mathbf{a}} \cdot \hat{\mathbf{k}}) \quad (8.38)$$

we can then write the transfer and exponential functions as

$$T_L(k, \hat{\mathbf{k}}, \mathbf{D}) = k \sum_{l=0}^L (-j)^{l+1} h_l^{(2)}(k|\mathbf{D}|) \sum_{m=-l}^l Y_l^{m*}(\hat{\mathbf{D}}) Y_l^m(\hat{\mathbf{k}}) \quad (8.39)$$

and

$$e^{-jka\cdot\hat{\mathbf{k}}} = \sum_{l=0}^{\infty} (-j)^l j_l(k|\mathbf{a}|) \sum_{m=-l}^l Y_l^{m*}(\hat{\mathbf{a}}) Y_l^m(\hat{\mathbf{k}}) \quad (8.40)$$

where the truncation of (8.32) can also be applied to (8.40) with low error [7].

Applying (8.32), the transfer functions will have a bandwidth of L and the radiation and receive functions a bandwidth of $L/2$, as they are dependent on the radius of the bounding spheres and not the diameter. The product of these functions has a combined bandwidth of $2L$. The present quadrature scheme is based on the exact integration of band-limited spherical harmonic functions $Y_l^m(\theta, \phi)$ of order $l \leq 2L$. The optimal choice in this case is an L -point Gauss-Legendre rule in θ and a $2L+1$ -point uniform Simpson's rule in ϕ , which requires a total of $(2L+1)L$ samples on the sphere [3, 8]. In a practical FMM implementation these functions will undergo interpolation, which impacts the actual sampling rate used. We discuss this impact in Section 8.5.3.

8.4.5 Transfer Functions

The transfer functions between far group pairs must be precomputed and stored. As these functions depend on the direction vector between group centers, they must be

computed for all unique vectors $|\mathbf{r}_{ab}|$. Grouping by cubes results in a set of these vectors whose lengths are multiples of the box size w in the cardinal directions. As a result, many of these vectors may be repeated among different group pairs, and in such cases only one transfer function is needed. When generating far groups, a list of unique transfer functions should be generated and each group pair assigned the appropriate transfer function from this list.

8.4.6 Radiation and Receive Functions

The radiation and receive functions (8.20), (8.21), (8.26) and (8.27) should also be precomputed and stored for each basis function. If using the EFIE, only the radiation functions need to be computed, as the corresponding receive functions can be obtained by taking the conjugate. If using the MFIE or CFIE, the radiation and receive functions are stored separately.

8.4.7 Near-Matrix Elements

Matrix elements between basis functions in near groups are computed the traditional way. Loops over triangle pairs can be used to compute these near elements, however, the groups to which the basis functions belong are compared to determine if they are near or far groups. Only if they are near groups are the matrix elements for that basis function pair computed. Instead of allocating space for a global system matrix, a standard sparse matrix storage scheme is used.

8.4.7.1 Compressed Sparse Row Format

A sparse matrix storage scheme called the compressed sparse row format [9] is used to store the near matrix. To illustrate the format, consider the following sparse matrix:

$$\mathbf{A} = \begin{bmatrix} 1 & 2 & 0 & 0 & 0 \\ 3 & 4 & 5 & 0 & 0 \\ 0 & 6 & 7 & 8 & 0 \\ 0 & 0 & 9 & 10 & 0 \\ 0 & 0 & 0 & 0 & 11 \end{bmatrix} \quad (8.41)$$

which is of rank $N = 5$ and has $N_z = 11$ nonzero entries. The CSR format comprises three vectors \mathbf{a} , \mathbf{j} and \mathbf{i} , which are in this case

$$\begin{aligned} \mathbf{a} &= [1 2 3 4 5 6 7 8 9 10 11] \\ \mathbf{n} &= [1 2 1 2 3 2 3 4 3 4 5] \\ \mathbf{m} &= [1 3 6 9 11 12] \end{aligned} \quad (8.42)$$

The array \mathbf{a} is of length N_z and contains the nonzero elements of \mathbf{A} assembled row by row. Array \mathbf{n} is also of length N_z and contains the column indices of the matrix

elements a_{mn} as stored in **a**. Array **m** is of length $N + 1$, and contains offsets that point to the beginning of each row in **a** and **n**. Note that the last element of **m** contains an offset to the fictional row $m = N + 1$. The total storage requirement of the CSR format in bytes is therefore

$$N_{bytes} = N_z s_f + (N_z + N + 1) s_i \quad (8.43)$$

where s_f and s_i are the sizes of the float and integer types, respectively.

8.4.8 Matrix-Vector Product

We are now ready to compute the matrix-vector product $\mathbf{c} = \mathbf{Z}\mathbf{b}$. The product vector elements can be written

$$c_m = c_m^{near} + c_m^{far} \quad (8.44)$$

where c_m^{near} and c_m^{far} are the near and far multiply contributions, respectively. The product vector elements in the near multiply can be written as

$$c_m^{near} = \sum_b \sum_{n \in b} z_{mn}^{ab} c_n \quad (8.45)$$

where basis function m belongs to group a and the groups b are those near to a , including itself. The complete near-multiply step loops over all near-group pairs computing parts of the matrix-vector product between each pair. The product vector elements computed in the far-multiply step can be written as

$$c_m^{far} = \sum_{p=1}^K w_s(\hat{\mathbf{k}}_p) \mathbf{R}_m(\hat{\mathbf{k}}_p) \cdot \sum_b T_L(k, \hat{\mathbf{k}}_p, \mathbf{r}_{ab}) \sum_{n \in b} \mathbf{T}_n(\hat{\mathbf{k}}_p) \quad (8.46)$$

The innermost part of (8.46) is an aggregation of radiation functions $\mathbf{T}_n(\hat{\mathbf{k}})$ in groups b that are far away from group a and basis function m . The aggregated field is then transmitted to the local group via multiplication with the appropriate transfer function $T_L(k, \hat{\mathbf{k}}, \mathbf{r}_{ab})$. The received field is multiplied with the receive function $\mathbf{R}_m(\hat{\mathbf{k}})$ and integrated on the sphere (disaggregated). To efficiently implement the far-multiply step, storage space for aggregated and received fields first should be allocated for all groups. The radiation functions in each group are then aggregated and stored in the local array. A loop is then performed over all groups, where each aggregated field is transmitted via the correct transfer function to every far group. When this is complete, each group will have a local array that is a sum of fields *received* from all far groups. A loop is again performed over all groups, where this received field is multiplied with the *individual* receive functions in that group and integrated on the sphere. The result is then added to the corresponding product vector element.

8.4.9 Computational Complexity

Let us summarize the computational complexity of the matrix-vector product. If we assume there are N basis functions divided among G groups, each group will have about $M = N/G$ basis functions and B near groups (including itself). The total cost of the near multiply is then

$$T_1 = c_1 B NM \quad (8.47)$$

where c_1 is platform and software dependent. The cost of aggregating the radiation functions $\sum_{n \in b} \mathbf{T}_n(\hat{\mathbf{k}})$ for all basis functions is

$$T_2 = c_2 K N \quad (8.48)$$

The cost for computing all transfers $\sum_b T_L(k, \hat{\mathbf{k}}, \mathbf{r}_{ab})$ is

$$T_3 = c_3 K G (G - B) \quad (8.49)$$

and the cost of disaggregations is similar to the aggregations and is

$$T_4 = c_4 K N \quad (8.50)$$

Numerical analysis shows the total computational cost of the matrix-vector multiply to be [3]

$$T = C_1 NG + C_2 N^2 / G \quad (8.51)$$

which is minimized by choosing $G = \sqrt{C_2 N / C_1}$. This results in an algorithm whose complexity is $O(N^{3/2})$.

8.5 MULTI-LEVEL FAST MULTIPOLE ALGORITHM (MLFMA)

In the one-level algorithm, the number of transfers grows exponentially with the number of groups. While it offers a potential $O(N^{3/2})$ complexity and an overall memory savings, greater efficiency can be obtained by extending the one-level algorithm to a multi-level one. The multi-level fast multipole algorithm (MLFMA) applies the aspects of a one-level algorithm to groups arranged in a tiered hierarchy, reducing the total number of transfers and greatly accelerating the fast multiply part of the matrix-vector product.

8.5.1 Grouping via Octree

First let us consider the impact of using larger cubes in the one-level FMM. This reduces the overall number of transfers at the expense of increasing the size of the near matrix, and shifts more of the compute time to the near-matrix product. The sampling rate on the unit sphere will also increase, resulting in larger storage requirements for the radiation and receive functions. If we can devise a way to

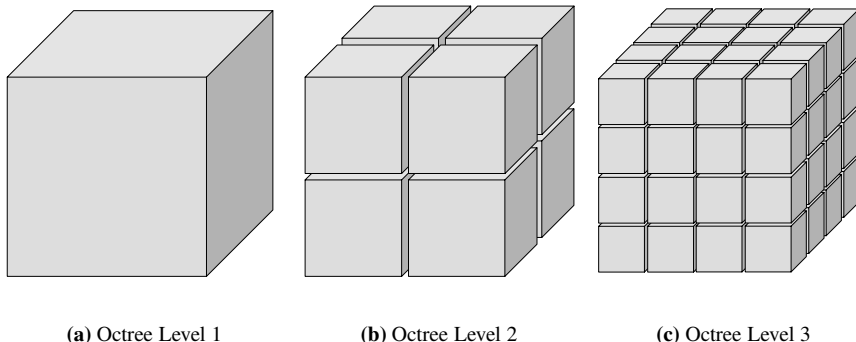


Figure 8.3: Octree levels 1–3.

use large and small boxes simultaneously, we can retain the storage benefits of smaller groups while reducing the transfer count. Subdivision of the geometry into a hierarchy of progressively smaller cubes allows us to do this. By applying a tree-based subdivision scheme, larger groups can be divided into recursively smaller groups with a clear parent-child relationship. An excellent choice for this is the octree [10], a commonly used hierarchical bounding box scheme in computer graphics. To generate an octree, the object is first enclosed in a single large cube. This cube is then divided into eight smaller cubes, which are themselves divided into eight smaller cubes, and so on, as illustrated in Figure 8.3. Edges are sorted into cubes at each level by testing them against the bounding box of each cube. This process is quite fast as only those edges belonging to a parent node become candidates for its children. The subdivision is stopped when the size of the cubes reaches some fraction of a wavelength, such as $\lambda/2$ or $\lambda/4$. The groups on this finest level of the tree (level l_{max}) are called *leaf* boxes.

Lists of near and far groups are constructed on all levels except the first two. The boxes on these levels are all near groups, and will not be used in the MLFMA algorithm. Beginning at the coarsest level (level 3), all near and far boxes are identified as usual. On the higher levels, only those child boxes that belong to cubes adjacent to a parent box (including itself) are considered as candidate near and far groups for its children. This greatly reduces the average number of far groups and also limits the number of unique transfer vectors to a maximum of 316 on each level. This is especially advantageous as the total number of transfers can be very high in larger problems.

8.5.2 Matrix-Vector Product

The matrix-vector product in the MLFMA operates on levels $l > 2$ in the tree. Because the radiation functions are stored on the finest level, an upward pass through the tree must be made where the radiation functions of the children are aggregated

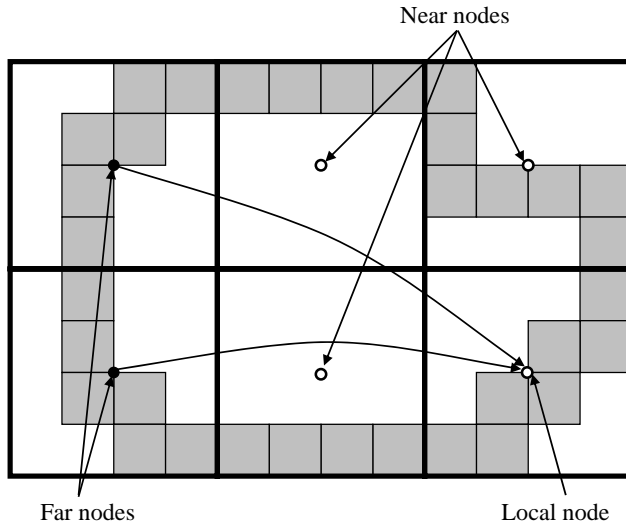


Figure 8.4: Transfers on MLFMA level $M - 2$.

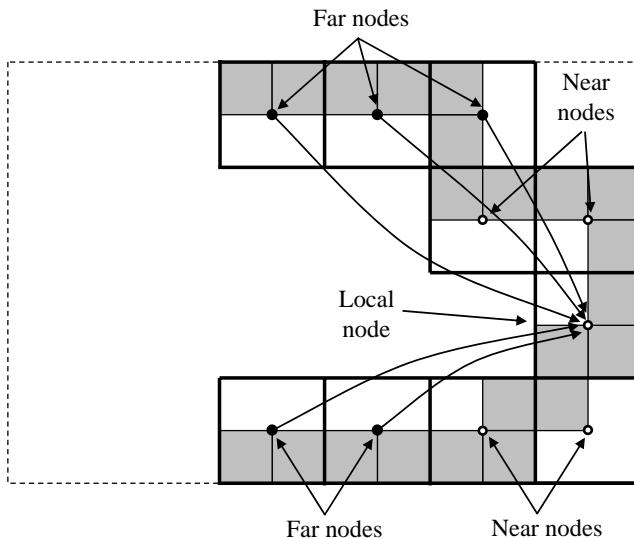


Figure 8.5: Transfers on MLFMA level $M - 1$.

and passed up to their parents using interpolation. A downward pass then begins at the coarsest level, where transfers are made between all far nodes, and then the received fields from all parent nodes are passed down to their children by combining integration on the sphere and “reverse interpolation” (anterpolation). The transfer

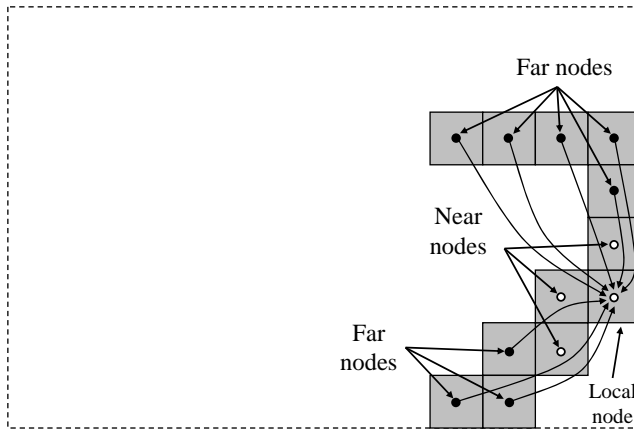


Figure 8.6: Transfers on MLFMA level M .

scheme in the MLFMA is illustrated in Figures 8.4–8.6. Figure 8.4 depicts the transfers between groups on one of the coarser levels. On the next highest level in Figure 8.5, all the far groups are children of groups considered to be near on the previous level. This is further emphasized on the finest level in Figure 8.6, where the number of far transfers is now far less than it would be in a one-level algorithm. We now describe the upward and downward passes in detail.

8.5.2.1 Upward Pass (Aggregation)

The aggregation step comprises an upward sweep through the tree. We begin at the finest level l_{max} , where aggregated local fields $\mathbf{C}_l(\hat{\mathbf{k}})$ are computed in individual groups using the radiation functions $\mathbf{T}_n(\hat{\mathbf{k}})$ and excitation vector elements b_n corresponding to basis functions in each group, i.e.,

$$\mathbf{C}_l(\hat{\mathbf{k}}) = \sum_n \mathbf{T}_n(\hat{\mathbf{k}}_l) b_n \quad (8.52)$$

The aggregated fields on the coarser levels are computed from phase shifted versions of the fields from children nodes, as illustrated in Figure 8.7. This can be written as

$$\mathbf{C}_{l-1}(\hat{\mathbf{k}}_{(l-1)}) = e^{jk\hat{\mathbf{k}}_{(l-1)} \cdot (\mathbf{r}_{b_l} - \mathbf{r}_{b_{l-1}})} \mathbf{C}_l(\hat{\mathbf{k}}_{(l)}) \quad (8.53)$$

where $(\mathbf{r}_{b_l} - \mathbf{r}_{b_{l-1}})$ is the vector from parent to child center. By applying the phase shift, $\mathbf{C}_{l-1}(\hat{\mathbf{k}}_{(l-1)})$ will have twice the bandwidth of $\mathbf{C}_l(\hat{\mathbf{k}}_l)$ and therefore requires the higher sampling rate K_{l-1} . Because $\mathbf{C}_l(\hat{\mathbf{k}}_l)$ was sampled at K_l points on the sphere, it must be upsampled to K_{l-1} points before applying the phase shift. This

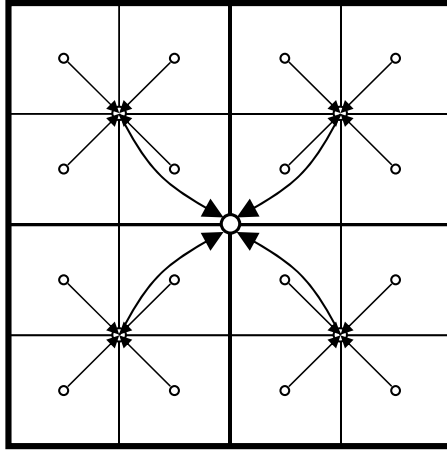


Figure 8.7: Upward pass in MLFMA.

interpolation can be written as [3]

$$\mathbf{C}_{l-1}(\hat{\mathbf{k}}_{(l-1)p}) = e^{-jk\hat{\mathbf{k}}_{(l-1)p} \cdot (\mathbf{r}_b - \mathbf{r}_{b,l-1})} \sum_{q=1}^{K_l} w_{pq} \mathbf{C}_l(\hat{\mathbf{k}}_{lq}) \quad (8.54)$$

where \mathbf{W} is a $K_{l-1} \times K_l$ interpolation matrix with elements w_{pq} , which allows the calculation of samples on the coarser level from those on the finer level. Note that the transpose of \mathbf{W} can be used to “reverse interpolate” the values of $\mathbf{C}_l(\hat{\mathbf{k}}_l)$ if $\mathbf{C}_{l-1}(\hat{\mathbf{k}}_{(l-1)})$ is known, a key element of the downward pass.

8.5.2.2 Downward Pass (Disaggregation)

Consider a group on level $l - 1$ in the tree. After all transfers on this level have been completed, this group contains a local field $\mathbf{B}_{(l-1)}(\hat{\mathbf{k}}_{(l-1)})$ comprising a sum of transfers from all its far nodes. Disaggregation with the receive function $\mathbf{R}_m(\hat{\mathbf{k}}_{(l-1)})$ can be written as

$$I = \sum_{p=1}^{K_{(l-1)}} w_s(\hat{\mathbf{k}}_{(l-1)p}) \mathbf{R}_{m(l-1)}(\hat{\mathbf{k}}_{(l-1)p}) \cdot \mathbf{B}_{l-1}(\hat{\mathbf{k}}_{(l-1)p}) \quad (8.55)$$

Because we store the receive function $\mathbf{R}_m(\hat{\mathbf{k}})$ on the finest level, it must be passed upward via interpolations and phase shifts to the coarser level to obtain $\mathbf{R}_{m(l-1)p}(\hat{\mathbf{k}}_{(l-1)})$. To do this for individual receive functions will be extremely inefficient, however, and another approach must be devised. To solve this problem, consider again the upsampling operation of (8.54). Substituting this expression into

(8.55) and interchanging the order of the summations yields

$$I = \sum_{q=1}^{K_l} \mathbf{R}_{ml}(\hat{\mathbf{k}}_{lq}) \cdot \sum_{p=1}^{K_{(l-1)}} w_{pq} \mathbf{B}_{(l-1)}(\hat{\mathbf{k}}_{(l-1)p}) e^{-jk\hat{\mathbf{k}}_{(l-1)p} \cdot (\mathbf{r}_{bl} - \mathbf{r}_{b_{l-1}})} w_s(\hat{\mathbf{k}}_{(l-1)p}) \quad (8.56)$$

which is called *adjoint interpolation* or *anterpolation* [3]. If we look closely, we see that this expression still upsamples the receive function $\mathbf{R}_{ml}(\hat{\mathbf{k}}_l)$ and performs integration on the sphere using weights $w_s(\hat{\mathbf{k}}_{(l-1)})$ on the coarser level. Because the innermost sum in (8.56) is now independent of the receive function, it can be used to create a “filtered” or “downsampled” field at the lesser sampling rate on the finer level, allowing us to work with each receive function individually.

We can now summarize the downward (disaggregation) pass as follows. We begin at the coarsest level (3) and perform transfers between all far groups. Because this is the lowest level, no anterpolations are required. We now move to the next higher level, and perform all transfers between far groups. To these fields we now add the anterpolated fields from the parent groups. This operation is then repeated for all higher levels until we reach the finest level. After transfers and anterpolations are done on this level, we can apply the outermost sum in (8.56) using the receive functions in each group, and add the results to the appropriate product vector elements. This completes the matrix-vector multiply using the MLFMA.

8.5.3 Interpolation Algorithms

Given a function $f(\theta, \phi)$ on the unit sphere, let us compute $K_1 = N_{\theta_1} \times N_{\phi_1}$ samples of this function and store them in vector \mathbf{a} . The interpolation problem involves computing one or more new samples of $f(\theta, \phi)$ using only the values stored in \mathbf{a} . If we now wish to compute $N_2 = N_{\theta_2} \times N_{\phi_2}$ samples in a new vector \mathbf{b} , this can be accomplished mathematically as

$$\mathbf{b} = \mathbf{W}\mathbf{a} \quad (8.57)$$

where \mathbf{W} is an $N_2 \times N_1$ matrix of carefully chosen interpolation coefficients. Individual elements b_i can be written as

$$b_i = \sum_{k=1}^{N_1} w_{ik} a_k \quad (8.58)$$

If $N_2 > N_1$, this operation *upsamples* \mathbf{a} , and if $N_1 < N_2$ it *downsamples* \mathbf{a} .

Methods for computing (8.57) fall into two general categories, *global* and *local*. In a global interpolation, the matrix \mathbf{W} is dense and each new sample b_i is computed using all the samples in \mathbf{a} . For a band-limited function, this interpolation can be exact provided the function is sampled at or above the Nyquist rate. In a local interpolation, \mathbf{W} is sparse and operates only on a subset of the original samples. Sparse interpolations do not typically produce an exact result, however

they are usually much faster and their error can be controlled. In the MLFMA, the interpolation and anterpolation steps must be fast, otherwise the performance of the matrix-vector multiply will suffer. Therefore, our interpolation scheme will use a local interpolation that attains a reasonable level of accuracy.

8.5.3.1 Global Interpolation by Spherical Harmonics

A band-limited function on the sphere can be interpolated using the spherical harmonic transform. In this, a function is said be *band-limited* with bandwidth L if it can be written as [11]

$$f(\theta, \phi) = \sum_{l=0}^L \sum_{m=-l}^l a_l^m Y_l^m(\theta, \phi) \quad (8.59)$$

where a_l^m are the spherical harmonic coefficients, and Y_l^m are the spherical harmonics of (8.36). The coefficients a_l^m are obtained via the integral over the unit sphere

$$a_l^m = \iint_1 Y_l^m(\theta, \phi) f(\theta, \phi) \sin \theta d\theta d\phi \quad (8.60)$$

which can be evaluated via a Gauss-Legendre quadrature in θ and Simpson's rule in ϕ . Once the coefficients have been calculated, an interpolated value can be evaluated at any angle pair (θ', ϕ') as

$$f(\theta', \phi') = \sum_{l=0}^L \sum_{m=-l}^l a_l^m Y_l^{m*}(\theta', \phi') \quad (8.61)$$

and substitution of (8.60) into the above yields

$$f(\theta', \phi') = \sum_{l=0}^L \sum_{m=-l}^l Y_l^{m*}(\theta', \phi') \sum_{k=1}^{K_1} w_k Y_l^m(\theta_k, \phi_k) f(\theta_k, \phi_k) \quad (8.62)$$

where $f(\theta, \phi)$ has been sampled at K_1 points and w_k is the quadrature weight on the sphere. The summations can next be exchanged, yielding

$$f(\theta', \phi') = \sum_{k=1}^{K_1} w_k \sum_{l=0}^L \sum_{m=-l}^l Y_l^{m*}(\theta', \phi') Y_l^m(\theta_k, \phi_k) f(\theta_k, \phi_k) \quad (8.63)$$

This leads to the interpolation matrix \mathbf{W} with elements given by

$$w_{ik} = w_k \sum_{l=0}^L \sum_{m=-l}^l Y_l^{m*}(\theta_i, \phi_i) Y_l^m(\theta_k, \phi_k) \quad (8.64)$$

Under this method, the matrix \mathbf{W} is full. To obtain an efficient interpolation, this method can be modified to utilize only those coefficients in the range of the interpolated value $f(\theta_i, \phi_i)$. A method of sparsifying the coefficients of (8.64) is discussed extensively in [8].

8.5.3.2 Global Interpolation By FFT

For a band-limited function, the fast fourier transform (FFT) can be used in the FMM to produce an upsampled version of $f(\theta, \phi)$ that is free from error. This can be accomplished by performing the forward FFT in each dimension, zero padding by the appropriate amount, and taking the inverse FFT [12]. Because the FFT requires equally spaced samples in each dimension, the integration in θ must be changed to a uniformly spaced quadrature rule. Because this would require more sample points in θ than the Gauss-Legendre quadrature, one could instead use the Fourier interpolation in ϕ and the dense interpolation of Section (8.5.3.1) along θ . The dense interpolation could then be improved via the spectral truncation method of [11].

8.5.3.3 Local Interpolation By Lagrange Polynomials

Lagrange polynomials are an effective means of creating an interpolator with local support. Given N samples of a function $f(x)$, this method generates a unique polynomial of order $N - 1$ to interpolate the samples. New values $f(x')$ can then be written as

$$f(x') = \sum_{i=1}^N w_i(x') f(x_i) \quad (8.65)$$

where the weights can be written as

$$w_i(x') = \frac{(x' - x_1) \cdots (x' - x_{i-1})(x' - x_{i+1}) \cdots (x' - x_{N+1})}{(x_i - x_1) \cdots (x_i - x_{k-1})(x_i - x_{i+1}) \cdots (x_i - x_{N+1})} \quad (8.66)$$

or

$$w_i(x') = \prod_{\substack{k=1 \\ k \neq i}}^N \frac{x' - x_k}{x_i - x_k} \quad (8.67)$$

Interpolation on the sphere employs an $N \times N$ interpolation *stencil* as illustrated in Figure 8.8 for $N = 3$. In this case, \mathbf{W} will have nine nonzero entries per row. The choice of a quadratic or cubic interpolator ($N = 3, N = 4$) can provide reasonable results with small error provided that oversampling is applied. An error analysis of this method is discussed in [13]. This method could also be combined with the FFT interpolation outlined in Section 8.5.3.2. We use the Lagrange stencil method in *Serenity* with $N = 3$ and an oversampling factor of $a \approx 2$ at each step with very good results.

8.5.4 Transfer Functions

In the octree, boxes on level l have a width and bounding sphere diameter of w_l and d_l , respectively. A set of transfer functions should be computed for all unique transfer vectors on each level (potentially 316). The number of multipoles L is determined via (8.32) using the values of w_l and d_l on each level, and should be limited for

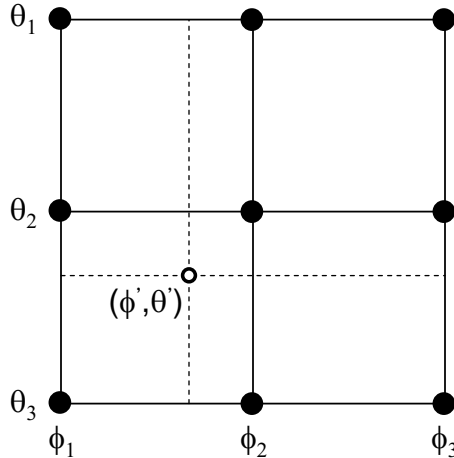


Figure 8.8: Interpolation stencil.

the closer groups as before. Because the maximum number of transfer functions is limited, they can be precomputed and stored at the sampling rate required for integration on each level. This eliminates the need to upsample the transfer functions when needed. If the Lagrange interpolator of Section 8.5.3.3 is used in the MLFMA, the transfer functions should be oversampled by a factor of a , resulting in a total of ($N_\theta = aL$, $N_\phi = a(2L + 1)$) samples for each function.

For very large problems, the time required to compute the transfer functions on the coarser levels can grow very large. Because they depend only on the value $\theta = \hat{\mathbf{k}} \cdot \hat{\mathbf{D}}$, the functions on each level can be computed via interpolation using an array of samples computed from (8.10) in the range $0 < \theta < \pi$. This can be accomplished using a Lagrange polynomial interpolation with oversampling [3]. It is also suggested in [14] that the various symmetries involved in the term $\hat{\mathbf{k}} \cdot \hat{\mathbf{D}}$ can be exploited to reduce the required storage of the transfer functions even further.

8.5.5 Radiation and Receive Functions

Radiation and receive functions should be computed and stored on the finest level, where the required sampling rate is smallest. If the Lagrange interpolator of Section 8.5.3.3 is used, the radiation functions should be oversampled by a factor of a , resulting in a total of ($N_\theta = aL/4$, $N_\phi = a(2L + 1)/4$) samples for each function.

8.5.6 Interpolation Steps in MLFMA

We now need to implement interpolation and anterpolation at the various stages of the MLFMA far multiply. The scheme described here is what we have implemented in *Serenity*.

8.5.6.1 Upward Pass

Starting at the finest level, interpolators are built to upsample radiation patterns between all levels up to the coarsest level (3). For points on each level, the interpolator contains interpolation weights and indexes pointing to samples on the next finest level. Aggregated radiation patterns are stored using ($N_\theta = aL/4$, $N_\phi = a(2L+1)/4$) samples on each level, where a is the oversampling factor. This choice minimizes the memory required to store all aggregated fields during the upward pass, however it requires an additional interpolation before the fields are multiplied with a transfer function.

8.5.6.2 Transfer Step

The aggregated radiation patterns must be upsampled again before they are transmitted between far groups. Because the transmitted fields will be immediately multiplied with the integration weights on the sphere, they must be at the rate required for integration when this is done. Therefore, interpolators are built to upsample the aggregated radiation patterns to ($N_\theta = aL$, $N_\phi = a(2L+1)$) points before the transfers are performed.

8.5.6.3 Downward Pass

Because the anterpolators “reverse interpolate” the received fields between levels in the downward pass, they are functionally equivalent to the interpolators in the upward pass but generate samples on the finer level from the coarser level. Anterpolators between levels 3 and $l_{max} - 1$ operate between the sampling rates for integration. The interpolator between levels $l_{max} - 1$ and l_{max} is slightly different, as it converts from the sampling rate of integration to that of the stored receive pattern.

8.5.7 Computational Complexity

Moving from the one-level FMM to the MLFMA reduces the computational complexity of the matrix-vector multiply in surface-scattering problems from $O(N^{3/2})$ to $O(N \log N)$. It has also been demonstrated through numerical simulations that the overall memory requirement of the MLFMA is also $O(N \log N)$ [3]. This reduction in memory and compute time is what makes the MLFMA such a powerful tool in the solution of very large MOM problems.

8.6 NOTES ON SOFTWARE IMPLEMENTATION

8.6.1 Initial Guess in Iterative Solution

When applying an iterative solver to a problem, there is usually little in the way of a priori knowledge about the solution vector. Therefore, for the first right-hand side

it usually makes sense to use a vector of zeros for the initial guess. If the excitation source is then slightly changed, the number of iterations can be greatly reduced if the previous solution is reused as the initial guess. This is especially advantageous in radar cross section calculations, where the RCS is usually computed over a range of closely spaced angles. It is suggested in [3] that for RCS problems, the improvement from reuse of the previous solution can be improved by adjusting its phase between angles. Given an incident vector $\hat{\mathbf{r}}_1$, the incident phase will be of the form

$$\psi_1(\mathbf{r}) = e^{jk\hat{\mathbf{r}}_1 \cdot \mathbf{r}} \quad (8.68)$$

Between angles, the following adjustment can then be made to the solution vector:

$$\Delta\psi(\mathbf{r}) = e^{jk(\hat{\mathbf{r}}_2 - \hat{\mathbf{r}}_1) \cdot \mathbf{r}} \quad (8.69)$$

As an example, consider the number of iterations required to compute the monostatic RCS of the ogive in Section 8.8.2.2 in 1-degree steps. In Figure 8.9, we compare the results for three different initial guesses: a zero right-hand side, previous solution with no phase adjustment, and previous solution with phase adjustment according to (8.69). It is seen that reuse of the previous solution vector without phase adjustment offers little to no improvement over the zero initial guess. With the phase adjustment, however, the iteration count drops significantly for almost all incident angles.

8.6.1.1 Physical Optics for Initial Guess

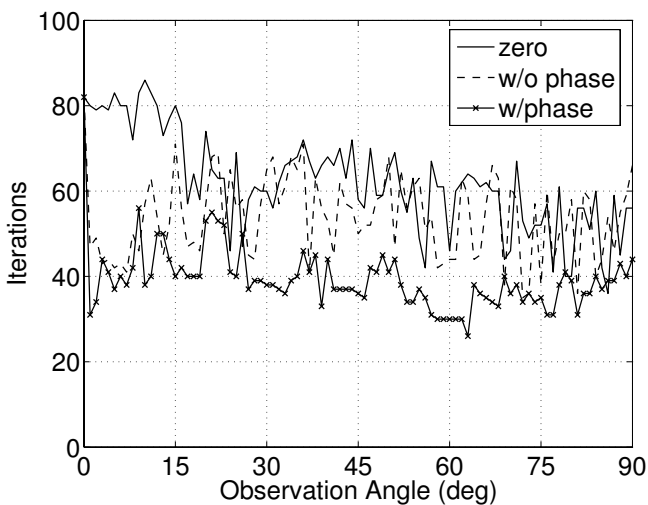
If no previous solution vector is available, the physical optics approximation (2.116) can be used to obtain a reasonable first-order approximation to the solution vector. To obtain the coefficient vector element for each RWG function, consider edge m shared by triangles T_m^+ and T_m^- . The coefficient a_m can then be estimated as

$$a_m = u(\mathbf{r}_c^+) \mathbf{f}_m(\mathbf{r}_c^+) \cdot \left[2\hat{\mathbf{n}}^+ \times \mathbf{H}^i(\mathbf{r}_c^+) \right] + u(\mathbf{r}_c^-) \mathbf{f}_m(\mathbf{r}_c^-) \cdot \left[2\hat{\mathbf{n}}^- \times \mathbf{H}^i(\mathbf{r}_c^-) \right] \quad (8.70)$$

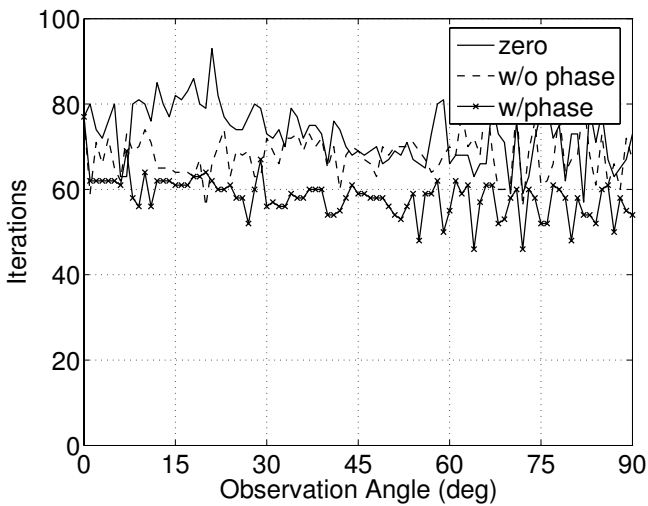
where \mathbf{r}_c^+ and \mathbf{r}_c^- are the centroids of triangles T_m^+ and T_m^- , respectively. The function $u(\mathbf{r})$ becomes zero or one when the centroids are illuminated or shadowed, respectively.

8.6.2 Memory Management

The local fields generated during aggregation are required during each transfer step. Therefore, the aggregated field arrays should be allocated during setup and remain static, or at least be allocated and deallocated before and after each iteration. Storage of the fields during disaggregation is more costly than that of the aggregation step, and should be managed to reduce the overall memory burden. Storage must be maintained for the fields on each level as well as those on the previous level until



(a) Vertical Polarization



(b) Horizontal Polarization

Figure 8.9: Iteration counts for different initial guesses.

interpolations have been performed. At that point, the field arrays for the previous level are no longer required and can be deallocated.

Because the near-matrix, transfer and radiation vector elements do not change between iterations, their memory space should be allocated during setup and remain static during the entire run.

8.6.3 Parallelization

Parallelization of an FMM algorithm is a challenging problem. In this section, we summarize the approach used to parallelize the MLFMA algorithms in *Serenity* for shared-memory systems. Parallelization on distributed-memory systems is a problem currently receiving considerable attention at the academic level, and is beyond the scope of this text. The reader is referred to several approaches discussed in the literature [7, 15, 16, 17, 18, 19] for additional information.

8.6.3.1 Shared-Memory Systems

When calculating the radiation and receive functions, the array space for each basis function may be accessed by different threads. Because the number of unknowns in an FMM problem is typically much greater than a full-matrix approach, assigning a mutex to each basis function is not practical. We instead assign a mutex to each leaf node, and lock the mutex of the node to which a basis function belongs. This approach is also used during the near-matrix calculation to protect elements in the near-matrix array.

The aggregation stage in the MLFMA can be parallelized by assigning individual octree nodes to a processing thread. Because the aggregated field in a node only depends on the fields of its child nodes, contention during this stage is avoided provided that all threads are synchronized before moving to the next coarsest level.

The disaggregation stage is also parallelized by individual node, with thread synchronization at several points. On each level, each thread first performs a transfer of the local field in its node to all far nodes. During the transfer, the mutex associated with each far node must be locked to ensure one thread at a time accesses its received field. A synchronization is done at the end of the transfer step. Interpolations are performed next, and threads are synchronized when complete. Because basis functions are assigned to unique nodes, no contention is encountered on the finest level when generating result vector elements. When each thread finishes on the finest level, the disaggregation is complete.

8.6.4 Vectorization

A section of code that performs multiplication and addition of long arrays is a good candidate for vectorization. In the past, most supercomputer processors were of the vector type, designed to operate on many data elements at once. Most of the consumer-level CPU architectures in the last 15 years have instead been largely

scalar, with registers operating on single data elements. Subsequent processor releases by manufacturers such as Intel, AMD and IBM have introduced new registers and instructions intended to operate on multiple data elements (typically four at a time). These new operations are commonly referred to as single instruction, multiple data (SIMD). The streaming SIMD extensions (SSE) present in Intel Pentium III and later processors can operate on arrays of four 32-bit floats (128 bits). The AMD Athlon processors also support these SSE instructions. The AltiVec instruction set in the PowerPC processor is very similar to SSE, and also operates on four floats at once.

In the FMM, the aggregation and transfer operations are composed of additions and multiplications that can be optimized using these SIMD instructions. If using SSE instructions, for example, the radiation and transfer functions must be stored in 16-byte aligned arrays, allowing for efficient transfers to and from the SSE registers. The complex additions and multiplications can then be performed using the **addps**, **subps** and **mulpss** instructions. Though some compilers will attempt to optimize sections of code given the appropriate directives, these portions of the code should be written in assembly language for maximum performance.

8.7 PRECONDITIONING

We briefly discussed the concepts of preconditioning in Section 3.4.5.1. The aim in preconditioning the iterations is to lessen the overall compute time per right-hand side, or to improve the overall convergence in ill-conditioned problems. Because the preconditioning step adds to the overall compute time per iteration, it should have at least the same general computational cost as the FMM, or less if possible.

Building a preconditioner that works with the FMM is somewhat different than a full-matrix solver, because many of the matrix elements are no longer explicitly available. Therefore, the preconditioner must be built from the near-matrix elements only. With this in mind, we will now briefly discuss some commonly used preconditioning schemes.

8.7.1 Diagonal Preconditioner

The diagonal or *Jacobi* preconditioner is the simplest form of preconditioner and is useful for illustrating the concept, however in practice it typically results in a very poor approximation for \mathbf{A}^{-1} and is not recommended for general use. The elements of the diagonal preconditioner matrix \mathbf{M} are defined as

$$m_{ij} = a_{ij} \quad i = j \quad (8.71)$$

$$m_{ij} = 0 \quad i \neq j \quad (8.72)$$

The diagonal preconditioner requires no extra storage as the elements in \mathbf{M}^{-1} can be computed on the fly during the preconditioning step. For computational efficiency, the diagonal elements would be precomputed and stored in their own

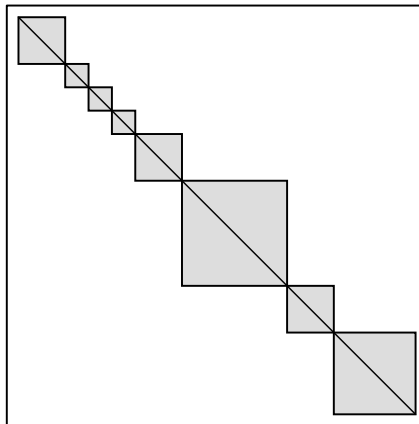


Figure 8.10: Block diagonal matrix.

vector, however this vector is of length N and does not appreciably increase the memory requirements.

8.7.2 Block Diagonal Preconditioner

Another conceptually simple preconditioner is the *block diagonal* preconditioner. In this case, \mathbf{M}^{-1} is constructed from blocks of \mathbf{A} comprising the larger-value elements close to the matrix diagonal, as illustrated in Figure 8.10. As a result, \mathbf{M}^{-1} will have the same block structure as \mathbf{A} and the LU factorization of each block can be computed independently of the others. If each block is relatively small, the preconditioning operation $\mathbf{z} = \mathbf{M}^{-1}\mathbf{r}$ can be performed relatively quickly, resulting in a small overhead. To implement this preconditioner in the FMM, consider the interactions between a group and all near groups (including itself). We expect that the strongest near-matrix elements are those between basis functions located close together. Therefore, it is reasonable to assume that most of these elements exist in the part of the matrix comprising the interactions of each group with itself. If we then use only the near-matrix elements in each group to generate the preconditioner, we will have the block diagonal structure of Figure 8.10. This preconditioner was previously reported in [3, 20].

8.7.3 Inverse LU Preconditioner

An incomplete LU (ILU) factorization computes an upper and lower triangular sparse matrix pair \mathbf{L} and \mathbf{U} such that the residual matrix $\mathbf{R} = \mathbf{A} - \mathbf{LU}$ satisfies certain criteria, such as a particular sparsity pattern. The simplest form of the ILU preconditioner is the incomplete LU factorization with no fill in, denoted as ILU(0). In this factorization, the factor \mathbf{L} has the same pattern as the lower part of \mathbf{A} and the factor \mathbf{U} has the same pattern as the upper part of \mathbf{A} . The problem with this

factorization is that the product \mathbf{LU} will have nonzero diagonals that are not present in \mathbf{A} [9]. As we will see in Section 8.7.4.1, the ILU(0) factorization can perform well despite this limitation. Because its sparsity pattern is defined to be that of the FMM near matrix, its memory requirements will be identical.

Improvements on this scheme, such as the incomplete LU factorization with thresholding (ILUT), are also useful. The ILUT algorithm generates the zero pattern of the factors on the fly by dropping elements based on their magnitudes instead of their location. As a result, the memory demands of ILUT may vary depending on the amount of fill-in, and may exceed the storage of the original near-matrix depending on the chosen fill-in parameters. For more detailed information on ILUT, the reader is referred to [9].

8.7.4 Sparse Approximate Inverse

Another method of finding an inverse to a sparse matrix is to minimize the Frobenius norm of the residual matrix $\mathbf{I} - \mathbf{AM}$:

$$F(\mathbf{M}) = \|\mathbf{I} - \mathbf{AM}\|_F^2 \quad (8.73)$$

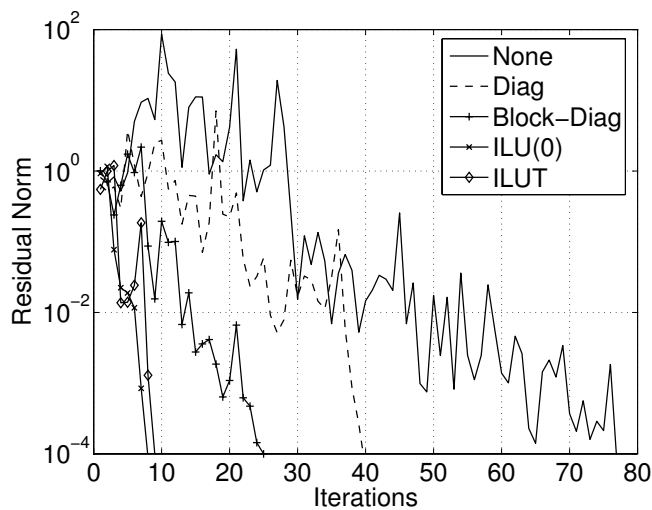
where \mathbf{M} is an *approximate inverse* [9]. The expression in (8.73) can be rewritten as

$$\|\mathbf{I} - \mathbf{AM}\|_F^2 = \sum_{n=1}^N \|\mathbf{e}_n - \mathbf{Am}_n\|_2^2 \quad (8.74)$$

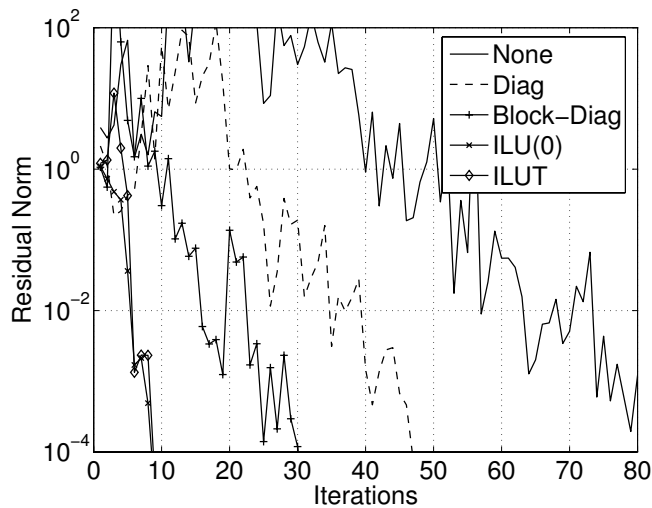
which is the sum of the squares of the 2-norms of the columns of the residual matrix. In [9], Saad discusses a global minimum residual iteration algorithm for solving (8.73), as well as column-oriented algorithms for solving the N independent subproblems in (8.74). In both algorithms, the current estimate of \mathbf{M} can be used to precondition subsequent iterations.

8.7.4.1 Comparison of Preconditioners

Let us consider the performance of several preconditioners in this section by computing the monostatic RCS of the ogive in Section 8.8.2.2. The CFIE formulation is used, and CGS iteration is applied to a residual norm of 10^{-4} . We first compare the rate of convergence of the diagonal, block diagonal, ILU(0) and ILUT preconditioners. The calculation is made at 0 degrees elevation and 20 degrees azimuth, and the initial guess is set to zero for both polarizations. For the ILUT preconditioner, 2 percent fill-in is allowed and a drop tolerance of 10^{-3} is used. The results are shown in Figures 8.11a and 8.11b for vertical and horizontal polarizations, respectively. The diagonal preconditioner yields a surprising improvement in the overall iteration count. The block diagonal preconditioner reduces the iterations by two thirds compared to no preconditioning. The ILU(0) and ILUT preconditioners yield the most dramatic improvement to the iteration count, and reach the desired residual norm in under ten iterations. We next consider the performance across multiple incident

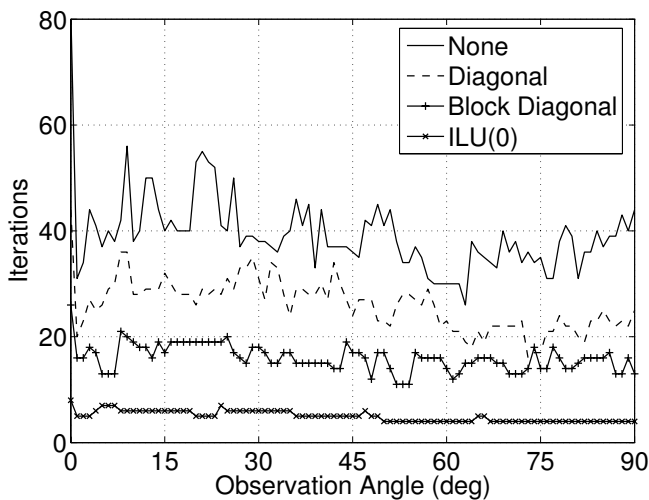


(a) Vertical Polarization

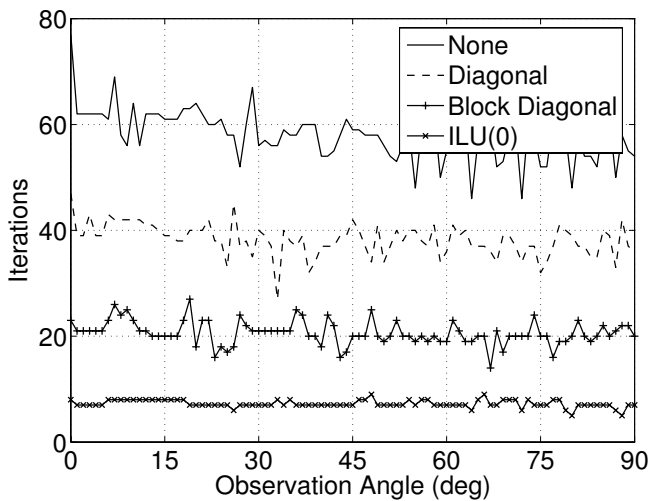


(b) Horizontal Polarization

Figure 8.11: Preconditioner performance on Ogive at 20° azimuth.



(a) Vertical Polarization



(b) Horizontal Polarization

Figure 8.12: Preconditioner performance on Ogive across multiple angles.

Table 8.1: Preconditioner Summary

Preconditioner	Near MB	Prec. MB	N_{iter} (V)	N_{iter} (H)
None	330.5	N/A	77	84
Diagonal	330.5	0.5	40	47
Block Diagonal	330.5	20.0	25	31
ILU(0)	330.5	330.5	8	9
ILUT	330.5	327.5	9	9

angles. We compute the RCS for azimuth angles between 0 and 90 degrees in 1-degree increments, and reuse the previous solution with phase correction according to (8.69). The iteration counts are shown in Figures 8.12a and 8.12b for vertical and horizontal polarizations, respectively. The results are consistent with those in Figures 8.11a and 8.11b. Because the results of the ILU(0) and ILUT preconditioners are almost identical, only the ILU(0) results are shown. The preconditioner memory requirements and iteration counts are summarized in Table 8.1.

8.8 EXAMPLES

In this section we look at some three-dimensional scattering problems that would be too large to solve using the full-matrix approach. In each example, we use the MLFMA-accelerated portion of our code *Serenity* with CFIE ($\alpha = 0.5$) and CGS iterations to a minimum residual of 10^{-4} . For each case, we use the ILUT preconditioner with 5 percent maximum fill-in and a drop tolerance of 10^{-3} .

8.8.1 Bistatic RCS of a Sphere

We first compute the bistatic RCS of the 2-meter sphere at 750 and 1500 MHz. The numerical results are compared to those of the Mie series in Figures 8.13 and 8.14. The comparison is excellent for both polarizations.

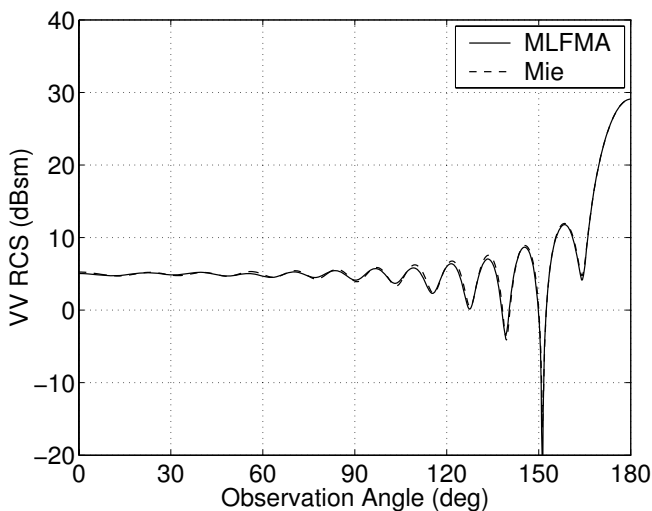
8.8.2 EMCC Benchmark Targets

We next compute the RCS of the EMCC benchmark radar targets described in [21].

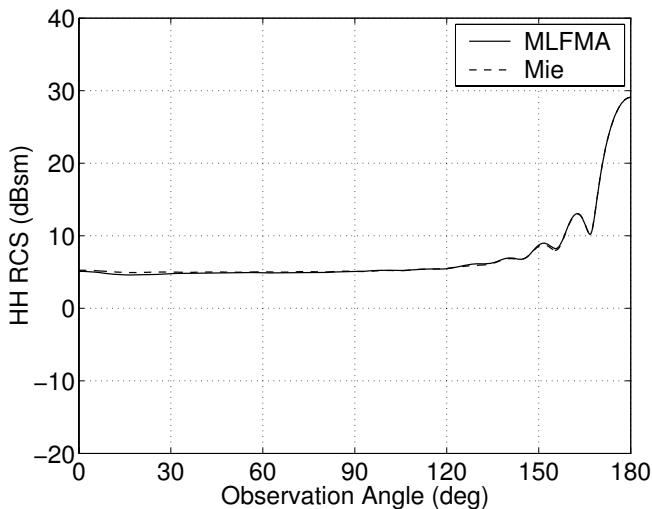
8.8.2.1 NASA Almond

The 9.936-inch NASA almond described in Figure 8.15 is a scattering-rich target composed of a smooth surface that supports traveling waves and a pointed end resulting in tip diffraction effects. It can be expressed for $0 < \phi < 2\pi$ as [21]

$$x = dt \quad (8.75)$$

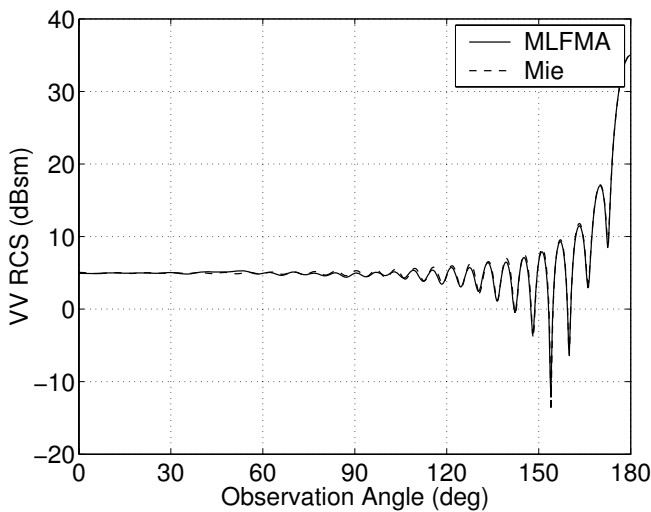


(a) Vertical Polarization

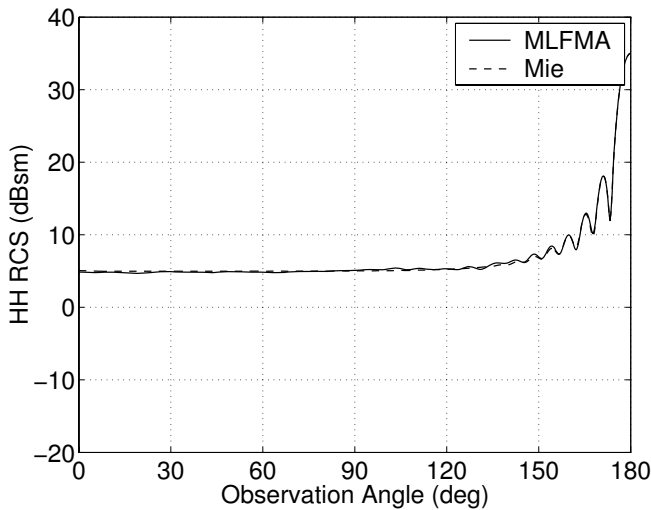


(b) Horizontal Polarization

Figure 8.13: 2-Meter sphere: bistatic RCS at 750 MHz.

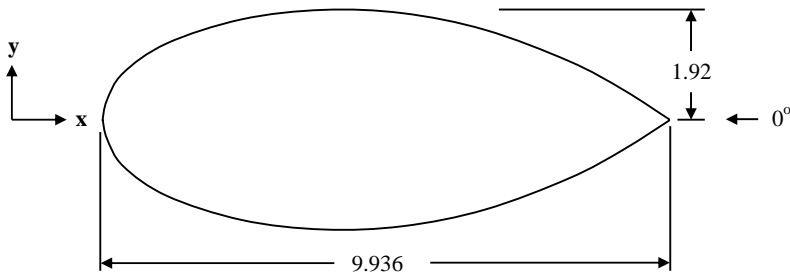
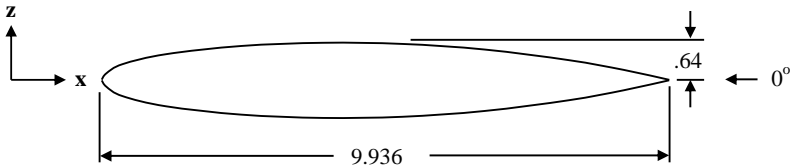


(a) Vertical Polarization



(b) Horizontal Polarization

Figure 8.14: 2-Meter sphere: bistatic RCS at 1.5 GHz.

(a) Profile in xy Plane(b) Profile in xz Plane**Figure 8.15:** NASA almond.

$$y(t) = 0.193333d \sqrt{1 - \left(\frac{t}{0.416667}\right)^2} \cos \phi \quad (8.76)$$

$$z(t) = 0.64444d \sqrt{1 - \left(\frac{t}{0.416667}\right)^2} \sin \phi \quad (8.77)$$

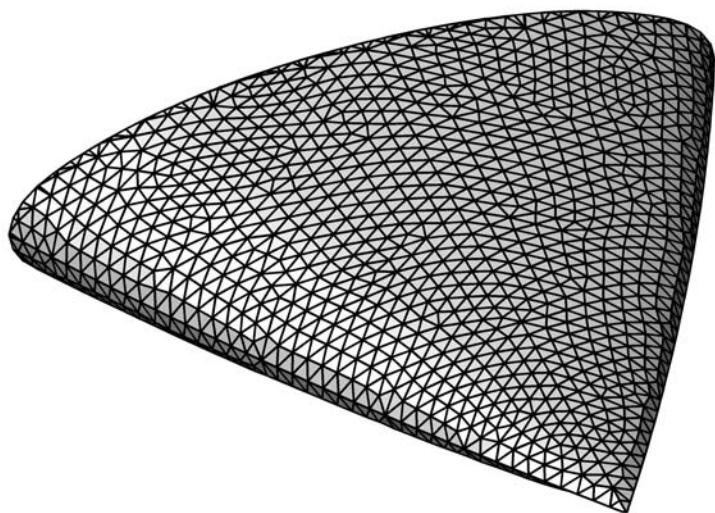
for $-0.41667 < t < 0$, and

$$x = dt \quad (8.78)$$

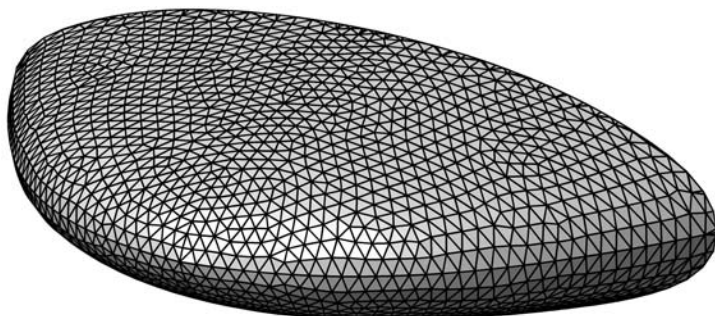
$$y(t) = 4.83345d \left[\sqrt{1 - \left(\frac{t}{2.08335}\right)^2} - 0.96 \right] \cos \phi \quad (8.79)$$

$$z(t) = 1.61115d \left[\sqrt{1 - \left(\frac{t}{2.08335}\right)^2} - 0.96 \right] \sin \phi \quad (8.80)$$

for $0 < t < 0.58333$. In our three-dimensional model we have attempted to create a facetization with the best possible aspect ratio. Surface detail of the model at 7 GHz is shown for the pointed and rounded regions in Figures 8.16a and 8.16b, respectively.



(a) Pointed End



(b) Rounded End

Figure 8.16: Almond facetization detail at 7 GHz.

The numerical results are compared to the EMCC measurements at 7 GHz in Figures 8.17a and 8.17b for vertical and horizontal polarizations, respectively. The computed results were lower than the measurements by approximately 1.5 dB across a large range of angles, and are adjusted in each plot. With this adjustment, the comparison is very good. Results at 9.92 GHz are shown in Figures 8.18a and 8.18b for vertical and horizontal polarizations, respectively. A similar bias was observed in this case as well, and after adjustment, the comparison is again very good. The reason for the bias in both cases is not known.

8.8.2.2 EMCC Ogive

The EMCC ogive was previously described in Section 6.6.3.1. The numerical results are compared to the EMCC measurements at 9.0 GHz in Figures 8.19a and 8.19b for vertical and horizontal polarizations, respectively. The agreement is very good.

8.8.2.3 EMCC Double Ogive

The EMCC double ogive was previously described in Section 6.6.3.2. The numerical results are compared to the EMCC measurements at 9.0 GHz in Figures 8.20a and 8.20b for vertical and horizontal polarizations, respectively. The agreement is very good, with some differences observed at end-on aspect angles.

8.8.2.4 EMCC Cone-Sphere

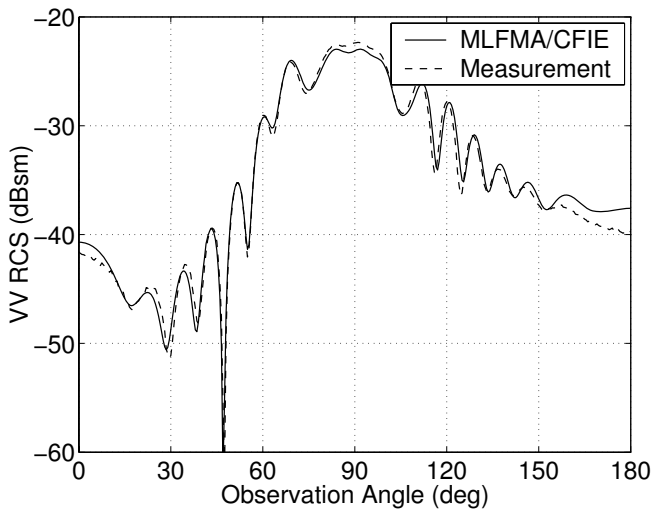
The EMCC cone-sphere was previously described in Section 6.6.3.3. The numerical results are compared to the EMCC measurements at 9.0 GHz in Figures 8.21a and 8.21b for vertical and horizontal polarizations, respectively. The agreement is fairly good, with the greatest differences observed in aspect angles near the tip. Because this is a region of very low backscattering intensity, the results are expected to compare less favorably.

8.8.2.5 EMCC Cone-Sphere with Gap

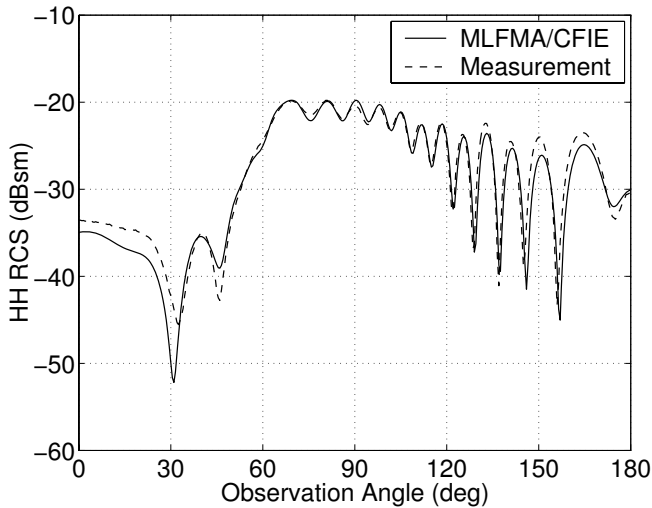
The EMCC cone-sphere with gap was previously described in Section 6.6.3.4. The numerical results are compared to the EMCC measurements at 9.0 GHz in Figures 8.22a and 8.22b for vertical and horizontal polarizations, respectively. The comparison is quite good at all aspect angles.

8.8.3 Summary of Examples

The run metrics for the examples in this chapter are summarized in Table 8.2. Listed for each case are the number of unknowns, number of MLFMA levels l_{max} , storage requirements for the near matrix and radiation and receive functions, number of right-hand sides and total compute time. The compute time comprises the entire

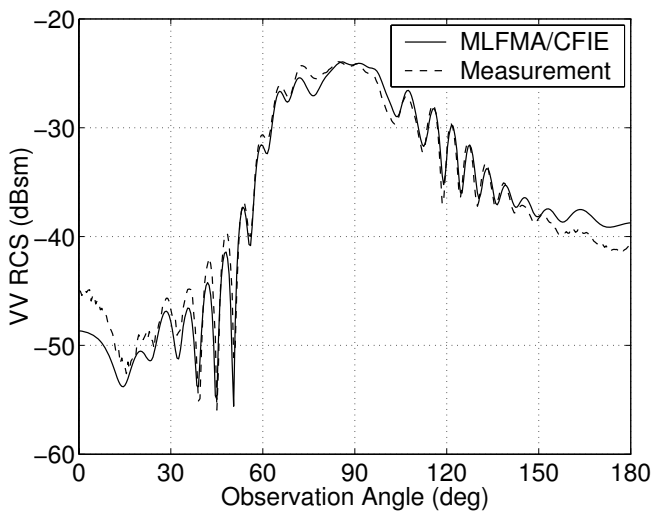


(a) Vertical Polarization

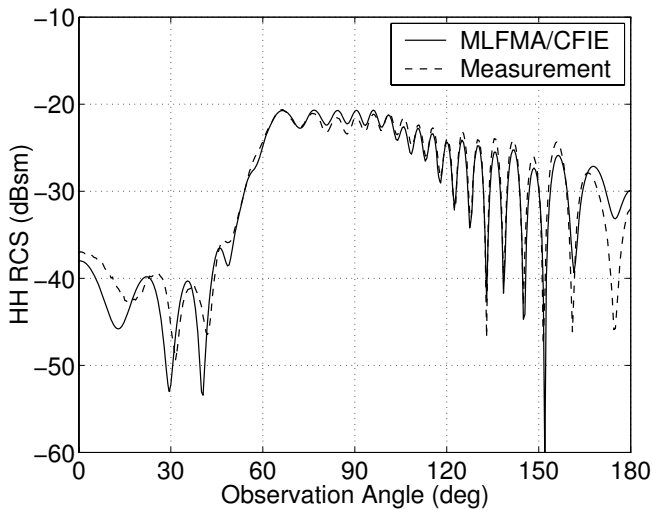


(b) Horizontal Polarization

Figure 8.17: NASA almond: MLFMA versus measurement at 7.0 GHz.

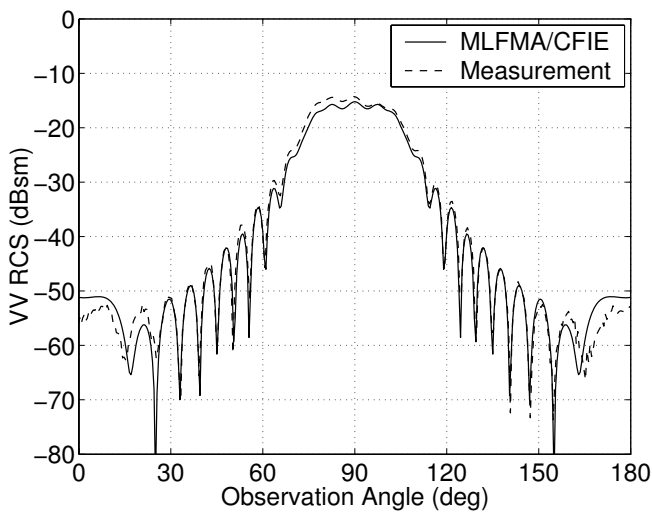


(a) Vertical Polarization

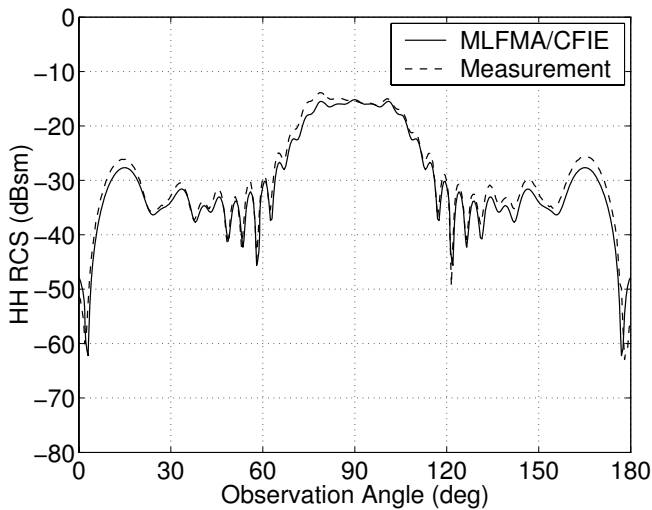


(b) Horizontal Polarization

Figure 8.18: NASA almond: MLFMA versus measurement at 9.92 GHz.

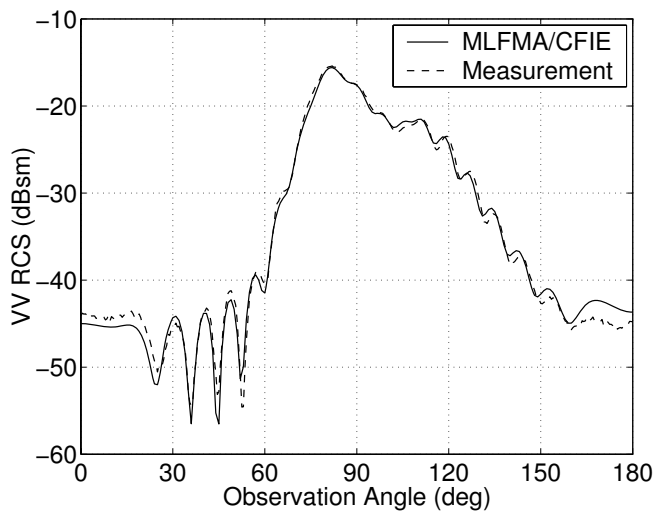


(a) Vertical Polarization

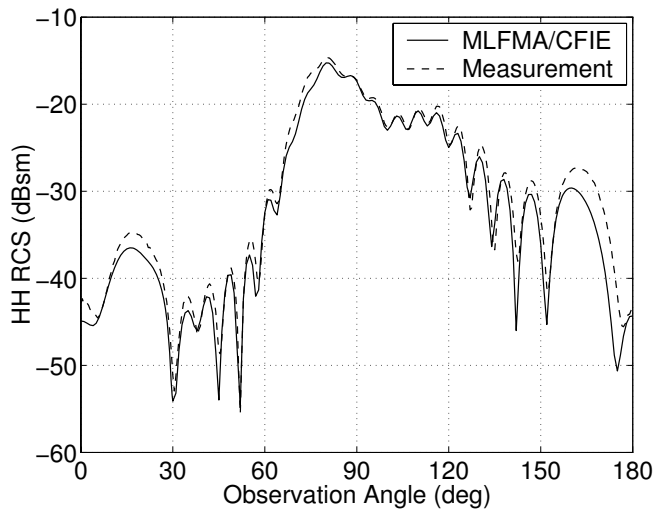


(b) Horizontal Polarization

Figure 8.19: EMCC ogive: MLFMA versus measurement at 9.0 GHz.

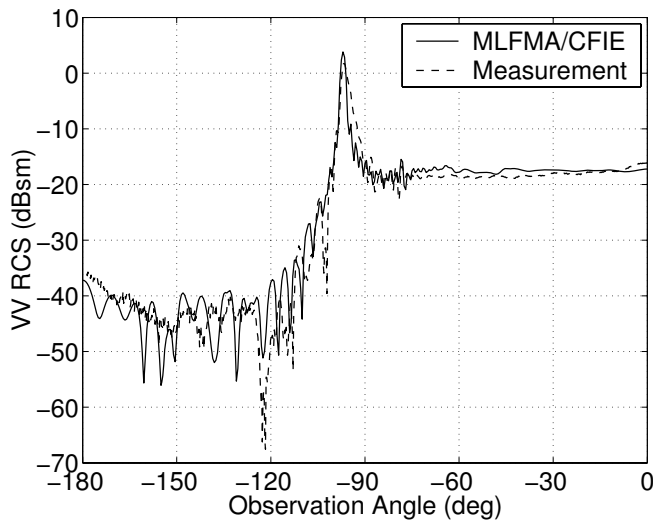


(a) Vertical Polarization

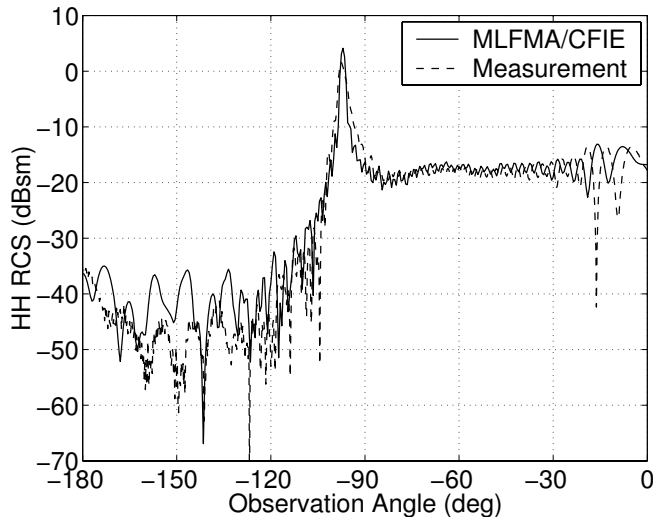


(b) Horizontal Polarization

Figure 8.20: EMCC double ogive: MLFMA versus measurement at 9.0 GHz.

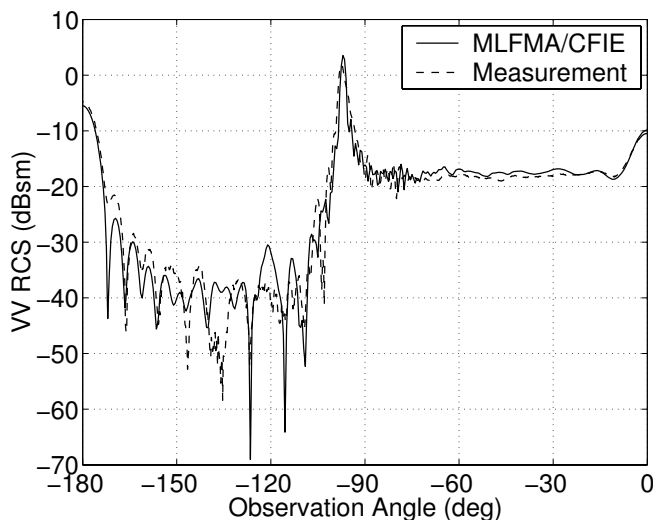


(a) Vertical Polarization

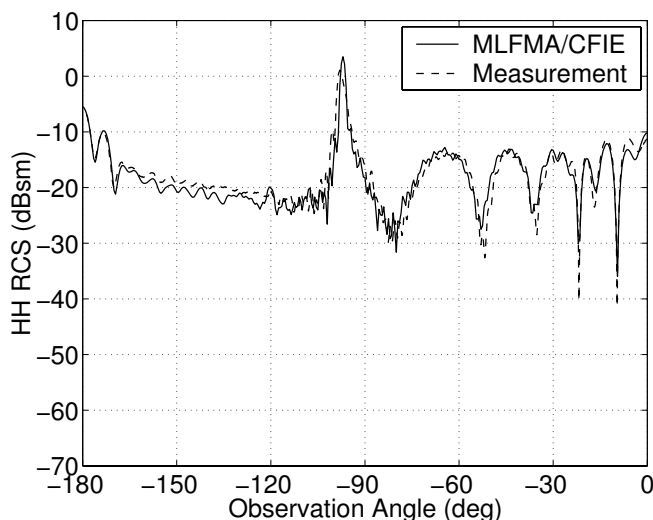


(b) Horizontal Polarization

Figure 8.21: EMCC cone-sphere: MLFMA versus measurement at 9.0 GHz.



(a) Vertical Polarization



(b) Horizontal Polarization

Figure 8.22: EMCC cone-sphere with gap: MLFMA versus measurement at 9.0 GHz.

Table 8.2: Summary of FMM Examples

Object	N	l_{max}	Near MB	FMM MB	NRHS	CPU
2-m Sphere (0.75)	30720	5	143.4	60.9	1	11 m
2-m Sphere (1.5)	122880	6	570.9	243.7	1	68 m
Almond (7.0)	70476	6	916.05	79.6	360	30.1 hr
Almond (9.92)	70476	6	916.05	131.2	360	33.9 hr
Ogive	32640	6	330.5	49.8	360	12.1 hr
Double Ogive	54360	6	578.25	61.38	360	22.6 hr
Cone-Sphere	116112	8	247.8	131.1	360	104 hr
Cone-Sphere/Gap	141000	8	391.5	159.2	360	125 hr

run including the near-matrix and radiation and receive function fills, MLFMA-accelerated iteration, and scattered field calculation. Runs are performed on an AMD Athlon MP 2600 at 2 GHz with 2GB memory under Red Hat Linux 7.3.

REFERENCES

- [1] L. Greengard and V. Rokhlin, “A fast algorithm for particle simulations,” *J. Comput. Phys.*, vol. 73, 325–348, 1987.
- [2] R. Coifman, V. Rokhlin, and S. Wandzura, “The fast multipole method for the wave equation: A pedestrian prescription,” *IEEE Antennas Propagat. Magazine*, vol. 35, 7–12, June 1993.
- [3] W. C. Chew, J. M. Jin, E. Michielssen, and J. Song, *Fast and Efficient Algorithms in Computational Electromagnetics*. Artech House, 2001.
- [4] J. Stratton, *Electromagnetic Theory*. McGraw-Hill, 1941.
- [5] J. M. Song and W. C. Chew, “Error analysis for the truncation of multipole expansion of vector green’s functions,” *IEEE Microwave Wireless Components Lett.*, vol. 11, no. 7, 311–313, 2001.
- [6] O. M. Bucci, C. Gennarelli, and C. Savarese, “Optimal interpolation of radiated fields over a sphere,” *IEEE Trans. Antennas Propagat.*, vol. 39, 1633–1643, November 1991.
- [7] P. Havé, “A parallel implementation of the fast multipole method for maxwell’s equations,” 2002.
- [8] E. Darve, “The fast multipole method: Numerical implementation,” *J. Comput. Phys.*, vol. 160, 195–240, 2000.
- [9] Y. Saad, *Iterative Methods for Sparse Linear Systems*. PWS, 1st ed., 1996.

- [10] J. Foley, A. van Dam, S. Feiner, and J. Hughes, *Computer Graphics: Principles and Practice*. Addison-Wesley, 1996.
- [11] R. Jakob-Chien and B. Alpert, “A fast spherical filter with uniform resolution,” *J. Comput. Phys.*, vol. 136, 580–584, 1997.
- [12] J. Sarvas, “Performing interpolation and anterpolation entirely by fast fourier transform in the 3-d multilevel fast multipole algorithm,” *SIAM J. Numer. Anal.*, vol. 41, no. 6, 2180–2196, 2003.
- [13] S. Koc, J. M. Song, and W. C. Chew, “Error analysis for the numerical evaluation of the diagonal forms of the spherical addition theorem,” *SIAM J. Numer. Anal.*, vol. 36, no. 3, 906–921, 1999.
- [14] M. Nilsson, “A parallel shared memory implementation of the fast multipole method for electromagnetics,” Tech. Rep. Technical Report 2003-049, Department of Information Technology, Scientific Computing, Uppsala University, October 2003.
- [15] B. Hariharan, S. Aluru, and B. Shanker, “A scalable parallel fast multipole method for analysis of scattering from perfect electrically conducting surfaces,” in *Supercomputing '02: Proceedings of the 2002 ACM/IEEE conference on Supercomputing*, 1–17, IEEE Computer Society Press, 2002.
- [16] K. Donepudi, J. Jin, S. Velampparambil, J. Song, and W. Chew, “A higher-order parallelized multilevel fast multipole algorithm for 3-d scattering,” *IEEE Trans. Antennas Propagat.*, vol. 49, 1069–1078, July 2001.
- [17] S. Velampparambil and W. C. Chew, “Parallelization of multilevel fast multipole algorithm on distributed memory computers,” Tech. Rep. 13-01, Center for Computational Electromagnetics, University of Illinois at Urbana–Champaign, 2001.
- [18] S. Velampparambil and W. C. Chew, “Analysis and performance of a distributed memory multilevel fast multipole algorithm,” *IEEE Trans. Antennas Propagat.*, vol. 53, 2719–2727, August 2005.
- [19] S. Velampparambil, W. C. Chew, and J. Song, “10 million unknowns: Is it that big?,” *IEEE Antennas Propagat. Mag.*, vol. 45, no. 2, 43–58, 2003.
- [20] J. M. Song, C. C. Lu, and W. C. Chew, “Multilevel fast multipole algorithm for electromagnetic scattering by large complex objects,” *IEEE Trans. Antennas Propagat.*, vol. 45, 1488–1493, October 1997.
- [21] A. C. Woo, H. T. G. Wang, M. J. Schuh, and M. L. Sanders, “Benchmark radar targets for the validation of computational electromagnetics programs,” *IEEE Antennas Propagat. Magazine*, vol. 35, 84–89, February 1993.

Chapter 9

Integration

Throughout this book we have considered many one- and two-dimensional integrals. While some of these integrals can be evaluated analytically, often we must employ a numerical integration (quadrature) scheme to obtain the results. Because the quality of the results obtained from the moment method depends on the accuracy of the matrix elements, a reliable and computationally efficient quadrature scheme is vital to any software implementation.

Numerical integration is a method for approximating a definite integral by a summation. A one-dimensional quadrature approximates an integral according to the formula

$$I = \int_a^b f(x) dx \approx \sum_{i=1}^N w(x_i) f(x_i) \quad (9.1)$$

where we have evaluated the function $f(x)$ at N unique locations x_i and employed quadrature *weights* w_i . The weights and abscissas are dependent on the type and order of quadrature being employed, and choices for these will be discussed in the following sections. The expression for a two-dimensional quadrature follows from (9.1) and is

$$I = \iint_S f(x, y) dx dy \approx \sum_{i=1}^N w(x_i, y_i) f(x_i, y_i) \quad (9.2)$$

In Chapter 7, we applied the MOM to surfaces described by triangular elements. In this chapter, we will consider analytic as well as numerical integration formulas designed specifically for these triangular regions.

9.1 ONE-DIMENSIONAL INTEGRATION

9.1.1 Centroidal Approximation

Many integrations in this book used a centroidal approximation. This method simply evaluates the function once and assumes that its value is constant throughout the entire domain. The function is typically evaluated at the center of the domain,

resulting in the expression

$$I = \int_a^b f(x) dx \approx (b - a) \cdot f([b + a]/2) \quad (9.3)$$

This centroidal or “one-point” integration rule is actually quite useful for small domains where the integrand varies slowly. A good example is when computing moment method matrix elements for basis function pairs located far away from one another. The results obtained using a one-point rule often differ very little from the results of a more accurate rule. The inaccuracy is often acceptable since the magnitude of these elements are usually very small compared to those much closer to the matrix diagonal.

9.1.2 Trapezoidal Rule

The classic trapezoidal rule applies a piecewise linear approximation to $f(x)$ throughout the range of integration. We subdivide the interval $[a, b]$ into $N = 2^{n-1}$, $n \geq 1$ small segments of equal length $h = (b - a)/N$ and compute the values $f(x_1), f(x_2), \dots, f(x_{N-1}), f(x_N)$, as shown in Figure 9.1. We compute the value of the integral inside each segment as

$$\int_{x_i}^{x_{i+1}} f(x) dx \approx h \left[\frac{1}{2} f_i + \frac{1}{2} f_{i+1} \right] \quad (9.4)$$

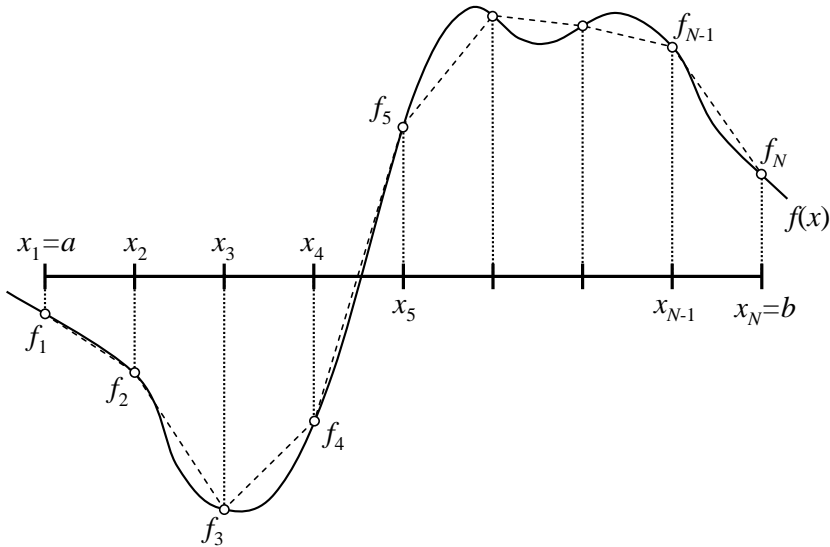


Figure 9.1: Piecewise linear approximation of $f(x)$.

Summing (9.4) across the entire interval, we derive the following expression for the integral, which we call the *trapezoidal rule*:

$$I = \int_a^b f(x) dx \approx h \left[\frac{f_1}{2} + f_2 + \cdots + f_{N-1} + \frac{f_N}{2} \right] + E_T \quad (9.5)$$

where the term E_T is the error. If $f''(x)$ is continuous and has upper bound M on $[a, b]$, then the bound on the error is [1]

$$|E_T| \leq \frac{b-a}{12} h^2 M \quad (9.6)$$

If additional accuracy is desired, the number of segments may be doubled and the previous N samples reused, requiring only $N - 1$ new evaluations of $f(x)$ for the new quadrature rule. This process may be repeated as necessary until the desired accuracy is reached.

9.1.2.1 Romberg Integration

Repeated applications of the trapezoidal rule results in an error comprising even powers of $1/N$ [2], which can be written as

$$I = I_{n,1} + \frac{A}{N^2} + \frac{B}{N^4} + \frac{C}{N^6} + \cdots \quad (9.7)$$

We note that the second-order term in the above decreases by a factor of four if we double the number of quadrature points. Using two applications of the rule, we can therefore write

$$I \approx I_{n,1} + \frac{K}{N^2} \quad (9.8)$$

and

$$I \approx I_{n+1,1} + \frac{K}{4N^2} \quad (9.9)$$

If we solve the above two equations for K we can eliminate the second order term and improve the previous solution to at least an $O(N^{-4})$ error. Doing so yields

$$I \approx I_{n+1,2} = \frac{4}{3} I_{n+1,1} - \frac{1}{3} I_{n,1} \quad (9.10)$$

which is a Richardson's extrapolation. Combining successive applications of the rule with higher and higher orders of extrapolation can greatly increase the accuracy of the solution and is known as *Romberg integration*. In this method, higher order extrapolates have the form

$$I_{n,m} = I_{n+1,m-1} + \frac{I_{n+1,m-1} - I_{n,m-1}}{4^{m-1} - 1} \quad (9.11)$$

An example heirarchy of extrapolates is illustrated in Figure 9.2 for $n \leq 4$. Applying Romberg integration using this heirarchy requires the results of the trapezoidal rule using 1, 2, 4, and 8 segments.

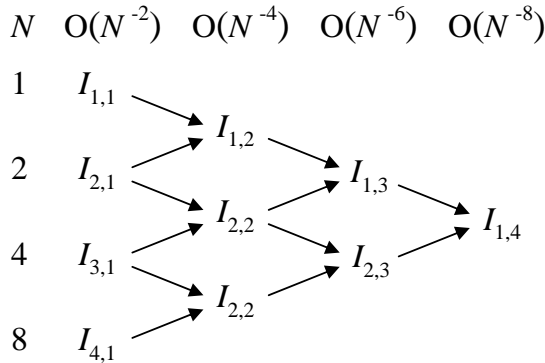


Figure 9.2: Heirarchy of Romberg extrapolates.

9.1.3 Simpson's Rule

Simpson's rule approximates $f(x)$ by a series of quadratic instead of linear polynomials, as shown in Figure 9.3. The interval $[a, b]$ is divided into N segments of equal length $h = (b - a)/N$, where $N \geq 2$ and even. Starting with the equation for a parabola,

$$f(x) = Ax^2 + Bx + C \quad (9.12)$$

we perform an integration over the two-segment interval $[-h, h]$, yielding

$$\int_{-h}^h (Ax^2 + Bx + C) dx = \left[A\frac{x^3}{3} + B\frac{x^2}{2} + Cx \right] \Big|_{-h}^h = \frac{h}{3}(2Ah^2 + 6C) \quad (9.13)$$

Since the parabola passes through the points $(-h, y_1)$, $(0, y_2)$, and (h, y_3) , we can compute the values

$$f_1 = Ah^2 - Bh + C \quad (9.14)$$

$$f_2 = C \quad (9.15)$$

and

$$f_3 = Ah^2 + Bh + C \quad (9.16)$$

from which we derive

$$2Ah^2 = f_1 + f_3 - 2f_2 \quad (9.17)$$

Inserting (9.15) and (9.17) into (9.13) yields

$$\int_{-h}^h (Ax^2 + Bx + C) dx = \frac{h}{3}[f_1 + 4f_2 + f_3] \quad (9.18)$$

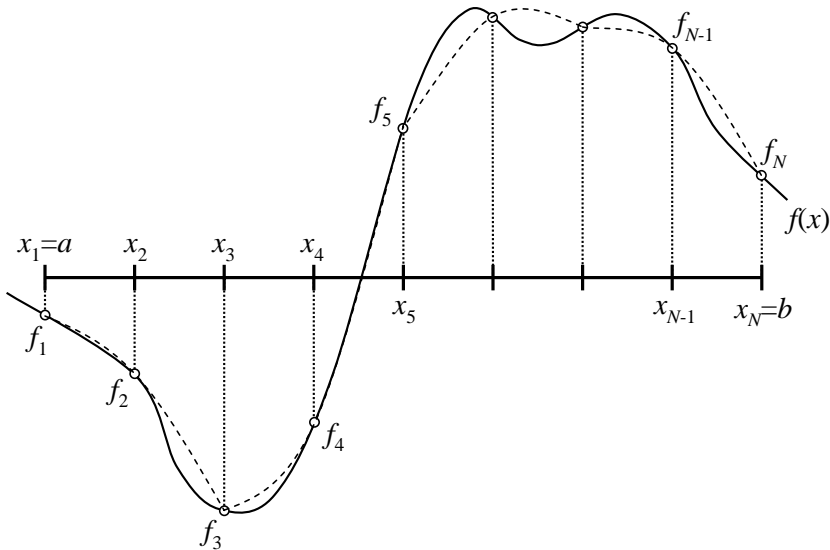


Figure 9.3: Piecewise parabolic approximation of $f(x)$.

Summing (9.18) across the entire interval, we derive the following expression which we call *Simpson's rule*:

$$\int_a^b f(x) dx = \frac{h}{3} \left[f_1 + 4f_2 + 2f_3 + 4f_4 + \cdots + 2f_{N-2} + 4f_{N-1} + f_N \right] + E_S \quad (9.19)$$

where the term E_S is the error. If $f^{(4)}(x)$ is continuous and has upper bound M on $[a, b]$, then the bound on the error is [1]

$$|E_S| \leq \frac{b-a}{180} h^4 M \quad (9.20)$$

Note that the result of (9.18) is equal to that obtained by the extrapolation of the trapezoidal rule in (9.10).

9.1.4 One-Dimensional Gaussian Quadrature

Using the trapezoidal or Simpson's rule, the interval $[a, b]$ is subdivided into equally spaced segments with fixed abscissas x_i . A more efficient integration rule can be developed if we allow the freedom to choose the optimal abscissas for integrating $f(x)$. Given the integral

$$\int_a^b W(x)f(x) dx \quad (9.21)$$

an N -point *Gaussian quadrature* integrates exactly a polynomial $f(x)$ of degree $2N - 1$ if the abscissas are chosen as the roots of the orthogonal polynomial for the same interval and *weighting function* $W(x)$. The most commonly used Gaussian quadrature is the *Gauss-Legendre* quadrature, of the form

$$\int_{-1}^1 f(x) dx = \sum_{i=1}^N w(x_i) f(x_i) \quad (9.22)$$

where $W(x) = 1$. The x_i for this rule are the roots of the Legendre polynomial of order N . The weights w_i are [3]

$$w_i = \frac{2}{(1 - x_i)^2 [P'_N(x_i)]^2} \quad (9.23)$$

A routine for computing an N -point Gauss-Legendre rule determines the locations of the zeros of $P_m(x)$ by Newton-Raphson iteration, and then the associated weights via (9.23). There are many short software routines for this available in books and through the Internet. Many of these retain the above range $[-1, 1]$, while some instead perform a mapping to $[0, 1]$. To use the rule, a change of variable should be used to map the interval $[a, b]$ to $[-1, 1]$ or $[0, 1]$.

9.2 INTEGRATION OVER TRIANGLES

Many of the integrals in this book are performed over triangular subdomains, and therefore efficient analytic and numerical integration techniques for triangular elements are essential. In this section, we consider these integrals in terms of *simplex coordinates*, also called *area coordinates* or *barycentric coordinates*. These coordinates comprise the transformation of a triangle of arbitrary shape to a canonical coordinate system. Analytic integrals are often easier to perform in simplex coordinates, and numerical quadrature rules are usually summarized using them as well.

9.2.1 Simplex Coordinates

To develop the simplex coordinate transformation, consider triangle T defined by the vertices \mathbf{v}_1 , \mathbf{v}_2 , and \mathbf{v}_3 and the edges $\mathbf{e}_1 = \mathbf{v}_2 - \mathbf{v}_1$, $\mathbf{e}_2 = \mathbf{v}_3 - \mathbf{v}_2$, and $\mathbf{e}_3 = \mathbf{v}_3 - \mathbf{v}_1$. Any point \mathbf{r} located on the triangle can be written as a weighted sum of these three nodes via

$$\mathbf{r} = \gamma \mathbf{v}_1 + \alpha \mathbf{v}_2 + \beta \mathbf{v}_3 \quad (9.24)$$

where α , β , and γ are the simplex coordinates

$$\alpha = \frac{A_1}{A}, \quad \beta = \frac{A_2}{A}, \quad \gamma = \frac{A_3}{A} \quad (9.25)$$

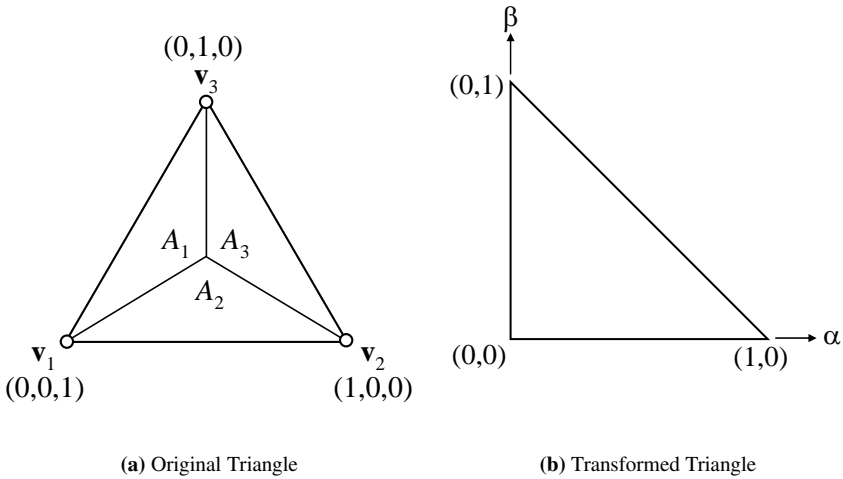


Figure 9.4: Simplex coordinates for a triangle.

and A is the area of T . These coordinates are subject to the constraint

$$\alpha + \beta + \gamma = 1 \quad (9.26)$$

therefore,

$$\gamma = 1 - \alpha - \beta \quad (9.27)$$

and

$$\mathbf{r} = (1 - \alpha - \beta)\mathbf{v}_1 + \alpha\mathbf{v}_2 + \beta\mathbf{v}_3 \quad (9.28)$$

Note that (9.24) has the form of a linear interpolation. Indeed, simplex coordinates will also allow us to perform a linear interpolation of a function $f(x, y)$ at points inside the triangle if its values are known at the vertices. The resulting transformation of the integral to simplex coordinates is

$$\iint_T f(\mathbf{r}) \, d\mathbf{r} = \iint_{T'} f(\alpha, \beta) |J(\alpha, \beta)| \, d\alpha \, d\beta = 2A \int_0^1 \int_0^{1-\alpha} f(\alpha, \beta) \, d\beta \, d\alpha \quad (9.29)$$

This transformation is illustrated in Figure 9.4.

Given a point \mathbf{r} inside a triangle, it is also desirable to obtain the simplex coordinates (α, β, γ) . We can write the barycentric expansion of $\mathbf{r} = (x, y, z)$ in terms of the components of the triangle vertices as

$$\begin{aligned} x &= \gamma x_1 + \alpha x_2 + \beta x_3 \\ y &= \gamma y_1 + \alpha y_2 + \beta y_3 \\ z &= \gamma z_1 + \alpha z_2 + \beta z_3 \end{aligned} \quad (9.30)$$

substituting $\gamma = 1 - \alpha - \beta$ into the above gives

$$\begin{aligned} x &= (1 - \alpha - \beta)x_1 + \alpha x_2 + \beta x_3 \\ y &= (1 - \alpha - \beta)y_1 + \alpha y_2 + \beta y_3 \\ z &= (1 - \alpha - \beta)z_1 + \alpha z_2 + \beta z_3 \end{aligned} \quad (9.31)$$

Rearranging, these are

$$\begin{aligned} \alpha(x_2 - x_1) + \beta(x_3 - x_1) + x_1 - x &= 0 \\ \alpha(y_2 - y_1) + \beta(y_3 - y_1) + y_1 - y &= 0 \\ \alpha(z_2 - z_1) + \beta(z_3 - z_1) + z_1 - z &= 0 \end{aligned} \quad (9.32)$$

and solving for α and β gives us

$$\alpha = \frac{B(F + I) - C(E + H)}{A(E + H) - B(D + G)} \quad (9.33)$$

and

$$\beta = \frac{A(F + I) - C(D + G)}{B(D + G) - A(E + H)} \quad (9.34)$$

where

$$\begin{aligned} A &= x_2 - x_1 \\ B &= x_3 - x_1 \\ C &= x_1 - x \\ D &= y_2 - y_1 \\ E &= y_3 - y_1 \\ F &= y_1 - y \\ G &= z_2 - z_1 \\ H &= z_3 - z_1 \\ I &= z_1 - z \end{aligned} \quad (9.35)$$

9.2.2 Radiation Integrals with a Constant Source

Far-field radiation integrals with a constant-valued source can be written as

$$I = \iint e^{j\mathbf{s} \cdot \mathbf{r}'} d\mathbf{r}' \quad (9.36)$$

Let us evaluate I over a triangular element of arbitrary shape. Using (9.29), this integral becomes

$$I = \iint_T e^{j\mathbf{s} \cdot \mathbf{r}'} d\mathbf{r}' = 2A \int_0^1 \int_0^{1-\alpha} e^{j\mathbf{s} \cdot (\alpha, \beta) \cdot \mathbf{r}'(\alpha, \beta)} d\beta d\alpha \quad (9.37)$$

Using (9.28) for $\mathbf{r}'(\alpha, \beta)$, we can write the above as

$$I = 2Ae^{j\mathbf{s} \cdot \mathbf{v}_1} \int_0^1 \int_0^{1-\alpha} e^{j\mathbf{s} \cdot \mathbf{e}_1 \alpha} e^{j\mathbf{s} \cdot \mathbf{e}_3 \beta} d\beta d\alpha \quad (9.38)$$

or

$$I = 2Ae^{js_1} \int_0^1 e^{js_2\alpha} \int_0^{1-\alpha} e^{js_3\beta} d\beta d\alpha \quad (9.39)$$

where $s_1 = \mathbf{s} \cdot \mathbf{v}_1$, $s_2 = \mathbf{s} \cdot \mathbf{e}_1$, and $s_3 = \mathbf{s} \cdot \mathbf{e}_3$. Evaluating the integral over β yields

$$I = 2Ae^{js_1} \int_0^1 e^{js_2\alpha} \left(\frac{e^{js_3\beta}}{js_3} \Big|_0^{1-\alpha} \right) d\alpha = 2Ae^{js_1} \int_0^1 e^{js_2\alpha} \left(\frac{e^{js_3(1-\alpha)}}{js_3} - \frac{1}{js_3} \right) d\alpha \quad (9.40)$$

which can be rewritten as

$$I = 2A \frac{e^{js_1}}{js_3} \int_0^1 \left(e^{js_3} e^{j\alpha(s_2-s_3)} - e^{j\alpha s_2} \right) d\alpha \quad (9.41)$$

Integrating over α yields

$$I = 2A \frac{e^{js_1}}{js_3} \left(\frac{e^{js_3} e^{j\alpha(s_2-s_3)}}{j(s_2-s_3)} - \frac{e^{j\alpha s_2}}{js_2} \right) \Big|_0^1 \quad (9.42)$$

$$I = 2A \frac{e^{js_1}}{js_3} \left(\frac{e^{js_2}}{j(s_2-s_3)} - \frac{e^{js_2}}{js_2} - \frac{e^{js_3}}{j(s_2-s_3)} + \frac{1}{js_2} \right) \quad (9.43)$$

and after some tedious but straightforward algebra, we obtain

$$I = -\frac{2Ae^{js_1}}{(s_2-s_3)} \left(\frac{1-e^{js_3}}{s_3} - \frac{1-e^{js_2}}{s_2} \right) \quad (9.44)$$

Let us now define the quantities $a_1 = \mathbf{s} \cdot \mathbf{v}_1$, $a_2 = \mathbf{s} \cdot \mathbf{v}_2$, and $a_3 = \mathbf{s} \cdot \mathbf{v}_3$. Therefore, $s_1 = a_1$, $s_2 = a_2 - a_1$, and $s_3 = a_3 - a_1$. Making these substitutions into the above equation yields

$$= \frac{2Ae^{ja_1}}{(a_2-a_3)} \left(\frac{1-e^{ja_2}e^{-ja_1}}{a_2-a_1} - \frac{1-e^{ja_3}e^{-ja_1}}{a_3-a_1} \right) \quad (9.45)$$

yielding

$$I = \frac{2A}{(a_3-a_2)} \left(\frac{e^{ja_1}-e^{ja_2}}{a_1-a_2} - \frac{e^{ja_1}-e^{ja_3}}{a_1-a_3} \right) \quad (9.46)$$

9.2.2.1 Special Cases

When \mathbf{s} is perpendicular to any of the three edges, (9.46) has a singularity and must be rewritten. When $\mathbf{s} \cdot \mathbf{e}_1 = a_2 - a_1 = 0$, we use the formula

$$I = \frac{2A}{(a_3-a_2)} \left(j e^{ja_1} - \frac{e^{ja_1}-e^{ja_3}}{a_1-a_3} \right) \quad (9.47)$$

Likewise, when $\mathbf{s} \cdot \mathbf{e}_3 = a_3 - a_1 = 0$,

$$I = \frac{2A}{(a_3 - a_2)} \left(\frac{e^{ja_1} - e^{ja_2}}{a_1 - a_2} - j e^{ja_1} \right) \quad (9.48)$$

and when $\mathbf{s} \cdot \mathbf{e}_2 = a_3 - a_2 = 0$,

$$I = \frac{2A}{(a_1 - a_2)} \left(j e^{ja_3} - \frac{e^{ja_1} - e^{ja_3}}{a_1 - a_3} \right) \quad (9.49)$$

When \mathbf{s} is normal to the triangle, we are left with

$$I = A e^{ja_1} \quad (9.50)$$

9.2.2.2 Radar Cross Section by Physical Optics

We can use the results of Section 9.2.2 to compute the scattered field of a triangle using the physical optics approximation (2.116). Given an incident electromagnetic plane wave with $\hat{\theta}^i$ (vertical) and $\hat{\phi}^i$ (horizontal) components, the incident electric field can be written as

$$\mathbf{E}^i(\mathbf{r}) = [E_\theta^i \hat{\theta}^i + E_\phi^i \hat{\phi}^i] e^{jk\hat{\mathbf{r}}^i \cdot \mathbf{r}} \quad (9.51)$$

and the incident magnetic field as

$$\mathbf{H}^i(\mathbf{r}) = -\frac{1}{\eta} \hat{\mathbf{r}} \times \mathbf{E}^i(\mathbf{r}) = \frac{1}{\eta} [E_\phi^i \hat{\theta}^i - E_\theta^i \hat{\phi}^i] e^{jk\hat{\mathbf{r}}^i \cdot \mathbf{r}} \quad (9.52)$$

and using (2.116), the scattered far electric field of (2.101) becomes

$$\mathbf{E}^s(\mathbf{r}) = -\frac{jk}{2\pi} \frac{e^{-jkr}}{r} \hat{\mathbf{n}} \times [E_\phi^i \hat{\theta}^i - E_\theta^i \hat{\phi}^i] \iint_T e^{jk(\hat{\mathbf{r}}^s + \hat{\mathbf{r}}^i) \cdot \mathbf{r}'} d\mathbf{r}' \quad (9.53)$$

where the region of integration is the triangle T whose surface normal $\hat{\mathbf{n}}$ is constant. The complete polarimetric response of an object can be represented by the *scattering matrix*, comprising a set of co-polarized and cross-polarized scattered fields. This can be written as

$$\begin{bmatrix} E_\theta^s \\ E_\phi^s \end{bmatrix} = \begin{bmatrix} I_{\theta\theta} & I_{\theta\phi} \\ I_{\phi\theta} & I_{\phi\phi} \end{bmatrix} \begin{bmatrix} E_\theta^i \\ E_\phi^i \end{bmatrix} C \quad (9.54)$$

where the identity $\mathbf{A} \cdot (\mathbf{B} \times \mathbf{C}) = \mathbf{B} \cdot (\mathbf{C} \times \mathbf{A})$ allows us to write

$$\begin{aligned} I_{\theta\theta} &= \hat{\mathbf{n}} \cdot (\hat{\theta}_s \times \hat{\phi}_i) \cdot I \\ I_{\phi\theta} &= \hat{\mathbf{n}} \cdot (\hat{\phi}_s \times \hat{\phi}_i) \cdot I \\ I_{\theta\phi} &= \hat{\mathbf{n}} \cdot (\hat{\theta}_i \times \hat{\theta}_s) \cdot I \\ I_{\phi\phi} &= \hat{\mathbf{n}} \cdot (\hat{\theta}_i \times \hat{\phi}_s) \cdot I \end{aligned} \quad (9.55)$$

with

$$I = \iint_T e^{jk(\hat{\mathbf{r}}^s + \hat{\mathbf{r}}^i) \cdot \mathbf{r}'} d\mathbf{r}' \quad (9.56)$$

and

$$C = -\frac{jk}{2\pi} \frac{e^{-jkr}}{r} \quad (9.57)$$

The integral (9.56) is evaluated via (9.46) with $\mathbf{s} = k(\hat{\mathbf{r}}^s + \hat{\mathbf{r}}^i)$. This result is similar to other PO-type integrals such as those evaluated in [4, 5, 6]. It can be used to compute the scattered field of an object composed of planar triangles if the shadowing of individual triangles can be determined. A polygon ray tracer is commonly used for this task, and forms the basis of high-frequency radar cross section codes such as Tripoint Industries' *lucernhammer MT*.

9.2.3 Radiation Integrals with a Linear Source

We next consider the far-field radiation integral with a linearly varying source, such as the RWG function of (7.1). This integral can be written as

$$\mathbf{I}(\mathbf{s}) = \iint_T \rho(\mathbf{r}') e^{j\mathbf{s} \cdot \mathbf{r}'} d\mathbf{r}' \quad (9.58)$$

where the source function is defined as

$$\rho(\mathbf{r}') = \mathbf{r}' - \mathbf{v}_1 \quad (9.59)$$

This corresponds to the RWG function defined on the edge opposite vertex \mathbf{v}_1 on T . Using (9.29), (9.58) becomes

$$\mathbf{I}(\mathbf{s}) = 2A \int_0^1 \int_0^{1-\alpha} e^{j\mathbf{s}(\alpha, \beta) \cdot \mathbf{r}'(\alpha, \beta)} d\beta d\alpha \quad (9.60)$$

and using (9.28) for $\mathbf{r}'(\alpha, \beta)$, we can write the above as

$$\mathbf{I}(\mathbf{s}) = 2A e^{j\mathbf{s} \cdot \mathbf{v}_1} \int_0^1 \int_0^{1-\alpha} (\alpha \mathbf{e}_1 + \beta \mathbf{e}_3) e^{j\mathbf{s} \cdot \mathbf{e}_1 \alpha} e^{j\mathbf{s} \cdot \mathbf{e}_3 \beta} d\beta d\alpha \quad (9.61)$$

or

$$\mathbf{I}(\mathbf{s}) = 2A e^{js_1} \int_0^1 \int_0^{1-\alpha} (\alpha \mathbf{e}_1 + \beta \mathbf{e}_3) e^{js_2 \alpha} e^{js_3 \beta} d\beta d\alpha \quad (9.62)$$

As in Section 9.2.2, this expression will have singularities when \mathbf{s} is perpendicular to any of the three edges. Therefore, we must consider the general form as well as the special cases.

9.2.3.1 General Case

For the general case, (9.62) evaluates to

$$\begin{aligned}\mathbf{I}(\mathbf{s}) = & -\frac{C}{s_3} \left[e^{js_2} \left(\frac{1-j(s_2-s_3)}{(s_2-s_3)^2} + \frac{js_2-1}{s_2^2} \right) - \frac{e^{js_3}}{(s_2-s_3)^2} + \frac{1}{s_2^2} \right] \mathbf{e}_1 \\ & - \frac{C}{s_2} \left[e^{js_3} \left(\frac{1-j(s_3-s_2)}{(s_3-s_2)^2} + \frac{js_3-1}{s_3^2} \right) - \frac{e^{js_2}}{(s_3-s_2)^2} + \frac{1}{s_3^2} \right] \mathbf{e}_3\end{aligned}\quad (9.63)$$

where

$$C = j2Ae^{js_1} \quad (9.64)$$

9.2.3.2 Special Cases

When \mathbf{s} is perpendicular to \mathbf{e}_1 ($s_2 = 0$), we can write (9.62) as

$$\mathbf{I}(\mathbf{s}) = 2Ae^{js_1} \int_0^1 \int_0^{1-\alpha} (\alpha \mathbf{e}_1 + \beta \mathbf{e}_3) e^{js_3 \beta} d\beta d\alpha \quad (9.65)$$

which evaluates to

$$\mathbf{I}(\mathbf{s}) = C \left[\frac{-1-j s_3}{s_3^3} + \frac{1}{2s_3} + \frac{e^{js_3}}{s_3^3} \right] \mathbf{e}_1 + C \left[e^{js_3} \left(\frac{js_3-2}{s_3^3} \right) + \frac{2}{s_3^3} + \frac{j}{s_3^2} \right] \mathbf{e}_3 \quad (9.66)$$

When \mathbf{s} is perpendicular to \mathbf{e}_3 ($s_3 = 0$), we can write (9.62) as

$$\mathbf{I}(\mathbf{s}) = 2Ae^{js_1} \int_0^1 \int_0^{1-\alpha} (\alpha \mathbf{e}_1 + \beta \mathbf{e}_3) e^{js_2 \alpha} d\beta d\alpha \quad (9.67)$$

which evaluates to

$$\mathbf{I}(\mathbf{s}) = C \left[e^{js_2} \left(\frac{js_2-2}{s_2^3} \right) + \frac{2}{s_2^3} + \frac{j}{s_2^2} \right] \mathbf{e}_1 + C \left[\frac{-1-j s_2}{s_2^3} + \frac{1}{2s_2} + \frac{e^{js_2}}{s_2^3} \right] \mathbf{e}_3 \quad (9.68)$$

When $s_2 = s_3 = s, s \neq 0$, we can write (9.62) as

$$\mathbf{I}(\mathbf{s}) = 2Ae^{js_1} \int_0^1 \int_0^{1-\alpha} (\alpha \mathbf{e}_1 + \beta \mathbf{e}_3) e^{js(\alpha+\beta)} d\beta d\alpha \quad (9.69)$$

which evaluates to

$$\mathbf{I}(\mathbf{s}) = C \left[e^{js} \left(\frac{1}{s^3} - \frac{1}{2s} - \frac{j}{s^2} \right) - \frac{1}{s^3} \right] [\mathbf{e}_1 + \mathbf{e}_3] \quad (9.70)$$

When \mathbf{s} is normal to the triangle, (9.62) becomes

$$\mathbf{I}(\mathbf{s}) = 2A e^{j\mathbf{s} \cdot \mathbf{v}_1} \int_0^1 \int_0^{1-\alpha} (\alpha \mathbf{e}_1 + \beta \mathbf{e}_3) d\beta d\alpha \quad (9.71)$$

which evaluates to

$$\mathbf{I}(\mathbf{s}) = \frac{A}{3} e^{js_1} (\mathbf{e}_1 + \mathbf{e}_3) \quad (9.72)$$

9.2.3.3 Comparison with Gaussian Quadrature

The formulas in Sections 9.2.3.1 and 9.2.3.2 are especially advantageous because they are valid for all frequencies. By comparison, an accurate numerical quadrature requires increasing numbers of integration points as the frequency increases, which is undesirable. Let us compare the analytical results to those obtained using a seven-point Gaussian quadrature rule (Section 9.2.4). The source triangle is equilateral and lies in the xy plane with vertices $\mathbf{v}_1 = (0, 0)$, $\mathbf{v}_2 = (l, 0)$, and $\mathbf{v}_3 = (l/2, l\sqrt{3}/2)$. The direction of radiation is $(\theta, \phi) = (\pi/2, \pi/4)$. In Figure 9.5a we compare the magnitude of the $\hat{\mathbf{x}}$ components of (9.62) versus the triangle edge length l in wavelengths. In Figure 9.5b we plot the difference between the results. We see that the analytical and numerical results compare very well to just over $l = 1\lambda$, at which point the numerical results start to diverge.

9.2.4 Gaussian Quadrature on Triangles

The most commonly referenced Gauss-Legendre locations and weights for triangles are the symmetric quadrature rules of [7]. This reference provides tables varying from degrees 1 to 20 (79 quadrature points). Tables for orders 2–5 are reproduced in Tables 9.1, 9.2, 9.3, and 9.4, respectively. The weights in these tables are normalized with respect to triangle area, i.e.,

$$\iint_S f(x, y) dx dy \approx A \sum_{i=1}^N w(\alpha_i, \beta_i) f(\alpha_i, \beta_i) \quad (9.73)$$

It is this author's experience that four- and seven-point quadrature rules work quite well for the MOM problems described in Chapters 7 and 8.

Table 9.1: Three-Point Quadrature Rule ($n = 2$)

i	α	β	γ	w
1	0.66666667	0.16666667	0.16666667	0.33333333
2	0.16666667	0.66666667	0.16666667	0.33333333
3	0.16666667	0.16666667	0.66666667	0.33333333

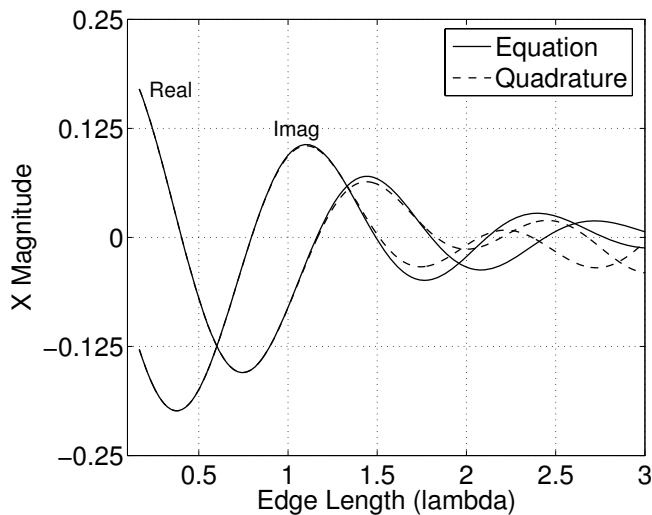
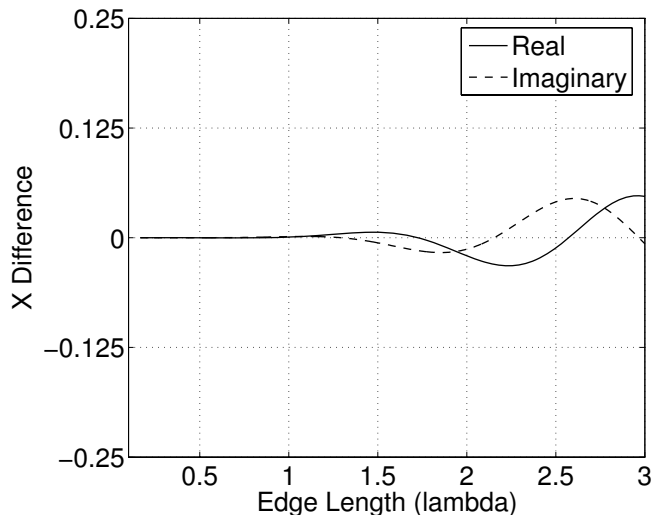
(a) \hat{x} -component(b) \hat{x} -difference**Figure 9.5:** Linear source radiation integral: equation versus quadrature.

Table 9.2: Four-Point Quadrature Rule ($n = 3$)

i	α	β	γ	w
1	0.33333333	0.33333333	0.33333333	-0.56250000
2	0.60000000	0.20000000	0.20000000	0.52083333
3	0.20000000	0.60000000	0.20000000	0.52083333
4	0.20000000	0.20000000	0.60000000	0.52083333

Table 9.3: Six-Point Quadrature Rule ($n = 4$)

i	α	β	γ	w
1	0.10810301	0.44594849	0.44594849	0.22338158
2	0.44594849	0.10810301	0.44594849	0.22338158
3	0.44594849	0.44594849	0.10810301	0.22338158
4	0.81684757	0.09157621	0.09157621	0.10995174
5	0.09157621	0.81684757	0.09157621	0.10995174
6	0.09157621	0.09157621	0.81684757	0.10995174

Table 9.4: Seven-Point Quadrature Rule ($n = 5$)

i	α	β	γ	w
1	0.33333333	0.33333333	0.33333333	0.22500000
2	0.05971587	0.47014206	0.47014206	0.13239415
3	0.47014206	0.05971587	0.47014206	0.13239415
4	0.47014206	0.47014206	0.05971587	0.13239415
5	0.79742698	0.10128650	0.10128650	0.12593918
6	0.10128650	0.79742698	0.10128650	0.12593918
7	0.10128650	0.10128650	0.79742698	0.12593918

REFERENCES

- [1] G. Thomas and R. Finney, *Calculus and Analytic Geometry*. Addison-Wesley, 1992.
- [2] A. F. Peterson, S. L. Ray, and R. Mittra, *Computational Methods for Electromagnetics*. IEEE Press, 1998.
- [3] W. H. Press, B. P. Flannery, S. A. Teukolsky, and W. T. Vetterling, *Numerical recipes in C: The Art of Scientific Computing*. Cambridge University Press, 1992.

- [4] W. B. Gordon, “Far-field approximations to the kirchoff-helmholtz representations of scattered fields,” *IEEE Trans. Antennas Propagat.*, vol. 23, 590–592, July 1975.
- [5] W. B. Gordon, “High frequency approximations to the physical optics scattering integral,” *IEEE Trans. Antennas Propagat.*, vol. 42, 427–432, March 1994.
- [6] S. Lee and R. Mittra, “Fourier transform of a polygonal shape function and its application in electromagnetics,” *IEEE Trans. Antennas Propagat.*, vol. 31, 99–103, January 1983.
- [7] D. Dunavant, “High degree efficient symmetrical gaussian quadrature rules for the triangle,” *Internat. J. Numer. Methods Engrg.*, vol. 21, 1129–1148, 1985.

Index

Antennas

- Archimedean spiral, 53, 201
- bowtie, 199
- circular loop, 83
- folded dipole, 86
- strip dipole, 198
- thin wire dipole, 79–83
- thin wire Yagi, 89

Basis functions, 45–48

- entire-domain, 47
- subdomain
 - piecewise sinusoidal, 46, 77
 - piecewise triangular, 45, 75, 99, 113, 114, 120, 124, 126
 - pulse, 45, 70, 73, 97, 105, 114, 120
 - RWG, 164

BLAS, 60

Centroidal approximation, 255

Combined field integral equation, 28–30, 141, 143, 215

Compressed sparse row format, 220

Condition number, 30, 52

EFIE and MFIE, 52

Delta-gap source

- thin wire, 65
- triangle, 178

Dual surface integral equation, 29

Duffy transform, 173

Edge finding algorithm, 165

Electric field integral equation

- three-dimensional
 - bodies of revolution, 127–136
 - FMM, 213–214
 - generalized, 25–26
 - using RWG functions, 167–179

two-dimensional

- TE polarization, 102–109, 120
- TM polarization, 100, 113
- TM polarization, 95

Electromagnetic boundary conditions, 6

Far field

- three-dimensional, 17
 - two-dimensional, 17
- Fast multipole method, 48
- addition theorem, 211
 - EFIE matrix elements, 213
 - matrix-vector product, 210
 - MFIE matrix elements, 214
 - radiation function, 213
 - transfer function, 212
 - wave translation, 212–213

Gaussian quadrature

- one-dimensional, 259
- two-dimensional, 267

Green's function

- three-dimensional, 9
- two-dimensional, 10

Hallén's equation, 65, 68–72

Huygen's principle, *see* Surface equivalent

Impedance matching, 78, 89

LAPACK, 60

Magnetic field integral equation

- three-dimensional
 - bodies of revolution, 136–141
 - FMM, 214–215
 - generalized, 26–28
 - using RWG functions, 179–184
- two-dimensional
 - TE polarization, 111–112, 120, 124
 - TM polarization, 109–111, 114

Magnetic frill, 66

MATLAB®, 60

Matrix-vector product, 48

- Maxwell's equations, 5
- Method of moments, 43–44
 - basis function, 43
 - Galerkin's method, 44
 - point matching, 44
 - testing function, 43
- MLFMA, *see* Multi-level FMM
- Multi-level FMM, 222–231
 - aggregation, 225
 - interpolation, 227, 231
 - computational complexity, 231
 - disaggregation, 226
 - grouping via octree, 222
 - interpolation, 227–230
 - via FFT, 229
 - via Lagrange polynomials, 229
 - via spherical harmonics, 228
 - matrix-vector product, 223
- Near field, 15
- One-level FMM, 215–222
 - computational complexity, 222
 - matrix-vector product, 221
 - number of multipoles, 216
 - radiation function, 220
 - sampling rates, 218
 - transfer function, 219
- Parallelization, 141, 185–186, 234
- Physical equivalent, 20
- Physical optics
 - approximation, 24
 - using for initial guess, 232
- Pocklington's equation, 65, 72–73
- Potential integrals, 40, 70–71, 76–78, 168–176, 180–182
- Preconditioning, 58, 235–240
 - block diagonal, 236
 - diagonal, 235
 - inverse LU, 236
 - sparse approximate inverse, 237
- Radar cross section
 - by physical optics, 264
 - examples
 - business card, 193
 - cone-sphere, 152, 245
 - cone-sphere with gap, 152, 245
 - double ogive, 149, 245
 - NASA almond, 240
 - ogive, 149, 245
 - plate cylinder, 192
 - reentry vehicle, 152
- sphere, 142, 189, 240
- two-dimensional cylinder, 113–124
 - wedge cylinder, 189
 - wedge-plate cylinder, 192
- three-dimensional, 17
- two-dimensional, 18
- Radiation integrals on triangles
 - constant source, 262
 - linear source, 265
- Range profile, 143
- Range-Doppler image, 156
- Resonance problem, 28
- Richardson's extrapolation, 257
- Romberg integration, 257
- Simplex coordinates, 260–262
- Simpson's rule, 258
- Singularity extraction, 168, 174, 181
- Solution of matrix equations, 48–57, 60
 - direct
 - Gaussian elimination, 48
 - LU decomposition, 50
 - iterative
 - biconjugate gradient, 54
 - biconjugate gradient stabilized, 55
 - conjugate gradient, 53
 - conjugate gradient squared, 55
 - stopping criteria, 56
- Surface equivalent, 18
- Thin wire kernel, 64
- Trapezoidal rule, 256
- Triangular surface model, 161–162
- Vector potential
 - electric, 12
 - magnetic, 11, 64, 103